



HAL
open science

Thin films based on Prussian blue analogues: growth mechanism and physical properties

Lili Lu

► **To cite this version:**

Lili Lu. Thin films based on Prussian blue analogues: growth mechanism and physical properties. Material chemistry. Ecole Polytechnique X, 2014. English. NNT : . pastel-01058915

HAL Id: pastel-01058915

<https://pastel.hal.science/pastel-01058915>

Submitted on 28 Aug 2014

HAL is a multi-disciplinary open access archive for the deposit and dissemination of scientific research documents, whether they are published or not. The documents may come from teaching and research institutions in France or abroad, or from public or private research centers.

L'archive ouverte pluridisciplinaire **HAL**, est destinée au dépôt et à la diffusion de documents scientifiques de niveau recherche, publiés ou non, émanant des établissements d'enseignement et de recherche français ou étrangers, des laboratoires publics ou privés.



Thèse présentée pour obtenir le grade de
DOCTEUR DE L'ÉCOLE POLYTECHNIQUE

Spécialité : Chimie des matériaux

Par

Lili LU

Thin films based on Prussian blue analogues: growth mechanism and physical properties

Thèse soutenue le 21 Mai 2014 devant le jury composé de :

Thierry GACOIN	LPMC, Ecole Polytechnique	Président
Anne BLEUZEN	ICMMO, Université Paris-Sud 11	Rapporteur
Yves DUMONT	GEMAC, Université de Versailles	Rapporteur
Jean-François LÉTARD	ICMCB, Université de Bordeaux	Examineur
Philippe ALLONGUE	LPMC, Ecole Polytechnique	Directeur de thèse
Isabelle MAURIN	LPMC, Ecole Polytechnique	Co-directeur de thèse

Acknowledgements

Chem is try.

This work was performed in the *Laboratory of Physique of Condensed Matter* (PMC), thanks to a China Scholarship Council (CSC) fellowship. I would like to show my gratitude to Francois OZANAM, director of PMC, who let me work in such a great laboratory.

I would like to express my sincere gratitude to the members of the jury. In particular, I am indebted to Anne BLEUZEN and Yves DUMONT, who acted as referees and wrote a report. I am also very grateful to Francois LETARD and Thierry GACOIN examined my work. I really appreciated that all the members of my jury had carefully read and corrected my manuscript. I also enjoyed the lively discussion during the thesis defense and the brilliant ideas they suggested.

I would like to thank Philippe ALLONGUE and Isabelle MAURIN, my supervisors, who offered me the opportunity to work on PBA. Philippe ALLONGUE showed me the real attitude for science and Isabelle MAURIN provided me her continuous enthusiasm on giving me invaluable advices, on facing and solving all the problems with me. I would like to say one sentence more to Isabelle, thanks for listening, for sharing, for always be there support me.

I also wish to thank other key team members, in particular Catherine HENRY de VILLENEUVE, for teaching me the surface chemistry and showing me the secrets of “micro”-wonderland of Si substrate and Thierry GACOIN, for the fruitful discussions and suggestions. Last but not least, I am deeply indebted to Robert CORTES, for putting so much of his time and interest in helping me performing the X ray characterizations, and explaining me the physics behind.

There are also other people in this lab who gave me suggestions and ever inspired me: thanks Fouad for always being so helpful (comme Encyclopédie), for the music that cheer me up; thanks Morgane, the first PhD student who picked up the wonderful subject of Prussian blue analogue in this lab, the experiments that we did together open the door of PBA for me; thanks Charlotte, my dearest previous officemate, for always share with me good and “free” scientific books, as well as the discussion that we had together about the spins, the orbitals, the anisotropy...

This research required various characterization techniques, which brought the help from outside of the lab: thank Emrick BRIAND and Ian. VICKRIDGE for the RBS measurement;

Isabelle KIEFFER and Denis TESTEMALE for the help in EXAS measurements; Sebastian PILLET and Pierrick DURAND for the testing XRD experiment. Thanks for putting so much enthusiasm on this PBA subject and providing plenty of interesting and useful ideas.

It is really a pleasure to be a member of PMC, as there are so many lovely people here, I want to thank Anne-Marie DUJARDIN, who is always very warm-hearted to help me with the administrative documents; Patrice, for the “bisou” every morning; the “thésa!”: Morgane, the girls’ party, shopping together, the speleology...thanks for sharing so many beautiful moments with me, they are unforgettable! Charlotte, those tea breaks, accompanied by sharing chocolates, snacks, as well as those little gossips, made days very interesting and vivid; Xiaoxin, the first Chinese I met in France, who helped me and made the first days in France not so difficult; Long, who can make the most delicious nem that I ever tasted, thanks for being so nice even though sometimes we have to “fight” for AFM; Nikoletta & Manon, the cutest French speaking group (including me), thanks for those post-it, the symbols (on the phone) and the chocolates, which contain so many courage and support; Fabien, the greatest magician during coffee break; Joseph, for sharing ur music and jokes during those difficult but happy days doing experiments in Grenoble, Lucie, Nicolas, Maxime, Jie, Maria, Tapajyoti.....Thank you all.

Finally, I would like to thank the people who mean most to me, those who are always there with unconditional support, keep faith in me, and listen to me: my parents, my friend Jin, especially my boyfriend Bei. Thanks you all for being so patient and thoughtful, for all the efforts that you have been done to make me feel beloved all the time.

Table of contents

Chapter 1: Introduction	1
1.1 Crystal structure and properties of Prussian blue analogues	1
1.1.1 Description of the crystal structure.....	1
1.1.2 Main properties of Prussian blue analogues	2
1.2 Thin film deposition of Prussian blue analogues.....	3
1.2.1 Techniques used in previous works	3
1.2.2 Multilayer and core-shell heterostructures.....	6
1.2.3 Morphology of Prussian blue analogue films	7
1.3 An alternative strategy for film growth	8
1.3.1 The choice of the substrate	9
1.3.2 The choice of the solution composition	10
1.4 Objectives and outline of the manuscript	13
1.5 References.....	14
Chapter 2: Functionalization of Si (111) surfaces	23
2.1 Introduction.....	23
2.2 Experimental protocols.....	24
2.2.1 Materials	24
2.2.2 Surface functionalization.....	25
2.3 Surface morphology	26
2.3.1 Atomic Force Microscopy (AFM).....	26
2.3.2 X-ray reflectivity (XRR).....	28
2.4 Surface composition	29
2.4.1 Qualitative analysis.....	29
2.4.2 Quantitative analysis	31
2.4.3 Discussion.....	34
2.5 Conclusion.....	35
2.6 References.....	36
Chapter 3: Growth and magnetic properties of $\text{Rb}_x\text{Ni}[\text{Cr}(\text{CN})_6]_y \cdot z\text{H}_2\text{O}$ films	39
3.1 Introduction.....	39
3.2 Experimental section.....	40
3.2.1 Preparation of the solution used for deposition.....	40

3.2.2 Rb _x Ni[Cr(CN) ₆] _y •zH ₂ O film deposition.....	40
3.3 Results	41
3.3.1 X-ray reflectivity (XRR) measurements.....	41
3.3.2 Atomic Force Microscopy (AFM) characterizations.....	45
3.3.3 X-ray diffraction (XRD).....	47
3.3.4 Rutherford backscattering (RBS) characterizations	50
3.3.5 Influence of sample rotation	52
3.3.6 Magnetic characterizations	54
3.4 Discussion.....	57
3.4.1 Chemical composition of the RbNiCr films.....	57
3.4.2 Nucleation and growth mechanism.....	57
3.4.3 Magnetic properties	61
3.5 Conclusion.....	65
3.6 References.....	67
Chapter 4: Growth and photo-switching properties of Rb_xCo[Fe(CN)₆]_y•zH₂O films	69
4.1 Introduction.....	69
4.2 Experimental section.....	70
4.2.1 Preparation of the solution of precursors	70
4.2.2 Set-up used for film deposition	71
4.3 Film nucleation and growth.....	72
4.3.1 Results	72
4.3.2 Discussion.....	81
4.4 Photo-switching properties.....	84
4.4.1 Results	84
4.4.2 Discussion.....	88
4.5 Conclusion.....	92
4.6 References.....	93
Chapter 5: Heterostructures made of Rb_xNi[Cr(CN)₆]_y•zH₂O and Rb_xCo[Fe(CN)₆]_y•zH₂O.	97
5.1 Introduction.....	97
5.2 Experimental section.....	98
5.2.1 Preparation of the solutions used for deposition.....	98
5.2.2 Set-up used for film deposition	99
5.3 Results and discussion.....	100
5.3.1 Heterostructure A: Si (111)/RbCoFe/RbNiCr	100

5.3.2 Heterostructure B: Si (111)/RbNiCr/RbCoFe	108
5.4 Conclusion	115
5.5 References	116
General Summary and Conclusion	119
Appendix 1: Experiments and techniques	123
A.1.1 Structural and microstructural characterizations	123
A.1.1.1 Atomic force microscopy (AFM)	123
A.1.1.2 Scanning Electron Microscopy (SEM)	124
A.1.1.3 X-ray reflectivity (XRR)	124
A.1.1.4 X-ray diffraction (XRD)	125
A.1.2 FTIR Spectroscopy	126
A.1.2.1 General method	126
A.1.2.2 Fitting procedure	127
A.1.3 Rutherford Backscattering Spectroscopy	129
A.1.3.1 General method	129
A.1.3.2 Calibration of the energy-channel curve ⁷	129
A.1.3.3 Conversion in absolute areal density values	130
A.1.4 Magnetic measurements	131
A.1.5 X-ray absorption spectroscopy measurements	132
A.1.5.1 General method	132
A.1.5.2 Sample preparation and measurement geometry	136
A.1.5.3 Data extraction, normalization and fitting	136
A.1.6 References	139
Appendix 2: Supplementary information on Chapter 2	141
A.2.1 Solution preparation	141
A.2.2 Complementary ATR-FTIR spectra	142
Appendix 3: Supplementary Information for Chapter 3	143
A.3.1 Synthesis and characterization of the RbNiCr reference particles	143
A.3.2 Scanning Electron Microscopy (SEM) imaging	144
A.3.3 RBS spectra for RbNiCr films with different deposition time.	145
A.3.4 Characterizations of RbNiCr films prepared with different rotation rates	146
A.3.4.1 AFM	146
A.3.4.2 XRR	147
A.3.4.3 XRD	148

A.3.4.4 RBS.....	149
A.3.5 Full $M - H$ curves	150
A.3.6 Analysis of T_c and β values from Field cooled magnetization curve	151
Appendix 4: Supplementary information for Chapter 4.....	153
A.4.1 Effect of solution deoxygenation.....	153
A.4.2 Scan Electronic Microscopy (SEM)	154
Appendix 5: Supplementary information for Chapter 5.....	155
A.5.1 Growth of Si (111)/RbNiCr layers monitored by FTIR measurements.....	155
A.5.2 Growth of Si (111)/RbCoFe layers monitored by FTIR measurements	158
A.5.3 References.....	161

Chapter 1

Introduction

Prussian blue analogues, with general formula $A_xM[M'(CN)_6]_y \cdot zH_2O$, where A is an alkali-metal cation, and M and M' are divalent and trivalent transition-metal cations respectively, have attracted considerable interest in the last decades. In addition to magnetic¹ and photo-magnetic properties^{2,3,4}, the availability of degenerate or quasi-degenerate electronic states has made them ideal systems to explore cooperative switching phenomena, with potential applications for memory devices and magneto-optical switching. As some of these applications require their elaboration as thin layers or heterostructures, we shortly describe in this introduction the crystal structure and the main properties of Prussian blue analogues. In a second part, we survey the different deposition methods described in the literature and end with an introduction to the original deposition route that will be used in this work.

1.1 Crystal structure and properties of Prussian blue analogues

1.1.1 Description of the crystal structure

Prussian blue, $Fe^{3+}[Fe^{2+}(CN)_6]_{0.75} \cdot 3H_2O$, is a well-known mixed valence system, used as a deep blue pigment. Prussian blue analogues, $A_xM[M'(CN)_6]_y \cdot zH_2O$ are isostructural compounds obtained by varying the nature of the M and M' metal cations. For divalent M cation and trivalent M'(CN)₆ cyanometallate, two types of crystal structure can be adopted: for y = 1, the Prussian blue derivative presents a regular face-centered cubic (fcc) structure, with two M and M' fcc networks interconnected via C≡N bridges (see **Figure 1.1b**). To compensate the charge balance between the M and [M'(CN)₆] species, alkali metal ions occupy half of the eight *sub*-octants of the lattice. For a description in terms of polyhedral units, the crystal structure may be represented as corner-shared [M'(CN)₆] and [MN₆] octahedra. For y < 1, Ludi et al.⁵ proposed a fractional occupancy of the [M'(CN)₆] sites, with additional ligand water molecules filling the vacant sites and coordinated to the nearby M metal cations (see **Figure 1.1a**). y values between 0 and 1 can also be observed, with a fractional number of alkali ions for charge compensation. In the two latter cases, the space group is $Fm\bar{3}m$ (No. 225). M ions occupy the apexes (position: 0, 0, 0) of the asymmetric unit and M' ions are in the middle of the edges (position: 0.5, 0, 0). Different alkali ions, such as Na, K, Rb or Cs, can be incorporated in the crystal structure at *Wyckoff* position 8c (1/4, 1/4, 1/4). According to a previous neutron diffraction study,^{6,7} water molecules occupy three

independent positions: one is ligand water (H_2O_L), coordinated to Co atoms ($24e$ site), while the two others are zeolitic water (H_2O_Z), with a large spatial distribution, either in the center of the empty *sub*-octants (H_2O_{Z1} , $8c$ site) or slightly off-centered at (x, x, x) due to hydrogen bonding with H_2O_L (H_2O_{Z2} , $32f$ site).

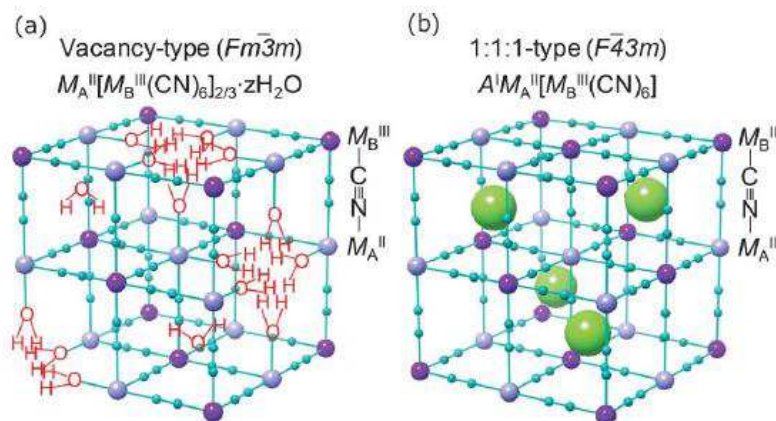


Figure 1.1. Scheme of the crystal structure of Prussian blue analogues: (a) $\text{M}^{2+}\text{M}'^{3+}[(\text{CN})_6]_{2/3} \cdot z\text{H}_2\text{O}$ and (b) $\text{A}^+\text{M}^{2+}\text{M}'^{3+}[(\text{CN})_6] \cdot z\text{H}_2\text{O}$.⁸

1.1.2 Main properties of Prussian blue analogues

Prussian blue analogues are commonly synthesized in aqueous solvents starting from $\text{M}'(\text{CN})_6^{m-}$ and $\text{M}(\text{OH}_2)_6^{n+}$ soluble precursors; and the variety of $\text{M}'(\text{CN})_6^{m-}$ and metal ions M building blocks that can be assembled leads to multiple functionalities. Their porous host-guest structure is used in exchanging of alkali ions, such as ^{137}Cs and Tl^+ ;⁹ in chemical and electrochemical sensors¹⁰ and gas storage^{11,12}. Electrochemical behaviors have been found in PBAs, associated with high proton conductivity in Co(II)-Cr(III) compounds, as well as Lithium incorporation for Li batteries in Cu(II)-Fe(III) PBAs.

In terms of magnetic exchange interaction between the two metal ions, superexchange coupling through the CN bridge led to a variety of behaviors up to relatively high ordering temperatures.¹ Ferromagnetism has been reported for Ni-Cr PBA compound up to 90 K,¹³ ferrimagnetism for Co-Fe PBAs up to 20 K,¹⁴ and ferrimagnetism in V-Cr PBA.¹ The magnetic ordering temperature typically depends on the M'/M ratio (number of magnetic neighbors), which is related to the alkali metal content because of charge compensation.¹⁵

Some Prussian blue analogues exhibit phase transitions induced by an electron transfer between the M and M' metal sites that can be triggered by temperature^{16,17}, light irradiation¹⁸, or pressure¹⁸. Among which the photo- or thermally-driven charge-transfer-induced spin transitions (CTIST) in cobalt hexacyanoferrates have been extensively studied.^{19,20,21,22,23} In these compounds, CTIST is accompanied by a large magnetization increase, due to the

transformation of $\text{Fe}^{2+}\text{-CN-Co}^{3+}$ diamagnetic pairs into $\text{Fe}^{3+}\text{-CN-Co}^{2+}$ magnetic pairs. Bleuzen *et al* investigated in a systematic way the conditions to observe photo-magnetization changes²⁴ and for the maximum photo-efficiency;²⁵ the electronic configuration and the local structure of both the ground and excited states have been analyzed,²⁶ as well as the influence of pressure and the relative stability of the low spin and high spin states²⁷. They also found that the nature of the alkali metal ion can significantly affect the properties of the PBAs.^{24,28,29} Meisel *et al* found that the magnetization can either increase or decrease under visible light irradiation depending on Ni content in the ternary metal Prussian blue analogue, $\text{Na}_\alpha\text{Ni}_{1-x}\text{Co}_x[\text{Fe}(\text{CN})_6]_\beta \cdot z\text{H}_2\text{O}$.²⁰

1.2 Thin film deposition of Prussian blue analogues

For applications in opto-electronics and memory devices, thin film deposition is essential. Preparing layers of photo-switchable $\text{A}_x\text{Co}[\text{Fe}(\text{CN})_6]_y \cdot z\text{H}_2\text{O}$ compounds with a thickness comparable or smaller than the depth of penetration of excitation light is also pivotal for a better understanding of the photo-switching properties of these systems. In addition, multiple properties or synergic effects^{30,31,32} could be expected in hybrid heterostructures due to surface and interface effects. In the following, we will present a short literature survey of the different deposition methods used to prepare films of Prussian blue analogues.

1.2.1 Techniques used in previous works

1.2.1.1 Electrochemical routes

Electrochemical deposition has been widely used for the growth of Prussian blue films and of its analogues.^{33,34,35} Sato *et al.*³⁶ reported the electrochemical deposition of the high T_C (270 K) $\text{Cr}_{2.12}\text{Cr}(\text{CN})_6 \cdot z\text{H}_2\text{O}$ compound onto SnO_2 coated glass electrode, and found an electrochemically induced switching phenomenon between a ferromagnetic and a paramagnetic state. They also reported that the electronic structure of electrochemically deposited $\text{Na}_{0.4}\text{Co}_{1.3}[\text{Fe}(\text{CN})_6] \cdot 5\text{H}_2\text{O}$ thin film can be switched from $\text{Fe}^{3+}\text{-CN-Co}^{2+}$ (high spin) to $\text{Fe}^{2+}\text{-CN-Co}^{3+}$ (low spin) by exchanging the alkali metal ion (from Na^+ to K^+).³⁷

Hashimoto and co-workers prepared high T_C (from 220 K to 300 K) magnetic films composed of mixed $\text{V}_x^{2+/3+}\text{Cr}^{2+}_{(1-x)}[\text{Cr}^{3+}(\text{CN})_6]_y \cdot z\text{H}_2\text{O}$, which shows various colors (from colorless to green and then blue) depending on the vanadium content.³⁸ A similar method has been used to prepare $(\text{Fe}_x\text{Cr}_{1-x})_3[\text{Cr}(\text{CN})_6]_2 \cdot z\text{H}_2\text{O}$ magnetic films, as shown in **Figure 1.2**.^{39,40,41} Ohkoshi *et al.*⁴¹ investigated the magneto-optical properties of these $(\text{Fe}_x\text{Cr}_{1-x})_3[\text{Cr}(\text{CN})_6]_2 \cdot z\text{H}_2\text{O}$ films, which display magnetization-induced second harmonic generation below their Curie temperature. A Faraday effect was also reported for

electrochemically deposited thin films of $K_{0.31}V^{2+}_{0.49}V^{3+}_{0.51}[Cr(CN)_6]_{0.94} \cdot 6.5H_2O$ and $K_{0.61}V^{2+}_{0.97}V^{3+}_{0.03}[Cr^{III}(CN)_6]_{0.88} \cdot 7.2H_2O \cdot 0.4C_2H_5OH$.⁴²

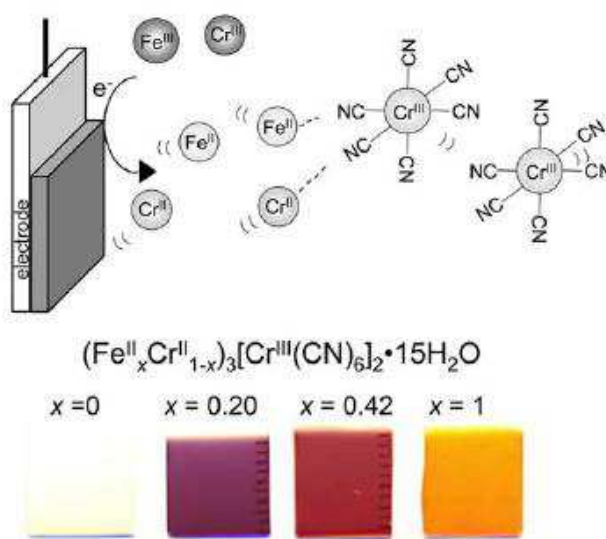


Figure 1.2. Scheme of the electrochemical deposition of magnetic films based on binary and ternary metal Prussian blue analogues.⁴¹

1.2.1.2 Layer-by-Layer (LBL) deposition using sequential adsorption

Other wet chemistry methods have also been developed. The mostly used is based on sequential adsorption. This method, which consists of the alternate adsorption of polyanions and polycations on a charged surface, was developed in the late 90s⁴³ and has known a significant throughput since then, due to its ease of implementation and applications of the as-obtained films in various fields (nonlinear optics, biomaterials, filtering, etc).

Culp *et al*⁴⁴ first modified the surface of a Langmuir monolayer with a two dimensional Ni-Fe cyanide grid network, this surface layer can be considered as the starting layer of a PBA lattice. A film of Prussian blue was further obtained by sequential immersion of this substrate in two solutions of precursors, one containing the $Fe(OH_2)_6^{2+}$ reactant and the other one, $Fe(CN)_6^{3-}$ species as shown in **Figure 1.3**. The film thickness can then be controlled by increasing the number of immersion cycles. Similar work have been conducted for Fe-Co^{45,32,46}, Fe-Mn⁴⁵, and Ni-Cr³¹ cyanide grid networks and the corresponding thin films. Films of the photo-switchable $Rb_xCo[Fe(CN)_6]_y \cdot zH_2O$ compounds were prepared by such LbL assembly process and showed photomagnetic effects similar to those observed in the bulk material.^{47,32,48}

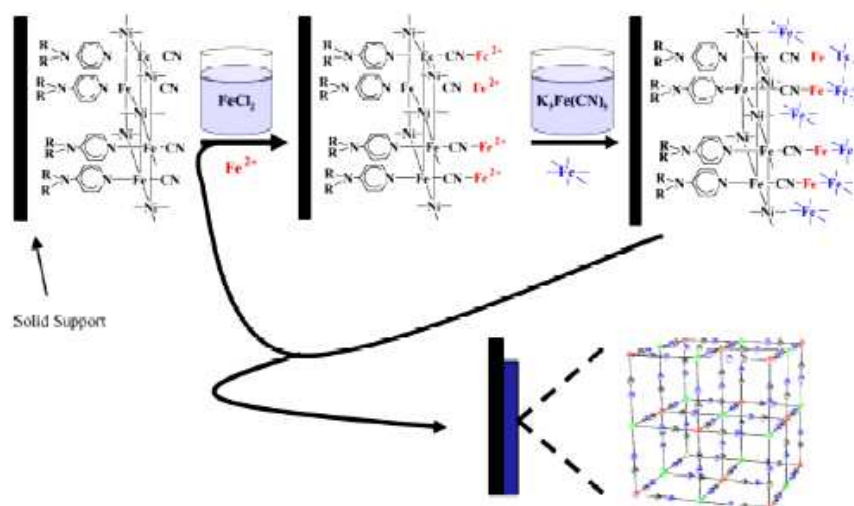


Figure 1.3. Sequential deposition of cationic and anionic building blocks to form Prussian blue onto a surface modified by a monolayer of a square grid template.⁴⁴

Recently, Mallah *et al.* prepared magnetic films and multilayers made of NiCr and NiFe/NiCr Prussian blue analogues on functionalized Si (100) surfaces by sequential growth. The Si (100) surface was firstly functionalized by monolayers bearing bipyridine end groups that were further immersed in a solution of Ni^{2+} salt. The resultant films have a minimum thickness of 6 nm. However, AFM imaging shows isolated dots and a rather low coverage of the substrate.⁴⁹

1.2.1.3 Formation of Langmuir mono and multi-layers

The Langmuir-Blodgett (LB) technique is based on the transfer of an assembled monolayer at the air/water interface onto a solid support. This method has been successfully used for the formation of the M-M' cyanide grid networks described in the previous section.⁵⁰ Mingotaud and coworkers also took use of it for the formation of Prussian blue-like mono and multilayers. They firstly dispersed a metal cation salt and the metalocyanide precursor (of diluted concentration, 10^{-6} mol/L) with positively charged dimethyldioctadecylammonium bromide, and transfer the as-formed Langmuir layer (see **Figure 1.4**) onto a solid substrate leading to LB monolayers (and multilayers by repeating the process) containing ferromagnetic entities.⁵¹ Thin films made of Prussian blue analogues and a ruthenium tris(bipyridine) complex⁵² (or a derivative of this complex⁵³) have also been grown this way. Yamamoto *et al.*^{54,55,56} used a modified Langmuir monolayer, i.e. amphiphilic molecules and clay platelets, to play a template role for the formation of Co-Fe PBA films of different thickness. Titania nano-sheets were also used as templates.⁵⁷

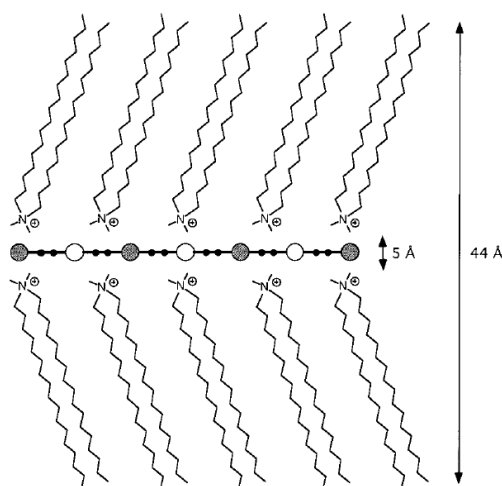


Figure 1.4. Schematic organization of a LB monolayer made of a Fe^{3+} -CN- Fe^{2+} grid.⁵¹

1.2.1.4 Other approaches for Prussian blue thin film deposition

Besides these widely used methods, other deposition techniques are described in the literature, such as composite films with a sol-gel matrix,⁵⁸ using polyelectrolyte coated surfaces^{59,60} or tailor-made nanometer-scale patterns.⁶¹

1.2.2 Multilayer and core-shell heterostructures

The preparation of multifunctional heterostructures based on Prussian blue analogues has also drawn a considerable attention in the past years. The properties of these heterostructures can derive from a simple addition of functionalities or from synergetic (or coupling) effects between functionalities. This coupling may have different origin: magnetic coupling (eg. exchange bias) or elastic coupling by combination of photo-strictive and piezomagnetic materials.^{62,63} A key point in this strategy is the control of the interface between the two materials.

In many works, core-shell heterostructures have been prepared.^{64,65,66} Catala *et al*⁶⁴ designed core-shell CsFeCr@CoCr and CsNiCr@CsCoCr particles, as well as core-multishell $\text{CsCoCr@CsFeCr@CsNiCr}$ particles to achieve multifunctionality at the nanoscale. The growth was carried out in aqueous solution and the size of the shell was well controlled. D.R. Talham and coworkers⁶⁵ also synthesized several core-shell and core-multishell nanoparticles that associate a photo-strictive $\text{Rb}_x\text{Co}[\text{Fe}(\text{CN})_6]_y \cdot z\text{H}_2\text{O}$ compound and a ferromagnetic $\text{K}_x\text{Ni}[\text{Cr}(\text{CN})_6]_y \cdot z\text{H}_2\text{O}$ phase with a relatively high T_C value of ca 70 K. The as-obtained core-shell particles exhibit persistent photo-induced magnetization change up to 70 K, which are absent from the individual components of the heterostructure. They interpret

their results by the transfer of strain through the interface between the two materials. They recently extend their investigations to core-shell particles for lithium battery made of a $\text{K}_{0.1}\text{Cu}[\text{Fe}(\text{CN})_6]_{0.7} \cdot 3.8\text{H}_2\text{O}$ core and of a $\text{K}_{0.1}\text{Ni}[\text{Fe}(\text{CN})_6]_{0.7} \cdot 4.1\text{H}_2\text{O}$ shell, to achieve higher capacity and enhanced cyclability, due to an increased stability of the crystal structure.⁶⁷

However, ultrathin films and multilayers present distinct advantages as one may control their growth and multiply the number of interfaces to favor the synergetic properties of the hybrid structure. In addition, new effects such as interface anisotropy may be anticipated for this class of materials. Talham and coworkers^{62,63} were the first to report the preparation of multilayers composed of a photo-switchable $\text{Rb}_{0.7}\text{Co}_4[\text{Fe}(\text{CN})_6]_3 \cdot z\text{H}_2\text{O}$ film sandwiched between two ferromagnetic $\text{Rb}_{0.8}\text{Ni}_4[\text{Cr}(\text{CN})_6]_3 \cdot z\text{H}_2\text{O}$ layers. The TEM cross section and the magnetic properties of this heterostructure is shown in **Figure 1.5**. The film exhibit a T_C value of 70 K, and a decreased magnetization after light irradiation, which could be associated to the building up of external stresses applied to the RbNiCr layers due to the expansion of the $\text{Rb}_{0.7}\text{Co}_4[\text{Fe}(\text{CN})_6]_3 \cdot z\text{H}_2\text{O}$ film upon illumination.⁶² These effects are similar to those reported for the core-shell particles made of NiCr and CoFe PBAs.⁶⁵

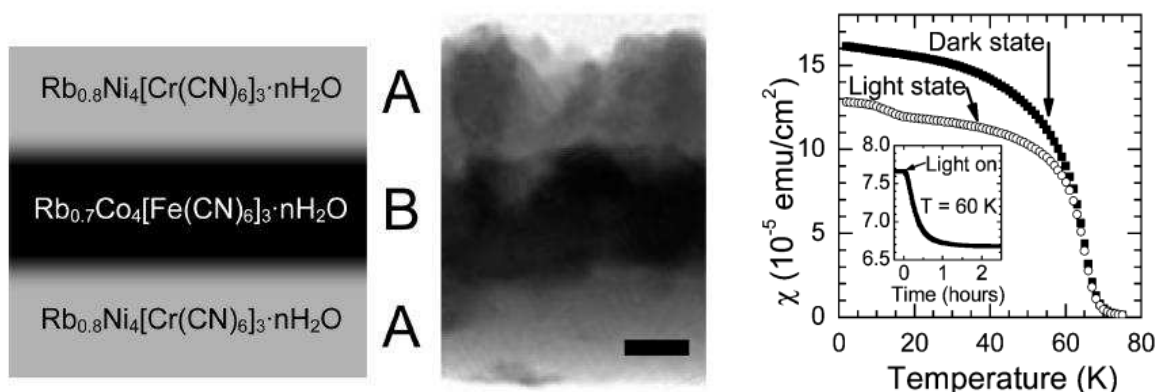


Figure 1.5. (left) Scheme of the NiCr/CoFe/NiCr heterostructure, and TEM micrograph showing a cross-section image of the sample. (right) Photo-induced magnetization changes under 100 G with the magnetic field applied parallel to the surface.

1.2.3 Morphology of Prussian blue analogue films

For the deposition methods described in **section 1.2**, the film thickness typically range from few nanometers^{44,46,68,47} to hundreds of nanometers^{41,31,69} or micrometers.^{42,31} One of the main challenges is the control of the growth of ultrathin and continuous films in the perspective of designing devices for spintronic applications, and the improvement of the surface homogeneity to enhance interface effects.

The film morphology varies from one method to the other, and the surface and interface roughness is difficult to be well-controlled. Formation of a film at a Langmuir monolayer interface can produce very thin PBA films,^{54,55} as there is only one or few alternating Co-Fe metallate cyanide stacks on the solid support. This way, the thinnest film was estimated to be 0.44 nm thick, but the continuity and surface morphology of the film were not fully characterized.⁵⁴ Layers and multilayers were also achieved down to ca. 6 nm by Layer-by-Layer (LbL) deposition using a functionalized Si (100) surface as a substrate,⁴⁶ with for instance two 2.5 nm thick NiCr layers separated by a paramagnetic NiFe stack with a calculated thickness of 1.5 nm.⁴⁹

Most of the films show a dependence of surface roughness on thickness.^{32,46,68} The roughness can range from 2.0 to 100 nm for thicknesses of 6.1 to 300 nm,⁴⁶ and the film continuity is a common problem for all deposition methods.^{46,31} A recent work shows the possibility of getting smooth surfaces with a RMS roughness of 0.63 nm for 6.0 nm films by LbL deposition,⁴⁹ while previous reports clearly show that a deposition cycle as described in **Figure 1.3** leads to the formation of the equivalent of several unit cells. The film growth does not proceed layer by layer, maybe because of not optimized rinsing steps or redissolution/reprecipitation processes.

1.3 An alternative strategy for film growth

In this PhD work, we develop a simple deposition route of Prussian blue analogue thin films based on heterogeneous nucleation on surfaces functionalized by organic monolayers. The original method that we have proposed consists of promoting the selective immobilization of one precursor of the solid phase on the surface to initiate the film nucleation and its subsequent growth using controlled diffusion by contact with a solution containing all the required precursors.

By comparison to the extensively studied layer-by-layer deposition routes^{30,49}, this “one-pot” or “one-bath” approach should allow for faster deposition rates but should also favor the formation of well-defined interfaces, both with the substrate and with a top layer in multilayer architectures. Indeed, this method allows avoiding many of the difficulties related to sequential deposition performed by dipping the sample in different baths that requires a controlled rinsing of the excess precursors and a drying stage often detrimental for the cleanliness of the surface and interfaces.

In this context, two main issues need to be considered, one is the choice of the substrate and of its functionalization, and the other one is the determination of the solution composition for deposition.

1.3.1 The choice of the substrate

To date, most of the thin films described in the literature were found to be very rough and polycrystalline. Obtaining individualized islands rather than continuous films is probably related to the difficulty in preparing a substrate suitable for an epitaxial growth of these coordination networks. The choice of the substrate is thus essential. Various materials have already been investigated as substrate because of their flatness, their surface chemistry or their surface charge, such as SnO₂ and TiO₂,³³ clay mineral,⁵⁴ Mylar,^{45,70} Melinex 535,^{46,31,30} Si (100),⁴⁹ or Au(110)⁷¹. In this context, the originality of our approach is to use functionalized Si (111) surfaces as model substrates for the assembly of the films and supported heterostructures. These surfaces, which exhibit a well-defined structure at the atomic scale and well controlled chemical composition, open new interesting perspectives for the monitoring of the layer and multilayer growth. Indeed, they will allow the implementation of novel strategies for the characterization of the heterostructures based on *in situ* FTIR and AFM.

In addition, surface chemistry of semiconductors has drawn a great attention for several decades because of their huge potential in modern technology. Silicon and silicon based substrate are one of the most investigated substrates. Their surface passivation is well established, as well as their chemical and biochemical functionalization. Chabal and co-workers^{72,73} firstly found a way to prepare ideal hydrogen terminated Si (111) surfaces, and concluded that by using basic solution (pH=9-10) or buffered HF followed by etching in 40%NH₄F solution can produce ideal hydrogen terminated Si (111) surfaces with ≡Si-H bonds normal to surface. Afterwards, many efforts have been made to get a stable coverage by a densely packed organic monolayer which is robustly linked to the silicon surface: Chidsey *et al.*^{74,74b} prepared close-packed alkyl-monolayer terminated Si (111) surfaces using free radicals. Many other methods have been studied, such as photochemical reactions^{75,76,77}, micro-wave assisted reaction⁷⁸ and Lewis acid-catalyzed hydrosilylation of alkenes⁷⁹ etc.

In the present work, the silicon surfaces will be prepared according to the methods developed by the Electrochemistry group of LPMC for (i) the preparation of H-Si(111) surfaces structured in atomically flat terraces, (ii) their functionalization by grafting of organic monolayers and (iii) quantitative analyses to determine the surface composition using *in situ* infra-red spectroscopy (FTIR) combined to AFM imaging^{80,81,82,83}. The anchoring of monolayers of photochromic organic compounds has already been successfully achieved on these surfaces and their photo-switching evidenced by FTIR spectroscopy⁸⁴. In the frame of this project, the Si surfaces were functionalized by pyridyl groups allowing the immobilization of the divalent metal cations, precursors of the Prussian blue analogue phases, by formation of dative metal-ligand bonds. Efficient immobilization of metal or organometallic precursors, as well as the self-assembly of gold nanoparticles on surfaces

based on the formation of pyridyl-metal complex have been already reported by several authors^{85,86,49}.

1.3.2 The choice of the solution composition

1.3.2.1 Kinetics of solid formation in solution: Nucleation and growth

In order to investigate the deposition of a film on a substrate, it is important to recall the basics of the nucleation and growth processes based on LaMer theory.⁸⁷ **Figure 1.6(a)** shows the evolution of the number and of the size of the particles formed during precipitation through the condensation of a soluble precursor. The condensation rate is first almost zero for undersaturated and slightly oversaturated solutions (regime I). When the concentration of the soluble precursor is beyond a critical concentration C_{min} , condensation abruptly takes place and nuclei of the solid phase are formed in an explosive way (regime II). As the formation of a large number of nuclei will consume a lot of the soluble precursor, there will be a competition between the formation of the soluble precursor (for instance its addition in the reaction bath) and its consumption by condensation in new nuclei. If the rate of generation of the precursor is significantly smaller, nucleation will significantly decrease the precursor concentration and reduce the nucleation rate accordingly (concentration of C_{max} in **Figure 1.6(b)**). Once the concentration of precursor is less than C_{min} , the nucleation process stops.

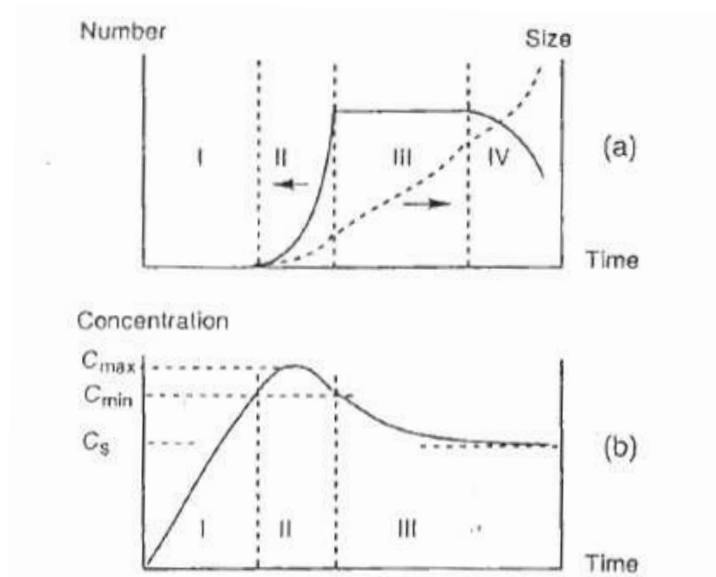


Figure 1.6. (a) Evolution of number and of the size of particles formed in solution. (b) Change in the concentration C of the soluble precursor during precipitation. C_s is the solubility of the solid phase, C_{min} is the threshold concentration of soluble precursor to form nuclei, C_{max} is the maximum concentration of the soluble precursor.

In regime II of **Figure 1.6(a)**, the growth process takes place simultaneous with nucleation. When the precursor concentration drops below C_{\min} (regime III), the precursors only condense on the preformed nuclei, which result in the particle growth until the precursor concentration reaches the solubility limit of the solid phase.

We have now to consider the case of the formation of the solid in the presence of a second solid phase (preformed particles for core-shell synthesis or a surface for film deposition). Indeed, heterogeneous nucleation is thermodynamically favoured by the fact that the solid-solid surface tension is smaller than the solid-solution surface tension. In the case of a shell grown onto core particles, or of a film grown on a surface, the strategy is to keep the precursor concentration below the threshold value for homogeneous nucleation in solution (C_{\min}^{hom}), but higher than that of heterogeneous nucleation on the surface (C_{\min}^{het}). This will avoid the nucleation and growth of particles in solution, that may be further adsorbed on the surface or simply decrease the precursor concentration and change the rate of shell/film growth.

1.3.2.2 Previous work on the growth of RbCoFe@RbNiCr core-shell particles

For deposition methods alternative to Layer-by-Layer (electrochemical or other solution routes), a key point is thus the determination of the solution composition, which should contain all necessary precursors and remain stable on the time scale of the deposition. Ideally, the concentration of the precursors should be kept below the threshold value for homogeneous nucleation, and above the value for heterogeneous nucleation. An example of this strategy is given by the work of Presle *et al.* for the synthesis of core-shell heterostructures made of Prussian blue analogues. This work focus on the growth of a $\text{Rb}_{0.1}\text{NiCr}(\text{CN})_6]_{0.7} \cdot z\text{H}_2\text{O}$ (RbNiCr) shell onto preformed $\text{Rb}_{0.5}\text{Co}[\text{Fe}(\text{CN})_6]_{0.8} \cdot z\text{H}_2\text{O}$ (RbCoFe) particles.⁸⁸ This synthesis was carried out in water, by drop-wise addition of two solutions of reactants: the first solution contained the $\text{K}_3\text{Cr}(\text{CN})_6$ reactant, and the second one the NiCl_2 and RbCl precursors and the shell growth was monitored by dynamic light scattering (DLS) for various concentrations of the reactants, and keeping the $[\text{Cr}]/[\text{Ni}]$ and $[\text{Rb}]/[\text{Ni}]$ concentration ratios constant.

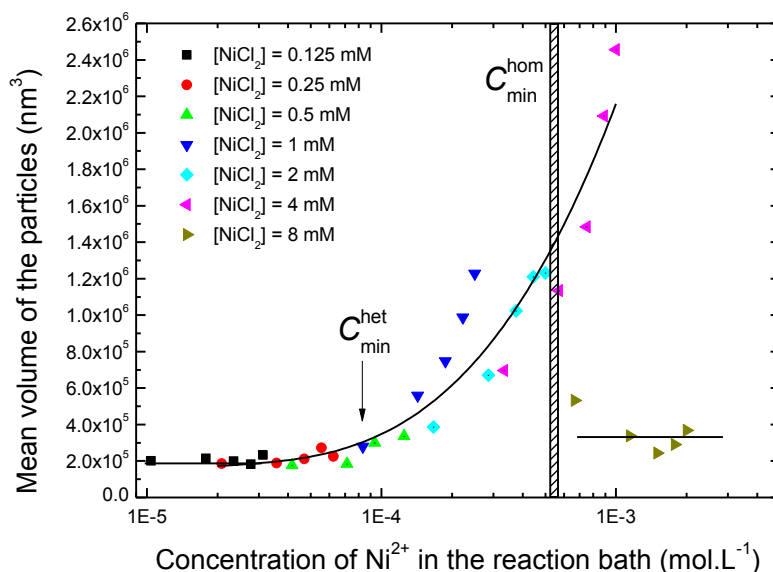


Figure 1.7. Average particle volume as a function of the nominal concentration of Ni^{2+} in the reaction medium. The addition rate used was 0.75 mL/min. The size of the nanoparticles was derived from DLS measurements, adapted from the PhD thesis of M. Presle⁸⁸.

From **Figure 1.7**, we can see that for Ni^{2+} concentrations lower than ca. $8 \times 10^{-5} \text{ mol/L}$, no increase in particle size is detected. The precursors accumulate in solution but their concentrations do not exceed the threshold values necessary for the shell formation by heterogeneous nucleation. For Ni^{2+} concentrations between ca. $8 \times 10^{-5} \text{ mol/L}$ and $5 \times 10^{-4} \text{ mol/L}$, the increase of the mean particle volume reflects the growth of a shell onto the pre-existing RbCoFe particles, with a growth rate that gradually increases with the concentration of the NiCl_2 solution. Eventually, for Ni^{2+} concentrations above $5 \times 10^{-4} \text{ mol/L}$, the particle size after addition is similar to the dimensions of the core particles, suggesting the side formation of small RbNiCr particles by homogeneous nucleation in solution. These new particles are not accounted for by DLS as this technique tends to overestimate the contribution of the largest particles. All these conclusions were supported by direct observations using transmission electron microscopy. From this series of experiments, M. Presle determined critical concentrations: $C_{min}^{het} = 8 \times 10^{-5} \text{ mol/L}$ for heterogeneous nucleation, and $C_{min}^{hom} = 5 \times 10^{-4} \text{ mol/L}$ for homogeneous nucleation. It should be noticed that these critical values correspond to the experimental conditions used in this work. In particular, the stoichiometry of the shell phase does not match the ratio of the precursors, so that the threshold concentrations obtained for Ni^{2+} take into account the accumulation of $[\text{Cr}(\text{CN})_6]^{3-}$ and Rb^+ species in the reaction medium. It is also worth mentioning that the C_{min}^{hom} value drastically depends on the presence of RbCoFe particles in the reaction medium. This critical value should be lower when decreasing the number of RbCoFe particles.

1.4 Objectives and outline of the manuscript

The main objective of this PhD thesis is to investigate the deposition of Prussian blue analogues using a solution route based on heterogeneous nucleation on functionalized silicon surfaces. Special attention is paid to understanding the growth mode of ultra-thin films and bilayers, which is pivotal for a fine control of the morphology and of the interface quality in heterostructures. The structure of this dissertation is as follows:

Chapter 2 provides a protocol of surface functionalization ended with a pyridine termination, qualitative and quantitative analyses of the surface composition will be presented at each step. Chapter 3 discusses the growth of $\text{Rb}_x\text{Ni}[\text{Cr}(\text{CN})_6]_y \cdot z\text{H}_2\text{O}$ layers by combining different structural and microstructural characterization techniques. The magnetic properties of these layers will be further analysed based on the film morphology. In Chapter 4, the growth of $\text{Rb}_x\text{Co}[\text{Fe}(\text{CN})_6]_y \cdot z\text{H}_2\text{O}$ thin films is presented, and their photo-switching properties are discussed on the basis of the chemical composition of the layers. At last, Chapter 5 presents preliminary results for the growth of bilayer structures of $\text{Si}/\text{Rb}_x\text{Co}[\text{Fe}(\text{CN})_6]_y \cdot z\text{H}_2\text{O}/\text{Rb}_x\text{Ni}[\text{Cr}(\text{CN})_6]_y \cdot z\text{H}_2\text{O}$ and $\text{Si}/\text{Rb}_x\text{Ni}[\text{Cr}(\text{CN})_6]_y \cdot z\text{H}_2\text{O}/\text{Rb}_x\text{Co}[\text{Fe}(\text{CN})_6]_y \cdot z\text{H}_2\text{O}$.

1.5 References

1. S. Ferlay, T. Mallah, R. Ouahes, P. Veillet, M. Verdaguer, A room-temperature organometallic magnet based on prussian blue. *Nature* **1995**, 378, 701-703.
2. O. Sato; T. Iyoda; A. Fujishima; K. Hashimoto, Photoinduced magnetization of a cobalt-iron cyanide. *Science* **1996**, 272, 704-705.
3. S. Ohkoshi; S. Yorozu; O. Sato; T. Iyoda; A. Fujishima; K. Hashimoto, Photoinduced magnetic pole inversion in a ferro-ferrimagnet: $(\text{Fe}_{0.40}\text{Mn}_{0.60})_{1.5}\text{Cr}^{\text{III}}(\text{CN})_6$. *Appl. Phys. Lett.* **1997**, 70, 1040-1042.
4. H. Tokoro; S. Ohkoshi; K. Hashimoto, One-shot-laser-pulse-induced demagnetization in rubidium manganese hexacyanoferrate. *Appl. Phys. Lett.* **2003**, 82 (8), 1245-1247.
5. A. Ludi; H. U. Gudel, Structural chemistry of polynuclear transition metal cyanides. *Struct. Bonding.* **1973**, 14, 1-21.
6. F. Herren; P. Fischer; A. Ludi; W. Halg, Neutron diffraction study of Prussian blue, $\text{Fe}_4[\text{Fe}(\text{CN})_6]_3 \cdot x\text{H}_2\text{O}$. Location of water molecules and long-range magnetic order. *Inorg. Chem.* **1980**, 19, 956-959.
7. H. J. Buser; D. Schwarzenbach; W. Petter; A. Ludi, The crystal structure of Prussian blue: $\text{Fe}_4[\text{Fe}(\text{CN})_6]_3 \cdot x\text{H}_2\text{O}$. *Inorg. Chem.* **1977**, 16, 2704-2710.
8. H. Tokoro; S. Ohkoshi, Novel magnetic functionalities of Prussian blue analogs. *Dalton Transactions* **2011**, 40 (26), 6825-6833.
9. W. E. Prout; E. R. Russell; H. J. Groh, Ion exchange absorption of cesium by potassium hexacyanocobalt (II) ferrate (II). *J. Inorg. Nucl. Chem.* **1965**, 27, 473-479.
10. A. A. Karyakin; E. E. Karyakina; L. Gorton, Amperometric biosensor for glutamate using Prussian blue-based "artificial peroxidase" as a transducer for hydrogen peroxide. *Anal. Chem* **2000**, 72, 1720-1723.
11. S. S. Kaye; J. R. Long, The role of vacancies in the hydrogen storage properties of Prussian blue analogues. *Catalysis Today* **2007**, 120, 311-316.
12. S. S. Kaye; J. R. Long, Hydrogen storage in the dehydrated Prussian blue analogues $\text{M}_3[\text{Co}(\text{CN})_6]_2$ (M = Mn, Fe, Co, Ni, Cu, Zn). *J. Am. Chem. Soc.* **2005**, 127, 6506-6507.
13. V. Gadet; T. Mallah; I. Castro; M. Verdaguer, High-Tc molecular-based magnets: a ferromagnetic bimetallic chromium(III)-nickel (II) cyanide with T=90K. *J. Am. Chem. Soc.* **1992**, 114, 9213-9214.
14. O. Sato; Y. Einaga; T. Iyoda; A. Fujishima; K. Hashimoto, Reversible photoinduced magnetization *J. Electrochem. Soc* **1997**, 144, L11-L13.

15. S. Ohkoshi; K. Hashimoto, Ferromagnetism of cobalt-chromium polycyanides. *Chem. Phys. Lett.* **1999**, 314 (3-4), 210-214.
16. T. Yokoyama; H. Tokoro; S. Ohkoshi; K. Hashimoto; K. Okamoto; T. Ohta, Photoinduced phase transition of $\text{RbMnFe}(\text{CN})_6$ studied by x-ray-absorption fine structure spectroscopy. *Physical Review B* **2002**, 66 (18), 184111.
17. S. Cobo; R. Fernández; L. Salmon; G. Molnár; A. Bousseksou, Correlation between the stoichiometry and the bistability of electronic states in valence-tautomeric $\text{Rb}_x\text{Mn}[\text{Fe}(\text{CN})_6]_y \cdot z\text{H}_2\text{O}$ complexes. *Eur. J. Inorg. Chem.* **2007**, 2007 (11), 1549-1555.
18. Y. Moritomo; M. Hanawa; Y. Ohishi; K. Kato; M. Takata; A. Kuriki; E. Nishibori; M. Sakata; S. Ohkoshi; H. Tokoro; K. Hashimoto, Pressure- and photoinduced transformation into a metastable phase in $\text{RbMn}[\text{Fe}(\text{CN})_6]$. *Physical Review B* **2003**, 68 (14), 144106.
19. D. Li; R. Clerac; O. Roubeau; E. Harte; C. Mathonie; R. Le Bris; S. M. Holmes, Magnetic and optical bistability driven by thermally and photoinduced intramolecular electron transfer in a molecular cobalt-iron Prussian blue analogue. *J. Am. Chem. Soc.* **2008**, 130, 252-258.
20. D. M. Pajerowski; J. E. Gardner; D. R. Talham; M. W. Meisel, Tuning the sign of photoinduced changes in magnetization: spin transitions in the ternary metal Prussian blue analogue $\text{Na}_\alpha\text{Ni}_{1-x}\text{Co}_x[\text{Fe}(\text{CN})_6] \cdot n\text{H}_2\text{O}$. *J. Am. Chem. Soc.* **2009**, 131, 12927-12936.
21. O. Sato; Y. Einaga; A. Fujishima; K. Hashimoto, Photoinduced long-range magnetic ordering of a cobalt-iron cyanide. *Inorg. Chem.* **1999**, 38, 4405-4412.
22. N. Shimamoto; S. Ohkoshi; O. Sato; K. Hashimoto, Control of charge-transfer-induced spin transition temperature on cobalt-iron Prussian blue analogues. *Inorg. Chem.* **2002**, 41, 678-684.
23. A. Goujon; O. Roubeau; F. Varret; A. Dolbecq; A. Bleuzen; M. Verdaguer, Photoexcitation from dia- to ferri-magnetism in a Rb-Co-hexacyanoferrate Prussian blue analogue. *Eur. Phys. J. B* **2000**, 14, 115-124.
24. A. Bleuzen; C. Lomenech; V. Escax; F. Villain; F. Varret; C. C. dit Moulin; M. Verdaguer, Photoinduced ferrimagnetic systems in Prussian blue analogues $\text{C}_x^I\text{Co}_4[\text{Fe}(\text{CN})_6]_y$ ($\text{C}^I = \text{Alkali Cation}$). 1. conditions to observe the phenomenon. *J. Am. Chem. Soc.* **2000**, 122, 6648-6652.
25. A. Bleuzen; V. Escax; J.-P. Itié; P. Münsch; M. Verdaguer, Photomagnetism in $\text{C}_x\text{Co}[\text{Fe}(\text{CN})_6]_{(8+x)/3} \cdot n\text{H}_2\text{O}$ Prussian blue analogues, looking for the maximum efficiency *C. R. Chimie* **2003**, 6, 343-352.

26. C. C. dit Moulin; F. Villain; A. Bleuzen; M.-A. Arrio; P. Saintavit; C. Lomenech; V. Escax; F. Baudalet; E. Dartyge; J.-J. Gallet; M. Verdaguer, Photoinduced ferrimagnetic systems in Prussian blue analogues $C_x^I Co_4[Fe(CN)_6]_y$ (C^I Alkali Cation). 2. X-ray absorption spectroscopy of the metastable state. *J. Am. Chem. Soc.* **2000**, *122*, 6653-6658.
27. J.-D. Cafun; J. Lejeune; F. Baudalet; P. Dumas; J.-P. Itie; A. Bleuzen, Room-temperature photoinduced electron transfer in a Prussian blue analogue under hydrostatic pressure. *Angew. Chem. Int. Ed.* **2012**, *51*, 9146-9148.
28. V. Escax; C. C. dit Moulin; F. Villain; G. Champion; J.-P. Itie; P. Münsch; M. Verdaguer; A. Bleuzen, Photo-induced electron transfer in ferrimagnetic Prussian-blue analogues $X_x^I Co_4[Fe(CN)_6]_y$ (X^I =alkali cation). *C. R. Chimie* **2003**, *6*, 1165-1173.
29. A. Bleuzen; V. Escax; A. Ferrier; F. Villain; M. Verdaguer; P. Munsch; J.-P. Itie, Thermally induced electron transfer in a CsCoFe Prussian blue derivative: the specific role of the alkali-metal ion. *Angew. Chem. Int. Ed.* **2004**, *43*, 3728-3731.
30. D. M. Pajerowski; J. E. Gardner; D. R. Talham; M. W. Meisel, Anisotropic magnetism in Prussian blue analogue films. *New J. Chem.* **2011**, *35*, 1320-1326.
31. D. M. Pajerowski; J. E. Gardner; M. J. Andrus; S. Datta; A. Gomez; S. W. Kycia; S. Hill; D. R. Talham; M. W. Meisel, Magnetic anisotropy in thin films of Prussian blue analogues. *Phys. Rev. B* **2010**, *82*, 214405-1-214405-5.
32. F. A. Frye; D. M. Pajerowski; J.-H. Park; M. W. Meisel; D. R. Talham, Anisotropic photoinduced magnetism in thin films of the Prussian blue analogue $A_j Co_k [Fe(CN)_6]_l \cdot nH_2O$. *Chem. Mater.* **2008**, *20*, 5706-5713.
33. K. Itaya; I. Uchida; V. D. Neff, Electrochemistry of polynuclear transition metal cyanides: Prussian blue and its analogues. *Acc. Chem. Res.* **1986**, *19*, 162-168.
34. V. D. Neff, Electrochemical oxidation and reduction of thin films of Prussian blue. *J. Electrochem. Soc.* **1978**, *125*, 886-887.
35. S. Sinha; B. D. Humphrey; A. B. Bocaesly, Reaction of nickel electrode surfaces with anionic metal-cyanide complexes: Formation of precipitated surfaces. *Inorg. Chem.* **1984**, *23* (2), 203-212.
36. O. Sato; T. Iyoda; A. Fujishima; K. Hashimoto, Electrochemically tunable magnetic phase transition in a high- T_c chromium cyanide thin film. *Science* **271**, 49-51.
37. O. Sato; Y. Einaga; T. Iyoda; A. Fujishima; K. Hashimoto, Cation-driven electron transfer involving a spin transition at room temperature in a cobalt iron cyanide thin film. *J. Phys. Chem. B* **1997**, *101*, 3903-3905.

38. M. Mizuno; S. Ohkoshi; K. Hashimoto, Electrochemical synthesis of high-T_c, colored magnetic thin films composed of vanadium chromium of hexacyanochromate. *Advanced materials* **2000**, *12*, 1955-1958.
39. S. I. Ohkoshi; A. Fujishima; K. Hashimoto, Transparent and colored magnetic thin films: (Fe^xCr^{1-x})_{1.5}[Cr^{III}(CN)₆]. *J. Am. Chem. Soc.* **1998**, *120*, 5349-5350.
40. S. Ohkoshi; K. Hashimoto, New magnetic functionalities presented by Prussian blue analogues. *The Electrochemical Society Interface* **2002**, 34-38.
41. T. Nuida; T. Hozumi; W. Kosaka; S. Sakurai; S. Ikeda; T. Matsuda; H. Tokoro; K. Hashimoto; S. Ohkoshi, Colored magnetic films composed of cyano-bridged metal assemblies and magneto-optical functionalities. *Polyhedron* **2005**, *24* (16-17), 2901-2905.
42. Ohkoshi, S.; M. Mizuno; G. Hung; K. Hashimoto, Magneto-optical effects of room temperature molecular-based magnetic films composed of vanadium hexacyanochromates. *J. Phys. Chem. B* **2000**, *104* (40), 9365-9367.
43. G. Decher, Fuzzy nanoassemblies: toward layered polymeric multicomposites. *Science* **1997**, *277*, 1232-1237.
44. J. T. Culp; J.-H. Park; I. O. Benitez; Y.-D. Huh; M. W. Meisel; D. R. Talham, Sequential assembly of homogeneous magnetic Prussian blue films on templated surfaces. *Chem. Mater.* **2003**, *15*, 3431-3436.
45. J. T. Culp; J.-H. Park; M. W. Meisel; D. R. Talham, Interface directed assembly of cyanide-bridged Fe-Co and Fe-Mn square grid networks. *Polyhedron* **2003**, *22*, 3059-3064.
46. F. A. Frye; D. M. Pajerowski; S. M. Lane; N. E. Anderson; J.-H. Park; M. W. Meisel; D. R. Talham, Effect of film thickness on the photoinduced decrease in magnetism for thin films of the cobalt iron Prussian blue analogue Rb_{0.7}Co₄[Fe(CN)₆]_{3.0}. *Polyhedron* **2007**, *26*, 2281-2286.
47. J.-H. Park; E. Cizmar; M. W. Meisel; Y. D. Huh; F. Frye; S. Lane; D. R. Talham, Anisotropic photoinduced magnetism of a Rb₇Co_k[Fe(CN)₆]_l·H₂O thin film. *Appl. Phys. Lett.* **2004**, *85*, 3798-3800.
48. J.-H. Park; Y.D. Huh; Cizmar., E.; S. G. Gamble; D.R. Talham; M. W. Meisel, Photoinduced magnetization in a thin Fe-CN-Co film. *Journal of Magnetism and Magnetic Materials* **2004**, *272*, 1116-1117.
49. S. Tricard; C. Costa-Coquelard; S. Mazerat; E. Rivière; V. Huc; C. David; F. Miserque; P. Jegou; S. Palacind; T. Mallah, Cyanide-bridged NiCr and alternate NiFe-NiCr magnetic ultrathin films on functionalized Si(100) surface. *Dalton Trans.* **2012**, *41*, 4445-4450.
50. V. Gadet. PhD thesis. Université Paris VI, Paris, 1992.

51. C. Mingotaud; C. Lafuente; J. Amiell; P. Delhaes, Ferromagnetic langmuir-blodgett film based on Prussian blue. *Langmuir* **1999**, *15* (2), 289-292.
52. G. R. Torres; E. Dupart; C. Mingotaud; S. Ravaine, Electrochemical and photoelectrochemical properties of new hybrid langmuir-blodgett films containing Prussian blue and a tris(bipyridine) ruthenium derivative. *J. Phys. Chem. B* **2000**, *104*, 9487-9490.
53. G. R. Torres; B. Agricole; C. Mingotaud; S. Ravaine; P. Delhaes, Hybrid organic-inorganic langmuir-blodgett films starting from colloidal Prussian blue solution. *Langmuir* **2003**, *19*, 4688-4693.
54. T. Yamamoto; Y. Umemura; O. Sato; Y. Einaga, Photomagnetic Co-Fe Prussian blue thin films fabricated by the modified langmuir-blodgett technique. *Chem. Lett.* **2004**, *33* (5), 500-501.
55. T. Yamamoto; Y. Umemura; O. Sato; Y. Einaga, Photoswitchable magnetic films: Prussian blue intercalated in langmuir-blodgett films consisting of an amphiphilic azobenzene and a clay mineral. *Chem. Mater.* **2004**, *16*, 1195-1201.
56. T. Yamamoto; Y. Umemura; O. Sato; Y. Einaga, Observation of the anisotropic photoinduced magnetization effect in Co-Fe Prussian blue thin films fabricated by using clay langmuir-blodgett films as a template. *J. Am. Chem. Soc.* **2005**, *127*, 16065-16073.
57. T. Yamamoto; N. Saso; Y. Umemura; Y. Einaga, Photoreduction of Prussian blue intercalated into titania nanosheet ultrathin films. *J. Am. Chem. Soc.* **2009**, *131*, 13196-13197.
58. Y. Guo; A. R. Guadalupe; O. Resto; L. F. Fonseca; S. Z. Weisz, Chemically derived Prussian blue sol-gel composite thin films. *Chem. Mater.* **1999**, *11*, 135-140.
59. M. Pyrasch; B. Tiede, Electro- and photoresponsive films of Prussian blue prepared upon multiple sequential adsorption. *Langmuir* **2001**, *17*, 7706-7709.
60. R. C. Millward; C. E. Madden; I. Sutherland; R. J. Mortimer; S. Fletcher; F. Marken, Directed assembly of multilayers – the case of Prussian Blue. *Chem. Commun.* **2001**, 1994-1995.
61. S. Lepoutre; D. Grosso; C. Sanchez; G. Fornasieri; E. Rivière; A. Bleuzen, Tailor-made nanometer-scale patterns of photo-switchable Prussian blue analogues. *Advanced Materials* **2010**, *22*, 3992-3996.
62. D. M. Pajerowski; M. J. Andrus; J. E. Gardner; E. S. Knowles; M. W. Meisel; D. R. Talham, Persistent photoinduced magnetism in heterostructures of Prussian blue analogues. *J. Am. Chem. Soc.* **2010**, *132*, 4058-4059.
63. D. M. Pajerowski; J. E. Gardner; E. S. Knowles; M. W. Meisel; D. R. Talham, Photoinduced magnetism in a series of Prussian blue analogue heterostructures. *Chem. Mater.* **2011**, *23*, 3045-3053.

64. L. Catala; D. Brinzei; Y. Prado; A. Gloter; O. Stephan; G. Rogez; T. Mallah, Core-multishell magnetic coordination nanoparticles: toward multifunctionality on the nanoscale. *Angew. Chem. Int. Ed.* **2009**, *48*, 183-187.
65. M. F. Dumont; E. S. Knowles; A. Guet; D. M. Pajerowski; A. Gomez; S. W. Kycia; M. W. Meisel; D. R. Talham, Photoinduced magnetism in core/shell Prussian blue analogue heterostructures of $K_jNi_k[Cr(CN)_6]_l \cdot nH_2O$ with $Rb_aCo_b[Fe(CN)_6]_c \cdot mH_2O$. *Inorg. Chem.* **2011**, *50*, 4295-4300.
66. M. Presle; J. Lemainque; J.-M. Guigner; E. Larquet; I. Maurin; J.-P. Boilot; T. Gacoin, Controlled growth of core and shell heterostructures based on Prussian blue analogue. *New Journal of Chemistry* **2011**, *35*, 1296-1301.
67. D. Asakura; C. H. Li; Y. Mizuno; M. Okubo; H. Zhou; D. R. Talham, Bimetallic cyanide-bridged coordination polymers as lithium ion cathode materials: core@shell nanoparticles with enhanced cyclability. *J. Am. Chem. Soc.* **2013**, *135*, 2793-2799.
68. M. Clemente-Leon; E. Coronado; A. Lopez-Munoz; D. Repetto; C. Mingotaud; D. Brinzei; L. Catala; T. Mallah, Magnetic langmuir-blodgett films of bimetallic coordination nanoparticles of $CS_{0.4}Ni[Cr(CN)_6]_{0.9}$. *Chem. Mater.* **2008**, *20*, 4642-4652.
69. S. Choudhury; N. Bagkar; G. K. Dey; H. Subramanian; J. V. Yakhmi, Crystallization of Prussian blue analogues at the air-water interface using an octadecylamine monolayer as a template. *Langmuir* **2002**, *18*, 7409-7414.
70. J. T. Culp; J.-H. Park; D. Stratakis; M. W. Meisel; D. R. Talham, Supramolecular assembly at interfaces: formation of an extended two-dimensional coordinate covalent square grid network at the air-water interface. *J. Am. Chem. Soc.* **2002**, 10083-10090.
71. S. Nakanishi; G. Lu; H. M. Kothari; E. W. Bohannon; J. A. Switzer, epitaxial electrodeposition of Prussian blue thin films on single-crystal Au (100). *J. Am. Chem. Soc.* **2003**, *125*, 14998-14999.
72. G. S. Higashi; Y. J. Chabal; G. W. Trucks; K. Raghavachari, Ideal hydrogen termination of the Si(111) surface. *Appl. Phys. Lett.* **1990**, *56*, 656-658.
73. P. Jakob; P. Dumas; Y. J. Chabal, Influence of silicon oxide on the morphology of HF etched Si(111) surfaces: Thermal versus chemical oxide. *Appl. Phys. Lett.* **1991**, *59*, 2968-2970.
74. (a) M. R. Linford; C. E. D. Chidsey, Alkyl monolayers covalently bonded to silicon surfaces. *J. Am. Chem. Soc.* **1993**, *115*, 12631-12632; (b) M. R. Linford; P. Fenter; P. M. Eisenberger; C. E. D. Chidsey, Alkyl monolayers on silicon prepared from 1-alkenes and hydrogen-terminated silicon. *J. Am. Chem. Soc.* **1995**, *117*, 3145-3155.

75. H. Asanuma; G. P. Lopinski; H. Yu, Kinetic control of the photochemical reactivity of hydrogen-terminated silicon with bifunctional molecules. *Langmuir* **2005**, *21*, 5013-5018.
76. L. A. Huck; J. M. Buriak, UV-Initiated hydrosilylation on hydrogen-terminated silicon (111): rate coefficient increase of two orders of magnitude in the presence of aromatic electron acceptors. *Langmuir* **2012**, *28*, 16285-16293.
77. R. Boukherroub; D. D. M. Wayner, Controlled functionalization and multistep chemical manipulation of covalently modified Si(111) surfaces *J. Am. Chem. Soc.* **1999**, *121*, 11513-11515.
78. R. Boukherroub; A. Petit; A. Loupy; J.-N. Chazalviel; F. Ozanam, Microwave-assisted chemical functionalization of hydrogen-terminated porous silicon surfaces. *J. Phys. Chem. B* **2003**, *107*, 13459-13462.
79. R. Boukherroub; S. Morin; F. Bensebaa; D. D. M. Wayner, New synthetic routes to alkyl monolayers on the Si(111) surface. *Langmuir* **1999**, *15*, 3831-3835.
80. A. Moraillon; A. C. Gouget-Laemmel; F. Ozanam; J.-N. Chazalviel, Amidation of monolayers on silicon in physiological buffers: A quantitative IR study. *J. Phys. Chem. C* **2008**, *112*, 7158-7167.
81. S. Sam; L. Touahir; J. S. Andresa; P. Allongue; J.-N. Chazalviel; A. C. Gouget-Laemmel; C. Henry de Villeneuve; A. Moraillon; F. Ozanam; N. Gabouze; S. Djebbar, Semiquantitative study of the EDC/NHS activation of acid terminal groups at modified porous silicon surfaces. *Langmuir* **2010**, *26* (2), 809-814.
82. D. Aureau; F. Ozanam; P. Allongue; J.-N. Chazalviel, The titration of carboxyl-terminated monolayers revisited: in situ calibrated fourier transform infrared study of well-defined monolayers on silicon. *Langmuir* **2008**, *24* (17), 9440-9448.
83. A. Faucheux; A. C. Gouget-Laemmel; C. Henry de Villeneuve; R. Boukherroub; F. Ozanam; P. Allongue; J.-N. Chazalviel, Well-defined carboxyl-terminated alkyl monolayers grafted onto H-Si(111): packing density from a combined AFM and quantitative IR study. *Langmuir* **2006**, *22*, 153-162.
84. C. Henry de Villeneuve; F. Michalik; J.-N. Chazalviel; K. Rück-Braun; P. Allongue, Photochromes: quantitative IR readout of fulgimide monolayer switching on Si(111) surfaces. *Advanced materials* **2013**, *25* (3), 416-421.
85. T. Zhu; X. Zhang; J. Wang; X. Fu; Z. Liu, Assembling colloidal Au nanoparticles with functionalized self-assembled monolayers. *Thin Solid Films* **1998**, 327-329, 595-598.

86. B. Fleury; F. Volatron; L. Catala; D. Brinzei; E. Rivière; V. Huc; C. David; F. Miserque; G. Rogez; L. Baraton; S. Palacin; T. Mallah, Grafting a monolayer of superparamagnetic cyanide-bridged coordination nanoparticles on Si(100). *Inorg. Chem.* **2008**, *47*, 1898-1900.
87. J.-P. Jolivet, *Metal oxide chemistry and synthesis: from solution to solid state*. John Wiley & Sons, Inc.: 2000.
88. M. Presle. Synthèse et propriétés d'hétérostructure moléculaires de type multiferroïque à base d'analogues du bleu de Prusse. PhD dissertation. Ecole Polytechnique, France, 2011.

Chapter 2

Functionalization of Si (111) surfaces

2.1 Introduction

The organic functionalization of *oxide free* Si surfaces has received strong interest during the past two decades because of its potential in many different fields of research. It is out of the scope of this thesis to review the many different processes that were developed and to explain the chemical mechanisms involved. The reader should consult recent reviews on the subject.^{1,2,3,4,5} It should be just recalled that one major interest of this approach is that it allows for the grafting of organic layers directly onto Si surfaces through robust covalent Si-C linkage. As a consequence of the large energy of the Si-C bonds (~4.5 eV) the grafting of organic monolayer onto oxide free silicon surfaces cannot be considered as a self-assembly process (the molecular chains are not mobile during the monolayer formation).⁶ The high energy of the Si-C bond and its weak electronic polarization confer however a superior chemical stability to organic monolayers on oxide free silicon surface. This is a key advantage in comparison with other systems, in particular thiol Self Assembled Monolayers (SAMs) on gold for which the monolayer stability may sometimes be a problem (Au-S bond energy of 3.5 eV).⁷ A second advantage of organic monolayers on oxide free silicon is the excellent *long range morphology* of the silicon substrate, with a very low roughness, especially the Si (111) surfaces which can be prepared flat at the atomic scale over long range.⁸

Considering the strong coordination between transition metal ions and the N from both the pyridine group and the cyanide group, we get inspired that by functionalizing the Si surface with pyridyl termination, films of Prussian blue analogue could be robustly coupled to with the surface through a coordination linkage, which could be easily found in the precursor solutions.

In this chapter, we will present the protocol used to functionalize Si (111) surfaces with a pyridine termination. The full protocol involves different steps: the grafting of undecylenic acid onto hydrogenated Silicon surfaces by photochemical (UV) hydrosilylation, the conversion of carboxylic acid end-groups into semi-stable succidimyl COOSuc-esters⁹ and finally the coupling of aminoethyl pyridine. The whole schematic route is shown in **Figure 2.1**. We used atomically flat H-terminated Si (111) surfaces. The surface morphology, as well as the quantification of terminal groups, will be discussed in detail in the following sections.

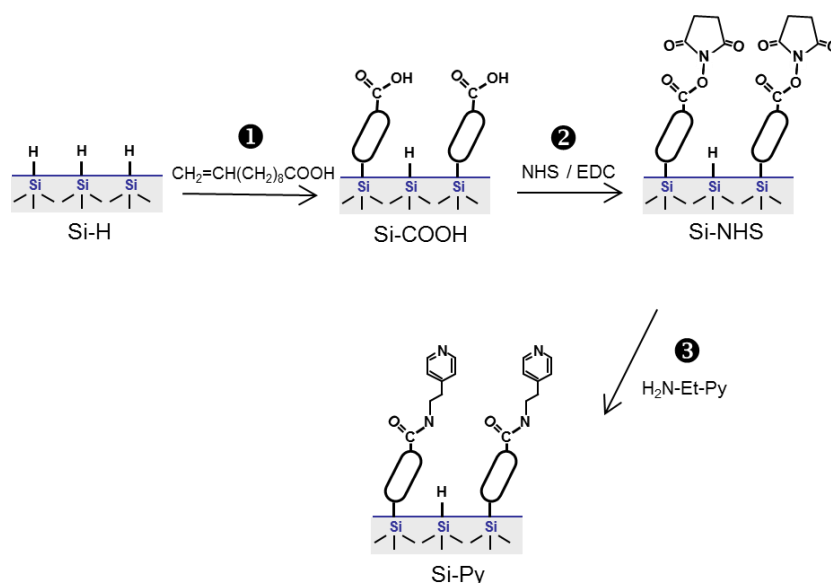


Figure 2.1. Scheme of the multistep protocol used for the functionalization of H-Si (111) surfaces by pyridyl end groups.

2.2 Experimental protocols

2.2.1 Materials

N-Ethyl-N'-(3-(dimethylamino) propyl) carbodiimide hydrochloride (EDC), N-hydroxysuccinimide (NHS, 98%), Undecylenic acid (99%), 4-(2-aminoethyl) pyridine (96%), ammonium sulfite monohydrate (92%), 2-(N-Morpholino) ethanesulfonic acid (MES, > 99.5%), and acetonitrile (> 99.9%) were purchased from Sigma-Aldrich. H_2O_2 (30%), H_2SO_4 (96%), acetic acid (100%) and etching (NH_4F , 40%) reagents were VLSI grade and supplied by Merck. All reagents were used without post-treatment. Ultrapure water (UPW, Milli-Q, 18.2 $\text{M}\Omega$ cm) was used throughout the whole manipulations and rinsing steps.

500-550 μm thick Si (111) wafers one side-polished, with a miscut angle of 0.2° toward the $[\bar{1}1\bar{2}]$ direction (Siltronix, France), were used as standard substrates. For IR spectroscopy measurements in Attenuated Total Reflectance (ATR) mode, we used Float Zone purified (FZ) and double-side polished wafers. Prior to use, the Silicon wafers were cut into squares of dimensions $10 \times 10 \text{ mm}^2$, and were cleaned by immersion into a Piranha solution. All the etching/hydrogenation reactions were carried out in Teflon pillbox.

2.2.2 Surface functionalization

Surface functionalization was carried out from H-terminated Si(111) surfaces (denoted Si-H) prepared by anisotropic etching in oxygen free 40% NH_4F ¹⁰. The Silicon samples and Teflon vials were first cleaned by immersion for 30 min in piranha solution (mixed aqueous solution of H_2O_2 30% and H_2SO_4 96% with a volume ratio 1:2) to remove organic contaminations. *Caution, Piranha solution reacts strongly with organic materials, it must be used under extreme care.* After copious rinsing with Milli-Q water, the Silicon substrates were then immersed for 15 min into 40% NH_4F aqueous solution in which ammonium sulfite ($(\text{NH}_4)_2\text{SO}_3 \cdot \text{H}_2\text{O}$) was added to remove the dissolved oxygen. A quick rinse with Milli-Q water was then performed.

The first step of functionalization (denoted ❶ in **Figure 2.1**) consists in preparing acid terminated surfaces (Si-COOH). The grafting protocol that we used was established by Faucheux et al.¹¹. The freshly hydrogenated surfaces were introduced into a schlenk tube containing a solution of undecylenic acid, previously heated at 90°C and outgassed under Argon for 30 min to remove traces of water and oxygen. After the introduction of the Si-H sample, the solution was further flushed with Ar for 15 min. Then, the schlenk tube was hermetically closed and transferred into a rayonnet reactor equipped with UV lamps (6 mW/cm², 312 nm). After 3 hours irradiation, the schlenk tube was first kept at 80°C in a water bath for 5 min with all openings closed, and then Ar gas was used to flush the solution for 5 min. In a further step, the grafting solution was exchanged with an acetic acid solution heated at 80°C and outgassed for 10 min. Then, the Si surface was taken out and introduced into another schlenk tube filled with acetic acid at 80°C. Ar flushing was maintained for another 30 min, and this procedure was repeated twice. This rinsing protocol allows for efficiently remove all physisorbed acid chains that have tendency to strongly interact with the acid monolayer through hydrogen bonding.¹² Finally the surface was carefully rinsed with water to make sure that there is no residual acetic acid remaining on the surface. Note that the Ar flushing was performed in order to avoid the oxidation of the surface.

The next step (step ❷ in **Figure 2.1**) is an activation step that consists in the transformation of carboxylic acids into succinimidyl ester (Si-COOSuc).¹³ The reaction was done by immersion of the Si-COOH surfaces into a freshly prepared solution containing 0.1 M N-hydroxysuccinimide (NHS) and 0.1 M N-Ethyl-N'-(3-(dimethylamino) propyl) carbodiimide (EDC) in 0.1 M buffer solution at pH 5. The reaction was let to proceed for 1h at 15°C. The "activated" ester terminated surfaces (Si-COOSuc) were afterward rinsed successively into i) warm NaH_2PO_4 (0.1 M, pH = 5, 50°C) solution for 10 min, ii) diluted NaH_2PO_4 solution (NaH_2PO_4 0.1 M/ H_2O , v:v = 1:1, 50°C) and then iii) in UPW for another 10 min. After carefully drying under Ar flow, the Si-COOSuc surfaces were stored in acetonitrile solution.

The final step (step ③ in **Figure 2.1**) consists in coupling pyridyl groups onto the surface by reacting the Si-COOSuc activated surface with aminethyl pyridine. The coupling reaction was done by immersion of the Si-COOSuc surfaces in 5 mM aminoethyl pyridine solution. After the introduction of the Si sample, the solution was outgassed with Ar for 5 min to remove O₂. The reaction was let to proceed for 1h at 25°C in the closed schlenck. The resulting pyridyl-terminated surface Si-Py was copiously rinsed with acetonitrile and water, and finally blown dried under a stream of nitrogen gas.

2.3 Surface morphology

2.3.1 Atomic Force Microscopy (AFM)

Representative AFM images of the surface at the different steps of the construction of the pyridine-terminated layer are displayed in **Figure 2.2**. The structure of the Si (111)-H surface prior grafting and the subsequent chemical modifications is shown on **Figure 2.2(a)**. The surface exhibits a staircase structure with terraces, flat at the atomic scale and separated by steps of height 3.1 Å (corresponding to the distance between two Si (111) atomic planes). After the grafting, the surface activation and the coupling of pyridyl groups, no significant modification of the surface topography is detected. The surfaces look homogeneous and free of significant amount of contaminants or residues. The fact that the staircase structure is preserved, and the lack of significant increase of the roughness on the terraces, suggest at this stage a homogeneous coverage of the surface by a dense monolayer. For the pyridyl terminated surfaces, the staircase structure of the initial Si (111)-H surfaces is still observed, as well as the cleanness and flatness.

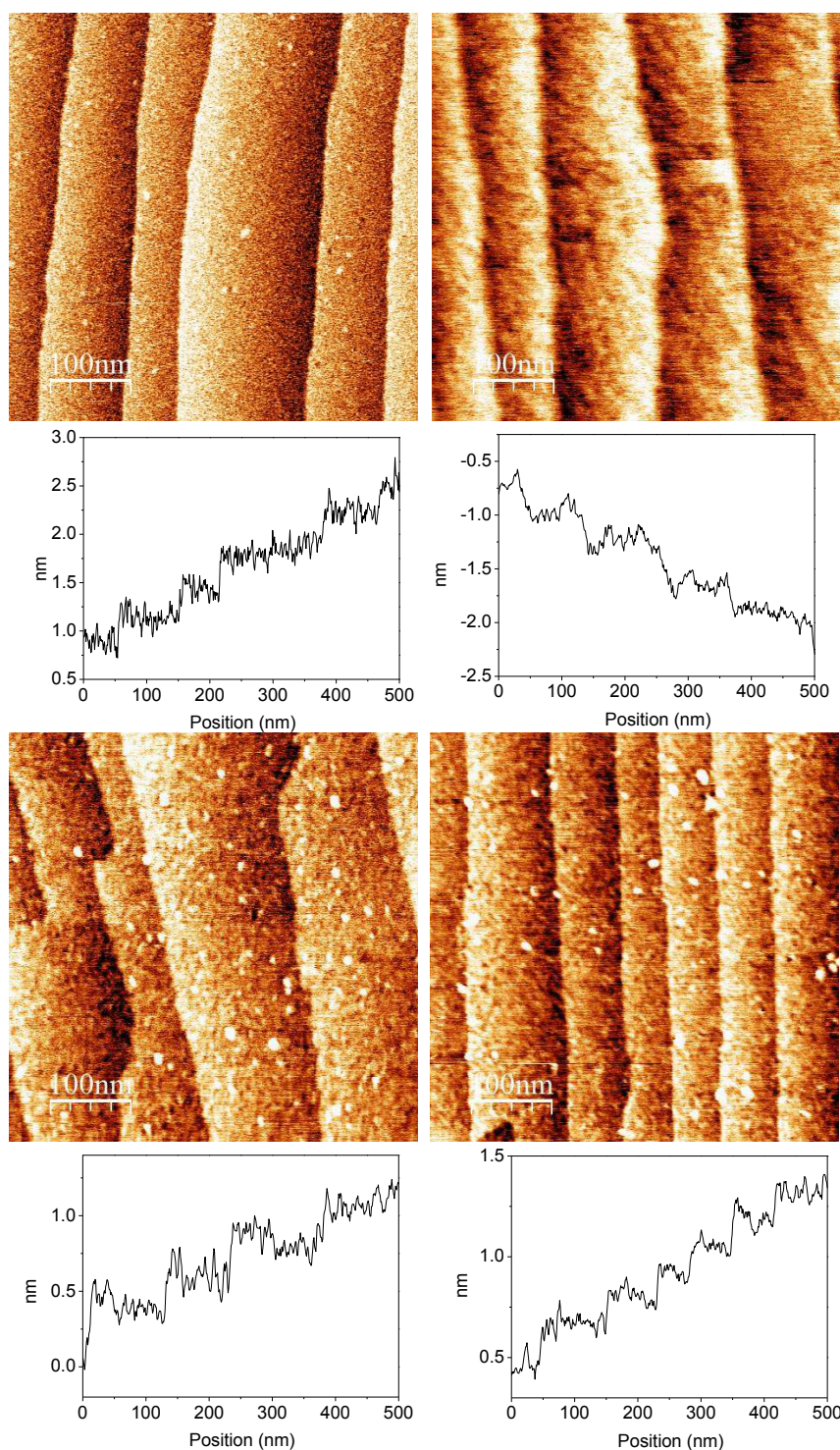


Figure 2.2. AFM images (500 × 500 nm²) of a Si (111) surface after each step of the functionalization: (a) hydrogenated Si-H surface; (b) acid terminated Si-COOH surface; (c) activated Si-COOSuc surface and (d) Si-Pyridine terminated surface. A line profile is given below each image.

2.3.2 X-ray reflectivity (XRR)

The surface functionalized by pyridyl groups was characterized by X-ray reflectivity (XRR) to determine the thickness (t_{ML}) and electronic density (ρ_{ML}) of the organic monolayer. As-obtained XRR curve is shown in **Figure 2.3**. The fitting model and parameters of the Si (111)-pyridine surface are summarized in **Table 2.1**. Notice that the roughness of the Si/organic layer interface was fixed to 0 Å.

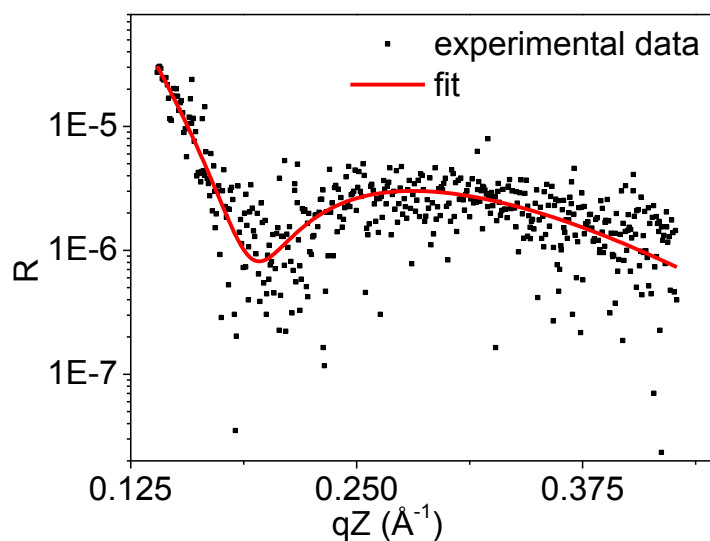


Figure 2.3. X-ray reflectivity curve for a Si (111)-pyridine surface. Black symbols represent experimental data and the red line is the best fit.

Table 2.1. Model and parameters used for the data fitting of the pyridine functionalized Si (111) surface.

	t (Å)	ρ (el.cm ⁻³)	σ (Å)
Pyridyl monolayer	17.14	4.46×10^{23}	3.4
Bulk	N/A	6.99×10^{23}	0

The thickness t_{ML} of the organic monolayer was found to be 17.14 Å, which is in good agreement with the optimized geometry of the organic chains in an all cis-trans conformation (17 Å as shown in **Figure 2.4**). This geometry was derived from molecular modelling using the Alchemy® software. The roughness of the layer is 3.4 Å, in accordance with the value derived from the topography studies by AFM. We also found that the electronic density of

the organic monolayer is $\rho_{\text{ML}} = 4.46 \times 10^{23} \text{ el. cm}^{-3}$. This electronic density is significantly higher than the expected value of $2.62 \times 10^{23} \text{ el. cm}^{-3}$ (calculated from the surface density of organic chains determined by IR spectroscopy, see **section 2.4.2**). This larger ρ_{ML} value may result from the presence of a water film onto the organic layer.

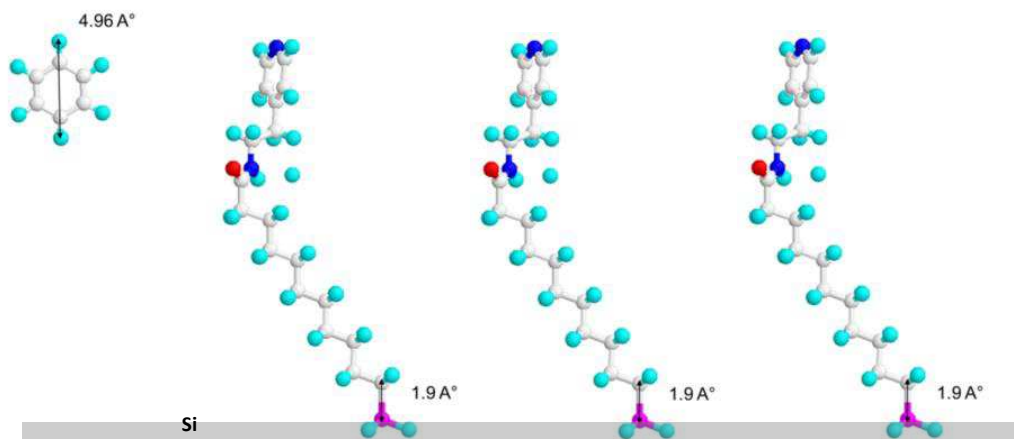


Figure 2.4. Molecular modeling of a pyridyl terminated alkyl chain grafted to the Si (111) surface. The purple balls represent the silicon atom, white balls denote carbon, cyan balls hydrogen, blue balls nitrogen atoms and red balls oxygen. The vertical length of the organic chain is 17 \AA , from the middle of the Si-C bond to the center of the terminal N atom. A benzene molecule is displayed as scaling factor (to calibrate the distances).

2.4 Surface composition

The evolution of chemical composition at the different steps of the surface modification has been investigated by IR spectroscopy, in ATR geometry for an improved sensitivity.

2.4.1 Qualitative analysis

Figure 2.5 shows wide range FTIR spectra (p polarization) of a silicon surface at the successive steps of functionalization. For each spectrum the reference is the as-prepared hydrogenated Si-H surface prior to any chemical modification. The positive bands are related to absorbance of chemical groups present on the surface at a given step. The sharp negative peak at 2083 cm^{-1} (stretching mode, $\nu_{\text{Si-H}}$) indicates the loss of Si-H bonds. After the grafting (step ①), we can observe a band at 1715 cm^{-1} , assigned to carbonyl $\nu_{\text{C=O}}$ involved in carboxylic acid groups (stretching mode), and additional bands in the range $2800\text{-}2950 \text{ cm}^{-1}$ assigned to the aliphatic chains. More specifically, the bands at 2922 cm^{-1} and 2853 cm^{-1} are attributed to the asymmetric and symmetric methylene stretching modes, respectively. Notice the rather low intensity of the bands corresponding to silicon oxide ($1000\text{-}1200 \text{ cm}^{-1}$).

Qualitatively, the low intensity of these bands indicates a high grafting yield (oxidation is a side reaction that limits the density of grafted alkyl chains on the surface if grafting conditions are not well controlled due to the presence of traces of water/oxygen). The observation of peaks characteristic of carboxyl chains together with the presence of the negative sharp peak at 2083 cm^{-1} clearly indicate the presence of the acid chains on the surface and strongly suggest the occurrence of hydrosilylation reaction $\text{Si-H} \rightarrow \text{Si}-(\text{CH}_2)_{10}\text{-COOH}$. Unfortunately, it is not possible to clear-cut the formation of Si-C bonds from FTIR spectra because the absorption band corresponding to $\nu\text{Si-C}$ stretching mode is weak and is expected at $500\text{-}900\text{ cm}^{-1}$, which is out of the wavenumber range that can be investigated in ATR geometry when using silicon prism. However for such alkyl monolayer, grafted by hydrosilylation, the formation of Si-C bonds has been confirmed by XPS characterizations.¹⁴ It is noteworthy that the sharp peak related to $\nu\text{Si-H}$ mode (at 2083 cm^{-1}) observed in p-polarization is nearly absent in s-polarization (see Appendix, **Figure A2.1**). This indicates that the Si-H bonds are normal to the surface, in agreement with expectations for a (111) oriented surface. The spectrum of this Si-COOH surface is consistent, in every points, with past reports¹¹ and pertains to the high quality of the surface.

After step ②, the CH band is essentially unchanged. Only the $\nu\text{C=O}$ band at 1715 cm^{-1} has vanished and is replaced by a triplet band at 1745 , 1787 and 1817 cm^{-1} which are assigned to $\nu\text{C=O}$ of the carbonyl involved in the succinimidyl cycle and in the ester linkage.¹³ The changes observed on the spectra confirm the efficiency of the surface activation ②. Qualitatively, it can be inferred, at first glance, that the reaction is close to be quantitative since the peak related to carboxylic acid has almost totally disappeared (a more accurate investigation of the spectrum shows that actually a shoulder is present on the left side of the main peak that indicates that few amount of acid are still present on the surface).

After the coupling of amino ethyl pyridine (step ③), the succinimidyl ester - COOSuc related bands have disappeared and have been replaced by new bands located at 1545 , 1603 and 1651 cm^{-1} for the most significant. The more intense band at 1651 cm^{-1} is assigned to amide bonds ($\nu\text{C=O}$ amide I stretching band). The two others bands can be assigned to vibration modes of the pyridine cycle (quadrant and semicircle stretch modes respectively at 1603 and 1545 cm^{-1}). However the assignment of the band at 1545 cm^{-1} is not so trivial because amide II band ($\nu\text{C-NH}$, $\sim 1550\text{ cm}^{-1}$) is also expected within this wavenumber range. Anyway, the presence of the three bands above discussed clearly indicates the covalent coupling of the pyridyl groups through amide linkage. It is noteworthy that the intensity of the methylene related bands ($2700\text{-}3000\text{ cm}^{-1}$) looks qualitatively unchanged, which is consistent with the addition of only 2 $-\text{CH}_2$ (brought by the amino linker) per alkyl chain (10 CH_2 per chain).

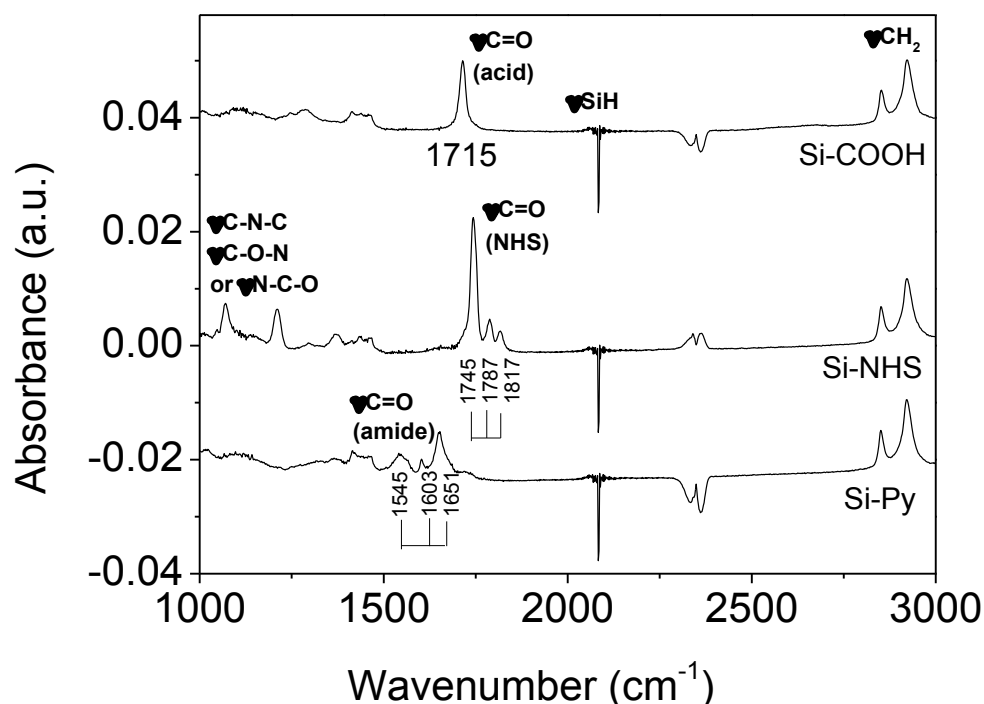


Figure 2.5. FTIR-spectra (p-polarization) of COOH, COOSuc and Pyridine terminated layers onto Si (111) surface. For each spectrum the reference is the as-prepared hydrogenated H-Si (111) surface prior to any modification. The band assignments are as indicated.

2.4.2 Quantitative analysis

The surface concentration of alkyl chains and tail groups at the different steps of the functionalization has been determined from a quantitative FTIR analysis method based on absorbance measurements using s and p-polarized IR beam and calibration of the intensity of IR bands by measurements in solution. Further details on the method can be found in ref.^{9, 11}. The method was employed for the quantification of carboxylic acid chains and succinimidyl (COOSuc) ester groups. In practice, the integrated absorbance of the ν C=O (corresponding to COOH or COOSuc groups) and ν CH₂ peaks has been determined from fitting the experimental spectra captured in p and s-polarization after the grafting of the monolayers and the subsequent activation of the COOH groups. The concentration of carboxylic chains and succinimidyl groups was then calculated using the equations given in reference^{9,11}, and the calibrated absorbances determined from measurements in carboxylic acid or succinimidyl ester solutions.

For the pyridyl groups, this latter method was not used because the overlap of the bands corresponding to the pyridine monolayers makes very difficult an accurate determination of

the integrated absorbances. Then, the concentration of pyridyl groups was inferred from the loss of COOSuc ester groups after the coupling.

Figure 2.6, **Figure 2.7** and **Figure 2.8** display examples of the $\nu\text{C}=\text{O}$ peak fitting used for the determination of the surface concentration of carboxylic acid COOH and succinimidyl COOSuc groups (formed after activation and lost after the pyridine coupling). For each experimental spectrum shown in the figures, the reference is the surface just prior to the chemical modification ca. the hydrogenated H-Si surface for the Si-COOH surface (**Figure 2.6**) and the Si-COOH surface for the Si-COOSuc surface (**Figure 2.7**). For the Si-COOH surfaces, the $\nu\text{C}=\text{O}$ peak of carboxylic acid was fitted with a Pseudo-Voigt function. For the activated Si-COOSuc surfaces, the experimental spectra (limited to the carbonyl region $1625\text{--}1875\text{ cm}^{-1}$) were fitted with 3 positive components (Pseudo-Voigt functions) accounting for the COOSuc (1745 , 1787 and 1815 cm^{-1}) and a negative component at 1715 cm^{-1} accounting for the disappeared COOH.

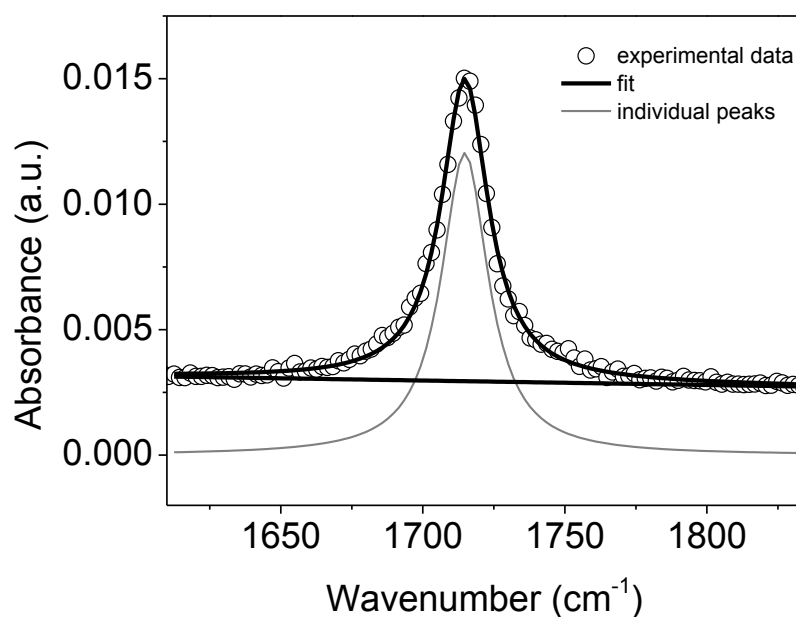


Figure 2.6. Spectral deconvolution of experimental spectrum (open symbols) of a Si-COOH surface. The spectrum (within the carbonyl range $1600\text{--}1875\text{ cm}^{-1}$) is fitted with a single component (pseudo Voigt function) and a linear baseline (solid line). The reference is the hydrogenated Si-H surface prior to the grafting of the carboxyl chains. The band corresponds to the $\nu\text{C}=\text{O}$ stretching mode of the carboxyl group.

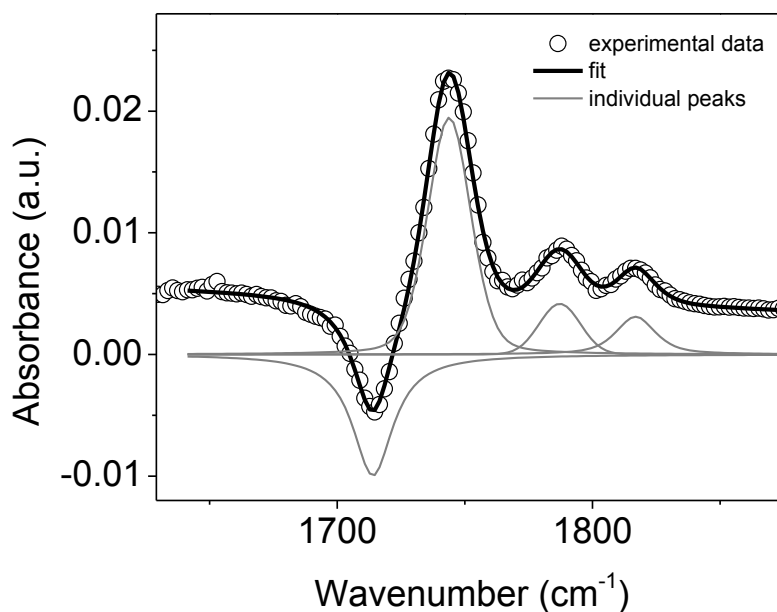


Figure 2.7. Spectral deconvolution of experimental spectrum (open symbols) of a Si-COOSuc surface. The reference is the Si-COOH surface prior to the activation reaction. The spectrum (within the carbonyl range 1625-1875 cm^{-1}) is fitted using 3 positive components (pseudo Voigt functions) corresponding to the COOSuc ester groups, a negative component corresponding to the disappeared COOH and a linear baseline (solid line).

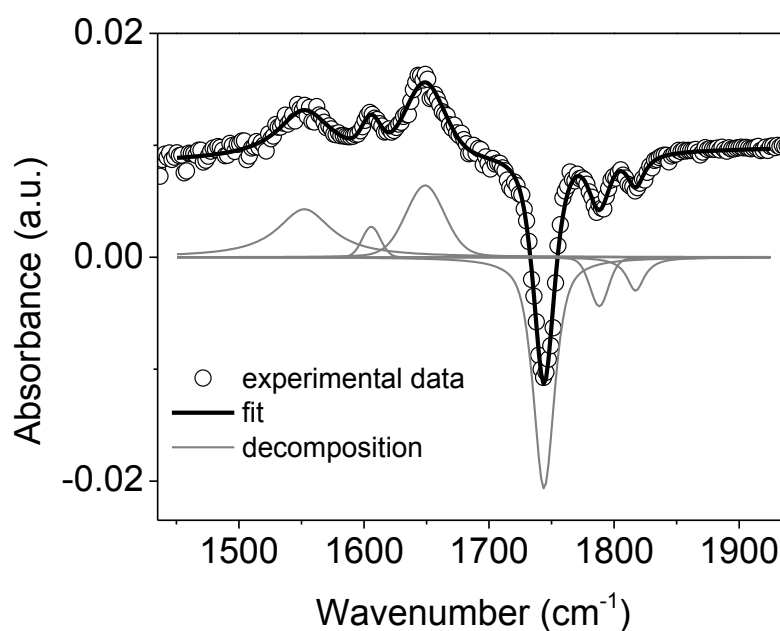


Figure 2.8. Spectral deconvolution of experimental spectrum (open symbols) of a Si-Pyridine surface. The reference is the Si-COOSuc surface prior to the pyridine coupling. The spectrum (within the carbonyl range 1380-1950 cm^{-1}) is fitted using 3 positive components (pseudo Voigt functions) related to amide linkage and pyridyl cycles, 3 negative components corresponding to the disappeared COOSuc esters and a linear baseline (solid line).

The as-determined surface concentrations of the different tail-groups are displayed in **Table 2.2**, the data were derived from the calibration of the integrated absorbances of $\nu\text{C=O}$ peak corresponding to the carboxylic acids COOH and succinimidyl ester COOSuc (*formed* after the activation step or *lost* after the pyridine coupling)

Table 2.2. Summary of the quantitative IR analysis: surface concentration of the tail groups at the different steps of the surface functionalization.

	COOH / cm ²	COOSuc / cm ²	Pyridyl / cm ²
Grafting Step ①	3.0×10^{14}	0	0
Surface activation Step ②	0.2×10^{14}	2.8×10^{14}	0
Pyridine coupling Step ③	0.2×10^{14}	0	2.8×10^{14}

2.4.3 Discussion

After the grafting, the surface concentration of acid chains derived from the FTIR analysis is 3×10^{14} chains per cm². This result is in agreement with surface concentrations previously reported for such acid monolayers.¹¹ This concentration represents a surface coverage of 38% with respect to the initial concentration of available Si-H anchoring sites on the hydrogenated Si (111) surface (7.83×10^{14} Si/cm²). This coverage indicates that the acid monolayers are rather dense since at most coverage of 50% is anticipated when accounting for the surface occupied by an alkyl chain standing in all cis-trans configuration on the surface as shown in **Figure 2.4** (ca. 20 - 21 Å²).¹⁵

The activation and coupling reaction (steps ② and ③) are quantitative. After activation, at least ~95% of the carboxylic acids are transformed into succinimidyl ester (step ②) that are in turn totally replaced by pyridyl groups during the subsequent coupling reaction (step ③). FTIR data show that the protocol implemented leads to very homogeneous surface (with respect to surface composition) exposing essentially pyridyl end-groups.

Figure 2.9 shows an *in plane* model structure of the organic monolayer with a surface coverage 50%.¹¹ The red symbols stand for the Si-H sites that have been substituted by Si-(CH₂)₁₀-R chains. As a consequence, the average distance between two pyridyl terminated chains should be 3.84 Å and 6.65 Å in the two perpendicular directions of the Si (111) plane. If we consider the crystal lattice of the Prussian blue analogues that will be studied in this

PhD work, the distance between two transition metal cations is expected to be in between 5 and 5.25 Å. Although there is no direct relationship with the spacing between the pyridyl functional groups, the flexibility of the organic chains and that of the Prussian blue lattice may favor an oriented growth.

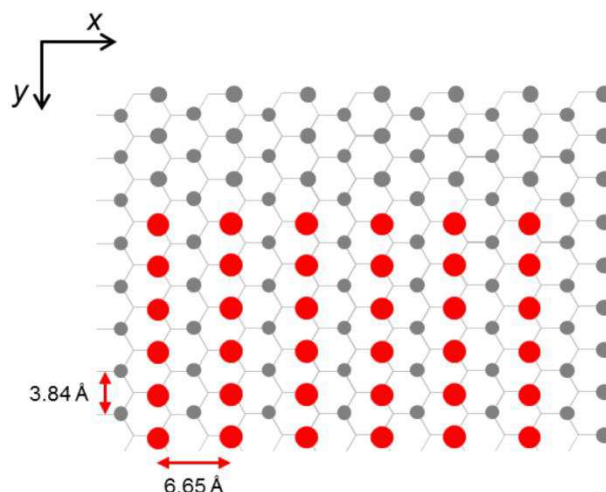


Figure 2.9. Expected structure of the alkyl chains onto Si (111) surfaces (top view). The grey symbols are the terminal hydrogen atoms, and the red symbols stand for the grafted sites (Si-(CH₂)₁₀-R chains).

2.5 Conclusion

In a summary, Silicon (111) surfaces have been successfully functionalized by a monolayer of alkyl chains bearing pyridyl tail-groups. The as-obtained surfaces exhibit well-defined structure and chemical composition. The surfaces are flat at the atomic scale with a staircase structure reminiscent of the hydrogenated surfaces. The final surface coverage by pyridyl groups is 2.8×10^{14} per cm², indicating that the organic chains are compact with distances between two chains of 3.84 Å and 6.65 Å in perpendicular directions of the (111) plane. These surfaces will be used as substrates in the next chapters to grow single-phase Rb_xNi[Cr(CN)₆]_y·zH₂O (RbNiCr) and Rb_xCo[Fe(CN)₆]_y·zH₂O (RbCoFe) layers and bilayer heterostructures.

2.6 References

1. S. Ciampi; J. B. Harper; J. J. Gooding, Wet chemical routes to the assembly of organic monolayers on silicon surfaces via the formation of Si-C bonds: surface preparation, passivation and functionalization. *Chem. Soc. Rev.* **2010**, *39* (6), 2158-2183.
2. J. M. Buriak, Organometallic chemistry on silicon and germanium surfaces. *Chem. Rev.* **2002**, *102* (5), 1272-1308.
3. D. D. M. Wayner; R. A. Wolkow, Organic modification of hydrogen terminated silicon surfaces. *J. Chem. Soc., Perkin Trans.* **2002**, (1), 23-34.
4. P. Thissen; O. Seitz; Y. J. Chabal, Wet chemical surface functionalization of oxide-free silicon. *Progress in Surface Science* **2012**, *87*, 272-290.
5. D. K. Aswal; S. Lenfant; D. Guerin; J. V. Yakhmi; D. Vuillaumea, Self assembled monolayers on silicon for molecular electronics. *Analytica Chimica Acta* **2006**, *568*, 84-108.
6. P. Gorostiza; C. Henry de Villeneuve; Q. Y. Sun; F. Sanz; X. Wallart; R. Boukherroub; P. Allongue, Water exclusion at the nanometer scale provides long-term passivation of silicon (111) grafted with alkyl monolayers. *J. Phys. Chem. B* **2006**, *110*, 5576-5585.
7. H. Häkkinen, The gold-sulfur interface at the nanoscale. *Nat. Chem.* **2012**, *4*, 443-455.
8. M. L. Munford; R. Cortès; P. Allongue, The preparation of ideally ordered flat H-Si(111) surface. *Sensors and Materials* **2001**, *13* (5), 259-269.
9. A. Moraillon; A. C. Gouget-Laemmel; F. Ozanam; J.-N. Chazalviel, Amidation of monolayers on silicon in physiological buffers: A quantitative IR study. *J. Phys. Chem. C* **2008**, *112*, 7158-7167.
10. P. Allongue; V. Kieling; H. Gerische, Etching mechanism and atomic structure of H-Si(111) surfaces prepared in NH₄F. *Electrochimica Acta.* **1995**, *40*, 1353-1360.
11. A. Faucheux; A. C. Gouget-Laemmel; C. Henry de Villeneuve; R. Boukherroub; F. Ozanam; P. Allongue; J.-N. Chazalviel, Well-defined carboxyl-terminated alkyl monolayers grafted onto H-Si(111): packing density from a combined AFM and quantitative IR study. *Langmuir* **2006**, *22*, 153-162.
12. H. Asanuma; G. P. Lopinski; H. Yu, Kinetic control of the photochemical reactivity of hydrogen-terminated silicon with bifunctional molecules. *Langmuir* **2005**, *21*, 5013-5018.
13. S. Sam; L. Touahir; J. S. Andresa; P. Allongue; J.-N. Chazalviel; A. C. Gouget-Laemmel; C. Henry de Villeneuve; A. Moraillon; F. Ozanam; N. Gabouze; S. Djebbar, Semiquantitative study of the EDC/NHS activation of acid terminal groups at modified porous silicon surfaces. *Langmuir* **2010**, *26* (2), 809-814.

14. X. Wallart; C. Henry de Villeneuve; P. Allongue, Truly quantitative XPS characterization of organic monolayers on silicon: study of alkyl and alkoxy monolayers on H-Si(111). *J. Am. chem. Soc.* **2005**, *127*, 7871-7878.
15. A. B. Sieval; B. van den Hout; H. Zuilhof; E. J. R. Sudholter, Molecular modeling of covalently attached alkyl monolayers on the hydrogen-terminated Si(111) surface. *Langmuir* **2001**, *17*, 2172-2181

Chapter 3

Growth and magnetic properties of $\text{Rb}_x\text{Ni}[\text{Cr}(\text{CN})_6]_y \cdot z\text{H}_2\text{O}$ films

3.1 Introduction

This chapter focuses on the growth of rubidium nickel hexacyanochromate, $\text{Rb}_x\text{Ni}[\text{Cr}(\text{CN})_6]_y \cdot z\text{H}_2\text{O}$, layers on the pyridine-terminated Si(111) surfaces described in Chapter 2. As bulk materials, these compounds are ferromagnets with a relatively large magnetic ordering temperature, from 50 K to 90 K depending on the Cr/Ni atomic ratio^{1,2,3}, and well documented magnetic characteristics. Their growth as thin films should be readily controlled, as the oxidation state of the Ni and Cr precursors in solution is identical to the valence state of these ions in the solid phase, in contrast with the case of the $\text{Rb}_x\text{Co}[\text{Fe}(\text{CN})_6]_y \cdot z\text{H}_2\text{O}$ layers that will be described in the next chapter.

In previous research work on nickel hexacyanochromates, most efforts have been put on nanoparticles. Catala and coworkers found a critical size of ca. 15 nm for the single magnetic domain regime in the case of the $\text{Cs}_{0.52}\text{Ni}[\text{Cr}(\text{CN})_6]_{0.97} \cdot z\text{H}_2\text{O}$ compound, by studying particles with a size tailored from 6 to 30 nm;⁴ they observed that by using different isolation techniques, different magnetic properties were observed.⁵ Investigations of NiCr films have also drawn a lot of attention in recent years. Sequential adsorption methods using Langmuir-Blodgett monolayers as templates have been largely studied^{6,7}, and researchers found a thickness dependence of the magnetic ordering temperature. Ni-Cr thin films down to 6 nm thickness were also prepared using sequential deposition on functionalized Si (100) surfaces, which led to isolated dots with a low surface coverage.⁸

In this chapter, we present a simple method to grow rubidium nickel hexacyanochromate (hereafter called RbNiCr) films onto functionalized Si(111) surfaces, using a one-bath approach. To limit the number of parameters to be varied (reactant concentration, addition rate, etc.), we used the results obtained by M. Presle who investigated the growth of a $\text{Rb}_{0.1}\text{NiCr}(\text{CN})_6]_{0.7} \cdot z\text{H}_2\text{O}$ shell phase onto preformed $\text{Rb}_{0.5}\text{Co}[\text{Fe}(\text{CN})_6]_{0.8} \cdot z\text{H}_2\text{O}$ particles.⁹ Even though the surface termination (and hence solid/solid surface tension) may be different from that of our functionalized surfaces, we selected precursor concentrations similar to those used in this previous work, i.e. in between the threshold values for

heterogeneous (C_{min}^{het}) and homogeneous (C_{min}^{hom}) nucleation to limit the formation of RbNiCr particles in solution. The films were characterized by a combination of different techniques, namely Atomic Force Microscopy (AFM), X-ray reflectivity (XRR), X-ray diffraction (XRD), Rutherford Backscattering Spectroscopy (RBS) and SQUID magnetometry. In this chapter, the growth mechanism is discussed in detail, by correlating the chemical composition, the film morphology and the magnetic properties. Special attention is paid to the magnetic anisotropy of these thin films.

3.2 Experimental section

3.2.1 Preparation of the solution used for deposition

Potassium hexacyanochromate ($K_3Cr(CN)_6$, 99.99%, 325.6 g/mol), Rubidium chloride (RbCl, 99.8%, 120.92g/mol) and anhydrous Nickel chloride ($NiCl_2$, 129.60g/mol) were used as precursors. $K_3Cr(CN)_6$ and RbCl reagents were purchased from Sigma-Aldrich, $NiCl_2$ was obtained from Vectron GMBH. All reagents were used without further treatment. Note that ultrapure water (Milli-Q, 18.2 M Ω cm) was systematically used during manipulation (preparation of solutions, rinsing steps, etc.).

The solution in which the functionalized Si (111) surfaces will be immersed was prepared by slowly mixing 80 mL of a 1 mM $K_3Cr(CN)_6$ solution and 80 mL of a mixture solution containing 1 mM $NiCl_2$ and 2 mM RbCl in a beaker filled with 300 mL of water. Moderate stirring (400 rotation per minute) was performed to favour precursors dispersion. Addition was carried out with a peristaltic pump, at a rate of 0.75 mL/min. The temperature was thermostated at 20 °C during the whole addition. The final solution composition was: 0.34 mM RbCl, 0.17 mM $NiCl_2$ and 0.17 mM $K_3[Cr(CN)_6]$.

In these conditions, the nucleation rate of RbNiCr particles in solution is strongly reduced (see in Chapter 1). However, we observed some aging of the solution that became turbid after ca. 100 min, with formation of big particles (120 nm diameter, number - average value) according to Dynamic Light Scattering measurements. For this reason we systematically used freshly prepared solutions to grow each film for a better control of the reactant concentrations.

3.2.2 $Rb_xNi[Cr(CN)_6]_y \cdot H_2O$ film deposition

The functionalized Si (111) substrate (10 × 10 mm²) was fixed with an electrolytic scotch tape onto a Teflon holder leaving a circular aperture of diameter 8 mm in contact with the

solution. The backside of the sample was not exposed to the solution. The Teflon holder was mounted on a rotating electrode system (rotation rate from 0 to 1400 rpm). The sample was mounted face down (see **Figure 3.1**). After deposition, the sample was thoroughly rinsed with water and then dried under a stream of Ar gas. Hereafter, the deposition time refers to the contact time between the substrate and the solution.

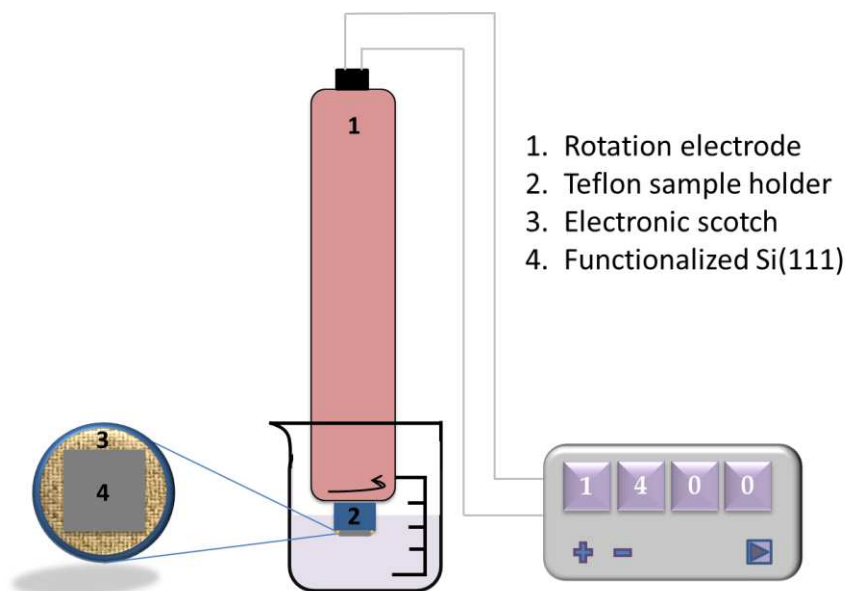


Figure 3.1. Scheme showing the mounting of the silicon substrate onto a custom rotating electrode system.

3.3 Results

To ease the correspondence between the different data sets, the deposits will be characterized by the deposition time or the thickness t_{XRR} derived from x-ray reflectivity (XRR).

3.3.1 X-ray reflectivity (XRR) measurements

Figure 3.2 shows x-ray reflectivity curves, up to $q_z = 0.23 \text{ \AA}^{-1}$ (maximum scan range in our experiments), for films grown with increasing deposition time. Qualitatively, the period of the reflectivity oscillations decreases with increasing the deposition time, which is consistent with an increasing film thickness. The damping of oscillations is a primary indication that the films have a uniform thickness and are smooth, as confirmed by the cross section SEM image shown in **Figure 3.3**.

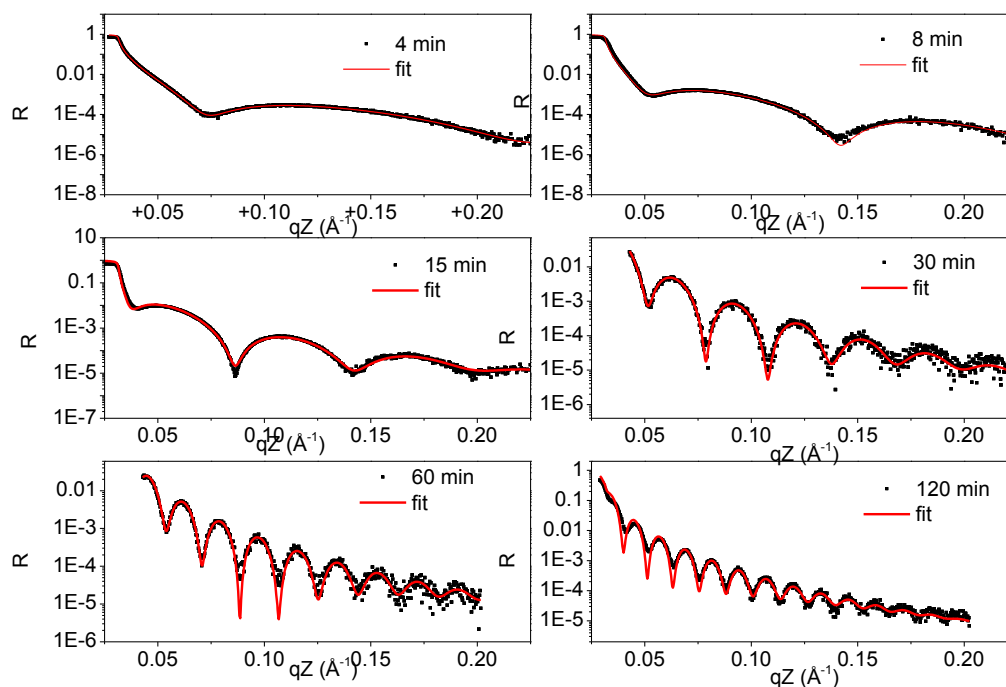


Figure 3.2. X-ray reflectivity plots of RbNiCr layers with increasing deposition time. The deposition time is given in each graph. Symbols are experimental data. Solid red line is the best fit.

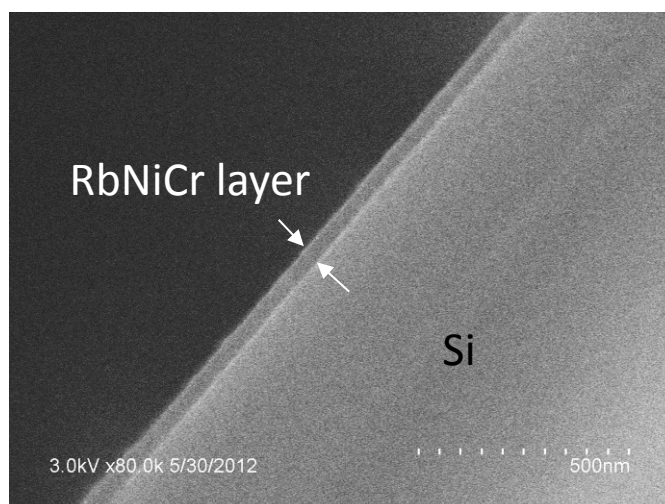


Figure 3.3. SEM cross section of the thicker film obtained after 120 min deposition. The full scale bar is 500 nm. The thickness is estimated to be less than 50 nm, in good agreement with the thickness determined by X-ray reflectivity.

Experimental data were analysed using PARRATT32 software¹⁰ according to the bi-layer model shown in **Figure 3.4**. This model is including a semi-infinite substrate of Si, an organic monolayer (ML) accounting for the functionalized organic chain, and a layer of RbNiCr. **Figure 3.4** shows the electronic density profile $\rho(z)$. The calculated values of electronic

density are expressed in unit of electrons per cm^3 , they are $\rho_{\text{Si}} = 6.99 \times 10^{23} \text{ el.cm}^{-3}$ for bulk Silicon, $\rho_{\text{ML}} = 2.16 \times 10^{23} \text{ el.cm}^{-3}$ for the pyridyl terminated monolayer accounting for the surface density of chains determined in Chapter 2, and $\rho_{\text{Layer}} = 5.39 \times 10^{23} \text{ el.cm}^{-3}$ for $\text{Rb}_{0.13}\text{NiCr}(\text{CN})_{0.71} \cdot 5\text{H}_2\text{O}$ (powder sample used as a reference and synthesized using an addition protocol and reactant concentrations close to those involved in the preparation of the solution used for deposition, see **section A.3.1** in Appendix). Any roughness at interfaces is smoothing the transition between two ρ values (see the dotted red line). Curve fitting gives access to the thickness (t), the electronic density (ρ) and the RMS value of roughness (σ) of the organic layer and of the deposit. It is important to notice that we applied a weighting factor $w = 1 / (y + 1)$ and y is the number of measured photons/s to even the error between the calculated and experimental plots over the whole q_z -range (this weighting minimizes the influence of experimental data at large q_z -value which is proved to be essential to obtain reliable parameters).

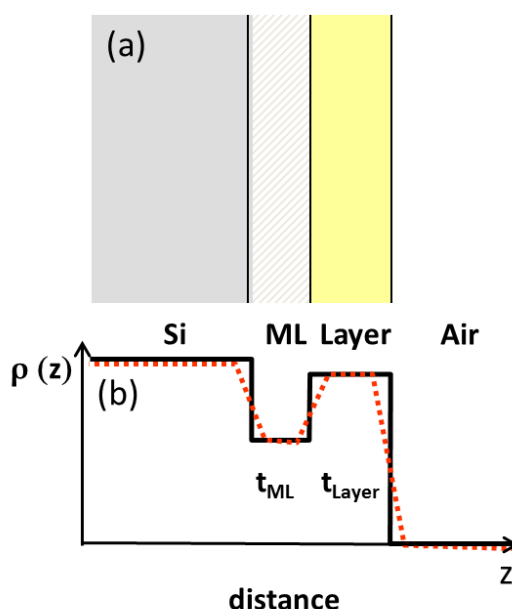


Figure 3.4. Bilayer structure used to fit the XRR curves. (a) Scheme of the structure and (b) corresponding profile of electronic density. The black line corresponds to a structure with no roughness at all. The red dashed line shows the influence of interface roughness.

We found that the procedure of XRR data fitting has a significant impact on the result since the XRR signal is primarily dominated by the deposit. In fact, if the parameters (t , ρ and σ) of each of the different layers are let free to vary, this leads to unrealistic parameter values for the organic film. To solve this issue, the curves in **Figure 3.2** were fitted in two steps. In a first step the organic monolayer parameters (ρ_{ML} , t_{ML} , and σ_{ML}) were kept *fixed* and equal to their value found in **Chapter 2** (i.e. $t_{\text{ML}} = 17.1 \text{ \AA}$, $\rho_{\text{ML}} = 4.5 \times 10^{23} \text{ el.cm}^{-3}$ and $\sigma_{\text{ML}} = 0.3 \text{ nm}$), while only those related to the deposit were free to vary. In a second step, the monolayer

parameters were let free to vary, which improved significantly the χ^2 of the fit. **Table 3.1** gives the final parameters for the RbNiCr films and organic monolayers. We can notice that the deposit parameters (ρ_{Layer} , t_{Layer} and σ_{Layer}) are quasi identical after step 1 and step 2, which gives confidence in the results. The final monolayer parameters (ρ_{ML} , t_{ML} , and σ_{ML}) have significantly varied but they nevertheless keep a physical meaning. Note that the sum of t_{ML} and t_{Layer} is typically defined with 1 to 2% standard deviation.

As shown in **Figure 3.5**, the thickness t_{Layer} increases nearly linearly with deposition time, except at long times (120 min) when the growth is probably slowed down because of the formation of RbNiCr particles in solution which significantly decreases the concentration of reactants. This is a first indication that the growth rate is constant. The slope of the straight line yields a growth rate of ca. 0.5 nm/min. All films show a RMS value of surface roughness determined by XRR $\sigma \sim 1$ nm, which is comparable with the RMS value of roughness derived from AFM imaging (see **Table 3.1** and **section 3.3.2**). In addition, the mean electronic density ρ_{Layer} is 4.9×10^{23} el.cm⁻³ (5.2×10^{23} el.cm⁻³ if we do not consider the thicker film), which is close to the value of 5.4×10^{23} el.cm⁻³ calculated for the Rb_{0.13}Ni[Cr(CN)₆]_{0.71}•5H₂O reference particles.

Table 3.1. Fitted parameters for RbNiCr films grown with different deposition times derived from X-ray reflectivity data. The parameters of the pyridyl terminated layer used for fitting are $t_{\text{ML}} = 1.71$ nm, $\rho_{\text{ML}} = 4.5 \times 10^{23}$ el.cm⁻³ and $\sigma_{\text{ML}} = 0.3$ nm (see Chapter 2, **Table 2.1**). In the last column, the RMS values refer to the roughness of the RbNiCr layers determined by AFM.

Deposition time [min]	RbNiCr layer			Pyridyl layer			AFM RMS roughness [nm]
	t_{Layer} [nm]	ρ_{Layer} [10 ²³ el.cm ⁻³]	σ_{Layer} [nm]	t_{ML} [nm]	ρ_{ML} [10 ²³ el.cm ⁻³]	σ_{ML} [nm]	
4	2.7	4.9	0.6	1.5	3.8	0	0.4
8	5.2	5.0	0.4	1.6	4.5	0	0.7
15	9.6	5.5	1	1.3	3.8	0.1	0.7
30	19.3	5.1	0.9	1.3	3.7	0.2	0.8
60	32.2	5.4	1.1	1.7	4.1	0.2	0.9
120	46.4	3.7	1.3	1.8	3.5	0.4	1.1

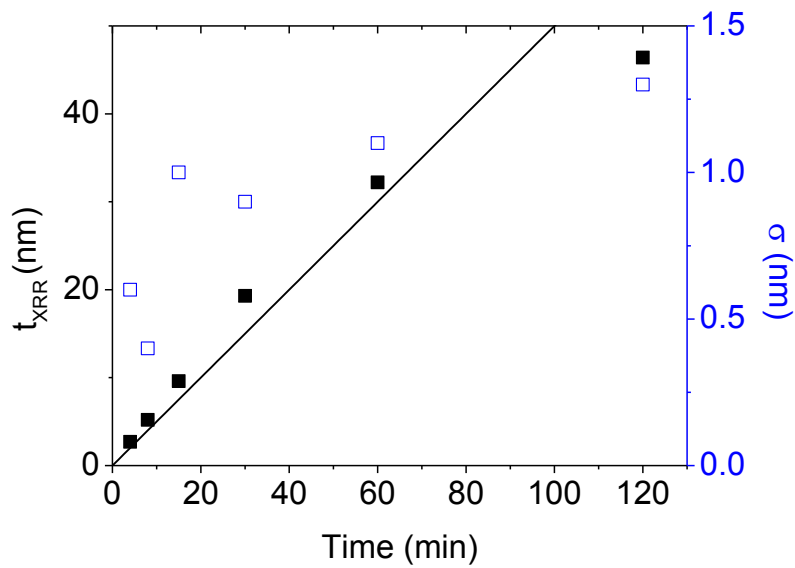


Figure 3.5. Time dependence of RbNiCr film thickness (black squares) and surface roughness (open squares) obtained by XRR.

3.3.2 Atomic Force Microscopy (AFM) characterizations

Representative AFM images of layers are displayed in **Figure 3.6** for different deposition times. They correspond to the films studied in the previous section. The thickness t_{XRR} given in each figure is the one derived from XRR characterizations (see **Table 3.1**). Line profiles are also presented below each image. These images show that the RbNiCr films look continuous, in agreement with XRR, and that they present a homogeneous granular morphology. For deposition times longer than 30 min, some cracks are observed. These are assigned to film shrinkage upon drying. Noticeably, layers are quite smooth on the scale of observation with a peak to peak roughness of ca. 1 nm at any thickness. Additional plane view SEM images showing the homogeneous character of the layers at larger scale are provided in Appendix (**Figure A3.2**).

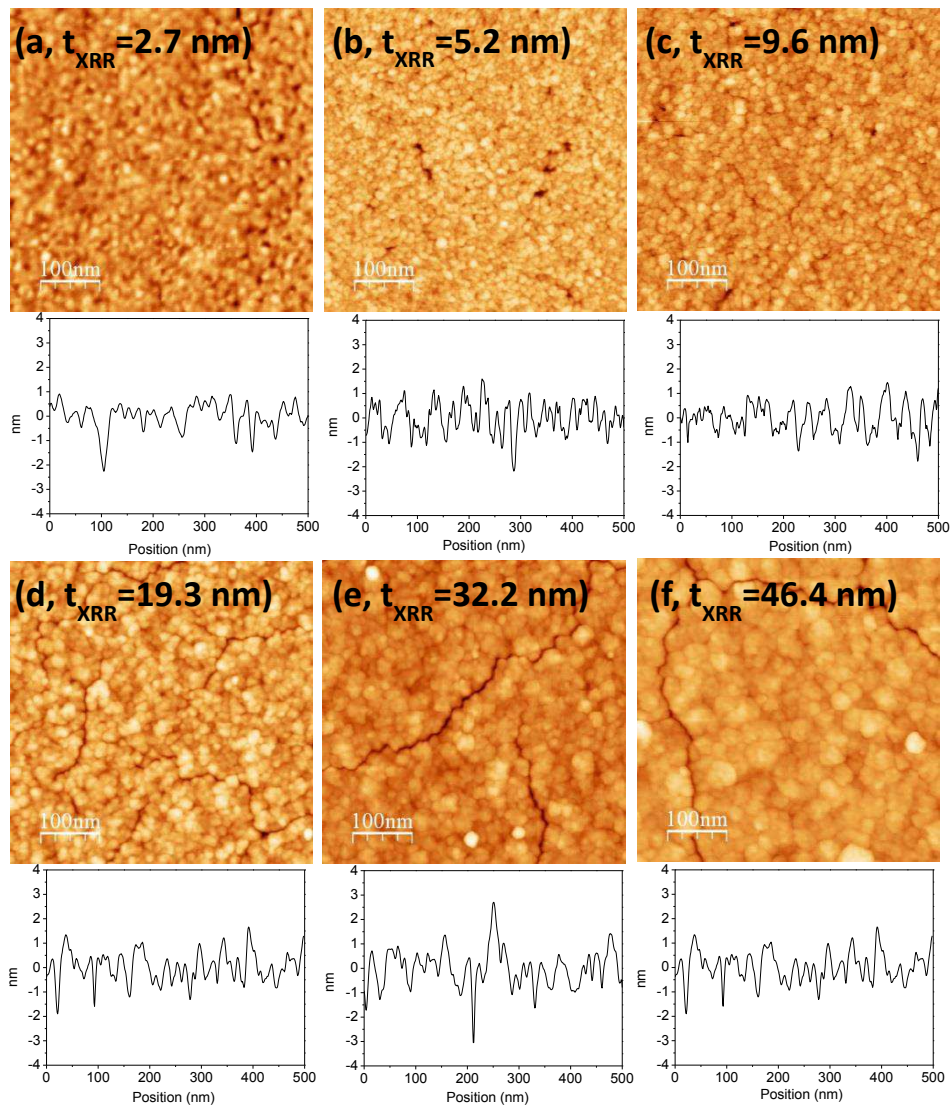


Figure 3.6. AFM images ($500 \times 500 \text{ nm}^2$) of the films corresponding to deposition time of: (a) 4 min, (b) 8 min, (c) 15 min, (d) 30 min, (e) 60 min and (f) 120 min; scale bar: 100 nm. A line profile is also given below each image. The film thickness derived from XRR is indicated for each film.

The WSxM 4.0 Beta 3.1 software¹¹ was used to determine the RMS (root mean square) roughness. RMS values (see **Table 3.1**) increase from 0.4 nm to 1.1 nm upon deposition, which is in agreement with XRR characterizations. We tentatively performed a grain analysis of the above images to determine the grain density and the grain size. **Figure 3.7** shows a plot of the grain density (filled squares) and the grain size (open circles) as a function of the thickness t_{XRR} . This figure shows that the grain density is nearly independent on the thickness (ca. 3.7×10^{11} grains/cm², see horizontal dashed line) which suggests an instantaneous nucleation process. The grain size (open circles) increases slowly with t_{XRR} .

However, one should bear in mind that the values of the grain size and density are strongly *coupled* quantities within the image analysis. We can only trust the grain size determination (ca. 20 nm) when the layer is *continuous*. The lateral size during the early stages of the growth is probably overestimated due to the finite size of the tip. This quantity will be evaluated later on by an independent method (see discussion, **section 3.4.2**).

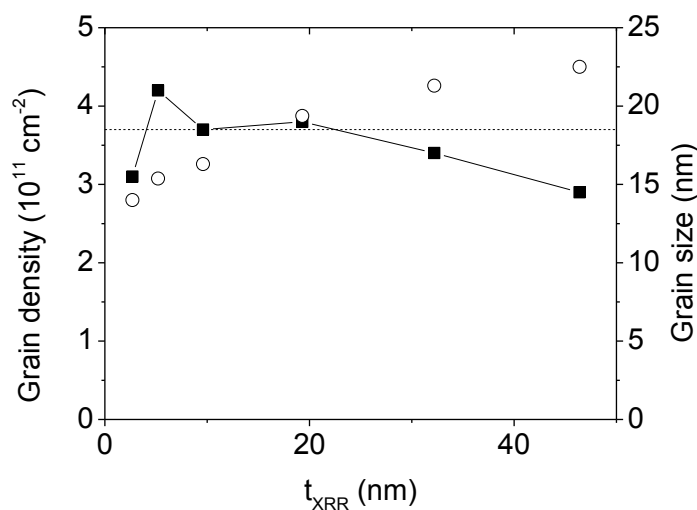


Figure 3.7. Variations with t_{XRR} of grain density (filled squares) and grain size (open circles) as measured from AFM image analysis.

3.3.3 X-ray diffraction (XRD)

Figure 3.8(a) compares $\theta/2\theta$ scans of RbNiCr layers (bottom panel) with that of $\text{Rb}_{0.13}\text{Ni}[\text{Cr}(\text{CN})_6]_{0.71} \cdot 5\text{H}_2\text{O}$ particles⁹ (upper panel) grown in solution. Detailed information about these particles is summarized in **section A.3.1** of the Appendix. For the latter sample, peak indexing is in perfect accordance with the well-known face centred cubic structure of Prussian blue.¹² The (222) peak of the silicon substrate was used as an internal reference for a precise determination of the 2θ positions in the case of films. It is remarkable that the XRD patterns of the layers (bottom panel in **Figure 3.8(a)**) exhibit *exclusively* the (002), (004) and (006) peaks, which means that the films are textured along the (00*l*) axis of the crystal structure, which is recalled in **Figure 3.8(b)**. Also noticeably the films are crystallized down to 8 min deposition time ($t_{\text{XRR}} = 5.2$ nm). In another series of samples, the (002) peak was resolved down to 2 min deposition time (ca. $t_{\text{XRR}} = 3.1$ nm). We performed complementary XRD characterizations using a 4-circle diffractometer and found no evidence for an in-plane orientation of the films at any thickness.

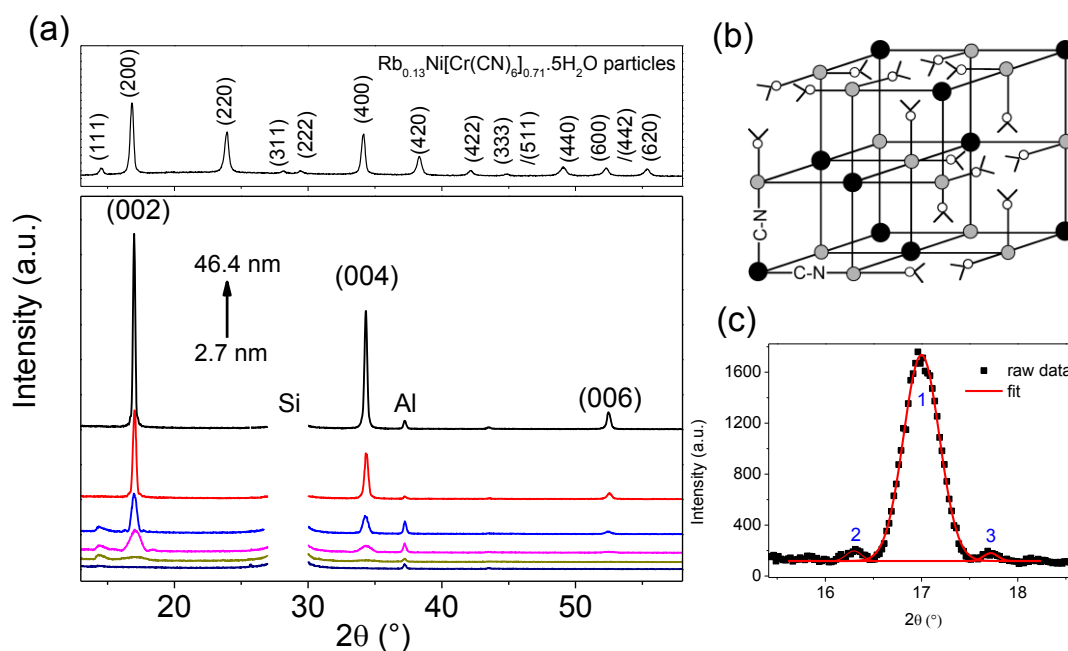


Figure 3.8. (a) $\theta - 2\theta$ scans ($\lambda = 1.5418 \text{ \AA}$) of $\text{Rb}_{0.13}\text{Ni}[\text{Cr}(\text{CN})_6]_{0.71}\cdot 5\text{H}_2\text{O}$ particles (top panel) and of RbNiCr films (bottom panel) of variable thickness (the deposition time is indicated in the figure). Notice that only $(00l)$ peaks are observed in the case of the layers. (b) Crystal structure of Prussian blue. Black and grey cycles stand for the two metallic ions. (c) Central (002) peak (1) and Laue oscillations (2, 3) observed for a RbNiCr layer corresponding to 30 min deposition, $t_{\text{XRR}} = 19.3 \text{ nm}$. Black symbols are the experimental data and red lines are fitted curves (see text for explanation).

Table 3.2 summarizes the results of XRD analysis. The lattice parameter a is calculated as the average value determined using Bragg law for peaks (002) and (004) . The fact that $a \sim 10.45 \text{ \AA}$ is essentially independent on thickness is a strong indication that the layers have a uniform structure. This assessment is supported by the symmetrical shape of the peaks and also by **Figure 3.8(c)**, which shows the presence of Laue oscillations with a period identical to the film thickness. The a value of 10.45 \AA is very close to that measured for the reference particles. This is a first indication that the layer composition must be close to that of the particles. This point will be further checked by an independent characterization (see **section 3.3.4**). The coherence length L_c was determined using a modified Scherrer formula:

$$L_c = \frac{0.9 \times \lambda}{\cos \theta \sqrt{(FWHM)^2 - 0.08^2 \times \pi / 180}} \quad \text{Eq.3.1}$$

where λ denotes the X-ray wavelength, θ is the diffraction angle and FWHM is the Full Width at Half Maximum of the (002) or (004) peaks. The correction 0.08° represents the intrinsic broadening due to the instrumental resolution. **Table 3.2** lists the FWHM and L_c

values. We did not detect significant changes in L_C as a function of the scattering order, confirming the absence of large strain along the c -axis.

Table 3.2. Calculated lattice parameter (a) and coherence length value (L_C). L_C refers to the (002) Bragg reflection. a is an average value derived from the analysis of peaks (002) and (004).

deposition [min]	a [Å]	FWHM (002)	FWHM (004)	L_C [nm]
4	-	-	-	-
8	10.43	1.51	1.43	5
15	10.44	0.87	0.85	9
30	10.46	0.42	0.43	20
60	10.45	0.26	0.30	32
120	10.46	0.18	0.21	50

The time dependence of L_C and of the intensity of the (002) and (004) peaks are shown in **Figure 3.9**. There is a quasi-linear increase of L_C , I_{004} and I_{200} with increasing deposition time, which is a good indication that the films are well crystallized with only the (00 l) orientation.

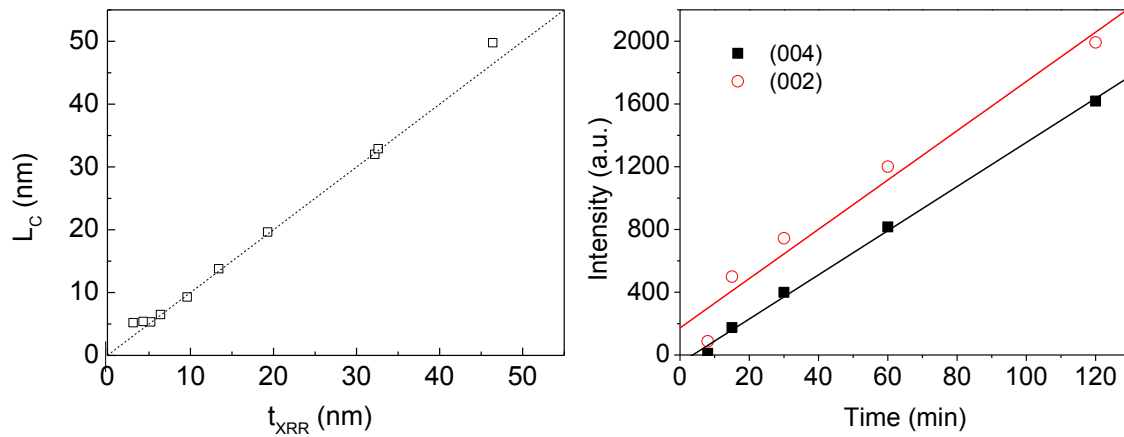


Figure 3.9. (left) Variation with t_{XRR} of the coherence length, L_C and (right) variation with time of the I_{004} and I_{002} integrated intensities derived from the XRD patterns of **Figure 3.8**. Note the linear relationship of these different quantities with t_{XRR} .

3.3.4 Rutherford backscattering (RBS) characterizations

Figure 3.10 shows a typical wide energy range RBS spectrum of a RbNiCr film with $t_{\text{XRR}} = 32.2$ nm (deposition time, 60 min). The plateau below 0.9 MeV corresponds to the silicon substrate. At higher energies, three peaks are well resolved (see the inset). According to the energy channel of the peak corresponding to a Bismuth reference sample, we can assign these peaks to Cr, Ni and Rb as labelled in the inset of **Figure 3.10**. No peak corresponding to potassium (at around 1.0 MeV) was observed. We checked that the RBS signal of each of the elements was proportional to the amount of charge passed during the measurement, which is taken as a sign that no matter is removed during the characterization.

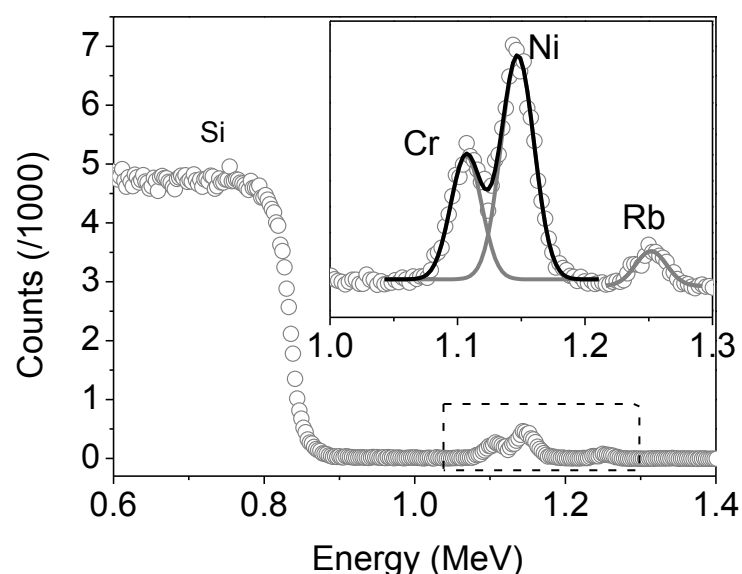


Figure 3.10. Typical RBS spectrum of a RbNiCr film with a thickness t_{XRR} of 32.2 nm. Inset is a zoom within the dotted rectangle. Symbols are experimental data and the solid lines are the three components (Gaussian function) used to account for the three peaks and determine their area.

By decomposing the peaks into three individual components, corresponding to Cr, Ni and Rb, we fitted each peak with a single Gaussian function in order to obtain its area. In this study, a Bismuth layer on silicon (5.62×10^{15} at./cm²) was used as a reference sample to determine absolute areal density values (see experimental method in Appendix). The areal densities of Cr, Ni and Rb in films with different deposition times are summarized in **Table 3.3**. Note that the presented areal density values are averaged values derived from measurements performed at different spots on the same sample. The last two columns of the table give the atomic ratios Rb/Ni and Cr/Ni.

In **Figure 3.11** we plot the variations of Ni, Cr and Rb areal densities (in at./cm³) as a function of t_{XRR} . The areal densities of these three elements vary almost linearly with film thickness. The ratio of slopes “Rb” to “Ni” yields the atomic ratio Rb/Ni = 0.08. In a similar way, one can derive the atomic ratio Cr/Ni = 0.73. Both ratio are therefore essentially independent on the film thickness which means that the RbNiCr layers have a uniform composition $\text{Rb}_{0.08}\text{Ni}[\text{Cr}(\text{CN})_6]_{0.73} \cdot z\text{H}_2\text{O}$ throughout the film depth. This chemical composition is close to the one of the $\text{Rb}_{0.13}\text{Ni}[\text{Cr}(\text{CN})_6]_{0.71} \cdot 5\text{H}_2\text{O}$ reference particles. Nuclear Reaction Analysis (NRA) was also performed (data not shown) to determine the O, N and C contents. The C and N areal densities were found to be consistent with the above composition. However no oxygen was detected, which suggests that water was removed from the lattice during secondary vacuum pumping.

Table 3.3. Areal density of the Ni, Cr and Rb elements derived from RBS analyses.

Sample	Deposition time [min]	Areal density 10^{14} atom / cm ²			Rb/Ni	Cr/Ni
		Ni	Cr	Rb		
1	4	5.07	3.37	0.75	0.15	0.66
2	8	12.98	9.94	0.99	0.08	0.77
3	15	26.76	19.79	2.00	0.07	0.74
4	30	62.69	43.38	5.45	0.09	0.69
5	60	98.37	71.20	8.04	0.08	0.72

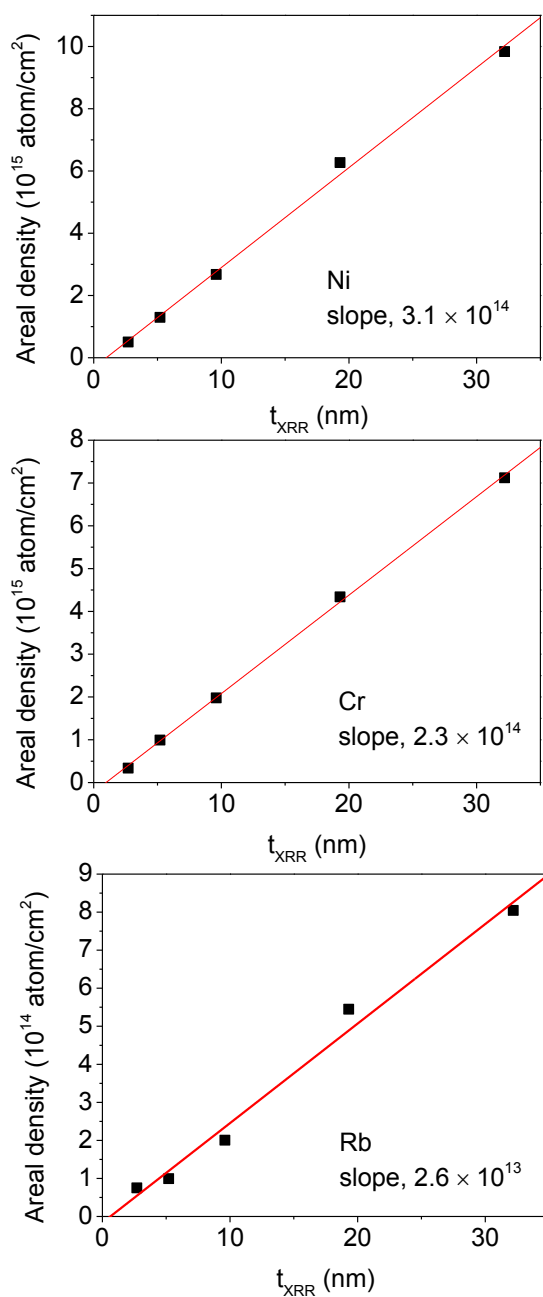


Figure 3.11. Areal density of Rb, Ni and Cr as a function of film thickness, t_{XRR} . The slopes of the straight lines are 3.1×10^{21} , 2.3×10^{21} and 2.6×10^{20} at/cm 3 for Ni, Cr and Rb respectively.

3.3.5 Influence of sample rotation

The influence of the mass transfer from the solution to the surface was briefly studied by preparing samples with different rotation rates. All films present the same characteristics (see Appendix, **section A.3.3**) as the ones presented above. At all rotation rates, films are

continuous and smooth with a granular structure. They are well crystallized, with a (00 l) texture and a lattice parameter ~ 10.45 Å. Their chemical composition derived from RBS is also consistent with the $\text{Rb}_{0.08}\text{Ni}[\text{Cr}(\text{CN})_6]_{0.73} \cdot z\text{H}_2\text{O}$ formula. **Table 3.4** shows that the deposit thickness t_{XRR} is essentially independent on the rotation rate. This is a primary indication that mass transport is not the limiting step of deposition. To be more quantitative one may compare the limiting ionic flux, using the equations below with the experimental flux of ions consumed during deposition. The latter is directly given by RBS (the flux of a given element is simply its areal density divided by the deposition time, see in **Table 3.4**)

The limiting flux ϕ_i (in unit of cm^{-2}/s) of a species i at a rotating electrode is given by:¹³

$$\phi_i = m_0 C_i = \frac{D_i}{\delta_0} C_i = 0.62 D_i^{2/3} \omega^{1/2} \nu^{-1/6} C_i \quad \text{Eq.3.2}$$

with C_i the concentration of ion i in the main solution, D_i the diffusion coefficient of this ion, δ_0 the diffusion layer thickness, ω the rotation rate of the electrode and ν the liquid viscosity. Numerically, the above expression yield $\phi_i = 3.83 \times 10^{14}$ and 7.66×10^{14} cm^2/s , respectively for $\omega = 350$ and 1400 rpm with $D_i = 10^{-5}$ cm^2s^{-1} (typical value of the diffusion coefficient of many metal cations in water), $\nu = 0.01$ cm^2/s for water. These values are several orders of magnitude greater than the experimental flux (**Table 3.4**), which confirms that mass transport in solution is not the rate determining step of deposition. This is also true at the immobile sample. In that case the flux $\phi_i = C_i D_i / \delta_0$. Using $\delta_0 = 200$ μm ¹³ (the accepted value due to residual convection), the calculated flux $\phi_i = 5.1 \times 10^{13}$ cm^2/s which is still much greater than the experimental flux. We therefore conclude that RbNiCr deposition is not limited by mass transport in our conditions.

Table 3.4. Theoretical and experimental diffusion speed limit for RbNiCr films with different rotation speed of the supporting electrode. The deposition time is 60 min for all deposits.

Sample	Rotation speed [rpm]	t_{XRR} [nm]	Experimental Diffusion Flux 10^{11} $\text{cm}^{-2}\text{s}^{-1}$			Theoretical Diffusion Flux 10^{11} $\text{cm}^{-2}\text{s}^{-1}$
			Rb	Ni	Cr	Ni
1	1400	24.60	2.2	27.33	19.78	7.66×10^3
2	350	24.92	2.22	27.69	20.21	3.83×10^3
3	0	17.15	1.52	19.06	13.91	5.10×10^2

3.3.6 Magnetic characterizations

In order to compare the samples, the measured magnetic moments (extracted from SQUID measurements) are expressed below in emu/cm^2 to account for the variation of deposit area.

3.3.6.1 Temperature dependent study

Field cooled (FC) magnetization curves were measured with a field $H = 250$ Gauss applied parallel to the film surface. **Figure 3.12** shows the temperature dependence of M_{250} (in emu/cm^2) for RbNiCr films of different thicknesses. All curves display an onset of ferromagnetic order, similarly to bulk samples, below a critical temperature. For very thin films (below 9 nm, deposition time < 15 min), the FC curves present a standard shape. Above this thickness, they look like the superposition of FC curves with different ordering temperatures. A qualitative analysis of these plots indicates, at this stage, that the magnetic ordering temperature is increasing from ca. 30 K (2.7 nm thick film) to ca. 70 K (46.2 nm thick film). The shape of FC plots and the determination of T_C will be discussed in **section 3.4.4**.

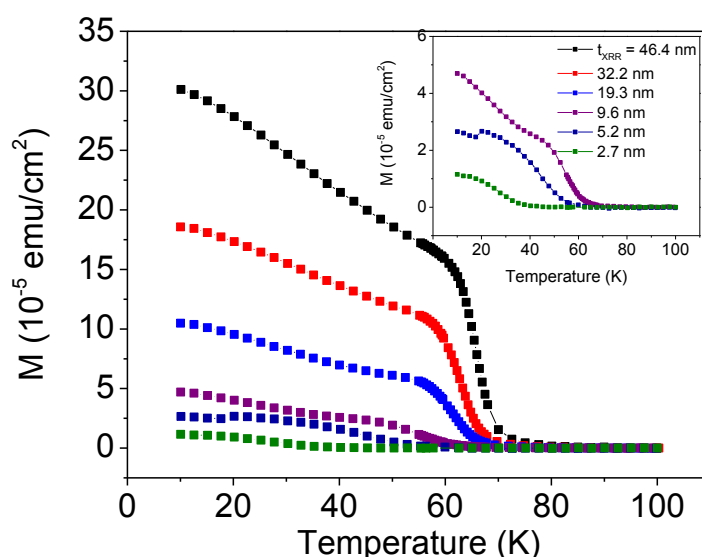


Figure 3.12. Field-cooled (FC) magnetization versus temperature (T) curves measured in an external field of 250 G. Inset is the FC curve of thinner films for better view.

3.3.6.2 Magnetization curves at 10 K

All $M - H$ curves were measured at 10 K, which is well below the ferromagnetic ordering temperature at all considered thicknesses (see above). The raw data are presented in Appendix (**Figure A3.7** and **Figure A3.8**). They were used to derive the thickness dependence of the magnetization at saturation (M_s). As shown in **Figure 3.13**, there is a strict linear dependence of M_s with t_{XRR} , with a slope $1.13 \times 10^2 \text{ emu}/\text{cm}^3$. This indicates that the magnetic moment per volume unit is independent of the thickness of the deposit and this is

in close agreement with the fact that the layer composition is independent of the thickness (see section 3.3.4).

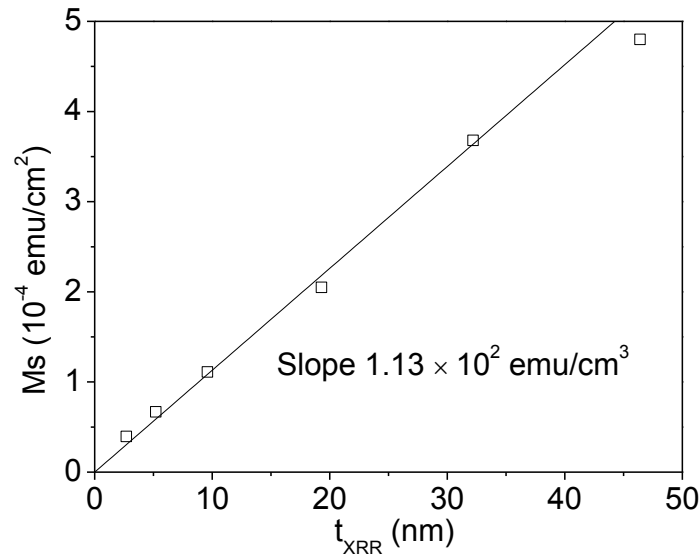


Figure 3.13. Thickness dependence of M_s measured at 10 K normalized to the film area. M_s is determined from measurements at large magnetic field (data taken from **Figure A3.7**).

Figure 3.14 presents a series of *normalized* $M - H$ curves of layers with increasing thickness, with the field applied parallel ($H//$, left column) and perpendicular ($H\perp$, right column) to the deposit plane. Curves were normalized using the M_s value measured above. Wide (symbols) and narrow (blue line) range $M - H$ curves are presented in both configurations. The black solid line in the right column is a guide to eye.

With $H//$, all wide range plots present a S-shape and they overlap perfectly for field $H > 0.05$ T and fall on a common plot after normalization. One example of such shape is given in **Figure 3.18(a)** (discussion section) for a 32 nm thick film. Saturation is reached for $H \sim 0.2$ T. At lower field, the blue curves overlap very well with the symbols. This indicates that these narrow curves are not minor loops.

When $H\perp$, the general shape of $M - H$ curve is clearly different from above, with (i) an hysteretic behavior for thick deposits which tend to vanish with decreasing thickness, and (ii) at all thicknesses a quasi linear region (see symbols) before saturation is reached for $H \sim 0.2$ T. Unfortunately the $M - H$ plots for the 2.7 and 5.2 nm-thick films are not available. For these films, parasitic signals dominate and the raw data could not be satisfactorily reproduced by the extraction curve characteristic of the second-order gradiometer geometry. The blue curve of the 9.6 nm film is quasi overlapping the symbols because of the lower coercivity. For thicker films, the blue curves, are however clearly minor loops because the field excursion is smaller than the coercive/reversibility field (> 100 Oe).

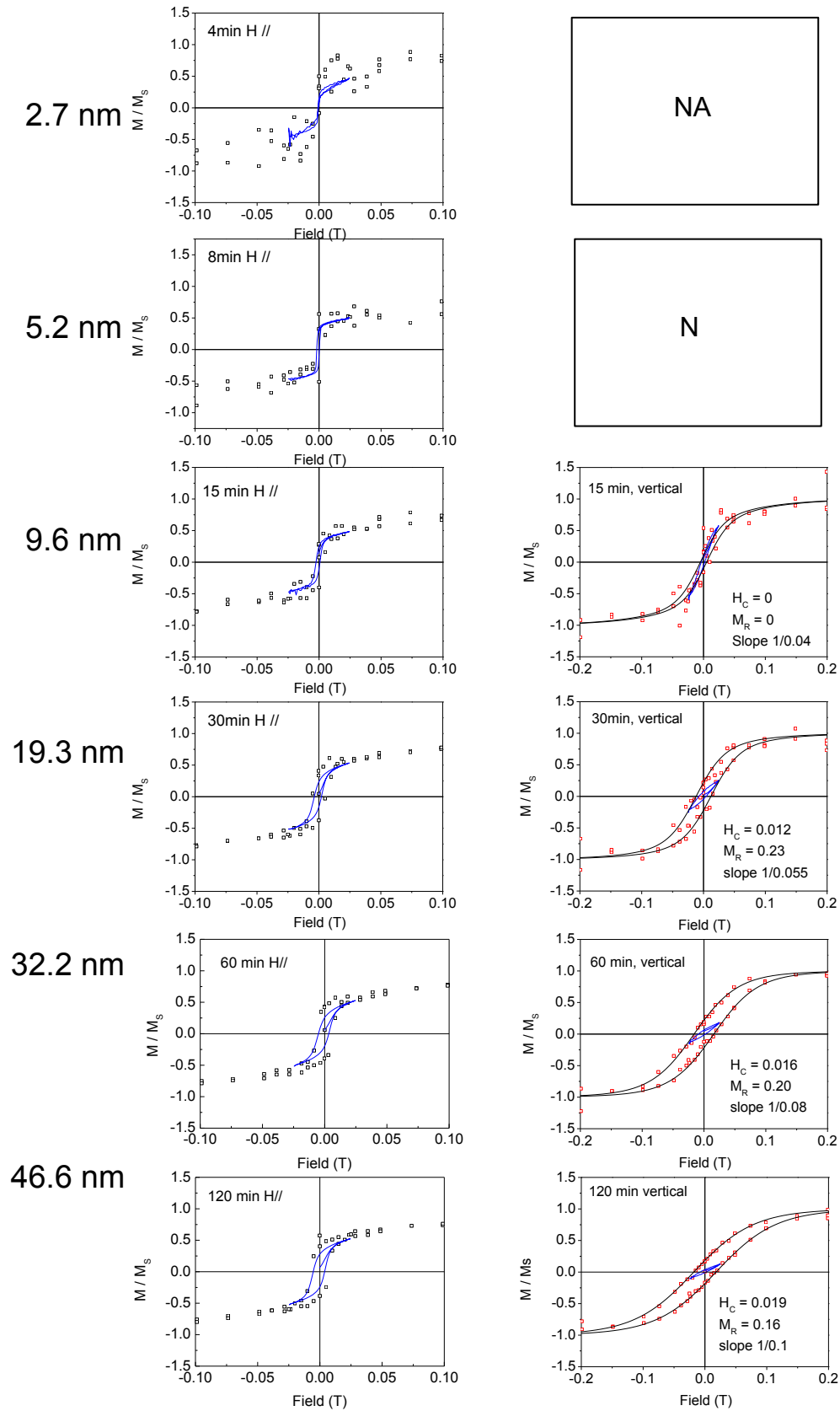


Figure 3.14. Normalized hysteresis loop measured at 10 K of RbNiCr films with different deposition times with the external field applied parallel (left) and normal (right) to surface.

Symbols are zooms of the plots shown in Appendix (**Figure A3.7** and **Figure A3.8**). Blue curves have been recorded for $-250 \text{ G} < H < 250 \text{ G}$. The black solid line is a guide to eye. The deposition time and t_{XRR} are given next to plots. NA means not available.

3.4 Discussion

3.4.1 Chemical composition of the RbNiCr films

The RbNiCr layers have a chemical composition $\text{Rb}_{0.08}\text{Ni}[\text{Cr}(\text{CN})_6]_{0.73} \cdot z\text{H}_2\text{O}$ as derived from RBS. The water content could not be obtained by NRA. We tentatively calculate it assuming that each $[\text{Cr}(\text{CN})_6]$ vacancies in the face centred cubic structure is replaced by a cluster of 6 water molecules¹², $(1-0.73) \times 6 = 1.62 \text{ H}_2\text{O}$ molecular per formula unit in the present case. In addition, due to the porous character of the crystal structure, zeolitic water molecules are expected in the 8 sub-octants of the fcc lattice¹². Assuming that each sub-octant is either filled by an alkali metal cation or by a water molecule, we find $2 - 0.08 = 1.92$ zeolitic H_2O molecules per formula unit. The total number of water molecules per formula is therefore 3.5 and the complete composition of the films is $\text{Rb}_{0.08 \pm 0.01}\text{Ni}[\text{Cr}(\text{CN})_6]_{0.73 \pm 0.07} \cdot 3.5 \pm 0.4\text{H}_2\text{O}$. Based on this chemical composition, the electronic density of as-obtained RbNiCr films could be calculated as $4.88 \times 10^{23} \text{ el.cm}^{-3}$, which is comparable with the electronic density derived from XRR, see **Table 3.1**. The fact that there is a significant variation of lattice constant with the Cr/Ni ratio in the $\text{A}_x\text{Ni}[\text{Cr}(\text{CN})_6]_y \cdot z\text{H}_2\text{O}$ series, from 10.40 \AA (Cr/Ni = 0.69) to 10.57 \AA (Cr/Ni = 0.96),^{2,3} also confirms that the chemical composition of the layer is similar to that of the $\text{Rb}_{0.13}\text{Ni}[\text{Cr}(\text{CN})_6]_{0.7} \cdot 5\text{H}_2\text{O}$ reference particles.

To conclude this short section, all the above results show great agreement with each other. Consequently, the obtained RbNiCr layers has a $\text{Rb}_{0.08 \pm 0.01}\text{Ni}[\text{Cr}(\text{CN})_6]_{0.73 \pm 0.07} \cdot 3.5 \pm 0.4\text{H}_2\text{O}$ chemical composition. In addition, we emphasize that this composition is uniform with depth because it is independent on film thickness.

3.4.2 Nucleation and growth mechanism

To discuss the nucleation and growth of the deposit it is useful to compare the *average* thickness with the *physical* thicknesses of the deposits. The physical thickness is given by X-ray reflectivity and will be called t_{XRR} . The average thickness is given by RBS because it is related to the total amount of deposited materials. We will call it t_{RBS} . The thickness t_{RBS} is simply given by:

$$t_{\text{RBS}} = \frac{A \times a^3 \times 10^{-24}}{4} \quad \text{Eq.3. 3}$$

where A is the atom areal density derived from data fitting of the RBS curve, and a is the lattice parameter of the film. In the above formula, a is in a unit of Å, areal density is with a unit of at.cm⁻², thus the final t_{RBS} is expressed in cm.

Using as lattice parameter $a = 10.45$ Å (see **Table 3.2**), we calculated t_{RBS} and plotted it as function of t_{XRR} (open squares in **Figure 3.15(a)**). There is a linear relationship between t_{RBS} and t_{XRR} . Note that the solid line in **Figure 3.15(a)** is not a fit. It is a straight line of slope of 0.89. While the data points are on the straight line if $t_{\text{XRR}} > 15\text{-}20$ nm, there is a clear deviation from the above linear law in the initial stages of the film growth. To better highlight this discrepancy we can plot $F = t_{\text{RBS}} / t_{\text{XRR}}$, which characterizes the filling factor of the film. The result is shown in **Figure 3.15(b)**. A monotonic increase of F is observed before it saturates close to 0.89. This behaviour confirms that the layers are rather compact above a critical thickness of 15 - 20 nm. This is also in agreement with the fact that XRR gives an electronic density close to the calculated one for $\text{Rb}_{0.08}\text{Ni}[\text{Cr}(\text{CN})_6]_{0.73} \cdot 3.5 \pm 0.4\text{H}_2\text{O}$ (see **section 3.4.1**). Below a thickness of 15 - 20 nm, the films are however not compact. They are constituted of grains which are *not connected*. The plot gives an order of magnitude of the free volume between the grains. Using the value of F and accounting for the average grain density (N_G) 3.7×10^{11} grains/cm² (see **Figure 3.7**), one can estimate the lateral dimensions of the grains before coalescence.

$$d_G = \sqrt{F/N_G} \quad \text{Eq.3.4}$$

Using the result we can then calculate the rate of *lateral* grain growth $R_L = d_G/t$ (t = deposition time) and compare it with the *vertical* grain growth rate $R_V = t_{\text{XRR}}/t$. As shown in **Figure 3.15(c)**, the ratio $R_L/R_V > 1$ (filled squares) in the initial stages of deposition and it decays rapidly to zero. Correspondingly, the grain aspect ratio (open circles in **Figure 3.15(c)**), defined as t_{XRR} / d_G , is increasing. This analysis indicates that the grains are initially platelets which grow laterally and vertically until coalescence.

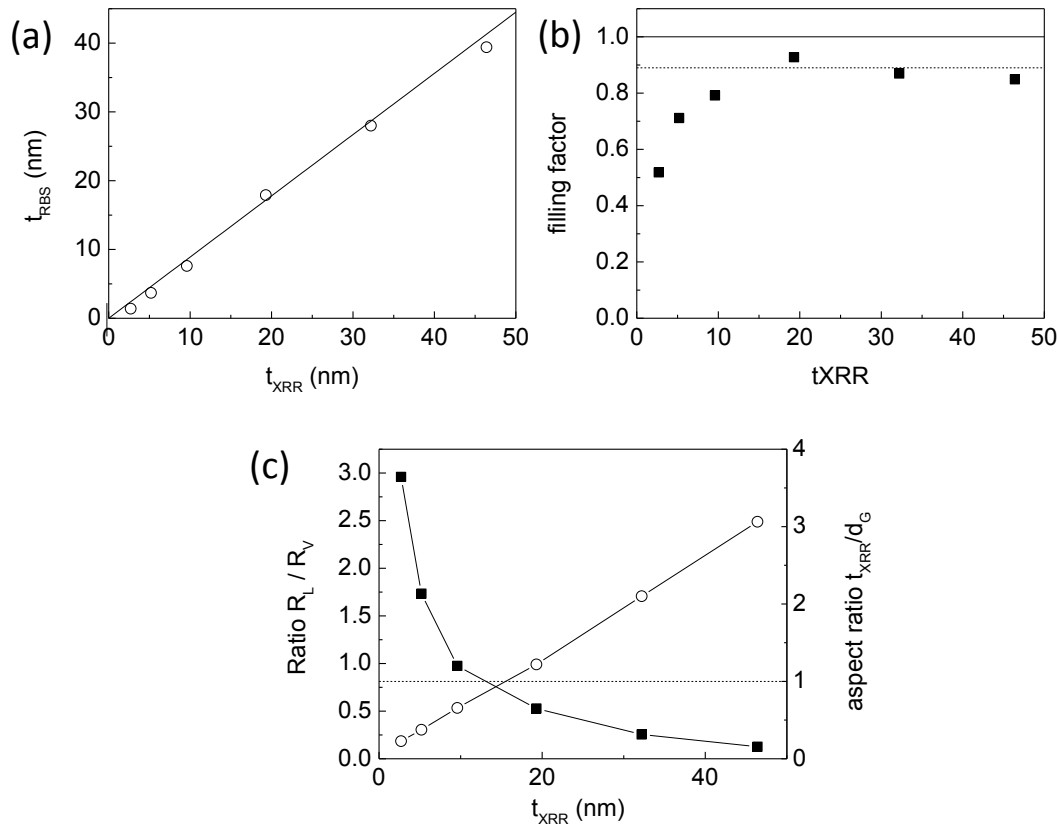


Figure 3.15. Thickness dependence of (a) t_{RBS} , (b) filling factor F and (c) of ratio R_L/R_V (filled squares) and aspect ratio (open circles). The lateral grain size was determined from Eq. 3.4.

From the above analysis we can infer a nucleation and growth mechanism (see Figure 3.16). Film nucleation (Figure 3.16(a)) is obviously a *homogenous* process on the functionalized Si (111) surface since the initial grains uniformly cover the surface. In addition we can state that nucleation is quasi *instantaneous* because the grain density remains quasi-independent on the deposition time. After nucleation grain growth proceeds laterally and also vertically though at a *slower* rate in this direction (Figure 3.15(c)). Grain coalescence is reached for films above 15-20 nm in thickness. Above this thickness, the films are *quasi* continuous (filling factor $\sim 90\%$, see Figure 3.15(b)) and grain growth is continuing vertically, very likely in quasi a layer by layer fashion because the deposit remains very smooth on the scale of the lattice parameter. We recall that the roughness 1 nm (Table 3.1) is close to the lattice parameter $a = 10.45 \text{ \AA}$.

A direct consequence of the above nucleation and growth mechanism is that the RbNiCr films cannot be perfectly continuous with a filling factor close but still smaller than unity (see Figure 3.15(b)). This behavior may be attributed to increasing mass transport limitations (between the grains) when one approaches grain coalescence. We can estimate the *average* width w of voids between grains, taking the ideal scheme shown in Figure 3.16(b). For the

sake of simplicity we consider square grains of uniform dimension d_0 , distributed on a square lattice. Under this hypothesis, the filling factor is $F = (d_0/d)^2$. Using the experimental data, one finds that $w = d - d_0$ decays rapidly after nucleation (**Figure 3.16(c)**). After coalescence a gap of ca. 1 nm is estimated, which is about one lattice parameter only.

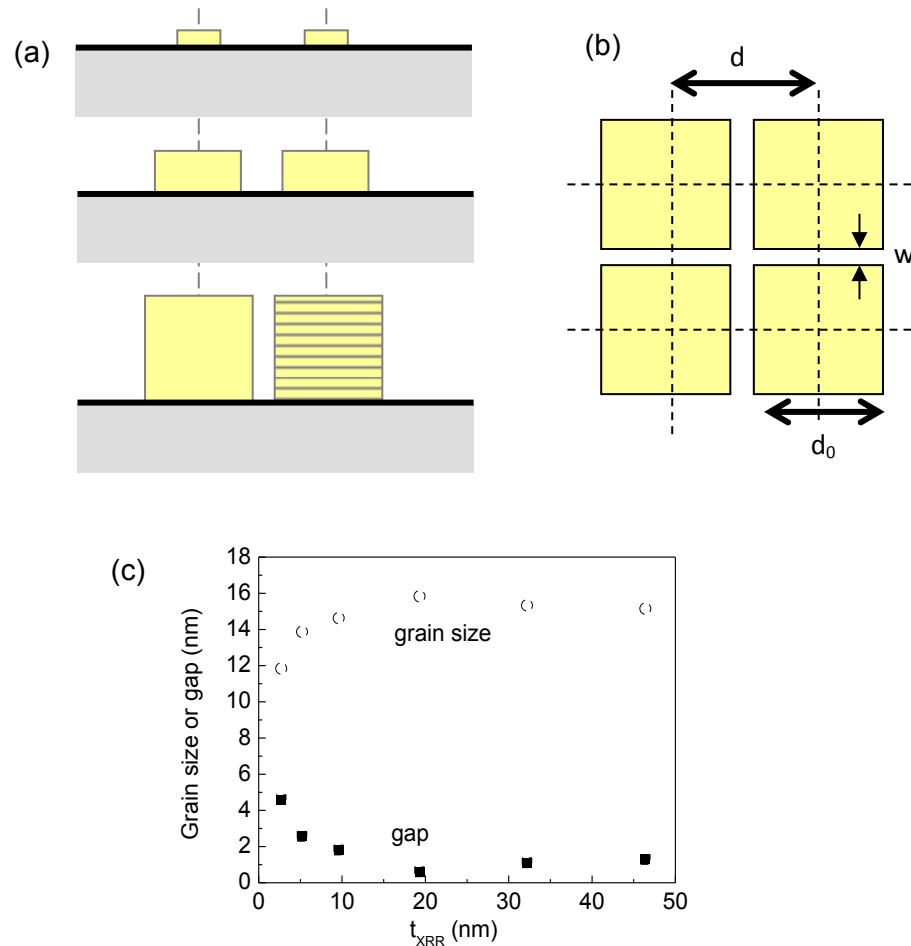


Figure 3.16. (a) Schematic (side view) representation of the nucleation and growth of RbNiCr layers until coalescence on functionalized Si (111). The organic monolayer is not represented for the sake of clarity. (b) Simplified scheme (top view of the deposit) used to estimate the width of the voids between grains. (c) Variations of grain size and of the *average* gap between the grains.

A key point to be discussed now is to whether the grains sketched in **Figure 3.16** are or are not single crystalline. The answer to this question is provided by **Figure 3.9**, which shows that the structural coherence length $L_C \sim t_{XRR}$, namely L_C is a linear function of t_{XRR} with a slope very close to unity. In other words, L_C coincides with the *physical* thickness of the grains, which means that the grains present a continuous crystal structure from bottom to top, and this is true from the very initial stages of the growth. To express this result, a grain in **Figure 3.16(a)** was sketched as a stack of layers.

3.4.3 Magnetic properties

3.4.3.1 Magnetic moment

The magnetic moment per formula may be experimentally and theoretically estimated. On one hand, the slope in **Figure 3.13** gives a magnetic moment per unit of volume of 1.13×10^2 emu/cm³. Dividing this quantity by the volume density of Ni atoms 3.1×10^{21} atom/cm³ (this is the slope of the straight line in **Figure 3.11**) gives an experimental moment per formula equal to 3.65×10^{-20} emu/atom (Ni) or 3.93 μ B per formula unit. On the other hand, the theoretical saturation magnetization in Bohr magneton for each formula unit may be calculated using the chemical composition we derived from RBS:

$$M_s = g_{Ni^{2+}} \times S_{Ni^{2+}} + y \times g_{Cr^{3+}} \times S_{Cr^{3+}} \quad \text{Eq.3.5}$$

where the Landé factors (g) of Ni²⁺ and Cr³⁺ are 2.1 and 2 respectively¹⁴ and S denotes the spin moment ($S_{Ni^{2+}} = 1$, $S_{Cr^{3+}} = 3/2$), and y is the Cr/Ni atomic ratio. Numerically, with $y = 0.73$, one finds $M_{S^{Th}} = 4.3 \mu$ B. The 8% discrepancy between the experimental determination of 3.93 μ B could be explained by the formation of Ni(CN)₄ diamagnetic species induced by the isomerism of some CN bridges, as already reported by other authors in nickel hexacyanoferrate bulk samples or nanoparticles.^{9,15}

In the following section we will discuss the thickness dependence of the temperature of ferromagnetic ordering and the magnetization anisotropy of deposits.

3.4.3.2 Thickness dependence of the magnetic ordering temperature

FC plots were analyzed using the methodology used for ferromagnetic films as outlined in a reference¹⁶ assuming a power-law behavior:

$$M = M_0 \left(1 - T/T_C\right)^\beta \quad \text{Eq.3.6}$$

for the magnetization as a function of temperature. The temperature T_C and the exponent β were extracted from log-log plots as shown in Appendix (**Figure A3.9**). The β value (slope measured for T approaching T_C) falls in the range 0.31-0.33 for all deposits. In **Figure 3.17(a)** we have plotted the thickness dependence of T_C (open symbols), as derived from the above analysis. Interestingly, one also notices that the T_C of 20 and 30 nm thick layers is close to that of a powder composed of 20 nm or 30 nm monodisperse particles of the same material (see red data point in **Figure 3.17(a)**). This strongly suggests that the magnetic behavior of RbNiCr films may be described as that of an assembly of magnetically coupled individual magnetic columns since the T_C of such deposits (~ 65 K) is very close to that of the powder.

The gray lines in **Figure 3.17(b)** are curves calculated using **Eq. 3.6**, with the parameter listed in **Table A3.4**. These curves are obviously not accounting for the entire temperature range, especially when the films are thicker than 10 nm. The discrepancy is essentially observed for temperatures lower than 40 K. This behavior may be assigned to the presence of grains which are too small to be ferromagnetic above 40 K and we tentatively account for the discrepancy between the gray line and experimental data, by adding contributions of the FC curves of a majority of 2.7 and a minority of 5.2 nm-thick films. This is a convenient way to account for the presence of grains with $T_C < 40$ K. The agreement between the colored lines and corresponding data points is now much better. To justify the validity of the above data treatment, we estimated the equivalent volume fraction of the above mentioned small grains (with a $T_C < 40$ K). As shown in **Figure 3.17(a)** (filled symbols), their volume fraction is, within accuracy of the estimate, slowly decaying with increasing film thickness. This strongly suggests that some of the initial grains stopped growing at some point, probably around the coalescence. The above growth model should therefore be refined in light of this new information. We shall refrain doing this however. It should be noticed that this information could not be gained before because such grains cannot be detected by XRD (they essentially contribute to broaden the main Bragg peaks at their bottom).

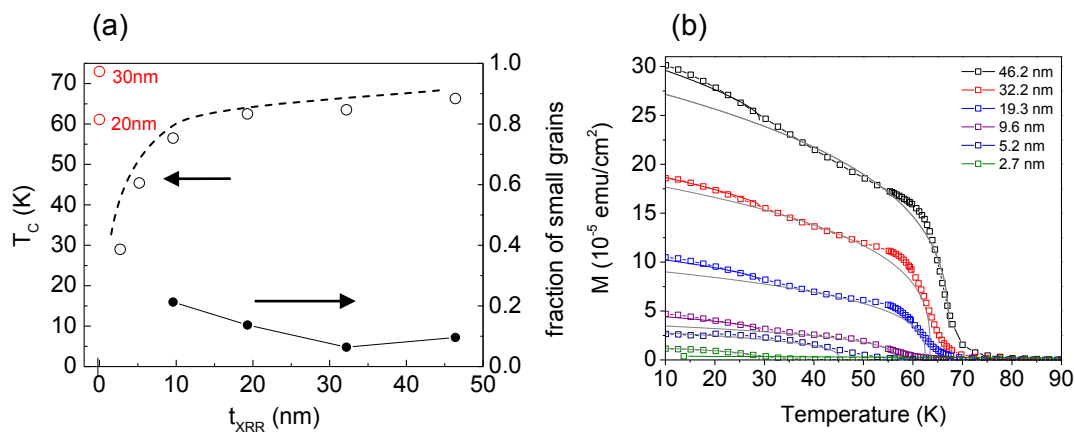


Figure 3.17. (a) Thickness dependence of T_C (open symbols) and of the volume fraction of grains smaller than ca. 5 nm (filled symbols), see text for explanations. The T_C values of 20 and 30 nm diameter particles are shown with red symbols. (b) FC plots: open symbols are experimental data. The gray solid lines were calculated using **Eq. 3.6** above and the parameters listed in **Table A3.4**. The colored plots have been calculated by adding a contribution arising from grains that are too small to be ferromagnetic at temperature above 30-40 K, see text for explanation.

3.4.3.3 Magnetic anisotropy

The easy axis is defined by the sum of the magnetocrystalline anisotropy (MCA), shape anisotropy energies (SA), plus eventually a surface/interface anisotropy energy (IA). Given the growth mechanism discussed above, we are going to separate the discussion about the magnetic anisotropy of RbNiCr deposits into the case of films after and before coalescence.

Case of continuous films (i.e. after coalescence): According to the previous sections, *continuous* RbNiCr deposits (i.e. thicker than 15-20 nm) are composed of grains of lateral dimension $d \sim 18$ nm and length $19 \text{ nm} < t_{\text{XRR}} < 46$ nm. Given these physical dimensions and by referring to the work of Prado *et al.*,⁴ we will assume that the grains are single magnetic domains. In addition, we can state that they are magnetically coupled because they are, on average, separated by a gap of 1 nm.

(i) A first piece of information is brought by **Figure 3.18(a)** which compares the *normalized* $M - H//$ (red line) of the 32-nm thick deposit with that of a powder (black line) composed of rather monodispersed 30 nm particles. The S-shape of the $M - H//$ (blue curve) is very similar to that of a powder (gray line) with $H_C \sim 50$ Oe. This is because in such a configuration, the field H is randomly oriented with respect to the crystal axis (recall that there is no in plane orientation of the grains). The film behaves therefore like a powder with no defined easy axis. The fact that $H_{C//} \sim 50$ Oe, even for the thickest layer, supports the assumption that the grains are essentially single magnetic domains.⁴ Comparing into more details, the S-shape of the $M - H//$ plot evidences however a higher saturation field for the films than for the powder. The size distribution of the grains, due to the presence of the small grains with T_C closer to the measurement temperature (see previous section), may only partially contribute to this behavior since the volume fraction of these grains remains below 20%. We rather infer that the higher saturation film measured for the films arises from the existence of an easy axis which is not parallel to the surface plane.

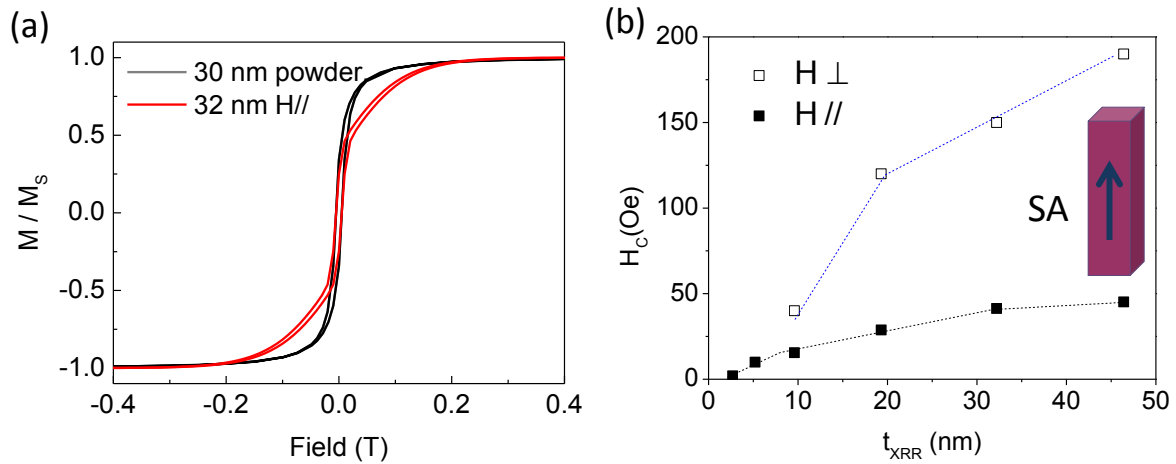


Figure 3.18. General shape of $M - H$ curves: (a) Comparison of the 32 nm-thick RbNiCr film with $H//$ (red line) with a powder made of 30 nm particles of the same material (black line); (b) Thickness dependence of the coercive field H_c measured with $H \perp$ (open squares) and $H//$ (filled squares).

(ii) A second piece of information is provided by the larger film coercive field measured with $H \perp$ with respect to that measured with $H//$ (see **Figure 3.18(b)**). Given the fact that the grain aspect ratio increases with the film thickness, we can conclude that the grain shape anisotropy is contributing to a significant out of plane anisotropy for continuous films (recall that $t_{XRR} > d_G$, see **Figure 3.15(c)**). The shape anisotropy is nevertheless not strong enough to keep the easy axis totally perpendicular to the surface since $M_R/M_s \sim 0.25$.

To summarize, one can estimate that the magnetization easy axis is tilted with respect to the normal of the deposit. We can further say that it is closer to the normal than to the surface plane. We infer that the magnetization easy axis results from a competition between the grain shape anisotropy and MCA. Since all grains share in common a $\langle 001 \rangle$ axis perpendicular to the surface (texture axis), we exclude that this is a direction of easy axis. Among high symmetry crystal axis, we tentatively propose that the $\langle 111 \rangle$ direction rise to the magnetocrystalline easy axis.

Case of films before coalescence (i.e. composed of platelets): Below 15 nm, one notices some significant changes in the magnetic property. In this case, the RbNiCr films are composed of platelets with $(00l)$ texture. We will also consider that these are single magnetic domains, magnetically coupled because the gap between grains never exceeds a few nm.

The main piece of information is given by **Figure 3.19**, which evidences that the $M - H \perp$ curve becomes steeper around $H = 0$ for the 9.6 nm film, i.e. before coalescence (see red line in **Figure 3.19**). In other words, though the measurements are performed at a temperature

closer to the corresponding T_C , the easy axis of magnetization seems to become closer to the surface normal than for the continuous film of 46.4 nm. This suggests a significant contribution of the surface or of the interface to the overall out of plane magnetization anisotropy, since the shape anisotropy of platelets should favor an in plane magnetization. Based on XMCD measurements, a recent work suggested that the presence of distorted Ni(II) sites located on the particle surface account for a uniaxial magnetic anisotropy.¹⁷ In our case, this conclusion needs however to be confirmed by re-measuring $M - H_{\perp}$ curves of RbNiCr films below coalescence.

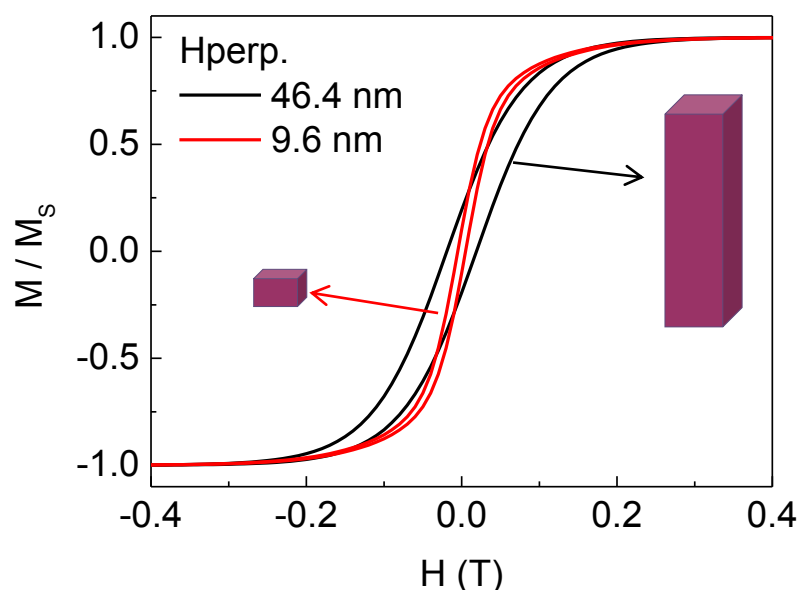


Figure 3.19. Comparison of $M - H$ curves with H_{\perp} for a 46.4 and a 9.6 nm-thick RbNiCr film.

3.5 Conclusion

Thin ferromagnetic $\text{Rb}_{0.1}\text{Ni}[\text{Cr}(\text{CN})_6]_{0.7} \cdot z\text{H}_2\text{O}$ films with a (001) texture and controlled thickness were prepared on pyridine-terminated Si(111) surfaces. This structure results from an instantaneous and homogeneous nucleation of (001) oriented grains which grow laterally until coalescence. After coalescence ($t_{\text{XRR}} > 15\text{-}20$ nm), grain growth is a layer by layer process, which results in very smooth films. However some of the initial grains stopped growing in the initial stages and temperature dependent magnetic characterizations suggest that these represent about 5-10% of the volume of a 46 nm RbNiCr film. When the film is continuous, the magnetic ordering temperature is close to $T_C = 65$ K and T_C drops to 30-50 K when the film is discontinuous. From a magnetic viewpoint, grains can be considered as individual magnets, coupled with each other. The magnetization easy axis is tilted by an angle which depends on the film *average* thickness. For continuous films the tilt angle is defined by the magnetocrystalline anisotropy, likely along the $\langle 111 \rangle$ direction, and the shape anisotropy of

grains which are columnar. In the case of discontinuous layers, an out of plane interface anisotropy is suggested.

3.6 References

1. M. F. Dumont; E. S. Knowles; A. Guet; D. M. Pajerowski; A. Gomez; S. W. Kycia; M. W. Meisel; D. R. Talham, Photoinduced magnetism in core/shell Prussian blue analogue heterostructures of $K_jNi_k[Cr(CN)_6]_l.nH_2O$ with $Rb_aCo_b[Fe(CN)_6]_c.mH_2O$. *Inorg. Chem.* **2011**, *50*, 4295-4300.
2. V. Gadet; T. Mallah; I. Castro; M. Verdaguer, High-Tc molecular-based magnets: a ferromagnetic bimetallic chromium(III)-nickel (II) cyanide with $T=90K$. *J. Am. Chem. Soc.* **1992**, *114*, 9213-9214.
3. V. Gadet. PhD thesis. Université Paris VI, Paris, 1992.
4. Y. Prado; L. Lisnard; D. Heurtaux; G. Rogez; A. Gloter; O. Stephan; N. Dia; E. Riviere; L. Catala; T. Mallah, Tailored coordination nanoparticles: assessing the magnetic single-domain critical size. *Chem. Commun.* **2011**, *47*, 1051-1053.
5. D. Brnzei; L. Catala; N. Louvain; G. Rogez; O. Ste; T. Mallah, Spontaneous stabilization and isolation of dispersible bimetallic coordination nanoparticles of $Cs_xNi[Cr(CN)_6]_y$. *J. Mater. Chem.* **2006**, *16*, 2593-2599.
6. J. T. Culp; J.-H. Park; I. O. Benitez; Y.-D. Huh; M. W. Meisel; D. R. Talham, Sequential assembly of homogeneous magnetic Prussian blue films on templated surfaces. *Chem. Mater.* **2003**, *15*, 3431-3436.
7. M. Clemente-Leon; E. Coronado; A. Lopez-Munoz; D. Repetto; C. Mingautaud; D. Brnzei; L. Catala; T. Malah, Magnetic langmuir-blodgett films of bimetallic coordination nanoparticles of $Cs_{0.4}Ni[Cr(CN)_6]_{0.9}$. *Chem. Mater.* **2008**, *20*, 4642-4652.
8. S. Tricard; C. Costa-Coquelard; S. Mazerat; E. Rivière; V. Huc; C. David; F. Miserque; P. Jegou; S. Palacind; T. Mallah, Cyanide-bridged NiCr and alternate NiFe-NiCr magnetic ultrathin films on functionalized Si(100) surface. *Dalton Trans.* **2012**, *41*, 4445-4450.
9. M. Presle. Synthèse et propriétés d'hétérostructure moléculaires de type multiferroïque à base d'analogues du bleu de Prusse. PhD dissertation. Ecole Polytechnique, France, 2011.
10. L. G. Parratt, Surface studies of solids by total reflection of X-rays. *Phys. Rev.* **1954**, 359-369.
11. I. Horcas; R. Fernández; J. M. Gómez-Rodríguez; J. Colchero; J. Gómez-Herrero; A. M. Baro, WSXM: A software for scanning probe microscopy and a tool for nanotechnology. *Review of Scientific Instruments* **2007**, *78*, 013705-1-013705-8.

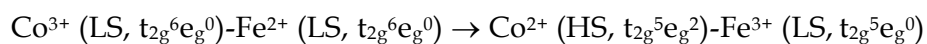
12. F. Herren; P. Fischer; A. Ludi; W. Halgi, Neutron diffraction study of prussian blue, $\text{Fe}_4[\text{Fe}(\text{CN})_6]_3 \cdot x\text{H}_2\text{O}$. Location of water molecules and long-range magnetic order. *Inorg. Chem.* **1980**, *19*, 956-959.
13. A. J. Bard; L. R. Faulkner, *Electrochemical methods: fundamentals and applications*. John Wiley & Sons, Inc.: United States of America, 2001.
14. Kahn, O., *Molecular magnetism*. Wiley-VCH: 1993; Vol. 14.
15. D. Brinzei, Thèse de l'Université Paris-Sud, Orsay. **2007**.
16. F. Huang; M. T. Kief; G. J. Mankey; R. F. Willis, Magnetism in the few-monolayers limit: A surface magneto-optic Kerr-effect study of the magnetic behavior of ultrathin films of Co, Ni, and Co-Ni alloys on Cu(100) and Cu(111). *Phys. Rev. B* *49*, 3962-3971.
17. Y. Prado; M.-A. Arrio; F. Volatron; E. Otero; C. C. dit Moulin; P. Sainctavit; Catala, L.; T. Mallah, Magnetic anisotropy of cyanide-bridged core and core-shell coordination nanoparticles probed by X-ray magnetic circular dichroism. *Chem. Eur. J.* **2013**, *19*, 6685 - 6694.

Chapter 4

Growth and photo-switching properties of $\text{Rb}_x\text{Co}[\text{Fe}(\text{CN})_6]_y \cdot z\text{H}_2\text{O}$ films

4.1 Introduction

The objective of this chapter is to study the growth of single layers of cobalt hexacyanoferrates, $\text{A}_x\text{Co}[\text{Fe}(\text{CN})_6]_y \cdot z\text{H}_2\text{O}$ with $\text{A}=\text{Rb}$. As mentioned in Chapter 1, these compounds may exhibit thermally- and photo-induced spin transitions, and have been extensively studied as model materials of molecular photomagnetic solids.¹ Their photo-switching properties result from a charge-transfer induced spin transition (CTIST),¹ which occurs under visible light irradiation as follows:



where LS and HS stand for low spin and high spin, respectively.

This optical electron transfer is accompanied by a rather large Co-N bond lengthening (by $\sim 0.18 \text{ \AA}$)² due to the population of the Co e_g antibonding orbitals, which finally leads to a volume expansion, $\Delta V/V \sim 9\%$, in the bulk phase.³ Early works have shown that the photo-switching properties of these compounds depend on several factors linked to the chemical environment, namely the presence of $\text{Co}^{3+}(\text{LS})-\text{Fe}^{2+}(\text{LS})$ pairs, leading to $\text{Co}^{2+}(\text{HS})-\text{Fe}^{3+}(\text{LS})$ pairs by optical electron transfer,⁴ the presence of $[\text{Fe}(\text{CN})_6]$ vacancies in sufficient amount to give the crystal lattice some flexibility⁵ and the nature of the counter ion A;⁶ the first two factors are related to the Fe/Co ratio, which has to be in the range 0.71-0.83 for an efficient photo-effect.⁷

The growth of cobalt hexacyanoferrate compounds as thin films or nanostructures on surfaces is thus a challenging issue for technological applications but also for fundamental aspects. For instance, a detailed analysis of the non-linear effects associated to the photo-induced spin transitions (incubation time, threshold intensity or quantum yield of the photo-excitation process⁸) is often hindered by a partial and inhomogeneous penetration of light in bulk samples. Besides, nanostructures based on two-dimensional layers may open the way to an investigation of these transitions at the nanoscale using local probes techniques. In this work, we choose to focus on the $\text{Rb}_x\text{Co}[\text{Fe}(\text{CN})_6]_y \cdot z\text{H}_2\text{O}$ composition, i.e., with Rb as the counter ion. The switching properties of rubidium cobalt hexacyanoferrates are well

documented for bulk phases^{3,5,9,10,11} and, to a lesser extent, for nanoparticles^{12,13} and thin films.^{14,15} For instance, the lifetime of the $\text{Rb}_{0.45}\text{Co}[\text{Fe}(\text{CN})_6]_{0.80}\cdot z\text{H}_2\text{O}$ photo-excited phase was shown to be rather long, at least up to 110 K in bulk phases.¹⁶ Another reason to choose Rubidium derivatives is that Prussian blue analogues are well-known for their capability in alkali-ion exchange, making them good candidates for the removal of radionuclides such as ^{137}Cs .¹⁷ As a consequence, it is better to use an identical counter ion for the NiCr and CoFe layers in the bilayer architectures that will be investigated in Chapter 5 in order to limit the risk of interdiffusion of the alkali metal ions that may change the switching properties of the CoFe compound⁶.

This chapter describes the preparation of $\text{Rb}_x\text{Co}[\text{Fe}(\text{CN})_6]_y\cdot z\text{H}_2\text{O}$ layers using the deposition route presented in Chapter 3, based on heterogeneous nucleation on Si (111) surfaces functionalized by organic monolayers bearing pyridyl end groups. These layers will be denoted RbCoFe in the following sections. The first part of this chapter is devoted to the investigation of the nucleation and growth mechanisms of RbCoFe films, by comparison to RbNiCr layers. The second part of the chapter focuses on the Co and Fe valence states and on the photo-switching properties of the films that will be compared to those of bulk samples.

4.2 Experimental section

4.2.1 Preparation of the solution of precursors

The protocol used for the preparation of the solution in which the functionalized substrates will be immersed is similar to the one described in Chapter 3. Potassium hexacyanoferrate ($\text{K}_3\text{Fe}(\text{CN})_6$, $\geq 99\%$, 329.26 g/mol), Rubidium nitrate (RbNO_3 , $\geq 99.7\%$, 147.47 g/mol) and Cobalt nitrate hexahydrate ($\text{Co}(\text{NO}_3)_6\cdot 6\text{H}_2\text{O}$, $\geq 99\%$, 291.03 g/mol) were chosen as precursors. They were purchased from Sigma-Aldrich Company and used without further treatment. The solutions were prepared from ultrapure water (Milli-Q, 18.2 M Ω cm) and their pH was adjusted to ca. 5 by adding 0.1 M Nitric acid (HNO_3 , 63.01 g/mol) in order to avoid precipitation of $\text{Co}(\text{OH})_2$.

80 mL of a 1 mM $\text{K}_3\text{Fe}(\text{CN})_6$ solution (pH = 5) and 80 mL of a mixture solution of $\text{Co}(\text{NO}_3)_6\cdot 6\text{H}_2\text{O}$ 1 mM and RbNO_3 2.5 mM (pH = 5) were slowly added in a beaker filled with 300 mL of acidified water (pH = 5). This procedure yields nominal concentrations of the reactants of 0.43 mM RbNO_3 , 0.17 mM $\text{Co}(\text{NO}_3)_6\cdot 6\text{H}_2\text{O}$ and 0.17 mM $\text{K}_3\text{Fe}(\text{CN})_6$. The addition rate was fixed to 0.75 mL/min using a peristaltic pump. The mixing was carried out at 20°C under moderate stirring (400 rpm). We systematically observed a color change during the preparation of the solutions, from transparent to light red indicating the nucleation of RbCoFe particles in solution. We thus used only freshly prepared solutions for the deposits.

4.2.2 Set-up used for film deposition

We used a modified design of the set-up described in Chapter 3. Each solution of precursors was first deoxygenated by bubbling Ar gas through it (see **Figure 4.1** for a scheme of the home-made set-up). Their mixing was also carried out under Ar bubbling and the as-obtained solution was transferred in another beaker used for the deposition step. This last beaker was maintained under Ar bubbling during deposition.

The functionalized Si (111) substrates were fixed with an electrolytic scotch tape onto a metallic support leaving a square aperture of $10 \times 10 \text{ mm}^2$ in contact with the solution. The backside of the sample was not exposed to the solution. We systematically left the substrates at rest and fixed them vertically in the beaker. After deposition, the layers were thoroughly rinsed with water and then dried under a stream of Ar gas. Again, the deposition time refers to the contact time between the substrate and the solution.

We performed trial experiments to investigate the influence of dissolved oxygen on the film growth. From Rutherford Backscattering Spectroscopy (RBS) measurements, which provide access to the Rb/Co and Fe/Co atomic ratios but also to the amount of deposited materials, we observe that a solution deoxygenation has no drastic influence on the final composition of the films (see the Appendix section). In addition, this parameter has no significant impact on the growth rate of the layers which can be derived from the atom areal densities, similarly to what was reported in Chapter 3.

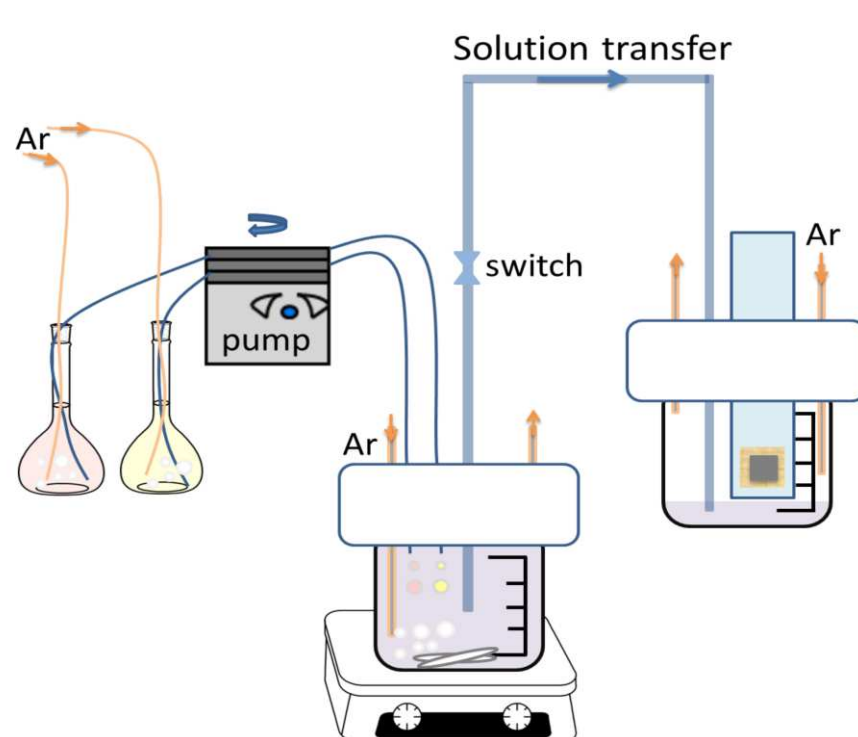


Figure 4.1. Scheme of the experimental set-up under Ar bubbling used for the growth of $\text{Rb}_x\text{Co}[\text{Fe}(\text{CN})_6]_y \cdot z\text{H}_2\text{O}$ films.

4.3 Film nucleation and growth

We first investigated the growth mechanism of the RbCoFe layers. To facilitate comparisons with the RbNiCr films studied in Chapter 3, we selected identical concentrations of the transition metal cations (i.e., 0.17 mM $\text{Co}(\text{NO}_3)_6$ and 0.17 mM $\text{K}_3\text{Fe}(\text{CN})_6$) in the solution used for deposition. We used a slightly larger excess of Rb (0.43 mM RbNO_3) to favor its incorporation in the film and the formation of Co^{3+} - Fe^{2+} photo-switchable pairs. In the following sections, the deposits will be characterized either by the deposition time or by their thickness derived from X-ray reflectivity measurements.

4.3.1 Results

4.3.1.1 X-ray reflectivity (XRR) measurements

Figure 4.2 shows the X-ray reflectivity curves of RbCoFe films with increasing deposition time. We observe an increase of frequency of the reflectivity oscillations with increasing deposition time, in agreement with an increasing film thickness. Note that for the films deposited for 30 and 60 min, the amplitude of the oscillations is less pronounced and the oscillations do not extend up to $q_z = 0.25 \text{ \AA}^{-1}$, as observed for RbNiCr films of comparable thickness (**section 3.3.1** in Chapter 3). This damping of the oscillations results from a substantial increase in surface roughness, in good accordance with the RMS roughness values derived from AFM that are shown in the next section. The period of the oscillations is however uniquely related to the film thickness, t_{XRR} , so that the t_{XRR} values can be accurately extracted from the XRR plot analysis. Due to roughness-induced damping of the oscillations, the determination of the electronic density will be rather inaccurate.

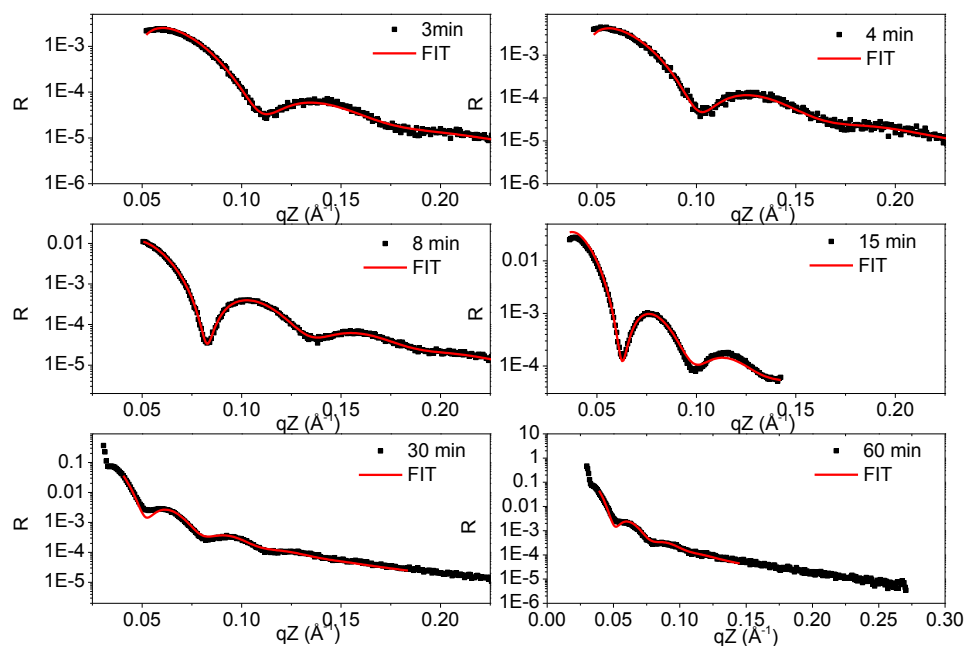


Figure 4.2. X-ray reflectivity curves for RbCoFe layers at representative deposition times. The deposition time is given in each graph. Symbols are experimental data. The solid red line is the best fit.

Experimental data were analysed with the PARRATT32 software using a bilayer model similar to the one presented in Chapter 3 (**Figure 3.4**) and the same two-step procedure of fitting (see **section 3.3.1**). The as-obtained parameters are summarized in **Table 4.1**. The thickness of the organic monolayer is found to be smaller than 17 Å (optimized geometry for the organic chains in an all cis-trans conformation), suggesting a slight overestimation of the thickness of the RbCoFe layers. Indeed, we found strong correlations between the thickness of the organic layer and that of the film. We can estimate a 10% error on t_{ML} while the sum of t_{ML} and t_{XRR} is defined with 1 to 2% standard deviation. As mentioned previously, electronic densities ρ are not well defined for the thicker and rougher films. However, for the thin ones, we got ρ_{ML} values close to what was found in the case of the RbNiCr layers.

Table 4.1. Fitted parameters for RbCoFe films grown with different deposition times derived from X-ray reflectivity data. The input parameters of the pyridyl terminated layer used for fitting are $t_{ML} = 17.1 \text{ \AA}$, $\rho_{ML} = 4.5 \times 10^{23} \text{ el.cm}^{-3}$ and $\sigma_{ML} = 0.3 \text{ nm}$ (see section 2.3.2, Chapter 2). In the last column, the RMS values characterize to the roughness of the RbCoFe layers determined by AFM.

deposition time [min]	RbCoFe layer			Pyridyl layer			AFM RMS [nm]
	t_{XRR} [nm]	ρ_{Layer} [$10^{23} \text{ el.cm}^{-3}$]	σ_{Layer} [nm]	t_{ML} [nm]	ρ_{ML} [$10^{23} \text{ el.cm}^{-3}$]	σ_{ML} [nm]	
3	7.1	4.97	1.5	1.2	3.76	0.2	1.7
4	7.6	4.97	1.4	1.4	3.55	0.2	1.1
8	10.1	4.51	1.2	1.4	3.08	0	1.1
15	14.5	6.03	1.9	1.2	3.47	0	0.9
30	19.0	3.46	2.1	1.0	2.82	0	1.1
60	19.9	3.54	2.5	0.4	2.13	0.3	2.1

For the RbCoFe layers, **Figure 4.3** shows the film thickness, t_{XRR} as a function of the deposition time. One observes a non-linear variation, contrary to the case of RbNiCr layers. The initial growth rate, approximated as the slope at origin, appears much larger (2.4 nm/min) than in Chapter 3. A clear saturation of the film thickness is found above 30 min of deposition. This phenomenon might be related to the simultaneous formation of RbCoFe particles in the solution, as their own growth consumes precursors in solution. The σ_{Layer} values follow the same trend as the RMS roughness derived from AFM analyses, i.e. a first decrease upon film growth presumably because of a densification of the layer, then an increase at long deposition times, as already observed for the RbNiCr layers.

Electronic density values are not accurately extracted because of the film roughness. We observe that the ρ_{Layer} values are systematically smaller than the theoretical ones, which range between $5.75 \times 10^{23} \text{ el.cm}^{-3}$ for $\text{Co}[\text{Fe}(\text{CN})_6]_{0.67} \cdot 4.6\text{H}_2\text{O}$ (i.e. no Rb insertion) to $7.18 \times 10^{23} \text{ el.cm}^{-3}$ for $\text{RbCo}[\text{Fe}(\text{CN})_6] \cdot \text{H}_2\text{O}$ (i.e. maximum insertion of Rb). We will see in the discussion section that part of the discrepancies may be explained by the porous character of the layers.

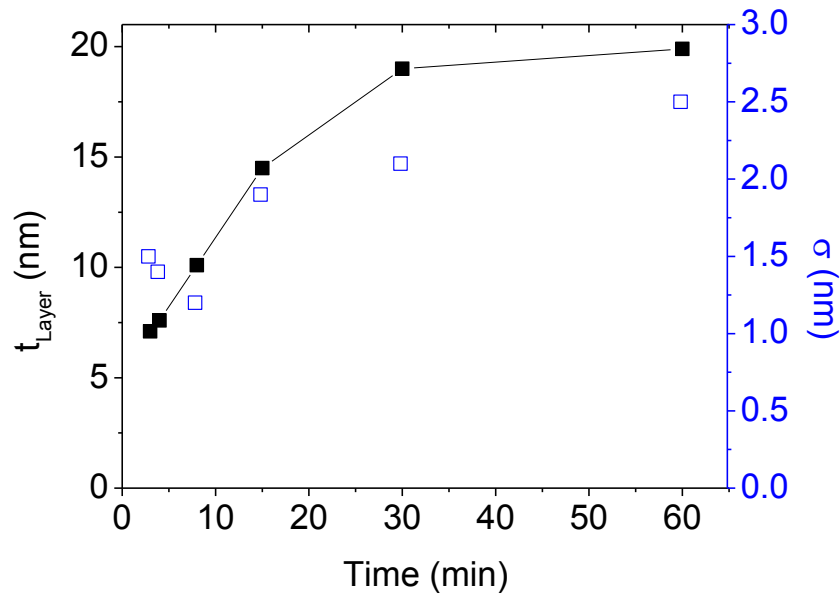


Figure 4.3. Dependence of the RbCoFe film thickness (black squares) and surface roughness (blue squares) with the deposition time, derived from X-ray reflectivity.

4.3.1.2 Atomic Force Microscopy (AFM) characterizations

Representative AFM images of the RbCoFe layers are displayed in **Figure 4.4** for deposition times ranging between 3 and 60 min. These films correspond to the ones studied in the previous section. A line profile is also displayed at the bottom of each image. These images show that all the films have a granular morphology. For instance, **Figure 4.4(a)** shows one layer of individual and poorly connected grains for 3 min of deposition.

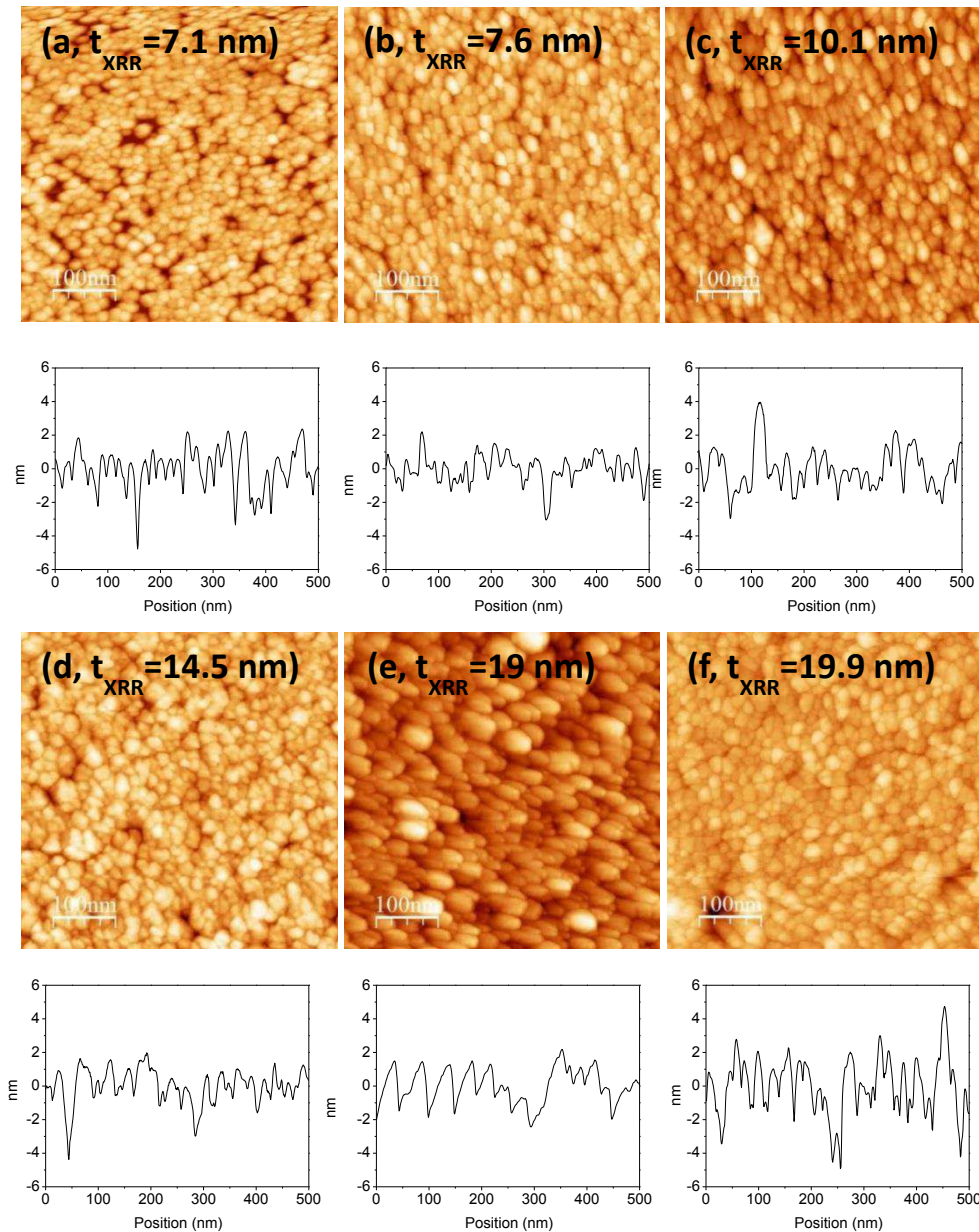


Figure 4.4. AFM images of RbCoFe films corresponding to deposition times of (a) 3 min, (b) 4 min, (c) 8 min, (d) 15 min, (e) 30 min and (f) 60 min. Scale bar: 100 nm. A line profile is given below each image and the film thickness derived from X-ray reflectivity (t_{XRR}) is also indicated.

The RbCoFe films are rather rough on the scale of observations with a typical peak to peak roughness of ca. 2 nm. The RMS values of roughness were determined using WSxM 4.0 Beta 3.1. These RMS values are presented in **Table 4.1**. The variation of grain density determined by the SPIP software is plotted as a function of thickness t_{XRR} in **Figure 4.5**. We observe that the grain density stays nearly constant, around 3.6×10^{11} grains/cm² upon deposition, which suggests an instantaneous nucleation process.

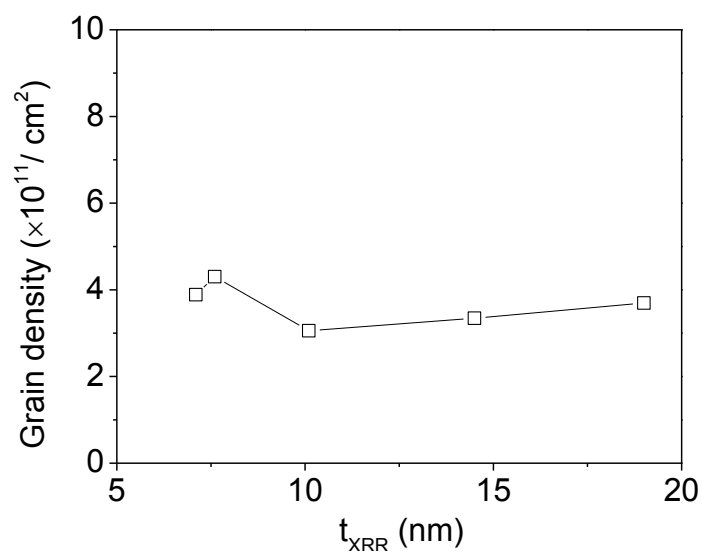


Figure 4.5. Variation of the grain density as a function of t_{XRR} .

Larger scale SEM plane view images are also reported in Appendix. They show that the surfaces are rather homogenous at both short (15 min) and long (1 hour) deposition times. We observe the presence of holes in the layer that may come from the adsorption of particles from the solution. This adsorption must be weak as particles are no longer present after the rinsing stage.

4.3.1.3 X-ray diffraction (XRD) measurements

Figure 4.6 compares the $\theta/2\theta$ scan of the RbCoFe layer corresponding to 15 min deposition (bottom panel) to those of two kinds of particles grown in solution (upper panels). The $\text{Co}[\text{Fe}(\text{CN})_6]_{0.67} \cdot 4.6\text{H}_2\text{O}$ powder sample, with a lattice parameter of 10.32 \AA , is representative of a material composed of $\text{Co}^{2+}\text{-Fe}^{3+}$ pairs, whereas the $\text{Rb}_{0.45}\text{Co}[\text{Fe}(\text{CN})_6]_{0.80} \cdot 3.5\text{H}_2\text{O}$ sample (lattice constant of 9.95 \AA) is representative of a photoswitchable material containing a majority of $\text{Co}^{3+}\text{-Fe}^{2+}$ pairs. Again, the (222) peak of the silicon substrate was used as an internal reference for an accurate determination of the 2θ positions. Similarly to what was reported for the RbNiCr layers in Chapter 3, the XRD patterns of the different films display only (00l) Bragg reflections indicating a texture of the films, but complementary measurements using a 4-circle diffractometer show no evidence for an in plane orientation.

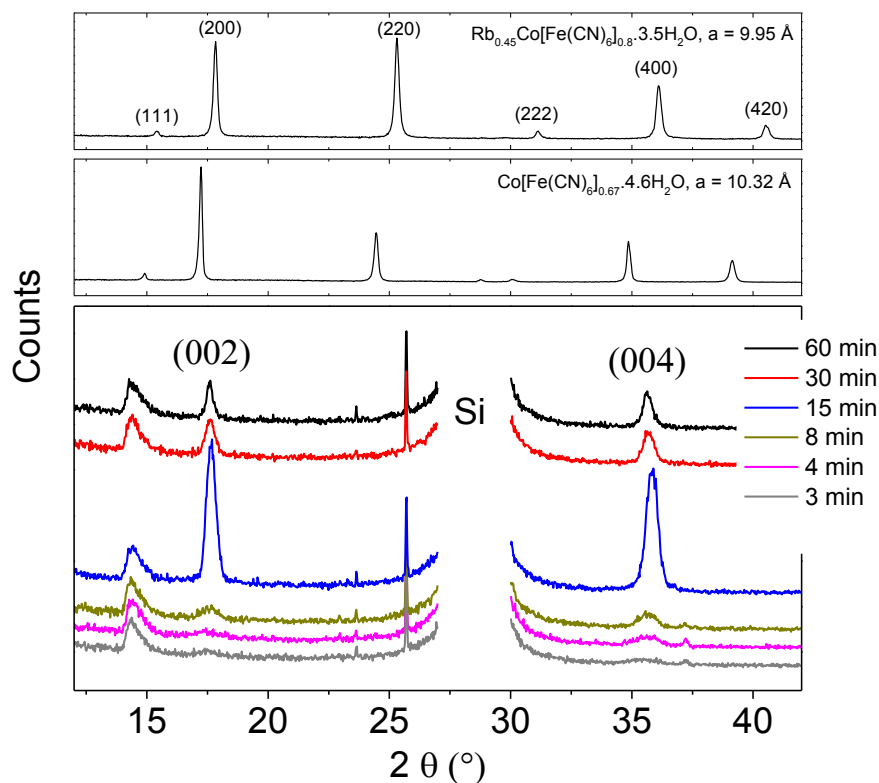


Figure 4.6. $\theta/2\theta$ scans of RbCoFe layers of variable deposition time (bottom panel) and of $\text{Co}[\text{Fe}(\text{CN})_6]_{0.67} \cdot 4.6\text{H}_2\text{O}$ ($a = 10.32 \text{ \AA}$) and $\text{Rb}_{0.45}\text{Co}[\text{Fe}(\text{CN})_6]_{0.80} \cdot 3.5\text{H}_2\text{O}$ ($a = 9.95 \text{ \AA}$) particles (top panel). The origin of the asymmetric peak at $2\theta = 14.4^\circ$ is yet unclear but it has also been observed without any deposit.

For all films, the positions of the diffraction lines are systematically in between those of the two reference samples, indicating an intermediate lattice parameter value. The position of the (002) and (004) reflections was determined from peak fitting and a mean lattice parameter was derived (see **Table 4.2**). It is systematically of the order of 10.1 \AA but tends to slightly decrease with the deposition time. The Full Width at Half Maximum (FWHM) of the (002) and (004) peaks was also determined from the fitting. A coherence length (L_C) value was then evaluated using the procedure described in Chapter 3 (**section 3.3.3**). The change of L_C with t_{XRR} is shown in **Figure 4.7(a)**. L_C increases with increasing t_{XRR} . **Figure 4.7(b)** shows however that the intensity of the (002) and (004) peaks stops increasing for films thicker than $\sim 15 \text{ nm}$. This behaviour was systematically observed with different growth conditions. It might be associated with some microstructural evolution of the deposits. It was however not further investigated and, in the following, we will only consider films grown in less than 15 min (or thinner than 15 nm under the present growth condition).

Table 4.2. Lattice parameter (a), intensity of the (002) and (004) peaks, and coherence length (L_c) derived from X-ray diffraction. a and L_c are average values from the (002) and (004) Bragg reflections. The error bars indicated for a and L_c are representative of the difference between the values derived from the two peaks.

deposition [min]	a [Å]	Intensity (002) [counts]	Intensity (004) [counts]	Ratio (004)/(002)	L_c [nm]
3	10.15±0.02	50.2	87	1.74	8 ± 4
4	10.12±0.05	65.7	134	2.04	6 ± 1
8	10.08±0.01	67.7	74	1.09	9.9 ± 0.6
15	10.05±0.02	377.8	468.4	1.24	17 ± 1
30	10.07±0.00	87.2	113.6	1.30	17 ± 1
60	10.08±0.01	93.2	127.6	1.45	25 ± 5

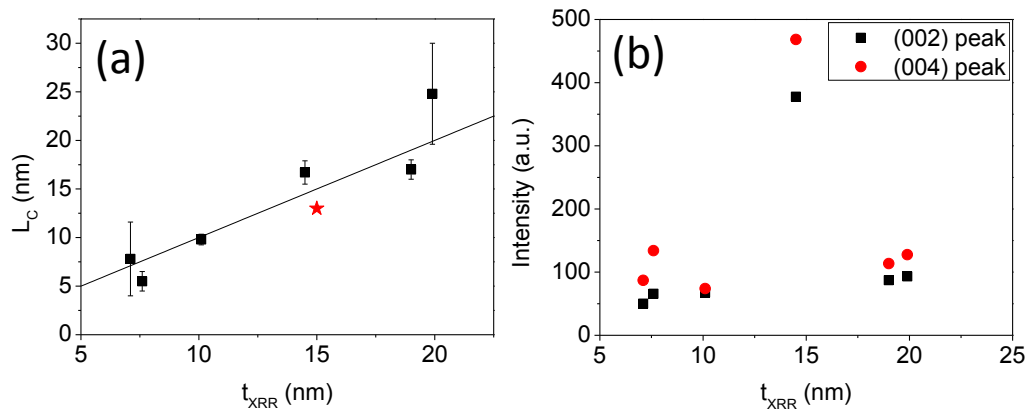


Figure 4.7. Evolution of (a) the vertical coherence length (L_c) and (b) the intensity of (002) and (004) Bragg reflections as a function of t_{XRR} . The grey line is a line of slope 1. The red symbol stands for the sample described in **section 4.4** and grown in a cell specially designed for in situ FTIR measurement.

4.3.1.4 Rutherford Backscattering Spectroscopy (RBS) measurements

A representative RBS spectrum of a RbCoFe film is shown in **Figure 4.8**. The plateau observed at energies $E < 1.4$ MeV corresponds to the contribution of the silicon substrate. At higher energy, three distinct peaks are present at 1.85, 1.88 and 2.05 MeV assigned to the Fe, Co and Rb elements, respectively. Note that the deconvolution of the peaks related to Fe and Co required using He^{2+} particles of energy higher than the ones used for the analysis of the RbNiCr layers (2.5 instead of 1.5 MeV). The Co, Fe and Rb areal density values were then obtained by comparing the area of the corresponding peaks in the RBS spectra to that of a

reference standard measured in the same conditions (see the Appendix for details on the data treatment).

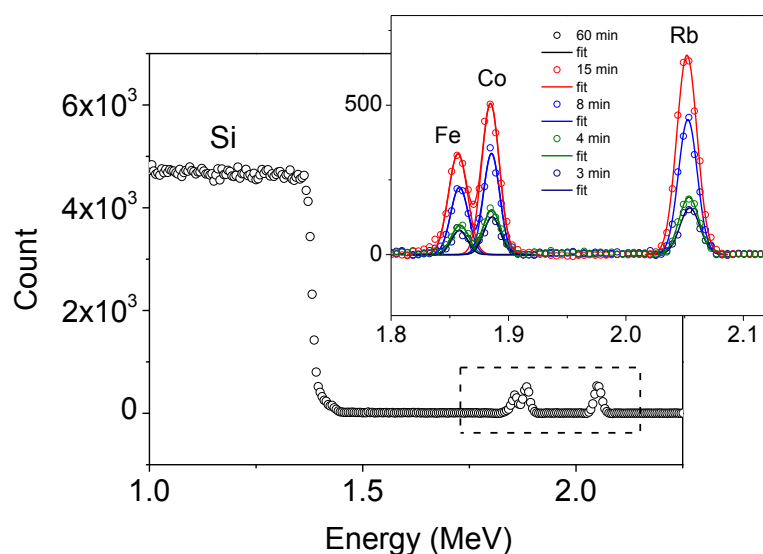


Figure 4.8. RBS spectra representative of RbCoFe films of increasing deposition times. Symbols are experimental data and solid lines are the three components (Gaussian functions) used to account for the Fe, Co and Rb peaks.

The atom areal density values were averaged from measurements performed on different spots on the sample (see **Table 4.3**). Their evolutions with the film thickness t_{XRR} are displayed in **Figure 4.9**. All three atom areal densities increase linearly with the deposition time. The Rb/Co and Fe/Co atomic ratios are also given in **Table 4.3** for the different films. These ratios do not significantly vary with the deposition time, indicating no composition change during the film growth. We thus used the mean value and standard deviation of these two ratios to derive the films composition, $\text{Rb}_{0.77 \pm 0.08} \text{Co}[\text{Fe}(\text{CN})_6]_{0.76 \pm 0.03} \cdot z\text{H}_2\text{O}$.

Table 4.3. Atom areal density values for RbCoFe films with different deposition times.

Time (min)	Atom areal density [10^{15} atom/ cm^2]			Rb/Co	Fe/Co
	Rb	Co	Fe		
3	1.3 ± 0.1	1.5 ± 0.2	1.2 ± 0.2	0.84	0.75
4	1.64 ± 0.08	2.1 ± 0.2	1.5 ± 0.2	0.79	0.73
8	3.2 ± 0.2	4.2 ± 0.5	3.1 ± 0.5	0.77	0.74
15	4.8 ± 0.2	6.2 ± 0.5	4.8 ± 0.6	0.78	0.78

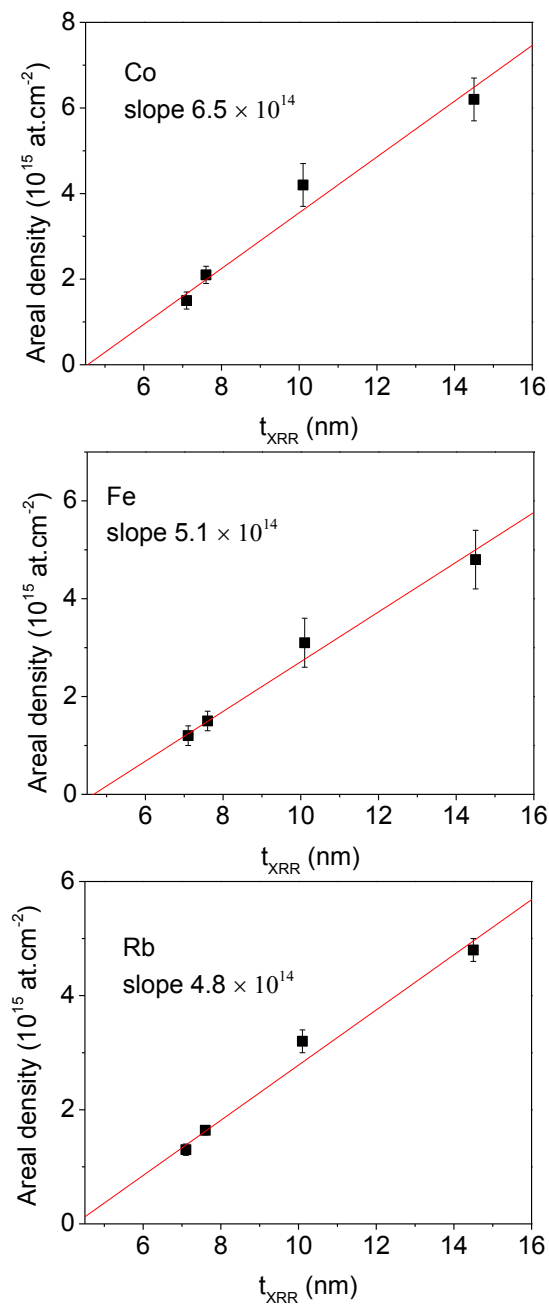


Figure 4.9. Areal density of Co, Fe and Rb as a function of film thickness (t_{XRR}). The red lines are fitted curves of slope 6.5×10^{14} , 5.1×10^{14} , and 4.8×10^{14} at./cm 2 for Co, Fe and Rb respectively.

4.3.2 Discussion

As mentioned in **section 4.3.1.3**, we restrict the discussion to the growth mechanism of RbCoFe films thinner than 15 nm. The chemical composition of the layers derived from the Rb/Co and Fe/Co atomic ratios derived from RBS should write as

$\text{Rb}_{0.77\pm 0.08}\text{Co}[\text{Fe}(\text{CN})_6]_{0.76\pm 0.03}\cdot z\text{H}_2\text{O}$. As in the case of RbNiCr layers, we found that this composition is independent on film thickness so that it is uniform in depth. We also calculate that the theoretical diffusion fluxes of Co^{2+} , $\text{Fe}(\text{CN})_6^{3-}$, and Rb^+ are typically one order of magnitude larger than the experimental fluxes obtained from the areal density values and the deposition time. We can thus conclude that mass transport is not the limiting step for the film formation similarly to what was reported for the RbNiCr layers.

At the initial stages of growth, the layers are clearly not continuous but formed of a monolayer of poorly connected grains. This is confirmed by the fact that the electronic density of the thin films obtained from XRR is 1.4 times smaller than the one calculated from the film composition, $\text{Rb}_{0.77\pm 0.08}\text{Co}[\text{Fe}(\text{CN})_6]_{0.76\pm 0.03}\cdot z\text{H}_2\text{O}$. Upon growth, the roughness of the RbCoFe layers first decreases suggesting a densification of the films. To further discuss the growth stage, we compare the *average* thickness (t_{RBS}) and the *physical* thickness (t_{XRR}). t_{RBS} is calculated according to Eq.3.7 using an average lattice parameter value of 10.06 Å. t_{RBS} (empty squares) is plotted as a function of t_{XRR} in **Figure 4.10**. There is a quasi linear relationship between t_{RBS} and t_{XRR} but no proportionality. Note that the grey line in **Figure 4.10** is not a fit, but a straight line of slope of 1. t_{RBS} is smaller than t_{XRR} at short deposition times, confirming the discontinuous character of the layers with a filling factor ($t_{\text{RBS}}/t_{\text{XRR}}$) of the order of 0.5. Upon growth, the filling factor increases and saturates above a critical thickness of 10 nm. At this stage of the growth, the layers are quasi compact since the *physical* thickness is then comparable to the *average* thickness (coalescence of the grains). All these experimental findings suggest that the growth mode of the RbCoFe films is similar to that of the RbNiCr layers (see **Figure 4.11** for a comparison of the growth rate in the two systems). The initial grains grow vertically and laterally up to coalescence, and then only vertically. As data related to very short deposition times are clearly missing, it is not justified to discuss with further details these nucleation and growth mechanisms.

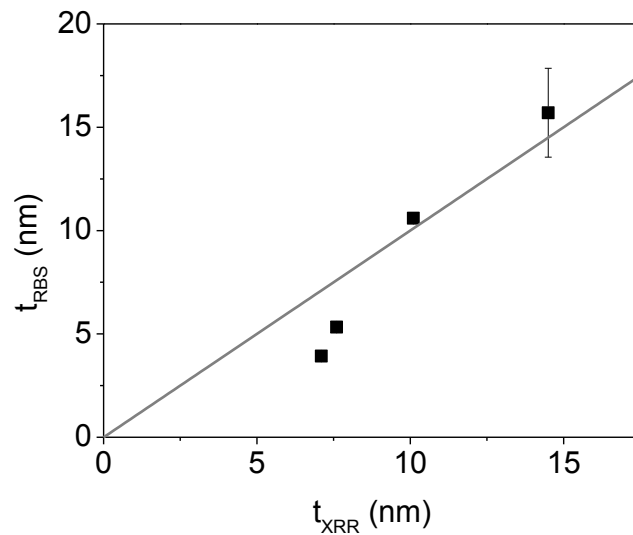


Figure 4.10. Variation of the *average* thickness t_{RBS} as a function of t_{XRR} . The grey line is a line of slope 1.

Another information is provided by the comparison between the coherence length (L_C) and t_{XRR} values. As shown in **Figure 4.7(a)**, the concordance between L_C and t_{XRR} for different samples confirm the presence of oriented grains of vertical height comparable to the film thickness (i.e., with a continuous lattice from bottom to top of the film). The red symbol in **Figure 4.7(a)** represents the L_C value of a sample prepared in a different cell designed for in situ FTIR measurements (see details in Chapter 5). For this sample, we found that the L_C value scales fairly well with the variation observed for the present series of samples indicating that the growth mode is not sensitive to the design of the deposition cell and to the fluid hydrodynamics.

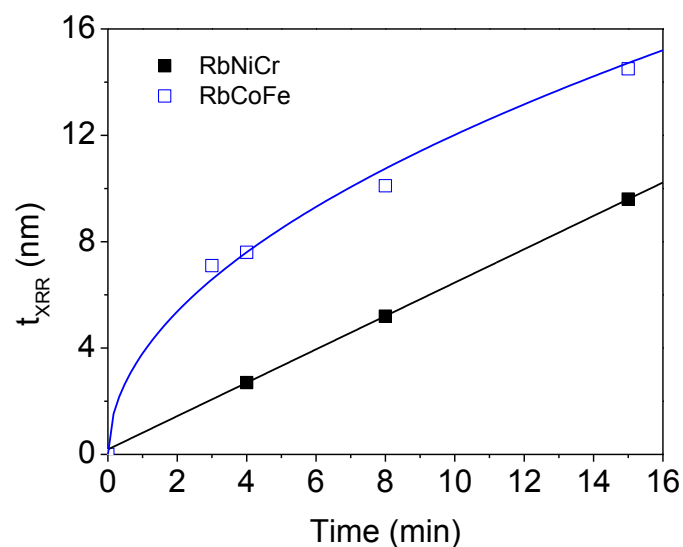


Figure 4.11. Evolution of the film thickness t_{XRR} for RbCoFe (close symbols) and RbNiCr layers (empty symbols) as a function of deposition time.

4.4 Photo-switching properties

4.4.1 Results

The aim of this section is to study the photo-switching properties of the as-obtained RbCoFe films. To this end, one needs first to determine the Co and Fe valence states, as Rutherford Backscattering Spectroscopy only gives access to the global chemical composition of the layers. We thus performed complementary X-ray absorption spectroscopy measurements. Indeed, it is well known that the energy of the main edge and that of the dipole allowed $1s (a_{1g}) \rightarrow 4p (t_{1u})$ transition is a clear signature of the valence state of these ions.⁴ Details related to data collection, normalization and band assignment are reported in Appendix.

All the following results refer to a 15 nm RbCoFe layer grown in the cell designed for in situ IR spectroscopy measurements.¹ For this sample, RBS characterizations yield Rb/Co and Fe/Co atomic ratios of 0.82 ± 0.03 and 0.74 ± 0.04 , respectively, in good accordance with the average composition of the films studied in **section 4.3.1.4** (i.e. $\text{Rb}_{0.77 \pm 0.08} \text{Co}[\text{Fe}(\text{CN})_6]_{0.76 \pm 0.03} \cdot z\text{H}_2\text{O}$). In addition, the structural characteristics and the morphology of this film are very similar to what was found for the layers described in the previous sections.

In **Figure 4.12(a)**, we compare the X-ray Absorption Near Edge Structures (XANES) at the Co K-edge of the RbCoFe layer with those of $\text{Co}[\text{Fe}(\text{CN})_6]_{0.67} \cdot 4.6\text{H}_2\text{O}$ and $\text{K}_3\text{Co}(\text{CN})_6$ bulk standards. The former reference sample is made of Co^{2+} ions, which are six-fold coordinated either to nitrogen atoms from the cyanide ligands or to oxygen atoms of water molecules. The $\text{K}_3\text{Co}(\text{CN})_6$ standard is only formed of Co^{3+} ions, with almost regular $[\text{Co}(\text{CN})_6]$ octahedra.¹⁸

¹ It is important to mention that we performed measurements both on fresh deposits and on layers prepared several months before that were stored under ambient conditions. For these latter samples, we observed some ageing or degradation leading to an expansion of the cobalt hexacyanoferrate lattice, associated with a $\text{Co}^{3+} \rightarrow \text{Co}^{2+}$ reduction according to XANES observations. The origin of this redox change is yet unknown.

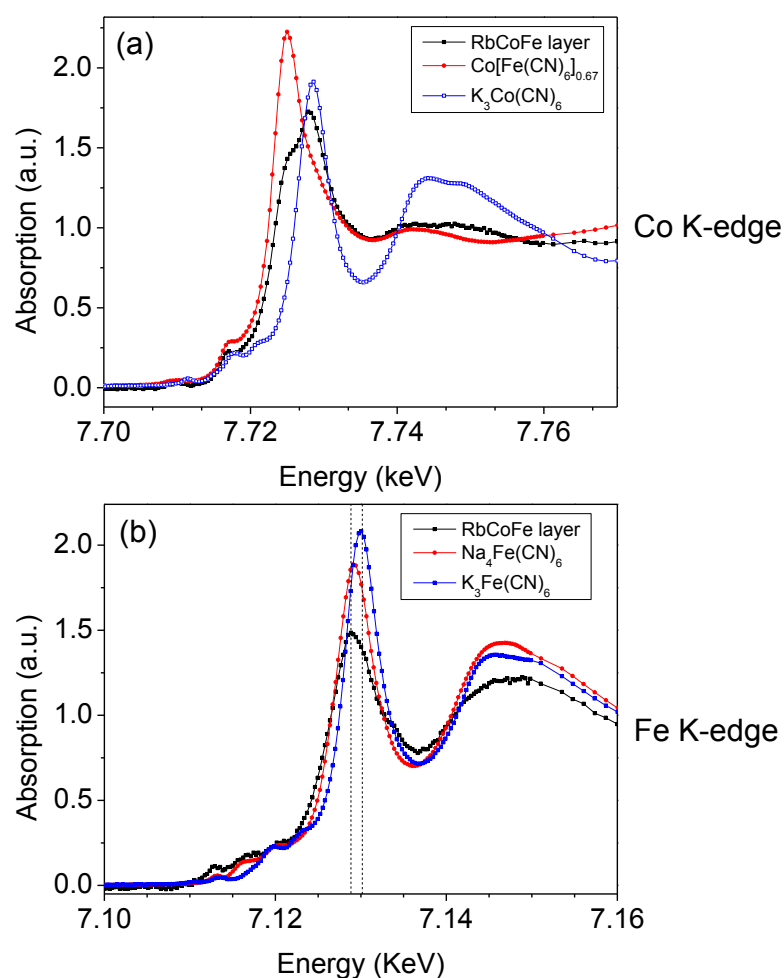


Figure 4.12. (a) XANES spectrum at the Co K-edge of a RbCoFe film recorded at room temperature. Comparison is made with Co[Fe(CN)₆]_{0.67}•4.6H₂O (red line) and K₃Co(CN)₆ (blue line) standards measured at 100 K. (b) XANES spectrum at the Fe K-edge of the same film, comparison with Na₄Fe(CN)₆ (red line) and K₃Fe(CN)₆ (blue line) reference compounds measured at 100 K.

The two reference compounds show a well-defined and intense absorption band, related to $1s \rightarrow 4p$ transition. These bands are separated by 4 eV, i.e. 7.725 keV and 7.729 keV for the Co²⁺ and Co³⁺ reference samples, respectively. In contrast, the spectrum of the RbCoFe layer shows a clear splitting of the main line representative of the sum of Co²⁺ and Co³⁺ contributions. To determine the proportion of these two species, a general method is to use linear combinations of reference spectra related to pure Co²⁺ and pure Co³⁺ ions in an environment similar to the one of the sample.¹⁹ As the crystal structure of the K₃Co(CN)₆ standard is different from that of Prussian blue analogues, we could not use this method and we had to implement a procedure of data fitting, using the sum of Lorentzian functions representative of the discrete $1s \rightarrow 4p$ transitions and an arctangent function representative

of transitions to continuum states.²⁰ The integral of the peak related to the Co^{2+} contribution was then compared to that found for the $\text{Co}[\text{Fe}(\text{CN})_6]_{0.67} \cdot 4.6\text{H}_2\text{O}$ standard (with 100% of Co^{2+}) to obtain the Co^{2+} fraction. For the RbCoFe film, the fitting procedure is fully described in Appendix (**section A.5**). It leads to a Co^{2+} fraction of $34 \pm 3\%$ for the XANES spectrum recorded at room temperature.

XAS measurements were also recorded at the Fe K-edge. The corresponding XANES spectrum is displayed in **Figure 4.12(b)**. Comparison with the $\text{K}_3\text{Fe}(\text{CN})_6$ and $\text{Na}_4\text{Fe}(\text{CN})_6$ reference compounds (representative of Fe^{3+} and Fe^{2+} species, respectively) indicates that the position of the main line weakly depends on the redox state of iron (the shift is only of 1 eV between the red and blue curves). It is thus difficult to assess a precise $\text{Fe}^{2+}/\text{Fe}^{3+}$ partition from experimental curves. However, we observe that the energy of the main absorption line is similar for the RbCoFe layer and the $\text{Na}_4\text{Fe}(\text{CN})_6$ powder sample, indicating that a majority of iron species are at the +II oxidation state. The RbCoFe layer is thus formed of a majority of $\text{Co}^{3+} - \text{Fe}^{2+}$ pairs.

Additional XAS experiments on this RbCoFe film were carried out at low temperature using a cryostat working under He exchange gas. Measurements were restricted to the Co K-edge which is more sensitive to charge transfers between Co and Fe and allow for quantitative analyses. Measurements were first performed at 100 K. The corresponding XANES spectrum is perfectly superimposable to the one collected at 293 K, indicating a similar Co^{2+} content and thus the absence of thermally induced CTIST. By further cooling down to 10 K, we observe an increase of the intensity of the main line ascribed to Co^{2+} species, and a decrease of the one related to the Co^{3+} contribution. **Figure 4.13(a)** shows successive XANES spectra recorded at 10 K (the acquisition time per spectrum is 16 min). They show a gradual increase of the Co^{2+} fraction as a function of scan number, which increases from 34% to 56% after 2 hours irradiation. Comparison was made with a $\text{Rb}_{0.46}\text{Co}[\text{Fe}(\text{CN})_6]_{0.79} \cdot z\text{H}_2\text{O}$ powder sample (particle size ~ 120 nm), which photo-switching properties are well documented.^{11,21} The XANES spectra relative to this sample (**Figure 4.13(b)**) show similar but more prominent changes.

These time evolutions are attributed to photo-excitation under the X-ray beam in this energy range. It is important to note that when the samples are warmed back to 100 K, we observed a relaxation toward the initial state indicating that the photo-excitation process is reversible. As a consequence, the valence change observed for Co is not ascribed to irreversible radiation damage associated with photonic effects (formation of radicals, isomerism and flipping of the cyano bridge,²² etc) or with photo-thermal processes due to X-ray absorption and subsequent sample heating (e.g. dehydration). Note that other authors have reported the possibility of photo-excitation induced by x-rays of specific energy in several photo-switchable Prussian blue analogues.^{3,23,24}

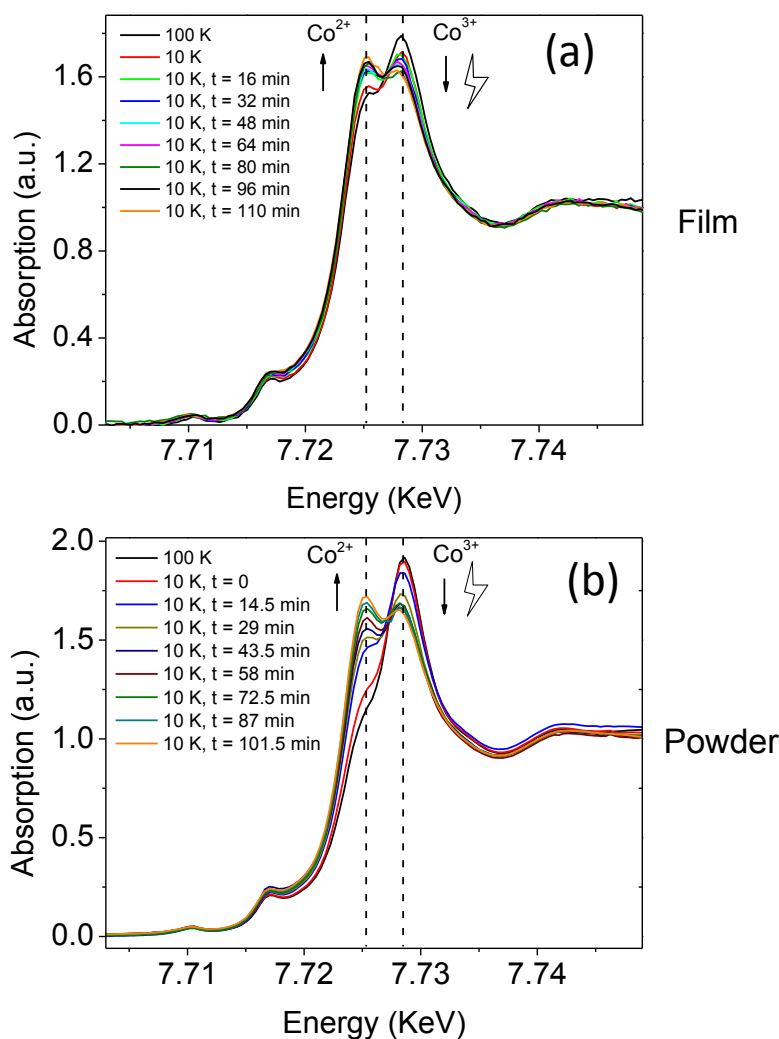


Figure 4.13. Successive XANES spectra at the Co K-edge for (a) the RbCoFe film and (b) $\text{Rb}_{0.46}\text{Co}[\text{Fe}(\text{CN})_6]_{0.79} \cdot z\text{H}_2\text{O}$ particles. Measurements were performed at 10 K. Comparison is made with spectra recorded at 100 K (black lines).

Although photo-excitation proceeds probably through a different mechanism due to the population of excited states of higher energy, it is likely that the metastable state reached after X-ray irradiation is similar to the one that would be obtained under visible light illumination by tuning the wavelength to the metal-to-metal charge transfer band (broad band centered around 550 nm, which is weakly dependent on the nature and on the amount of alkali ion^{1,6,25}). These preliminary measurements give a first indication that the RbCoFe layer displays photo-switching properties. We tried to confirm these results by performing X-ray diffraction measurements under visible light irradiation (600 nm, incident power of 20 to 60 $\text{mW}\cdot\text{cm}^{-2}$). These test experiments were performed at Laboratoire de Cristallographie, Résonance Magnétique et Modélisations of Université de Nancy. However, photo-excitation was found to be unsuccessful. It is likely that the temperature below which thermal

relaxation does not efficiently compete with photo-excitation is below 80 K. At this temperature, cryopumping occurs leading to a decrease of the pressure in the cryostat to 0.03 mbar. For $\text{Rb}_{0.46}\text{Co}[\text{Fe}(\text{CN})_6]_{0.79}\cdot z\text{H}_2\text{O}$ powder samples, we observed that this reduced pressure leads to the suppression of the switching properties of the materials,²¹ similarly to what was reported by other authors.²⁶ Such modifications of the switching properties are likely due to sample dehydration.

4.4.2 Discussion

As mentioned in the introduction, photo-induced effects in cobalt hexacyanoferrates (i.e., photo-magnetism, photo-striction, photo-chromism) require that the compound should be composed of a majority of $\text{Co}^{3+}(\text{LS}, 6t_{2g}^0e_g) - \text{Fe}^{2+}(\text{LS}, 6t_{2g}^0e_g)$ pairs. Previous work by the group of Anne Bleuzen has suggested that there is a direct relationship between the insertion of the alkali metal ion and that of the cyanometalate, yielding the general formula $\text{A}_x\text{Co}[\text{Fe}(\text{CN})_6]_{(x+2)/3}\cdot z\text{H}_2\text{O}$ (A: alkali metal ion). At first, it was assumed that a larger cyanometalate content should increase the Co ligand field strength as oxygen atoms from water are replaced by nitrogen atoms from the cyanides. This would then favor a low spin state for the cobalt ions and an increase of their reducing power leading to a spontaneous electron transfer with formation of $\text{Co}^{3+} - \text{Fe}^{2+}$ pairs.²⁷ However, recent x-ray absorption spectroscopy measurements by Cafun and coworkers have shown that the ligand field strength exerted by the cyanide ligand is weak and comparable to that provided by the water molecules OH_2 .²⁸ These authors propose that the redox process may be driven by the formation of Co-NC-Fe bridges, which increases the reduction power of the $\text{Co}^{2+}(\text{NC})_5(\text{OH}_2)$ entities and the redox potential of the $\text{Fe}^{3+}(\text{CN})_6/\text{Fe}^{2+}(\text{CN})_6$ couple.

For the RbCoFe layer studied in this section, the average film composition derived from RBS is $\text{Rb}_{0.82}\text{Co}[\text{Fe}(\text{CN})_6]_{0.74}\cdot z\text{H}_2\text{O}$. We also know that the fraction of Co^{2+} measured from XAS at Co K edge is $\sim 34\%$. It is difficult to get a precise value of the Fe^{2+} content because the absorption edges of $[\text{Fe}(\text{CN})_6]^{3-}$ and $[\text{Fe}(\text{CN})_6]^{4-}$ species are too close in energy (1 eV difference). The above Co^{2+} fraction can be cross-checked by considering the measured lattice parameter a . According to EXAFS measurements², typical $\text{Fe}^{3+}\text{-C}$ and $\text{Fe}^{2+}\text{-C}$ distances are 1.91 Å and 1.93 Å while there is a much larger difference in the $\text{Co}^{3+}\text{-N}$ and $\text{Co}^{2+}\text{-N}$ distances, 1.90 Å and 2.08 Å respectively. As a consequence, the lattice parameter, a was found to depend linearly on the Co^{3+} content,¹¹ as shown in **Figure 4.14**. This linear relationship can be used as chart plot to estimate the Co^{2+} content in films. For the sample under study, the lattice constant is 10.07 Å, yielding a Co^{2+} content of 38 %, which is in very good agreement with the value of 34% obtained from quantitative XANES analyses.

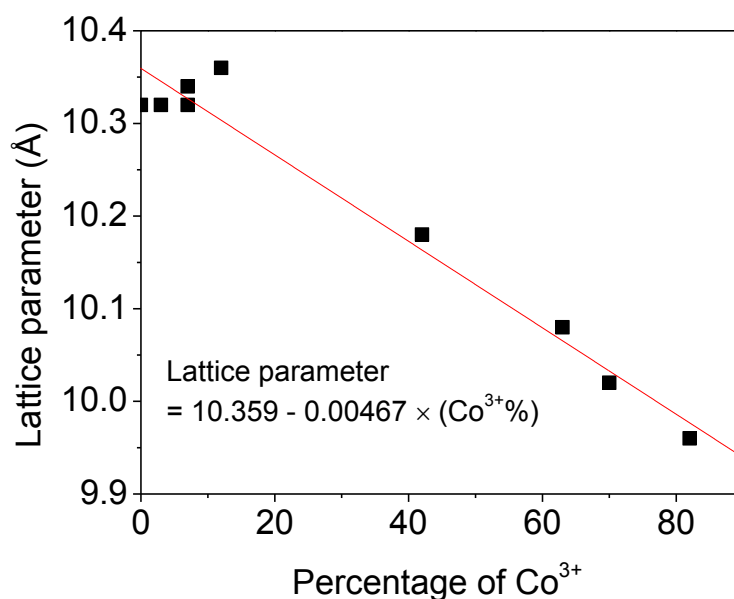


Figure 4.14. Variation of the lattice parameter for $\text{Cs}_x\text{Co}[\text{Fe}(\text{CN})_6]_{(x+2)/3} \cdot z\text{H}_2\text{O}$ powder samples as a function of the Co^{3+} content. Data were adapted from the PhD thesis of V. Escax-Bastet, the data point with 80% Co^{3+} refers to a $\text{Rb}_{0.45}\text{Co}[\text{Fe}(\text{CN})_6]_{0.8} \cdot z\text{H}_2\text{O}$ compound synthesized by the same group.¹¹

We can further notice that there is no agreement between the chemical composition of the layer and the $\text{Rb}_x\text{Co}[\text{Fe}(\text{CN})_6]_{(x+2)/3} \cdot z\text{H}_2\text{O}$ formula proposed for particles grown in water using similar precursors.¹¹ We actually observe a larger insertion of Rb^+ ions. To confirm the incorporation of Rb in the cobalt hexacyanoferrate lattice, we plot in **Figure 4.15** the ratio between the integrated intensity of the (004) and (002) Bragg reflections as a function of Rb content per primitive cell. Integrated intensities were calculated using the atomic scattering factors and their q -dependence as tabulated in the International Tables of Crystallography.²⁹ As RbCoFe films are highly textured, we assimilate the layer to a single crystal and use a Lorentz polarization factor $L_p = 1/\sin(2\theta)$.³⁰ We also display in **Figure 4.15** the data point corresponding to our RbCoFe sample. The fact that we found a ratio of 1.8 between the (004) and (002) lines confirm a large incorporation of Rb within the lattice. This was also the case for all the films described in **section 4.3.1.3** (see **Table 4.2**).

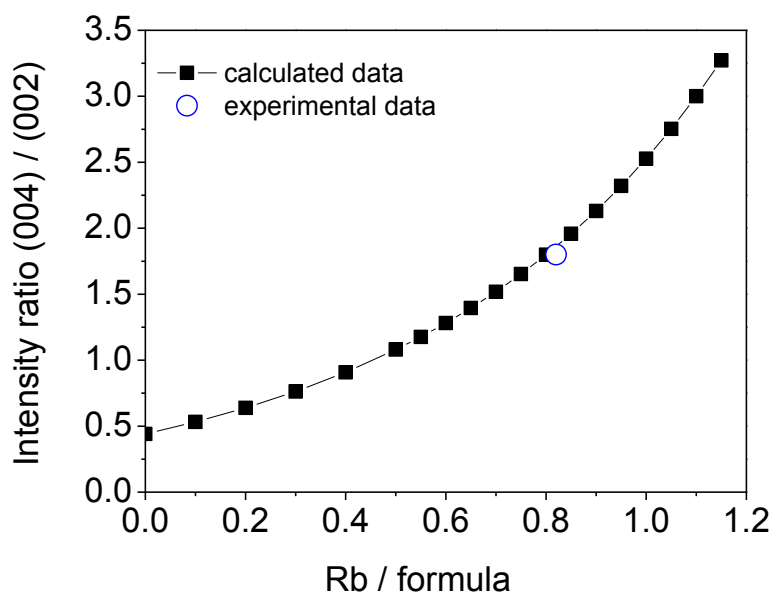


Figure 4.15. Ratio between the integrated intensity of the (004) and (002) Bragg reflections as a function of Rb content per primitive cell. Black symbols correspond to calculated values (see the main text), while the blue symbol refers to the RbCoFe layer studied in the present section.

Putting together the above chemical composition of the film and accounting for the fact that the fraction of Co^{2+} is about 34%, one can decompose the formula $\text{Rb}_{0.82}\text{Co}[\text{Fe}(\text{CN})_6]_{0.74} \cdot z\text{H}_2\text{O}$ as $\text{Rb}_{0.82}\text{Co}^{2+}_{0.34}\text{Co}^{3+}_{0.66}[\text{Fe}^{2+}_x\text{Fe}^{3+}_{1-x}(\text{CN})_6]_{0.74} \cdot z\text{H}_2\text{O}$ where x is the fraction of Fe^{2+} . Electro-neutrality requires:

$$0.82 + 0.34 \times 2 + 3 \times 0.66 - 0.74 \times [4x + 3(1-x)] = 0$$

leading to $x = 1.7$, which is not possible. In this case, extra negative charges have to be available to compensate the excessive positive charges coming from Rb^+ .

The above x value is evidently unrealistic and the simplest hypothesis is the insertion of anions within the lattice, NO_3^- in the present case. As each $\text{Co}^{3+}\text{-Fe}^{2+}$ pairs in the final compound originate from a pair of $\text{Co}^{2+}/[\text{Fe}(\text{CN})_6]^{3-}$ precursors in solution, we can assume that the amount of Fe^{2+} content in the film should be equal to that of Co^{3+} . If y is the fraction of NO_3^- inserted per unit cell, electro-neutrality requires that:

$$0.82 + 0.34 \times 2 + 3 \times 0.66 - 0.74 \times [4 \times 0.89 + 3 \times (1 - 0.89)] - y = 0$$

leading to $y = 0.6 \pm 0.2$. The standard deviation was derived from the error bar on the Rb/Co and Fe/Co ratios and on the Co^{2+} fraction.

NO_3^- has a reasonable size to be incorporated to the unit cell, either in the sub-octant of the fcc structure (thus replacing a zeolitic water molecule) or coordinated with Co ions at vacant $[\text{Fe}(\text{CN})_6]$ sites. There is obviously enough space within the cell to accommodate about one anion per formula unit, as there are 1.2 accessible sub-octants and also 1.6 Co coordination sites. As the N content in the RbCoFe layers was not measured by NRA technique, we could not verify the hypothesis of NO_3^- incorporation. To prove this interpretation, we plan to deposit RbCoFe film with other counter anions, such as Cl^- instead of NO_3^- . It is probably the insertion of nitrate which is at the root of the excess of Rb^+ and not the reverse.

The insertion of large amounts of Rb and of additional NO_3^- ions in the lattice may significantly impact the switching properties of the materials. In the following, we reconsider the yield of photo-excitation in the RbCoFe layer and in the $\text{Rb}_{0.45}\text{Co}[\text{Fe}(\text{CN})_6]_{0.79} \cdot z\text{H}_2\text{O}$ powder sample. From quantitative XANES analyses, we derive the change of the Co^{2+} fraction as a function of irradiation time in the two materials (**Figure 4.16**). For the 15 nm thick film, X-ray penetration in the sample depth should be considered as uniform and a photo-stationary state is reached within the first 25 min. In contrast, we calculate that x-ray penetration is not homogeneous for the powder sample because of absorption, thus slowing down the photo-excitation kinetics. In spite of this, the powder sample shows a faster photo-excitation rate. In addition after two hours of irradiation, the number of converted pairs is 2.4 times larger in the powder sample than in the thin film. The fact that only one third of the initial Co^{3+} - Fe^{2+} pairs are converted in the layer sample may be explained by a reduced flexibility of the crystal structure associated with the incorporation of both Rb and NO_3^- . As proposed by Bleuzen and coworkers, the flexibility of the lattice is an important ingredient of the CTIST process, as it makes easier the lattice expansion, which accompanies the spin transition.²⁷ As discussed by C. Cartier dit Moulin, the yield of photo-excitation is also related to the presence of non-photoactive Co-Fe pairs in the lattice associated with different Co local environments.¹⁹ As consequence, a coordination linkage between Co^{3+} and NO_3^- may also affect the switching properties of the RbCoFe layer.

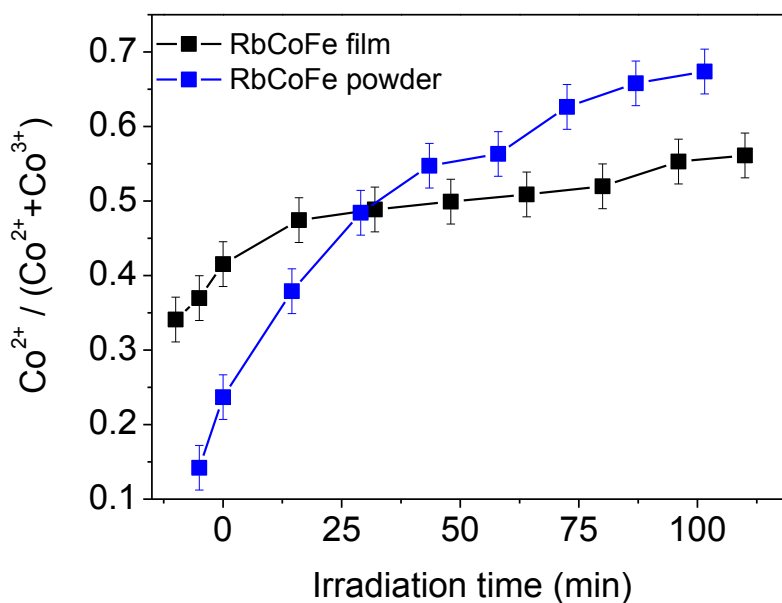


Figure 4.16. Evolution of the Co^{2+} fraction as a function of irradiation time. The black symbols refer to the RbCoFe layer ($t_{\text{XRR}} = 15$ nm), and the blue symbols correspond to $\text{Rb}_{0.45}\text{Co}[\text{Fe}(\text{CN})_6]_{0.79} \cdot z\text{H}_2\text{O}$ particles.

4.5 Conclusion

In summary, photo-switchable $\text{Rb}_{0.77 \pm 0.08}\text{Co}[\text{Fe}(\text{CN})_6]_{0.76 \pm 0.03} \cdot z\text{H}_2\text{O}$ thin films were prepared on Si (111) surfaces using a one-bath solution approach. The film thickness was subsequently controlled, from 7 to about 20 nm, by changing the immersion time. No proportionality was observed between the film thickness and the deposition time. All films exhibit a (00 l) texture. By comparison to the $\text{Rb}_x\text{Ni}[\text{Cr}(\text{CN})_6]_y \cdot z\text{H}_2\text{O}$ layers studied in Chapter 3, the RbCoFe films show a larger initial growth rate, but then growth proceeds at similar rate in the two systems, limited by the kinetics of the precursors incorporation in the solid phase. Film deposition likely consists of a uniform nucleation on the surface, followed by a vertical and lateral growth of the grains up to coalescence. These films present a rather large Rb content that has to be related to a hypothetical insertion of nitrate ions (NO_3^-) for charge balance. Despite a large fraction of Co^{3+} - Fe^{2+} pairs in the obtained films, the yield of the photo-excitation was shown to be strongly reduced, maybe due to a reduced flexibility of the crystal lattice and/or to a change of the Co environment and ligand field.

4.6 References

1. O. Sato; T. Iyoda; A. Fujishima; Hashimoto, K., Photoinduced magnetization of a cobalt-iron cyanide. *Science* **1996**, 272, 704-705.
2. T. Yokoyama; T. Ohta, Characterization of magnetic CoFe cyanides by x-ray-absorption fine-structure spectroscopy. *Phys. Rev. B* **1998**, 58, 8257-8266.
3. V. Escax; A. Bleuzen; J. P. Itie; P. Munsch; F. Varret; M. Verdaguer, Nature of the long-range structural changes induced by the molecular photoexcitation and by the relaxation in the Prussian blue analogue $\text{Rb}_{1.8}\text{Co}_4[\text{Fe}(\text{CN})_6]_{3.3}\cdot 13\text{H}_2\text{O}$. A synchrotron X-ray diffraction study. *J. Phys. Chem. B* **2003**, 107, 4763-4767.
4. A. Bleuzen; C. Lomenech; V. Escax; F. Villain; F. Varret; C. C. dit Moulin; M. Verdaguer, Photoinduced ferrimagnetic systems in Prussian blue analogues $\text{C}_x^{\text{I}}\text{Co}_4[\text{Fe}(\text{CN})_6]_y$ (C^I=Alkali Cation). 1. conditions to observe the phenomenon. *J. Am. Chem. Soc.* **2000**, 122, 6648-6652.
5. V. Escax; A. Bleuzen; C. C. dit Moulin; F. Villain; A. Goujon; F. Varret; M. Verdaguer, Photoinduced ferrimagnetic systems in Prussian blue analogues $\text{C}_x^{\text{I}}\text{Co}_4[\text{Fe}(\text{CN})_6]_y$ (C^I = alkali cation). 3. Control of the photo- and thermally induced electron transfer by the $[\text{Fe}(\text{CN})_6]$ vacancies in cesium derivatives. *J. Am. Chem. Soc.* **2001**, 123, 12536-12543.
6. O. Sato; Y. Einaga; T. Iyoda; A. Fujishima; K. Hashimoto, Cation-driven electron transfer involving a spin transition at room temperature in a cobalt iron cyanide thin film. *J. Phys. Chem. B* **1997**, 101, 3903-3905.
7. S. Ohkoshi; K. Hashimoto, Photo-magnetic and magneto-optical effects of functionalized metal polycyanides. *J. Photochem. and Photobio. C: Photochem. Rev.* **2001**, 2, 71-88.
8. Y. Ogawa; S. Koshihara; K. Koshino; T. Ogawa; C. Urano; H. Takagi, Dynamical aspects of the photoinduced phase transition in spin-crossover complexes. *phys. Rev.Lett.* **2000**, 84 (14), 3181-3184.
9. V. Escax; G. Champion; M.-A. Arrio; M. Zacchigna; C. C. dit Moulin; A. Bleuzen, The Co ligand field: A key parameter in photomagnetic CoFe Prussian blue derivatives. *Angew. Chem.* **2005**, 117, 4876-4879.
10. V. Escax; C. C. dit Moulin; F. Villain; G. Champion; J.-P. Itie; P. Munsch; M. Verdaguer; A. Bleuzen, Photo-induced electron transfer in ferrimagnetic Prussian-blue analogues $\text{X}_x^{\text{I}}\text{Co}_4[\text{Fe}(\text{CN})_6]_y$ (X^I=alkali cation). *C. R. Chimie* **2003**, 6, 1165-1173.
11. Escax-Bastet, V. Photomagnétisme dans des analogues cobalt-fer du bleu de Prusse : de l'excitation moléculaire à l'aimantation macroscopique. Université Paris VI, 2002.

12. F. A. Frye; D. M. Pajerowski; N. E. Anderson; J. Long; J.-H. Park; M. W. Meisel; D. R. Talham, Photoinduced magnetism in rubidium cobalt hexacyanoferrate Prussian blue analogue nanoparticles. *Polyhedron* **2007**, *26*, 2273-2275.
13. D. M. Pajerowski; F. A. Frye; D. R. Talham; M. W. Meisel, Size dependence of the photoinduced magnetism and long-range ordering in Prussian blue analogue nanoparticles of rubidium cobalt hexacyanoferrate. *New J. Phys.* **2007**, *9*, 222-232.
14. J.-H. Park; E. Cizmar; M. W. Meisel; Y. D. Huh; F. Frye; S. Lane; D. R. Talham, Anisotropic photoinduced magnetism of a $\text{Rb}_7\text{Co}_k[\text{Fe}(\text{CN})_6]_l \cdot \text{H}_2\text{O}$ thin film. *Appl. Phys. Lett.* **2004**, *85*, 3798-3800.
15. J.-H. Park; Y.D. Huh; Cizmar., E.; S. G. Gamble; D.R. Talham; M. W. Meisel, Photoinduced magnetization in a thin Fe-CN-Co film. *Journal of Magnetism and Magnetic Materials* **2004**, *272*, 1116-1117.
16. A. Goujon; O. Roubeau; F. Varret; A. Dolbecq; A. Bleuzen; M. Verdaguer, Photo-excitation from dia- to ferri-magnetism in a Rb-Co-hexacyanoferrate Prussian blue analogue. *Eur. Phys. J. B* **2000**, *14*, 115-124.
17. W. E. Prout; E. R. Russell; H. J. Groh, Ion exchange absorption of cesium by potassium hexacyanocobalt (II) ferrate (II). *J. Inorg. Nucl. Chem.* **1965**, *27*, 473-479.
18. P. Zhou; F. Xue; S. C. F. Au-Yeung, Potassium hexacyanocobaltate, a redetermination. *Acta Cryst.* **1998**, *54* (12), IUC9800062.
19. C. C. dit Moulin; F. Villain; A. Bleuzen; M.-A. Arrio; P. Sainctavit; C. Lomenech; V. Escax; F. Baudalet; E. Dartyge; J.-J. Gallet; M. Verdaguer, Photoinduced ferrimagnetic systems in Prussian blue analogues $\text{C}_x^l\text{Co}_4[\text{Fe}(\text{CN})_6]_y$ (C^l Alkali Cation). 2. X-ray absorption spectroscopy of the metastable state. *J. Am. Chem. Soc.* **2000**, *122*, 6653-6658.
20. D. C. Koningsberger; R. Prins, *X-ray absorption*. John Wiley & Sons: 1988.
21. M. Presle. Synthèse et propriétés d'hétérostructure moléculaires de type multiferroïque à base d'analogues du bleu de Prusse. PhD dissertation. Ecole Polytechnique, France, 2011.
22. E. Coronado; M. C. Gimenez-Lopez; G. Levchenko; F. M. Romero; V. Garcia-Baonza; A. Milner; M. Paz-Pasternak, Pressure-tuning of magnetism and linkage isomerism in iron(II) hexacyanochromate. *J. Am. Chem. Soc.* **2005**, *127*, 4580-4581.
23. D. Papanikolaou; S. Margadonna; W. Kosaka; S. Ohkoshi; M. Brunelli; K. Prassides, X-ray illumination induced Fe(II) spin crossover in the Prussian blue analogue cesium iron hexacyanochromate. *J. Am. Chem. Soc.* **2006**, *128*, 8358-8363.

24. S. Margadonna; K. Prassides; A. N. Fitch, Large lattice responses in a mixed-valence prussian blue analogue owing to electronic and spin transitions induced by X-ray irradiation. *Angew. Chem. Int. Ed.* **2004**, *43*, 6316–6319.
25. O. Sato; Y. Einaga; A. Fujishima; K. Hashimoto, Photoinduced long-range magnetic ordering of a cobalt-iron cyanide. *Inorg. Chem.* **1999**, *38*, 4405–4412.
26. S. Gawali-Salunke; F. Varret; I. Maurin; C. Enachescu; M. Malarova; K. Boukheddaden; E. Coudjovi; H. Tokoro; S. Ohkoshi; K. Hashimoto, Magnetic and mossbauer investigation of the photomagnetic prussian blue analogue $\text{Na}_{0.32}\text{Co}[\text{Fe}(\text{CN})_6]_{0.74} \cdot 3.4\text{H}_2\text{O}$: Cooperative relaxation of the thermally quenched state. *J. Phys. Chem. B* **2005**, *109*, 8251–8256.
27. A. Bleuzen; V. Escax; J.-P. Itié; P. Münsch; M. Verdaguer, Photomagnetism in $\text{C}_x\text{Co}[\text{Fe}(\text{CN})_6]_{(8+x)/3} \cdot n\text{H}_2\text{O}$ Prussian blue analogues, looking for the maximum efficiency *C. R. Chimie* **2003**, *6*, 343–352.
28. J.-D. Cafun; G. Champion; M.-A. Arrio; C. C. dit Moulin; A. Bleuzen, Photomagnetic CoFe Prussian blue analogues roles of the cyanide ions as active electron transfer bridges modulated by cyanide-alkali metal ion interaction. *J. Am. Chem. Soc.* **2010**, *132*, 11552–11559.
29. *International Tables for X-ray crystallography (vol. IV)*. The Kynoch Press: Birmingham, England, 1974.
30. A. Guinier, *Théorie et technique de la radiocristallographie*. 3ème Edition ed.; Ed. Dunod: Paris, 1964.

Chapter 5

Heterostructures made of $\text{Rb}_x\text{Ni}[\text{Cr}(\text{CN})_6]_y \cdot z\text{H}_2\text{O}$ and $\text{Rb}_x\text{Co}[\text{Fe}(\text{CN})_6]_y \cdot z\text{H}_2\text{O}$

5.1 Introduction

As mentioned in the introduction chapter, various photomagnetic effects have been reported for Prussian blue analogues, such photo-induced dia- to ferrimagnetic transitions¹, magnetic pole inversion² or demagnetization³. These light-induced changes were nevertheless restricted to low temperatures, typically below 30 K. So far, rationalized approaches to the design of single-phase materials that exhibit photomagnetic effects at, or close to, room temperature failed. An alternative approach is to use the concept of strain-mediated magnetic switching developed for oxide-based and metal/polymer multiferroic composites⁴ by combining a magnetostrictive subsystem to a switchable subsystem that undergoes large and reversible striction effects under light irradiation. Exploiting the coupling of elastic origin between these properties should allow the observation of photomagnetic effects at temperatures higher than those reported for single-phase materials. Recent works have shown that Prussian blue analogues are promising candidates for such photostrictive/piezomagnetic heterostructures, with the observation of photomagnetic effects up to 70 K instead of 20 K.^{5,6,7} We shall recall that the high flexibility of the metalocyanide backbone allows for large deformations with virtually no fatigue, *e.g.* up to 3% change in the lattice parameter value for the $\text{Rb}_{0.5}\text{Co}[\text{Fe}(\text{CN})_6]_{0.8} \cdot z\text{H}_2\text{O}$ photostrictive compound (*fcc* lattice, $a = 9.96 \text{ \AA}$ before and $a = 10.27 \text{ \AA}$ after photoexcitation).⁸

Based on the existing knowledge on artificial multiferroics, intimate mixing, large interface/volume ratio and high quality interfaces are crucial to increase the coupling effects. The most relevant configurations found in the literature correspond to a (2-2) connectivity in Newnhan's notation,⁹ such as laminates and layered composites. Epitaxy is not mandatory but usually yields interfaces of higher quality, with low defect concentrations, that will favor an efficient coupling. A controlled chemical composition for the two layers phases with limited, if any, intermixing is mandatory. At last, as the coupling effects are based on the transfer of mechanical stresses, an optimized interface in terms of abruptness and of crystalline orientation of the two layers is also required.

In this chapter, we present preliminary results related to the growth and properties of bilayers made of the ferromagnetic $\text{RbNi}[\text{Cr}(\text{CN})_6]_y \cdot z\text{H}_2\text{O}$ and photostrictive $\text{Rb}_x\text{Co}[\text{Fe}(\text{CN})_6]_y \cdot z\text{H}_2\text{O}$ compounds, as schematized in **Figure 5.1**. We chose to focus on thin layers, typically of 10 nm. The growth was monitored in situ by Fourier transform infrared spectroscopy in ATR mode. The morphology and the structure of the as-obtained heterostructures were investigated by complementary XRR, AFM and XRD measurements.

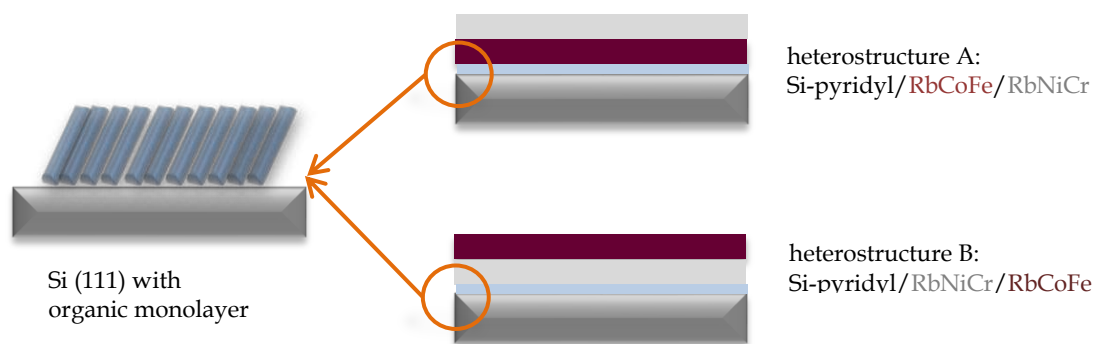


Figure 5.1. Scheme of the two heterostructures: the purple (grey) layer refers to RbCoFe (RbNiCr). Heterostructure A is a sandwich structure with a photo-switchable RbCoFe film in between the Si (111)-pyridyl substrate and the ferromagnetic RbNiCr film; Heterostructure B is a bilayer with the photo-switchable RbCoFe layer on top of the RbNiCr film grown on Si (111)-pyridyl substrate.

5.2 Experimental section

5.2.1 Preparation of the solutions used for deposition

For the RbNiCr and RbCoFe layers, the solutions of reactants were prepared according to the protocols detailed in **section 3.1** of Chapter 3 and in **section 4.1** of Chapter 4, respectively. As we have to prepare two solutions, that are both metastable (due to homogeneous nucleation of RbCoFe and RbNiCr particles), we used ice-water to keep the solutions before film deposition and slow down the formation of particles in solution. As we have observed that RbCoFe nanoparticles in solution impact the film formation (see the SEM images in **Figure A.4.1**), the solution containing the Rb, Co and Fe precursors was systematically prepared at the last moment. Note that for heterostructure B: Si/RbNiCr/RbCoFe, deposition of the RbNiCr layer was carried out directly from the ice-water solution.

5.2.2 Set-up used for film deposition

A set-up was designed for in-situ FT-IR spectroscopy measurements. The scheme of the homemade flow cell is displayed in **Figure 5.2**. An O-ring was placed between the exposed surface and the Teflon cell to avoid liquid leak (approximate volume of the cell: 0.4 mL). For these specific experiments, the silicon wafers used as substrates were shaped as prisms with two opposite sides polished at 45° allowing for measurements in Attenuated Total Reflectance (ATR) geometry. They were subsequently functionalized according to the procedure described in Chapter 2. The whole set-up was then placed in a nitrogen purged chamber for measurements in reflectivity mode. Hereafter, IR absorbance values are normalized per reflection to facilitate comparisons. As only one face of the substrate is exposed to the solution and as the O-ring limits the active surface, the number of effective reflections is reduced to 9.

The two solutions used for deposition were sequentially flowed through the cell. To avoid intermixing of the reactants, a rinsing step (2 mL of water is introduced in the cell and then removed, procedure repeated 5 times) was carried out between the two deposition stages. After deposition of the two layers, the Si substrate was dismantled, thoroughly rinsed with water and dried by a stream of Ar gas.

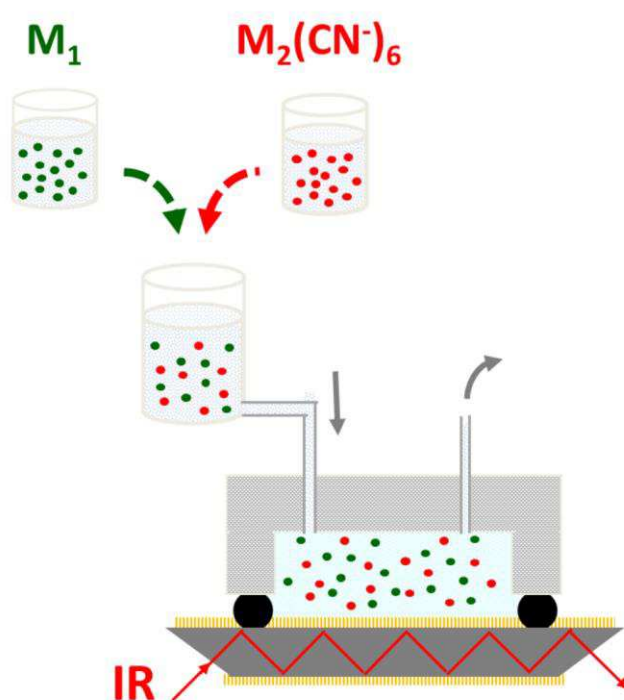


Figure 5.2. Scheme of the cell designed to monitor the film growth by in situ FT-IR in ATR geometry.

5.3 Results and discussion

The growth of the RbNiCr and RbCoFe single layers was firstly monitored by IR spectroscopy measurements. These results are summarized in Appendix.

5.3.1 Heterostructure A: Si (111)/RbCoFe/RbNiCr

5.3.1.1 Growth of heterostructure A monitored by FTIR measurements

The growth of the first RbCoFe layer is similar to the one described in Appendix. The IR spectrum after 15 min deposition is shown in **Figure 5.3**. According to literature, the four peaks located at 2063 cm^{-1} , 2095 cm^{-1} , 2113 cm^{-1} and 2150 cm^{-1} are assigned to the cyanide stretches of non-bridging Fe^{3+} -CN species, Co^{2+} -NC- Fe^{2+} , Co^{3+} -NC- Fe^{2+} and Co^{2+} -NC- Fe^{3+} bridges, respectively.^{7,10,11}

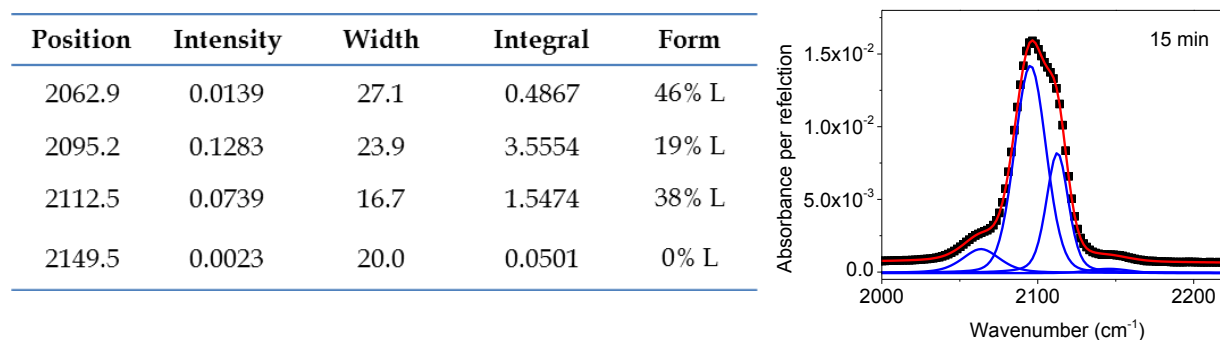


Figure 5.3. In-situ IR spectra in p polarization of the RbCoFe underlayer measured at 15 min deposition time.

After rinsing the surface by flowing water through the cell, the solution containing the RbCl, NiCl_2 and $\text{K}_3\text{Cr}(\text{CN})_6$ precursors was injected. Time zero of the experiment corresponds to the exposure of the Si surface to the new solution. **Figure 5.4** shows the evolution of the IR spectra in the spectral range characteristics of the RbNiCr coordination network. Note that we did not show the νCN contributions relative to the RbCoFe underlayer, as the intensity of the corresponding peaks are much larger than those coming from the RbNiCr layer (large difference of extinction coefficient for $\text{Fe}(\text{CN})_3^-$ and $\text{Cr}(\text{CN})_3^-$ species). Note that only the peak at 2174 cm^{-1} is detectable, as the peak at 2130 cm^{-1} is in the wavenumber range of the cyanide stretches related to the RbCoFe layer. The linear increase of the integral of the peak at 2174 cm^{-1} with deposition time confirms the formation of a RbNiCr lattice, at a constant growth rate.

Position	Intensity	Width	Integral	Form
2062.9	0.0105	25.6	0.3158	22% Lor
2092.8	0.1579	20.9	4.1741	40% Lor
2109.9	0.0980	16.7	1.9097	20% Lor
2146.8	0.0022	13.6	0.0471	100% Lor

Position	Intensity	Width	Integral	Form
2060.8	0.0092	25.6	0.2512	0% Lor
2092.1	0.1619	20.9	4.3259	42% Lor
2109.0	0.0944	16.7	1.8025	16% Lor
2146.0	0.0020	13.6	0.0424	100% Lor
2175.0	0.0009	17.8	0.0170	0% Lor

Position	Intensity	Width	Integral	Form
2059.7	0.0093	25.6	0.2857	26% Lor
2091.7	0.1632	20.9	4.3859	44% Lor
2108.4	0.0924	16.7	1.7519	14% Lor
2146.1	0.0019	13.6	0.0415	100% Lor
2174.8	0.0022	17.8	0.0413	0% Lor

Position	Intensity	Width	Integral	Form
2058.8	0.0093	25.6	0.2822	23% Lor
2091.4	0.1641	20.9	4.4108	44% Lor
2107.9	0.0912	16.7	1.7302	14% Lor
2146.1	0.0018	13.6	0.0391	100% Lor
2174.7	0.0034	17.8	0.0645	0% Lor

Position	Intensity	Width	Integral	Form
2058.2	0.0093	25.6	0.2730	15% Lor
2091.1	0.1645	20.9	4.4189	44% Lor
2107.4	0.0904	16.7	1.7268	16% Lor
2146.0	0.0016	13.6	0.0285	44% Lor
2174.5	0.0047	17.8	0.0896	0% Lor

Position	Intensity	Width	Integral	Form
2058.1	0.0094	25.6	0.2548	0% Lor
2090.9	0.1648	20.9	4.3990	42% Lor
2107.1	0.0898	16.7	1.7240	17% Lor
2146.1	0.0015	13.6	0.0215	0% Lor
2174.3	0.0058	17.8	0.1092	0% Lor

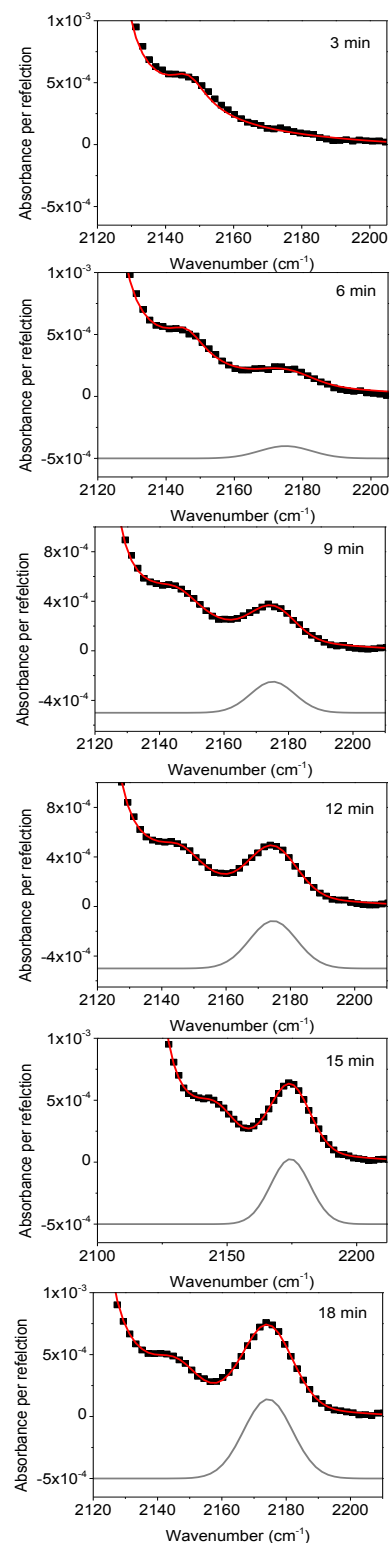


Figure 5.4. In-situ IR spectra in p polarization measured during the growth of the RbNiCr top layer. The black symbols are the experimental data, and the gray lines are fits.

5.3.1.2 Film morphology: XRR and AFM studies

Figure 5.5 shows the X-ray reflectivity curve of the as-obtained heterostructure, up to $q_z = 0.23 \text{ \AA}^{-1}$. Note that the oscillations extend above 0.2 \AA^{-1} , indicating a rather smooth surface. Experimental data were analysed with PARRATT32 software, using a bilayer model similar to the one presented in Chapters 3 and 4 for single layers. Indeed, the small contrast in electronic density between the RbCoFe and RbNiCr compounds makes difficult the discrimination of the two layers. The two-step fitting procedure used for the single layers yields the parameters summarized in **Table 5.1**. The total film thickness, t_{XRR} is 17.6 nm. The electronic density of $3.36 \times 10^{23} \text{ el.cm}^{-3}$ is smaller than the ones found for the single RbCoFe and RbNiCr films. This value may be affected by some porosity of the heterostructure but also by the surface and interface roughness, which systematically tends to decrease the ρ_{Layer} and ρ_{ML} fitted values.

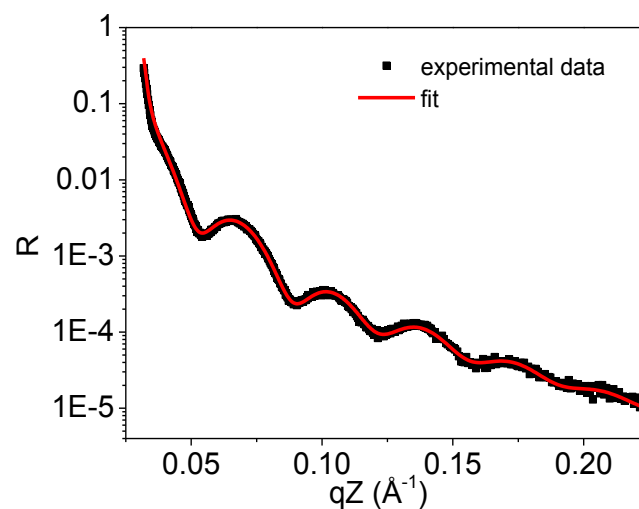


Figure 5.5. X-ray reflectivity curve of heterostructure A: Si(111)/RbCoFe/RbNiCr. Symbols are experimental data. The solid red line is the best fit.

Table 5.1. Fitted parameters for the Si(111)/RbCoFe/RbNiCr bilayer. The input parameters of the pyridyl terminated layer used for fitting are $t_{\text{ML}} = 1.71 \text{ nm}$, $\rho_{\text{ML}} = 4.5 \times 10^{23} \text{ el.cm}^{-3}$ and $\sigma_{\text{ML}} = 0.3 \text{ nm}$ (see Chapter 2). In the last column, the RMS values characterize the roughness determined by AFM.

	t_{XRR} [nm]	ρ [el.cm ⁻³]	σ [nm]	AFM RMS [nm]
Air	N/A	0	N/A	
RbCoFe/RbNiCr	17.6	3.36×10^{23}	2.0	2.2
Pyridyl monolayer	1.1	2.34×10^{23}	0.5	
Bulk	N/A	6.99×10^{23}	0	

A representative AFM image of the as-obtained heterostructure is displayed in **Figure 5.6**, including a line profile. It shows that the RbNiCr top layer has a homogeneous granular morphology, rather similar to the ones observed for single layers of RbNiCr and RbCoFe directly grown on pyridine-terminated Si (111) surfaces. For the top layer, the peak to peak roughness is ca. 2 nm on the scale of observation, which is larger than the one found for single RbNiCr layers (about 1 nm, see **section 3.3.2** in Chapter 3). This might be due to the larger roughness of the RbCoFe underlayer. From the line profile, we can see that the depth of the film is ca. 18 nm, i.e. comparable to the overall thickness of the bilayer derived from XRR (17.6 nm).

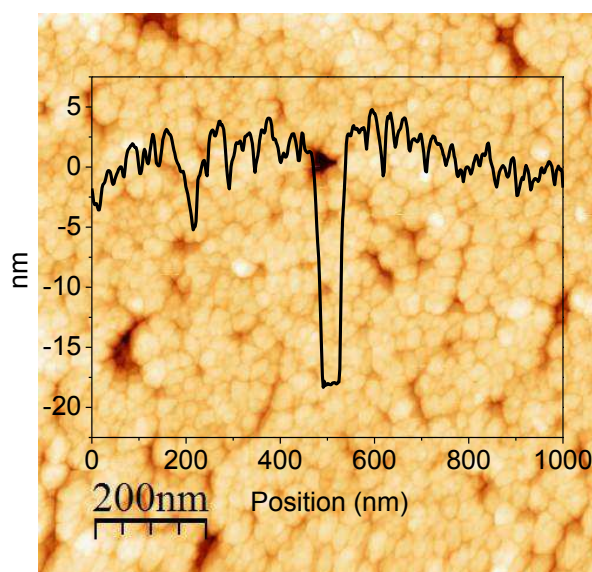


Figure 5.6. AFM image of heterostructure A: Si(111)/RbCoFe/RbNiCr (1000×1000 nm²). In insert is a line profile.

5.3.1.3 Additional microstructural characterization by combined FTIR and RBS spectroscopies

The previous characterizations do not allow for a precise determination of the respective thickness of the two layers. We thus tried to derive additional information from RBS spectroscopy measurements. The RBS spectrum of the Si(111)/RbCoFe/RbNiCr film is shown in **Figure 5.7(a)**. The main difficulty is that the Fe, Co and Ni contributions largely overlap, even for He²⁺ particles of 2.5 MeV energy. The Ni contribution tends to increase the integral of the peak at 1.88 MeV with respect to that of the peak at 1.85 MeV that mostly comes from Fe species.

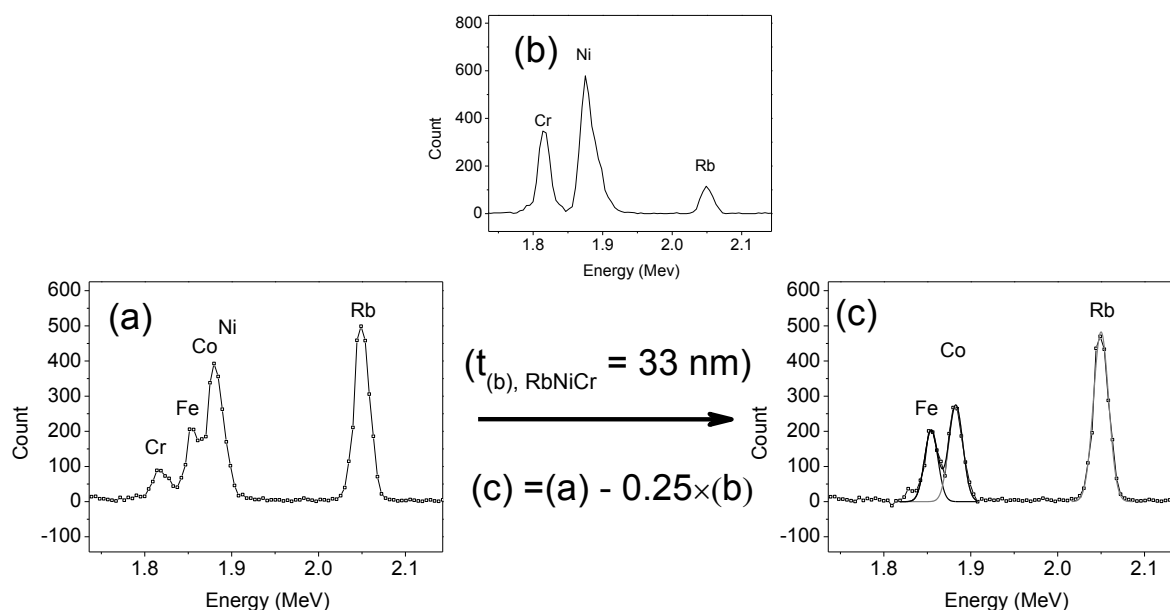


Figure 5.7. RBS spectrum of heterostructure A: Si(111)/RbCoFe/RbNiCr (a) before and (c) after subtraction of RbNiCr contribution. (b) The spectrum of a RbNiCr layer with a known thickness used for subtraction. The Cr, Co, Fe, Ni and Rb peaks are indexed.

To separate these contributions, we subtract from the experimental data (**Figure 5.7(a)**) a certain fraction of the RBS spectrum of a RbNiCr film (0.25 times, **Figure 5.7(b)**) of known thickness, which has been measured under the same condition. By fitting the integral of the residual Fe and Co peaks and by comparison with **Figure 4.9** in Chapter 4 (atom areal density values of Fe and Co as a function of film thickness for single RbCoFe layers), we can derive a thickness of 10 nm for the RbCoFe underlayer. The spectrum of the RbNiCr layer which was used for the subtraction corresponds to a layer with an equivalent thickness 8.3 nm . The small peak in the tail of the Fe contribution in **Figure 5.7(c)** cannot be further removed as a negative peak starts appearing at 1.81 MeV . This semi-quantitative analysis has still a physical meaning as the sum of these two thicknesses, 18.3 nm , is in good agreement with the total film thickness deduced from XRR and AFM.

We tried to cross-check the thickness of the RbNiCr layer from the calibration of the vCN bands by IR spectroscopy. This calibration curve was obtained from the growth of a pure RbNiCr layer on Si (111)-pyridyl surface (see **section A.5.2** in Appendix). We used the vCN at 2174 cm^{-1} , characteristic of the $\text{Ni}^{2+}\text{-NC-Cr}^{3+}$ bridges. Comparison of the integral of this peak in the heterostructure with the calibration curve of **Figure A5.4(b)** shows that the amount of deposit is two thirds of that found for the RbNiCr single layer made with the same deposition time. As the thickness of this later layer is 9.6 nm , we can estimate the RbNiCr thickness in the heterostructure to ca. 6.5 nm . A similar analysis for the IR bands (2090 cm^{-1}) characteristics of the RbCoFe layer leads to a thickness of 11.3 nm .

5.3.1.4 Structural characterization by X-ray diffraction and X-ray absorption spectroscopy

Figure 5.8 presents the $\theta/2\theta$ scans of the Si(111)/RbCoFe/RbNiCr heterostructure compared to the XRD patterns of RbNiCr (bottom panel, $t_{\text{XRR}} = 9.6$ nm) and RbCoFe (top panel, $t_{\text{XRR}} = 15$ nm) layers. As observed for the single layers, only the (002), (004) and (006) Bragg reflections are detected, indicating a texture of the RbNiCr top layer that may be driven by heteroepitaxial growth on the RbCoFe underlayer, as already reported for core-shell nanoparticles of similar composition.¹²

The XRD pattern of the heterostructure shows systematically two peaks for the (001) crystallographic planes. Comparison with the single-phase layers suggests that the low-angle peaks refer to a RbNiCr phase, while the high-angle Bragg reflections must be attributed to the RbCoFe layer (**Figure 5.8(a)**). By deconvolution of the (004) peaks (see **Figure 5.9**), we derive a lattice parameter value $a = 10.43$ Å for the RbNiCr-like layer, which is in very good agreement with the a -values found for pure RbNiCr films (10.45 Å on average).

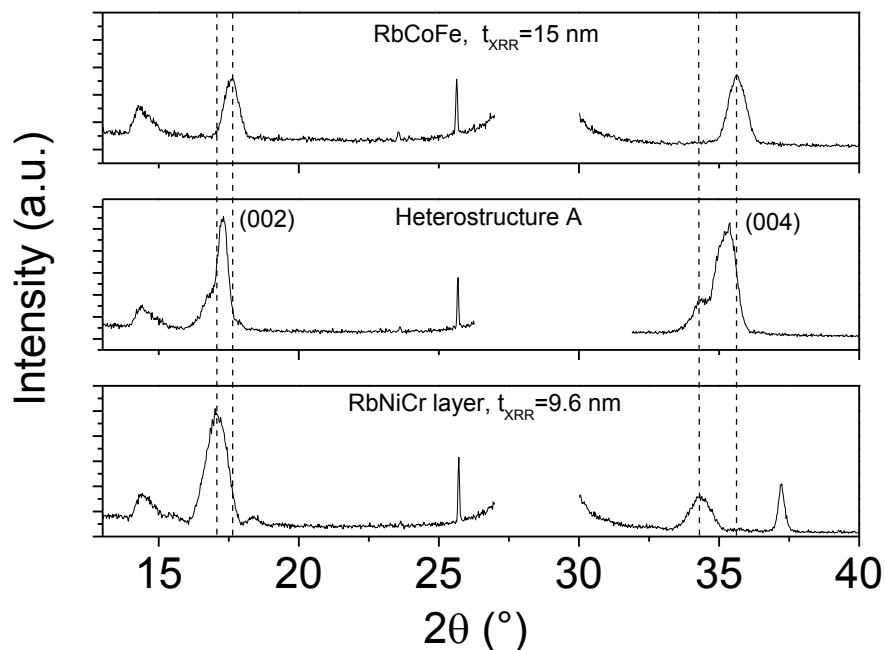


Figure 5.8. θ - 2θ scan of heterostructure A: Si(111)/RbCoFe/RbNiCr, compared to the XRD patterns of a 15 nm thick RbCoFe layer (top panel) and of a 9.6 nm thick RbNiCr layer (bottom panel).

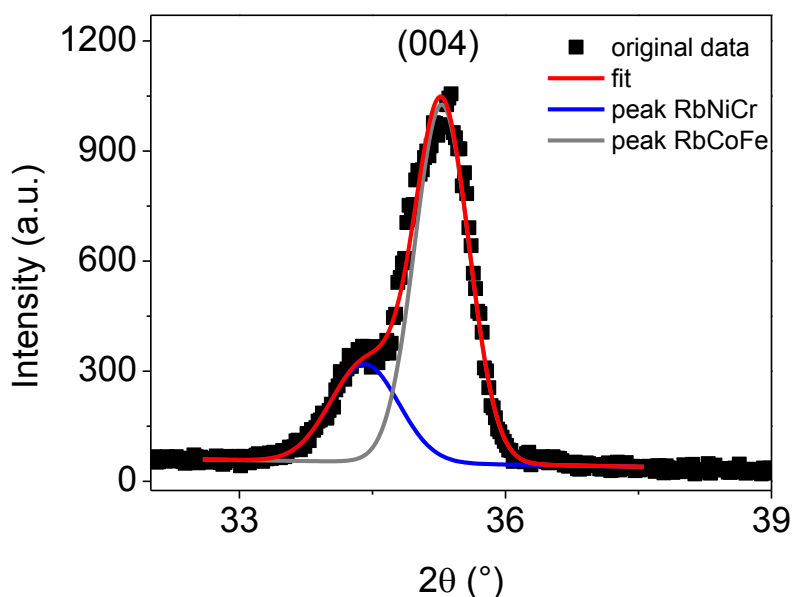


Figure 5.9. Enlarged view of the (004) peaks and deconvolution into two contributions. The black scatters are the original data, the red line is the cumulative fit, and lines in blue and gray are the individual contributions.

In contrast, we observe a significant peak shift for the RbCoFe underlayer, indicative of a lattice expansion. a increases from 10.07 Å in the single layers (**Figure 4.7** in Chapter 4) to 10.18 Å in the heterostructure. Coherence lengths, L_C were also determined from this deconvolution; the as-derived values are about 11 nm for the two RbNiCr and RbCoFe layers. These values are in rather good accordance with the estimations of **section 5.3.1.3**.

Another information is provided by the comparison of the (002) and (004) peaks for the high-angle (RbCoFe-like) contribution. The a -parameter values obtained from Bragg law are rather different: $a = 10.25$ Å for the (002) line and $a = 10.18$ Å for the (004) peak. In addition, the width of the (004) peak is twice that of the (002) peak. This latter peak is particularly narrow, with a Full Width at Half Maximum of the order of 0.36°. Conversion in coherence length using Scherrer formula gives a value of 22 nm, comparable to the total thickness of the heterostructure.

Other proofs of a profound structural modification in the heterostructure, with respect to pure layers, were provided by X-ray Absorption Spectroscopy measurements. In **Figure 5.10(a)**, we compare the XANES spectrum at the Co K-edge of the Si(111)/RbCoFe/RbNiCr film with those of $\text{Co}[\text{Fe}(\text{CN})_6]_{0.67} \cdot 4.6\text{H}_2\text{O}$ and $\text{K}_3\text{Co}(\text{CN})_6$ bulk standards. The figure also shows the spectrum of the Si(111)/RbCoFe film studied in Chapter 4 and grown using the FTIR cell (deposition time of 15 min, $t_{\text{XRR}} = 15$ nm). The striking point is a complete change of the shape of the spectrum after deposition of the RbNiCr layer, which becomes very similar to that of the $\text{Co}[\text{Fe}(\text{CN})_6]_{0.67} \cdot 4.6\text{H}_2\text{O}$ standard characteristics of only Co^{2+} species. Fitting of the XANES spectrum according to the procedure described in Chapter 4 (**section 4.4.1**) yields

a Co^{2+} fraction of $86 \pm 3\%$. The lattice expansion observed from X-ray diffraction measurements has thus to be associated with a change in the valence state of the Co^{2+} ions possibly induced by biaxial stresses with the top layer or interdiffusion. For the heterostructure, we also observe a significant modification of the XANES spectrum at the Fe K-edge that may come from an important distortion of the $[\text{Fe}(\text{CN})_6]$ octahedra. The analysis of these recent measurements is still under way.

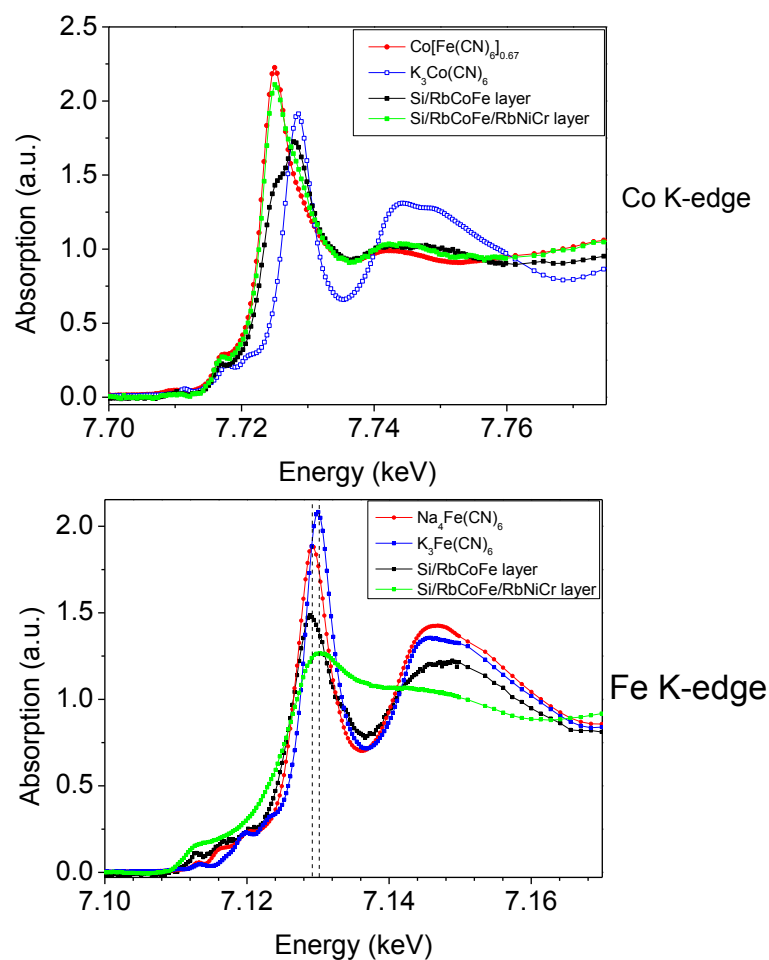


Figure 5.10(a) XANES spectrum at the Co K-edge of the Si (111)/RbCoFe/RbNiCr film recorded at room temperature. Comparison is made with $\text{Co}[\text{Fe}(\text{CN})_6]_{0.67} \cdot 4.6\text{H}_2\text{O}$ (red line) and $\text{K}_3\text{Co}(\text{CN})_6$ (blue line) standards measured at 100 K. The XANES spectrum of a Si (111)/RbCoFe layer is also shown. (b) XANES spectrum at the Fe K-edge of the same heterostructure, comparison with $\text{Na}_4\text{Fe}(\text{CN})_6$ (red line) and $\text{K}_3\text{Fe}(\text{CN})_6$ (blue line) reference compounds measured at 10 K.

All these findings raise the question of a possible interdiffusion between the two layers within the heterostructure. This interdiffusion is difficult to assess from XRD because of peak

overlap as the lattice parameter values for $A_xNi[Fe(CN)_6]_y \cdot zH_2O$ (typically 10.24 \AA)¹³ and $A_xCo[Cr(CN)_6]_y \cdot zH_2O$ (about 10.3 \AA)¹⁴ are close to the one found in $A_xNi[Cr(CN)_6]_y \cdot zH_2O$ series.

5.3.2 Heterostructure B: Si (111)/RbNiCr/RbCoFe

5.3.2.1 Growth of heterostructure B monitored by FTIR measurements

Again, the IR spectra upon growth of the RbNiCr layer on Si (111)-pyridyl surfaces are not displayed for simplification. **Figure 5.11** shows the last spectrum after 18 min deposition. Two characteristic peaks corresponding to the cyanide stretches of Cr^{3+} -CN- Ni^{2+} bridges (2173 cm^{-1}) and surface Cr^{3+} -CN (2130 cm^{-1}) are well-resolved.

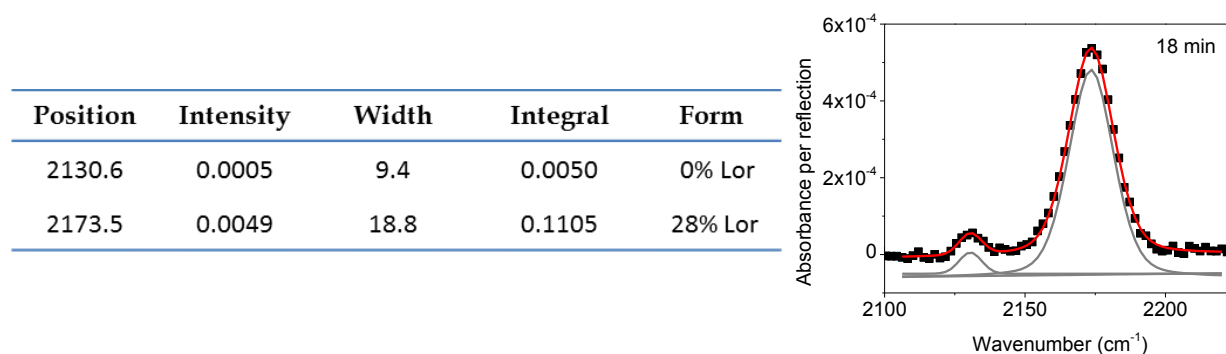


Figure 5.11. In-situ IR spectra in p polarization of the RbNiCr underlayer measured at 15 min deposition time.

After rinsing, the solution containing the $RbNO_3$, $Co(NO_3)_2$ and $K_3Fe(CN)_6$ precursors was injected. Time zero of the experiment corresponds to the exposure of the Si surface to this new solution. **Figure 5.12** shows the evolution of the IR spectra in the spectral range characteristics of the RbCoFe coordination network. After spectral deconvolution, one can note that the intensity of the peak at 2174 cm^{-1} related to Cr^{3+} -CN- Ni^{2+} bridges remains nearly unchanged upon the growth of the RbCoFe overlayer. A broad asymmetric band is also observed in the 2025 - 2200 cm^{-1} range. Its shape is similar to that observed for the RbCoFe film directly grown on Si (111)-pyridyl surfaces (**Figure A5.1**). This broad band was fitted into four peaks, at 2063 cm^{-1} , 2095 cm^{-1} , 2113 cm^{-1} and 2150 cm^{-1} for the cyanide stretches of non-bridging Fe^{3+} -CN species, Co^{2+} -NC- Fe^{2+} , Co^{3+} -NC- Fe^{2+} and Co^{2+} -NC- Fe^{3+} bridges, respectively. The fitted parameters are also displayed in **Figure 5.12**.

Position	Intensity	Width	Integral	Form
2059.2	0.0009	27.3	0.0249	0% Lor
2096.7	0.0056	26.2	0.1559	0% Lor
2109.3	0.0018	19.4	0.0380	0% Lor
2127.3	0.0009	19.2	0.0268	87% Lor
2160.1	0.0009	20.3	0.0205	7% Lor
2174.2	0.0056	17.8	0.1124	13% Lor

Position	Intensity	Width	Integral	Form
2059.9	0.0018	27.3	0.0522	0% Lor
2097.1	0.0180	26.2	0.5462	18% Lor
2110.5	0.0082	19.4	0.1697	0% Lor
2127.7	0.0011	19.2	0.0233	14% Lor
2158.1	0.0016	20.3	0.0411	33% Lor
2174.1	0.0054	17.8	0.1027	0% Lor

Position	Intensity	Width	Integral	Form
2060.7	0.0027	27.3	0.0861	19% Lor
2097.4	0.0310	26.2	0.9358	17% Lor
2111.6	0.0152	19.4	0.3131	0% Lor
2129.7	0.0015	19.2	0.0346	28% Lor
2157.7	0.0024	20.3	0.0562	15% Lor
2174.1	0.0054	17.8	0.1031	0% Lor

Position	Intensity	Width	Integral	Form
2061.2	0.0035	27.3	0.1170	33% Lor
2097.5	0.0408	26.2	1.2317	17% Lor
2112.1	0.0204	19.4	0.4205	0% Lor
2131.6	0.0017	19.2	0.0356	2% Lor
2157.5	0.0029	20.3	0.0635	0% Lor
2174.1	0.0055	17.8	0.1069	4% Lor

Position	Intensity	Width	Integral	Form
2061.4	0.0041	27.3	0.1387	34% Lor
2097.6	0.0497	26.2	1.4988	17% Lor
2112.5	0.0248	19.4	0.5127	0% Lor
2132.1	0.0020	19.2	0.0604	100% Lor
2157.5	0.0034	20.3	0.0838	33% Lor
2174.1	0.0054	17.8	0.1017	0% Lor

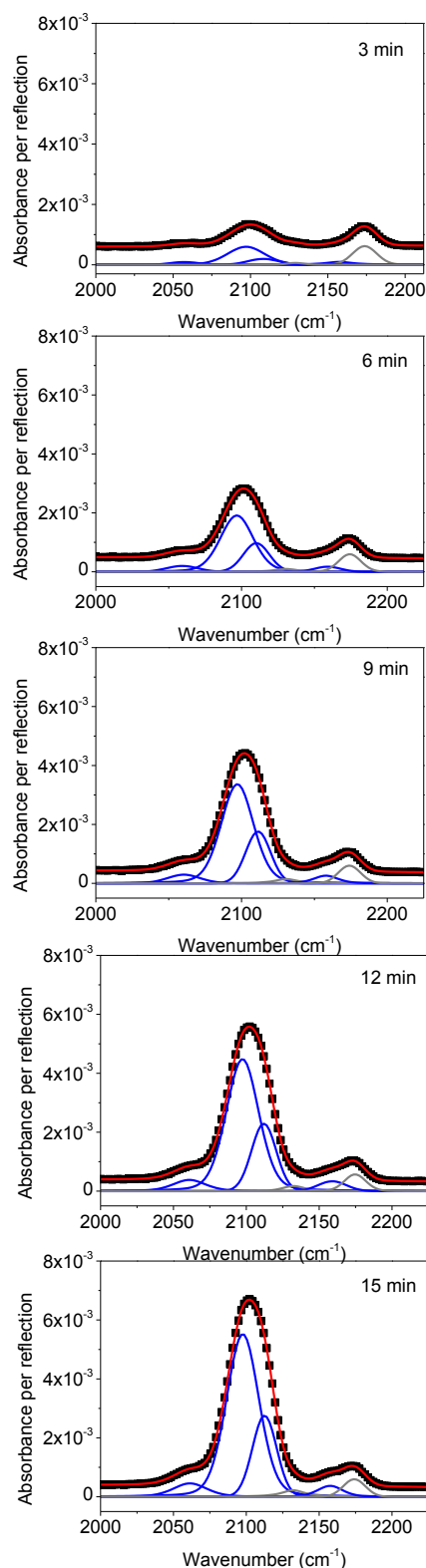


Figure 5.12. In-situ IR spectra in p polarization measured during the growth of the RbCoFe top layer. The black symbols are the experimental data, and the red lines are fits (individual components in blue).

5.3.2.2 Film morphology: XRR and AFM studies

Figure 5.13(a) shows the X-ray reflectivity curve of the as-obtained heterostructure, up to $qz = 0.23 \text{ \AA}^{-1}$. The striking point is the difference with the XRR plot of the reverse heterostructure studied in **section 5.3.1**. (**Figure 5.13(b)**). The frequency of the oscillations is much increased for the Si/RbNiCr/RbCoFe bilayer indicating a smaller thickness while we used identical deposition times for the two heterostructures. Experimental data were analyzed with PARRATT32 software using a bilayer model. The fit yields the parameters summarized in **Table 5.2**. The total film thickness, t_{XRR} is 7.0 nm.

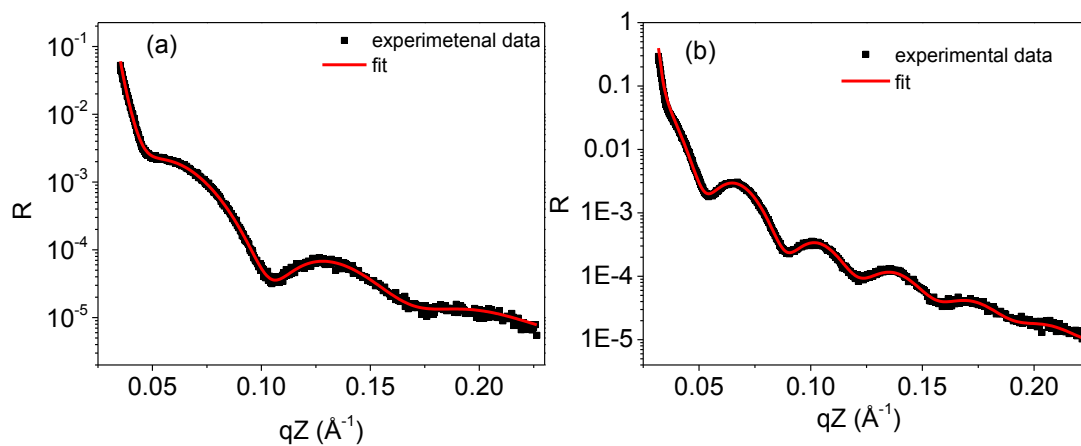


Figure 5.13. X-ray reflectivity curves for (a) heterostructure B: Si(111)/RbNiCr/RbCoFe and (b) heterostructure A: Si(111)/RbCoFe/RbNiCr. Symbols are experimental data. The solid red line is the best fit.

Table 5.2. Fitted parameters for the Si(111)/RbNiCr/RbCoFe bilayer. The input parameters of the pyridyl terminated layer used for fitting are $t_{\text{ML}} = 1.71 \text{ nm}$, $\rho_{\text{ML}} = 4.5 \times 10^{23} \text{ el.cm}^{-3}$ and $\sigma_{\text{ML}} = 0.3 \text{ nm}$ (see Chapter 2). In the last column, the RMS values characterize the roughness determined by AFM.

	t_{XRR} [nm]	ρ [el.cm ⁻³]	σ [nm]	AFM RMS [nm]
Air	N/A	0	N/A	
RbNiCr/RbCoFe	7.0	5.93×10^{23}	1.9	1.6
Pyridyl monolayer	1.3	4.47×10^{23}	0.3	
Si Bulk	N/A	6.99×10^{23}	0	

An AFM image of this heterostructure is shown in **Figure 5.14**, with a line profile in insert. One can observe an underlying granular morphology comparable to those previously reported for single RbNiCr and RbCoFe layers and heterostructure A. The peak to peak roughness from the line profile is ca.2 nm while the RMS analysis indicates a roughness of 1.6 nm. Additional images show that the thickness of this layer is about 6 nm, i.e. comparable to t_{XRR} . However, bigger grains are also present on the surface, with an average lateral size of 45 nm and a height of 14 nm.

Figure 5.15(a) shows a 3D AFM image of heterostructure B Si/RbNiCr/RbCoFe, with a large distribution of grains of maximum height 20 nm on the surface. A comparison is made by a Si/RbNiCr layer with t_{XRR} of 5.2 nm in **Figure 5.15(b)**.

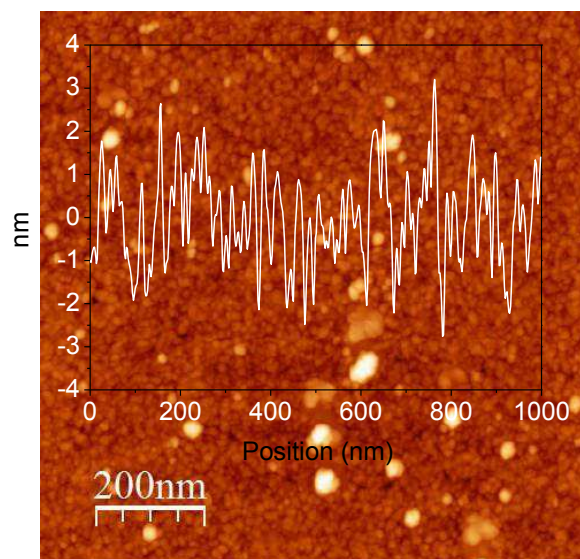


Figure 5.14. AFM image of heterostructure B: Si (111)/RbNiCr/RbCoFe with a line profile in insert. Scale bar: 1000×1000 nm².

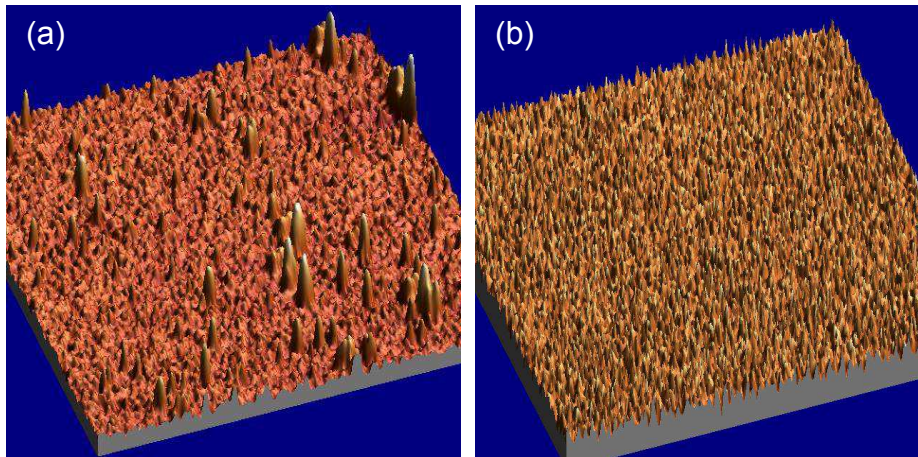


Figure 5.15. 3D AFM image of (a) heterostructure B: Si (111)/RbNiCr/RbCoFe and (b) a Si/RbNiCr layer with $t_{\text{XRR}} = 5.2$ nm. Scale bar: 1000×1000 nm².

5.3.2.3 Additional microstructural information from FTIR spectroscopy

Like in **section 5.3.1.3**, we tried to evaluate the thickness of the RbCoFe and RbNiCr deposits. In the absence of RBS data, we focus on IR spectroscopy measurements. By comparing the integral of the peak at 2174 cm^{-1} (νCN band characteristic of $\text{Ni}^{2+}\text{-NC-Cr}^{3+}$ bridges) with the calibration curve of **Figure A5.4(b)**, we derive an apparent thickness of 5.5 nm. A similar analysis for the peak at 2097 cm^{-1} characteristic of the RbCoFe coordination network leads to an equivalent deposition time of 3 min, i.e. a very small amount of deposit. It is thus likely that the continuous film observed by XRR and AFM corresponds to the RbNiCr underlayer, while the grains on the surface are made of RbCoFe.

5.3.2.4 Structural characterization by X-ray diffraction and X-ray absorption spectroscopy

Figure 5.16 compares the $\theta/2\theta$ scans of the Si(111)/RbNiCr/RbCoFe heterostructure and those of RbNiCr (bottom panel, $t_{\text{XRR}} = 5.2$ nm) and RbCoFe (top panel, $t_{\text{XRR}} = 15$ nm) layers. As observed for the single layers, only the (002), (004) and (006) Bragg reflections are detected and two peaks are systematically observed for each family of crystallographic planes. From their 2θ positions, the low-angle peaks should be assigned to the RbNiCr underlayer, while the high-angle peaks overlap with the ones of the Si/RbCoFe reference sample.

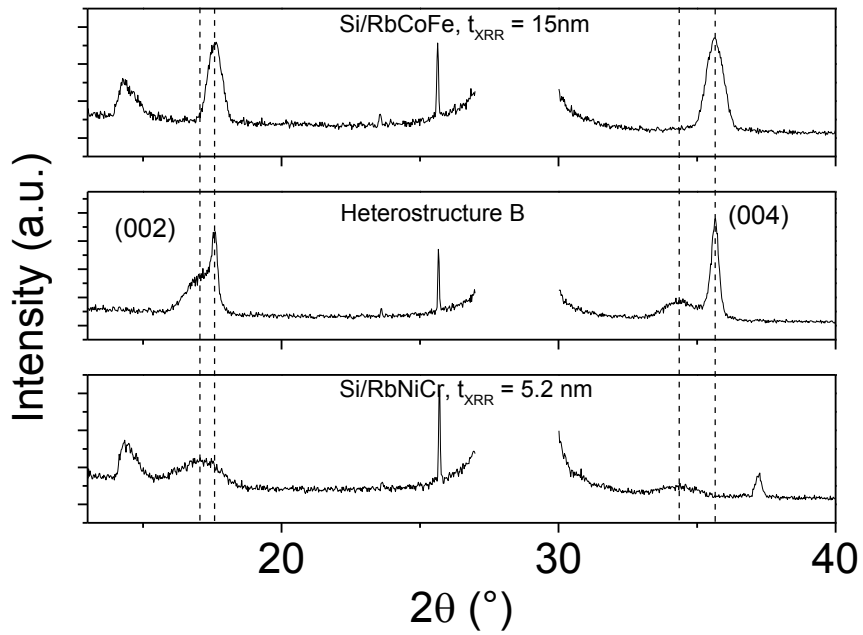


Figure 5.16. θ - 2θ scan of heterostructure B: Si(111)/RbNiCr/RbCoFe, compared to the XRD patterns of a 15 nm thick RbCoFe layer (top panel) and of a 5.2 nm thick RbNiCr layer (bottom panel).

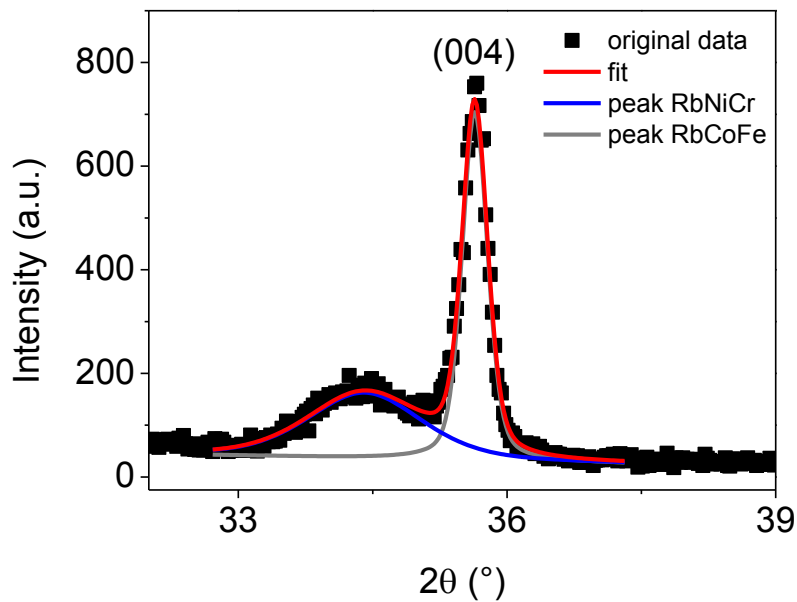


Figure 5.17. Enlarged view of the (004) peaks and deconvolution into two contributions. The black scatters are the original data, the red line is the cumulative fit, and lines in blue and gray are the individual contributions.

From the deconvolution of the (002) and (004) peaks, a mean coherence length of 6.6 ± 0.6 nm was determined for the RbNiCr-like phase (a -parameter 10.43 \AA). This value is comparable to the thickness derived from XRR and AFM, 7 and 6 nm, respectively.

For the RbCoFe-like phase, the mean L_C value is 32 ± 4 nm, i.e. comparable to the maximum height of the big grains present on the surface of the film. The rather good concordance between the a -parameter (10.08 \AA) of the heterostructure and that of the Si/RbCoFe reference layer (10.07 \AA) suggests a similar Co^{2+} fraction. This is confirmed by the XANES measurements at the Co K-edge shown in **Figure 5.18**. However, similarly to heterostructure A, the XANES spectrum at the Fe K-edge is significantly modified in the Si (111)/RbNiCr/RbCoFe bilayer suggesting a distortion of the $[\text{Fe}(\text{CN})_6]$ entities.

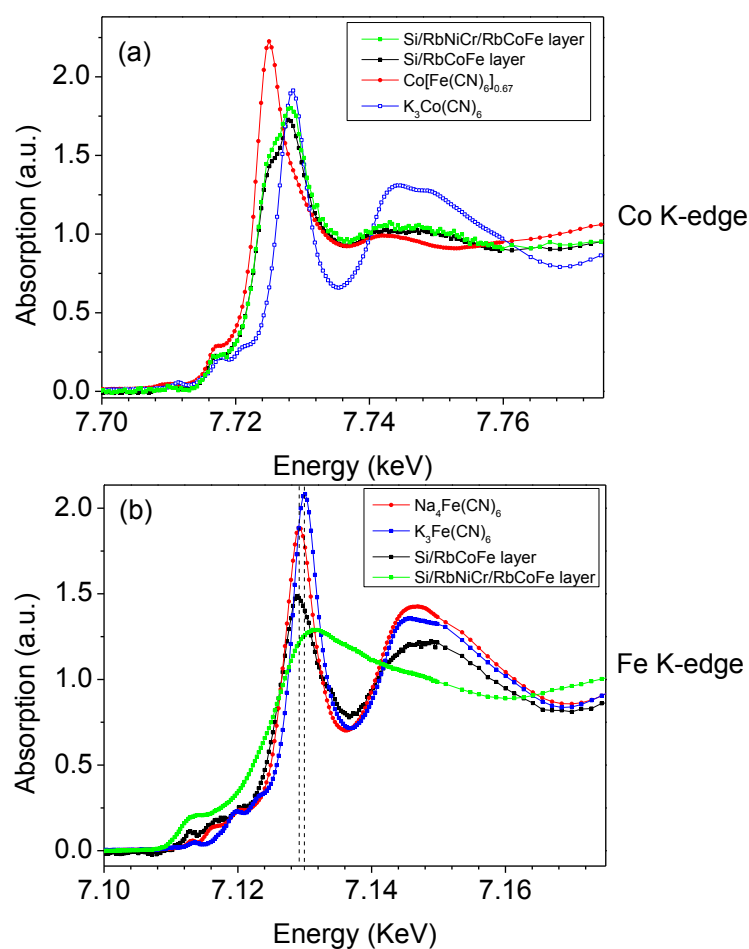


Figure 5.18. XANES spectrum at the Co K-edge of the Si (111)/RbNiCr/RbCoFe film recorded at room temperature. Comparison is made with $\text{Co}[\text{Fe}(\text{CN})_6]_{0.67} \cdot 4.6\text{H}_2\text{O}$ (red line) and $\text{K}_3\text{Co}(\text{CN})_6$ (blue line) standards measured at 100 K. The XANES spectrum of a Si (111)/RbCoFe layer is also shown. (b) XANES spectrum at the Fe K-edge of the same

heterostructure, comparison with $\text{Na}_4\text{Fe}(\text{CN})_6$ (red line) and $\text{K}_3\text{Fe}(\text{CN})_6$ (blue line) reference compounds measured at 10 K.

As 7 nm thick RbNiCr films are not continuous (see **Chapter 3, section 3.4.2**), one possibility is that the RbCoFe grains directly grew on the Si (111) surface, in the voids of the RbNiCr layer. Indeed, the sum of the apparent height of the RbCoFe grains determined by AFM and the RbNiCr thickness is in good agreement with the vertical coherence length of the RbCoFe phase derived from XRD.

5.4 Conclusion

These preliminary results raises the difficulty in growing bilayer heterostructures combining the $\text{RbNi}[\text{Cr}(\text{CN})_6]_y \cdot z\text{H}_2\text{O}$ and $\text{Rb}_x\text{Co}[\text{Fe}(\text{CN})_6]_y \cdot z\text{H}_2\text{O}$ compounds. Starting from a $\text{Rb}_x\text{Co}[\text{Fe}(\text{CN})_6]_y \cdot z\text{H}_2\text{O}$ underlayer, the growth of a $\text{RbNi}[\text{Cr}(\text{CN})_6]_y \cdot z\text{H}_2\text{O}$ top layer leads to a probable intermixing that may be driven by interdiffusion or by some solubility of the $\text{RbNi}[\text{Cr}(\text{CN})_6]_y \cdot z\text{H}_2\text{O}$ and $\text{Rb}_x\text{Co}[\text{Fe}(\text{CN})_6]_y \cdot z\text{H}_2\text{O}$ phases. Note however that heterostructures based on core-shell nanoparticles associating RbCoFe and RbNiCr were shown to be stable at the time scale of more than one year.¹⁵ In the case of the reverse configuration, i.e. Si (111)/RbNiCr/RbCoFe, we have observed that the RbCoFe grains preferentially nucleate on the Si (111) surface with pyridyl termination in the case of discontinuous RbNiCr underlayer.

5.5 References

1. O. Sato; T. Iyoda; A. Fujishima; Hashimoto, K., Photoinduced magnetization of a cobalt-iron cyanide. *Science* **1996**, 272, 704-705.
2. S. Ohkoshi; S. Yorozu; O. Sato; T. Iyoda; A. Fujishima; K. Hashimoto, Photoinduced magnetic pole inversion in a ferro-ferrimagnet: $(\text{Fe}_{0.40}\text{Mn}_{0.60})_{1.5}\text{Cr}^{\text{III}}(\text{CN})_6$. *Appl. Phys. Lett.* **1997**, 70, 1040-1042.
3. H. Tokoro; S. Ohkoshi; K. Hashimoto, One-shot-laser-pulse-induced demagnetization in rubidium manganese hexacyanoferrate. *Appl. Phys. Lett.* **2003**, 82 (8), 1245-1247.
4. G. Srinivasan, Magnetoelectric composites. *Annu. Rev. Mater. Res.* **2010**, 40, 153-178.
5. D. M. Pajerowski; J. E. Gardner; E. S. Knowles; M. W. Meisel; D. R. Talham, Photoinduced magnetism in a series of Prussian blue analogue heterostructures. *Chem. Mater.* **2011**, 23, 3045-3053.
6. D. M. Pajerowski; M. J. Andrus; J. E. Gardner; E. S. Knowles; M. W. Meisel; D. R. Talham, Persistent photoinduced magnetism in heterostructures of Prussian blue analogues. *J. Am. Chem. Soc.* **2010**, 132, 4058-4059.
7. M. F. Dumont; E. S. Knowles; A. Guet; D. M. Pajerowski; A. Gomez; S. W. Kycia; M. W. Meisel; D. R. Talham, Photoinduced magnetism in core/shell Prussian blue analogue heterostructures of $\text{K}_j\text{Ni}_k[\text{Cr}(\text{CN})_6]_{l.n}\text{H}_2\text{O}$ with $\text{Rb}_a\text{Co}_b[\text{Fe}(\text{CN})_6]_c.m\text{H}_2\text{O}$. *Inorg. Chem.* **2011**, 50, 4295-4300.
8. V. Escax; A. Bleuzen; J. P. Itie; P. Munsch; F. Varret; M. Verdagner, Nature of the long-range structural changes induced by the molecular photoexcitation and by the relaxation in the Prussian blue analogue $\text{Rb}_{1.8}\text{Co}_4[\text{Fe}(\text{CN})_6]_{3.3}, 13\text{H}_2\text{O}$. A synchrotron X-ray diffraction study. *J. Phys. Chem. B* **2003**, 107, 4763-4767.
9. R. E. Newnham; D. P. Skinner; L. E. Cross, Connectivity and piezoelectric-pyroelectric composites. *Materials Research Bulletin* **1978**, 13 (5), 525-536.
10. D. M. Pajerowski; T. Yamamoto; Y. Einaga, Photomagnetic $\text{K}_{0.25}\text{Ni}_{1-x}\text{Co}_x[\text{Fe}(\text{CN})_6]_n\text{H}_2\text{O}$ and $\text{K}_{0.25}\text{Co}[\text{Fe}(\text{CN})_6]_{0.75y}[\text{Cr}(\text{CN})_6]_{0.75(1-y)}_n\text{H}_2\text{O}$ Prussian blue analogue solid solutions. *Inorg. Chem.* **2012**, 51, 3648-3655.
11. D. M. Pajerowski; J. E. Gardner; D. R. Talham; M. W. Meisel, Anisotropic magnetism in Prussian blue analogue films. *New J. Chem.* **2011**, 35, 1320-1326.
12. M. Presle; I. Maurin; F. Maroun; R. Cortès; L. Lu; R. Sayed Hassan; E. Larquet; J.-M. Guigner; E. Rivière; J. P. Wright; J.-P. Boilot; T. Gacoin, Photosrictive/piezomagnetic core-

shell particles based on Prussian blue analogues: evidence for confinement effects? *J. Phys. Chem. C* **2014**, *118*, 13186–13195.

13. A. Kumar; S. M. Yusuf; L. Keller; J. V. Yakhmi; J. K. Srivastava; P. L. Paulose, Variation of structural and magnetic properties with composition in the $(\text{Co}_x\text{Ni}_{1-x})_{1.5}[\text{Fe}(\text{CN})_6] \cdot z\text{H}_2\text{O}$ series. *Phys. Rev. B* **2007**, *75*, 224419-224429.

14. P. Bhatt; S. M. Yusuf; R. Bhatt; G. Schutz, Magnetic properties of nanoparticles of Prussian blue-based molecular magnets $\text{M}_3[\text{Cr}(\text{CN})_6]_2 \cdot z\text{H}_2\text{O}$ (M=Fe, Co, and Ni). *Appl. Phys. A* **2012**, *109* (2), 459-469.

15. M. Presle. Synthèse et propriétés d'hétérostructure moléculaires de type multiferroïque à base d'analogues du bleu de Prusse. PhD dissertation. Ecole Polytechnique, France, 2011.

General Summary and Conclusion

There were three main motivations to this work; the first one was to study the growth mechanism of Prussian blue analogue thin films, with a largely improved quality in terms of morphology and structure. The second target was to study the properties of layers made of two specific Prussian blue analogues, namely ferromagnetic rubidium nickel hexacyanochromates (RbNiCr) and photo-switchable rubidium cobalt hexacyanoferrates (RbCoFe). These investigations implied correlating the chemical composition, the microstructure and some physical properties, including a thorough analysis of the magnetic anisotropy of RbNiCr films and a comparative study of the photo-switching properties of RbCoFe layer and powder samples. Finally, the third motivation was the controlled growth of heterostructures combining RbCoFe and RbNiCr layers with thicknesses down to 10 nm, which is a key step to the investigation of interface effects.

Chapter 2 illustrates the protocol used for the functionalization of Si (111) surfaces by organic monolayers bearing a pyridyl termination favorable to the growth of Prussian blue analogue layers. Special care was taken to establish the morphology and the structure of the organic monolayers on the Si (111) surface by both experimental methods including X-ray reflectivity and Atomic Force Microscopy, and by molecular modeling. Qualitative and quantitative characterization of the surface termination after each functionalization step was performed by FTIR spectroscopy. These studies indicated that the obtained Si-pyridyl surfaces are well defined and good candidates for Prussian blue analogue deposition because of their capability to a robust linkage with the film through a coordination binding.

The growth of ultra-thin films of rubidium nickel hexacyanochromate is discussed in Chapter 3. RbNiCr films were prepared by immersing the functionalized Si-pyridyl surface in a solution containing all the precursors of the solid phase, at reduced concentration to favor heterogeneous nucleation and limit the formation of RbNiCr particles in solution. This method allows a good control of the film growth in terms of morphology and crystal structure, as all the obtained RbNiCr films are homogeneous, with very small surface roughness, and exclusively textured along [001] direction. In addition, the layers have an identical composition through the whole thickness depth. We put lots of efforts on studying the growth mechanism by cross-relating different techniques and establish that the film was initially made of discontinuous platelet-like grains, which further grow vertically and

laterally until coalescence. All studied films showed a thickness dependence of their magnetic properties, in particular their magnetic ordering temperature which decreases with decreasing the film thickness while the saturation magnetization remains unchanged. Attention was paid to understand the shape of the FC curves at low temperature, which are indicative of a grain size polydispersity and consistent with the proposed growth model. All films showed a magnetic anisotropy, with an easy axis which is neither strictly in plane nor out of plane, but lies in a direction close to the surface normal. The underlying source of anisotropy in RbNiCr films probably has multiple origins, including magnetocrystalline, shape and interface effects.

Chapter 4 described the preparation of RbCoFe thin films using the same method. These films showed a morphology similar to that of RbNiCr films, i.e., homogeneous and flat with a granular structure. All the RbCoFe layers showed a texture along the (00l) direction, but a non uniform crystallization state. The growth mode of the RbCoFe films is similar to that found for the RbNiCr films, but with a much larger initial growth rate, which leads to the formation of cubic instead of platelet-like domains at the beginning of the growth. The overall chemical composition and Fe and Co valence states were quantitatively derived from combined Rutherford Backscattering and X-ray absorption spectroscopies (RBS/XAS). Their photoswitching properties were tentatively assessed by XAS experiments. The yield of photo-excitation was found to be smaller than that of a reference powder sample. This latter result may be explained by a larger insertion of Rb alkali ions and a hypothetical incorporation of NO_3^- ions, that impedes the photo-switching properties due to a reduced structural flexibility and/or a change in the Co ligand field strength. The reason of the higher initial growth rate of RbCoFe films compared with RbNiCr films is not clear yet, future work is required by focusing on the shorter time scale, as well as exchanging the transition metal ions to build coordination networks such as Ni-NC-Fe and Co-NC-Cr using the same methodology, in order to establish which are the main driving factors at the initial stage of growth.

Based on the previous results, a preliminary study of heterostructure composed of $\text{Rb}_x\text{Ni}[\text{Cr}(\text{CN})_6]_y \cdot z\text{H}_2\text{O}$ and $\text{Rb}_x\text{Co}[\text{Fe}(\text{CN})_6]_y \cdot z\text{H}_2\text{O}$ layers with different configurations is presented in Chapter 5. The growth has been monitored by *in situ* FTIR measurements through the evolution of the cyanide stretching modes characteristics of different linkages in the RbCoFe and RbNiCr compounds. The first study was carried out for on an architecture, starting from a $\text{Rb}_x\text{Co}[\text{Fe}(\text{CN})_6]_y \cdot z\text{H}_2\text{O}$ underlayer; the growth of a $\text{RbNi}[\text{Cr}(\text{CN})_6]_y \cdot z\text{H}_2\text{O}$ top layer leads to a probable interdiffusion with the bottom layer. However, quantification of the intermixing is difficult because of the similarity of the different crystal structures. For the Si (111)/RbNiCr/RbCoFe heterostructure, results come out to be that RbCoFe grains

preferentially nucleate on the Si (111) surface with pyridyl termination in the case of discontinuous RbNiCr underlayer. Nevertheless, some results are still in process of being understood and further study on this direction is full of interests.

To conclude, this dissertation has provided a novel method to deposit thin layers of Prussian blue analogues and heterostructures made of bilayers, establish their growth mechanism and explain their physical properties.

Appendix 1

Experiments and techniques

A.1.1 Structural and microstructural characterizations

A.1.1.1 Atomic force microscopy (AFM)

The morphology of the films was investigated using a Pico SPM microscope (Molecular Imaging, Phoenix, AZ) equipped with silicon nitride cantilevers (Nanoprobe, spring constant of 0.2 Nm^{-1}). Images were recorded in contact mode under a protected N_2 atmosphere.

RMS roughness was evaluated using WSxM 5.0 develop 5.3 software¹ from Nanotec Electronics S.L. The lateral size of the grains on the film surface was determined using the surface analyzing software (SPIP™; Image Metrology A/S). One example is given in **Figure A1.1**. Note that it is not easy to separate all of the grain by automatic procedures. Some manual splitting has to be done. By varying the parameters, we observed that the best ones for imaging analysis are: smoothing filter size: 25 Pixels; number of detail level: 1; slope noise reduction: 20%.

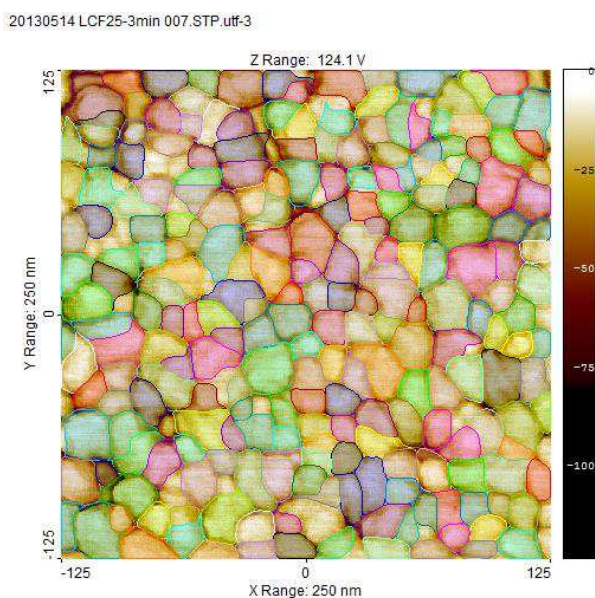


Figure A1.1. Lateral size and grain density determined from the SPIP software for a RbCoFe film with 3 min deposition time. Image scale: $250 \text{ nm} \times 250 \text{ nm}$.

A.1.1.2 Scanning Electron Microscopy (SEM)

Microstructural characterizations were also carried out by scanning electron microscopy (SEM) using a Hitachi S4800 microscope equipped with a field emission gun. Plane view and cross section images were recorded using secondary electrons and an acceleration voltage of 3.0 kV.

A.1.1.3 X-ray reflectivity (XRR)

A.1.1.3.1 General method

For X-rays, all materials have a refraction index slightly below 1: $n = 1 - \delta - i\beta$, so total external reflectance occurs when the incident angle θ (angle between the sample surface and the X-ray incident beam) is extremely small, below a critical angle $\theta_c = \sqrt{2\delta}$. Above θ_c , the intensity falls off rapidly as θ^{-4} . If there is a deposit on the substrate, the intensity is modulated by oscillations, the so-called Kiessig fringes. These fringes result from constructive and destructive interferences between the x-ray beams reflected by the two interfaces (air/film and film/substrate). The oscillation period is solely determined by the thickness of the layer. Kiessig fringes are also sensitive to the quality of the two interfaces, in particular to their roughness. Typically when the surface roughness is more than 10 Å, the interferences produced by the reflections at the different interfaces will be poorly defined, leading to a decreased amplitude of the reflectivity signal and to a damping of the oscillations.

The XRR data were recorded using a 4-circle diffractometer equipped with $\text{CuK}_{\alpha 1}$ radiation ($\lambda = 0.15406$ nm). Data were collected with an acquisition time per step which was increasing with the θ angle. In order to improve the signal-to-noise ratio at high θ angles, up to 5 scans were averaged and/or scans over different θ ranges were merged. At last, to obtain the reflectivity signal R_{exp} , the reflected flux of photons y was divided by the nominal X-ray flux y_0 which corresponds to the direct incident beam without sample: $R_{exp} = y / y_0$. R_{exp} was then expressed as a function of $q_z = 4\pi\sin\theta / \lambda$.

A.1.1.3.2. XRR data analysis

The data were analysed with the PARRAT32 software.³ First of all, the electronic density ρ expressed in units of electrons per Å³ needs to be converted into PARRAT units used by the software:

$$\rho_{PARRATT} = \frac{2\pi}{\lambda^2} \delta = r_e \times \rho \quad \text{Eq. A1.1}$$

where $\rho = Z/a^3$ in the case of a cubic crystal of lattice parameter a , with Z the total number of electrons in the unit cell. r_e is the classical radius of the electron (2.818×10^{-5} Å). ρ_{parratt} values are thus expressed in unit of Å⁻².

The XRR data were analysed using “independent model layers”. The fit of parameters is done by minimization of χ^2 which is

$$\chi^2 = \frac{1}{n} \sum_n \left(\frac{R_{\text{exp}} - R_{\text{cal}}}{w} \right)^2 \quad \text{Eq. A1.2}$$

over all the n data points. R_{exp} is the measured reflectance and R_{cal} the reflectance calculated from the model. w is a weighting factor, $w = 1 / (y + A)$ where y is the number of measured photons/s and A is a constant equals to 1 or 2. This weighting minimizes the influence of very low counts at large θ angles.

Note that it is not possible to fit the imaginary part β of the index n (due to absorption) because the reflectivity is not very sensitive to absorption in the range of θ used. In the following we fixed the value of the imaginary part to the theoretical value calculated from the International Tables of Crystallography.⁴

For the functionalization layer, the model includes a semi-infinite substrate of Si and an organic monolayer. The parameters used for the Si substrate are $\rho = 1.971 \times 10^{-5}$ in PARRATT unit and a roughness (σ) of 0 Å. These two parameters were fixed during the refinements. Note that the value of σ does not changes the final results when $\sigma < 3$ Å.

For the Si/RbCoFe, Si/RbNiCr layers and their heterostructures, a two-layer model was used and the XRR data were fitted in two steps: (1) the organic monolayer parameters (ρ_{ML} , t_{ML} and σ_{ML}) were kept equal to $t_{\text{ML}} = 1.71$ nm, $\rho_{\text{ML}} = 4.5 \times 10^{23}$ el.cm⁻³ and $\sigma_{\text{ML}} = 0.3$ nm. In a second stage (2), these parameters were let free to vary. This procedure is justified by the fact that the XRR signal is dominated by RbNiCr or RbCoFe layer and if one lets all parameters free at the same time, a local minimum of χ^2 is found with unrealistic parameter values for the organic film. It is worth noting that this fitting process works better only if the initial input data are very close to the real values.

A.1.1.4 X-ray diffraction (XRD)

X-ray powder diffraction (XRPD) patterns were recorded in Bragg-Brentano geometry using a PANalytical X'Pert diffractometer equipped with Cu K α radiation ($\lambda = 0.15418$ nm) and a rear-side (0002) graphite monochromator. The instrumental resolution function was evaluated using a silicon powder (Strem Chemicals, 2N⁺, 325 mesh).

Peak positions were extracted using the Fit subroutine of the Fullprof suite of programs.⁵ The structural coherence length, L_C was evaluated through Pseudo-Voigt peak profile analysis. L_C was calculated using a modified Scherrer formula as below:

$$L_C = \frac{0.9 \times \lambda}{\cos \theta \sqrt{(FWHM)^2 - 0.08^2} \times \pi / 180} \quad \text{Eq. A1.3}$$

where λ denotes the x-ray wavelength, θ is the Bragg angle, 0.08° represents the instrumental resolution and FWHM (expressed in degree) is the full width of half maximum of the Bragg peak. Note that the previous approximation stands for Gaussian lineshapes. For Lorentzian lineshapes, we should use:

$$L_C = \frac{0.9 \times \lambda}{\cos \theta (FWHM - 0.08) \times \pi / 180} \quad \text{Eq. A1.4}$$

However, by applying Eq. A1.4, we systematically found L_C values that were larger than the physical film thickness determined by X-ray reflectivity.

The interplanar distance d was calculated according to Bragg's law:

$$2d \sin \theta = n\lambda \quad \text{Eq. A1.5}$$

Based on the face centered cubic structure of the Prussian blue analogues, the lattice parameter (a) was calculated as:

$$a = d \sqrt{h^2 + k^2 + l^2} \quad \text{Eq. A1.6}$$

for a given (hkl) peak.

A.1.2 FTIR Spectroscopy

A.1.2.1 General method

The Fourier Transform Infrared (FT-IR) spectra were recorded at room temperature using a Bruker (Equinox5) spectrometer in Attenuated Total Reflectance (ATR) geometry. The functionalized Si (111) surface was mounted in a homemade flow cell for the *in situ* monitoring of the film growth. The cell was placed in a nitrogen purged chamber. A typical sample is a Si prism of 12 mm height and 14 mm width bevels on the two opposite sides with 44 to 46° angle with respect to the surface plane. These prisms give rise to ~26 internal reflections (13 per each surface). For the *in-situ* monitoring of the film growth only one side of the Si prism was in contact with the solution. The active area was limited by a viton O-ring of diameter 10 mm. In that case, the number of "useful" reflections was restricted to 9.

A.1.2.2 Fitting procedure

The OPUS 4.2 software was used for the spectral deconvolution of the $\nu\text{C}\equiv\text{N}$ bands.

This procedure is justified by the fact that the $\nu\text{C}\equiv\text{N}$ peak of RbCoFe film has four contributions which overlap, the fitting is dominated by the two main peaks which will be already affect each other, if one let all parameters free at the same time, a local minimum of χ^2 is found with unrealistic parameter values for the slight change in positions and intensity.

Different fitting procedures were performed, and we show two examples in **Figure A1.2**, with RbCoFe films corresponding to 3 min (top panel) and 12 min (bottom panel) deposition. Red lines represent the fitting by fixing the peak positions, blue lines show the fitting by fixing the peak width, and green lines are the fitting curves by letting all parameter free. We observed a larger discrepancy among the different fittings in the thin film than in the thicker one. The red lines show the poorest agreement with the experimental data, and the width of individual peaks are far too large (normally the width should not be more than 30 cm^{-1}), indicate that fixing the peak position is not appropriate and that the peak positions indeed shift upon film growth. The blue lines and green lines are rather similar and both fit well to the original data. Considering the correlations among the parameters, it is reasonable to fix the width of the peaks and to check more precisely the shift of peak positions.

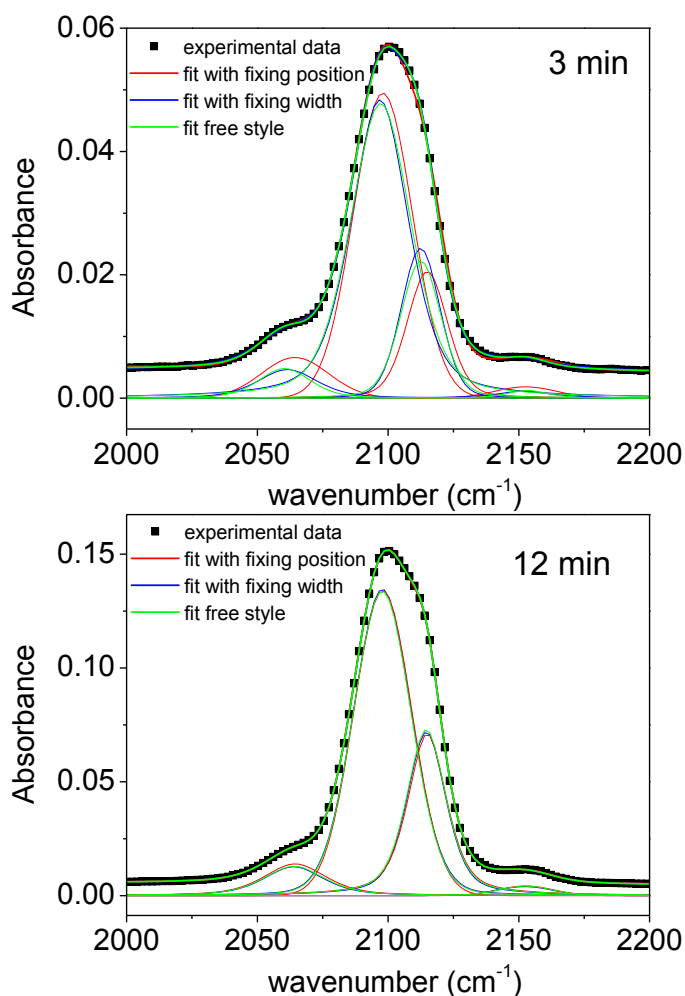


Figure A1.2. Spectral deconvolution of $\nu\text{C}\equiv\text{N}$ bands using different methods: fixing the peak position (red line), fixing the peak width (blue line) and letting free all parameters (green line). The top spectrum is the spectrum of a RbCoFe film after 3 min deposition, bottom spectrum after 12 min deposition.

The procedure we have used is the following: (1) the spectrum of the thicker film has been fitted by letting all the parameters free. (2) The width of each peak inferred from step (1) was then used as fixed parameters for the fitting of the spectra of other films.

A.1.3 Rutherford Backscattering Spectroscopy

A.1.3.1 General method

Rutherford backscattering spectroscopy is an analytical technique often used as a tool to detect heavy elements and probe their depth distribution in single and multi-layers⁶. In the present case, alpha particles (He^{2+}) were projected onto a film, and they were then backscattered and detected by a solid state detector, which discriminates the particles according to their energy. Indeed, the energy of the backscattered particles is sensitive to the mass of the scattering nucleus and also to its depth profile.

RBS measurements were performed at the SAFIR (Système d'Analyse par Faisceaux d'ions rapides) platform, at Université Pierre et Marie Curie (Paris), in collaboration with Emrick Briand and Ian Vickridge. Films were bombarded with 1.5 MeV He^{2+} ions beam. The beam probing area is about 1 mm². Additional RBS measurements were performed at Université de Namur, Belgium, with 2.5 MeV He^{2+} ion beam.

A.1.3.2 Calibration of the energy-channel curve⁷

The energy E_1 of a backscattered projectile with incident energy E_0 (1.5 MeV) and mass M_1 (He^{4+} , 4 g/mol) after scattering is given in the laboratory system by

$$E_1 = KE_0 \quad \text{Eq. A1.7}$$

where the kinematic factor K is given by

$$K = \frac{M_1^2}{(M_1 + M_2)^2} \left\{ \cos \theta \pm \left[\left(\frac{M_2}{M_1} \right)^2 - (\sin \theta)^2 \right]^{1/2} \right\}^2 \quad \text{Eq. A1.8}$$

where θ (165° in our case) is the scattering angle and M_2 the mass of the target nucleus initially at rest.

For instance, under the configuration used on the SAFIR platform for RbNiCr films, the atoms involved and the associated channels in the RBS measurements are listed in **Table A1.1**.

Table A1.1. Calculated value of the K factor for the different elements involved in the RBS measurements. K is used for the calibration of channel to energy curve.

	Mass (M_2) [g/mol]	Channel	K
Cr	52.0	357	0.73813
Ni	58.7	371	0.76425
Rb	85.5	410	0.83157
Bi	209.0	458	0.92737

By applying Eq. A1.8, we obtain the K value for each atom, as also listed in Table A1.1, and from Eq. A1.7 we evaluate the corresponding backscattered energy E_1 for each atom. E_1 energy is plotted as a function of channel in Figure A1.3, to get a calibration curve.

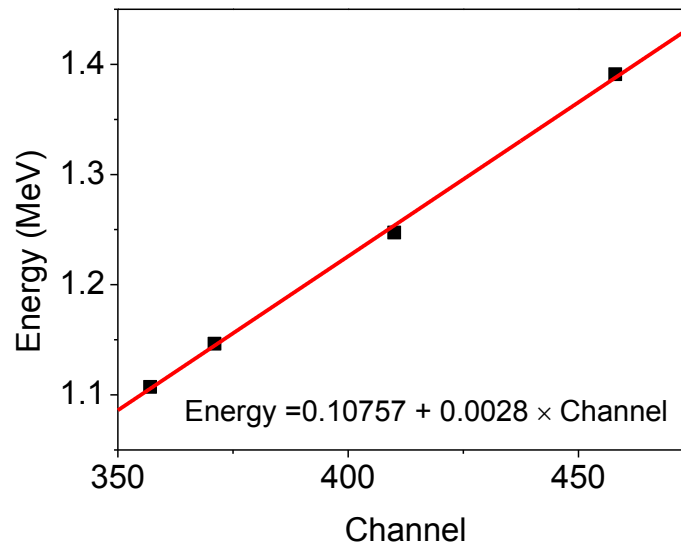


Figure A1.3. Example of channel to energy conversion curve for RBS measurements. The atoms involved are Cr, Ni, Rb and Bi, the incidence energy is 1.5 MeV.

A.1.3.3 Conversion in absolute areal density values

In RBS, it is well known that the scattering cross-section of a given element is proportional to the atomic number squared of this element. We can thus easily derive the atomic ratio between two elements from the area of the peaks representative of these two elements. Indeed, the areal density between elements A and B writes as:

$$\frac{\text{Areal density (A)}}{\text{Areal density (B)}} \propto \frac{\text{Area (A)}}{\text{Area (B)}} \times \left(\frac{Z(B)}{Z(A)} \right)^2 \quad \text{Eq. A1.9}$$

where Z is the atomic number of element i , and “area” the integral of the corresponding peak in the RBS spectrum.

Quantitative values of the areal density can also be calculated by comparison with a standard spectrum recorded in the same experimental conditions. We used a Bismuth (Bi) layer sample as reference: Bi ions implanted in amorphized Si with an areal density of 5.62×10^{16} atom/cm².

A.1.4 Magnetic measurements

All the magnetic properties were measured using a Cryogenic SX600 SQUID magnetometer. Data treatment first includes a subtraction of the diamagnetic contribution related to the Si substrate. This was done by simply removing the slope of the $M - H$ curve at high magnetic fields, and the raw $M - H$ curve is shown in **Figure A1.4**. This slope was derived from fits and averaged over the negative and positive branches of the $M - H$ curve.

The magnetization of the films is systematically expressed in unit of emu/cm². The film area was easily derived for the deposits which could be visualized. For thinner deposits, we used the average area values obtained for the visible films. This is a reasonable assumption, as all films have the same lateral dimensions given by the aperture of the scotch tape.

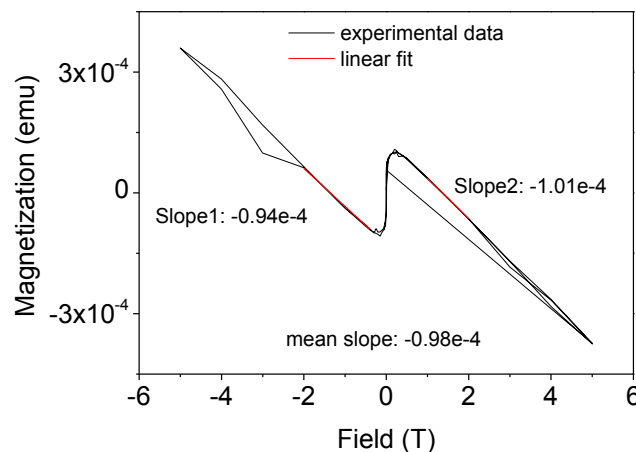


Figure A1.4. $M - H$ curve of a RbNiCr film (thickness, $t_{\text{XRR}} = 32$ nm) before slope correction in the -5 T to 5 T field range. The external field was applied parallel to the surface.

A.1.5 X-ray absorption spectroscopy measurements

X-ray absorption spectroscopy (XAS) experiments were performed on the FAME/BM30B beamline at the ESRF, Grenoble (France) with the help of Isabelle Kieffer and Denis Testemale. XAS spectra were collected at Fe, Co and Ni K-edges using a Si(220) pseudochannel-cut monochromator.⁸ A piece of Co foil was used for energy calibration (7709 eV, at the first inflection point of the absorption edge). Measurements were performed at variable temperature (10-293 K) using an ILL "orange" cryostat working under helium exchange gas.

A.1.5.1 General method

The interaction between an electromagnetic radiation and matter gives rise to two processes: scattering and absorption by photoelectric effect. Scattering phenomena result from collisions between the atoms of the materials and the photons, leading to a change in the wave trajectory without loss of energy (coherent or Thompson scattering) or with some energy loss (incoherent or Compton scattering). The photoelectric effect corresponds to the absorption by one atom of a photon, which energy is equal or larger than the binding energy of its core electrons. This results in the emission of a photoelectron and in the creation of a hole in the inner orbitals of the absorber atom. For photons of energy lower than 20 KeV, as those considered in this work, the main interaction process is the photoelectric effect. It will be the only one to be taken into account in the following absorption experiments.

X-ray Absorption Spectroscopy is used to measure the variation of the adsorption coefficient μ as a function of the incident photon energy E . μ is a decaying function of E , except close to absorption edges. For a free atom, μ decreases monotonously beyond the edge, while for a molecule or a condensed phase, this coefficient will show oscillations called EXAFS. Their analysis allows extracting structural information: number of neighbors of a target atom, distances to the central atom up to 2 to 3 coordination spheres. As a result, an absorption spectrum can be typically divided into three parts (**Figure A1.5**):

- the pre-edge, the corresponding curve may show discrete absorption peaks due to transitions between bound states, this region contains the information related to the electronic structure of the absorber atom and the symmetry of its site in a crystal lattice or in all amorphous matrix.
- the region between the edge and 40 eV above the edge is related to multielectronic interactions and multiple scattering of the photoelectron. Edge and pre-edge are the region of XANES (X-ray Absorption Near Edge Structure).
- the EXAFS region (Extended X -ray Absorption Fine Structure), from 40 to 1000 eV above the edge.

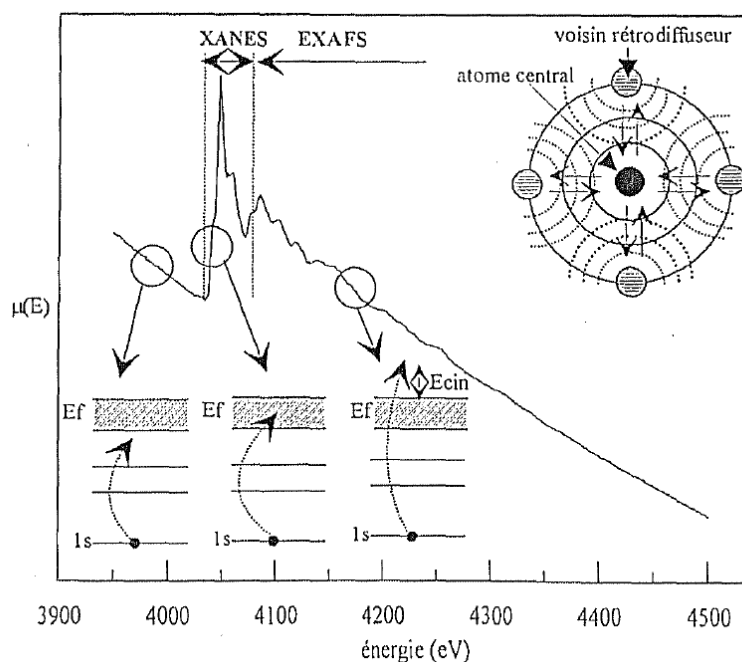


Figure A1.5. General scheme of x-ray absorption (XAS) in a condensed phase.

The XANES region exhibits distinct substructures in the main line for the compounds under study, that will be shortly revised here. **Figure A1.6** shows the spectra at Fe K-edge of $\text{K}_3\text{Fe}(\text{CN})_6$ (Fe^{3+} , low spin) and $\text{Na}_4\text{Fe}(\text{CN})_6$ (Fe^{2+} , low spin) standards measured at 100 K. Spectra were shifted vertically to facilitate comparison.

The pre-edge structures are related to $1s \rightarrow 3d$ electronic transitions that are forbidden by dipole selection rules and hence have a weak intensity. As a result, non-centrosymmetric positions result in more intense pre-edge features compared to centrosymmetric (*e.g.* octahedral) positions, due to dipole-quadrupole mixing. We can observe in **Figure A1.6** an absorption band of very low intensity (at 7.113 keV for Fe^{2+} and at 7.114 keV for Fe^{3+}), which corresponds to the dipolar transition from $1s$ (a_{1g} symmetry in a regular octahedron) to the empty d levels (t_{2g} and e_g symmetry).

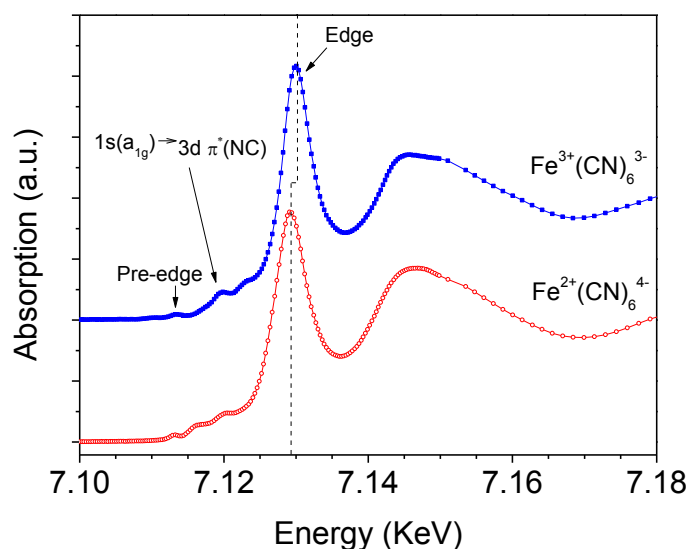


Figure A1.6. XANES spectra at the Fe K-edge of $\text{K}_3\text{Fe}(\text{CN})_6$ (blue line) and $\text{Na}_4\text{Fe}(\text{CN})_6$ (red line) standards measured at 100 K.

Around 7.120 keV, one shoulder band is observed. This shoulder was attributed to dipolar transition to t_{1u} state.⁹ These t_{1u} molecular orbitals are formed by the combination of the 4p orbitals of Fe with the π^* molecular orbitals of the cyanide ligands. This transition is systematically observed in complexes which possess π^* orbital vacancies. The very intense and sharp band at 7.129 keV for $\text{Na}_4\text{Fe}(\text{CN})_6$ and 7.130 keV for $\text{K}_3\text{Fe}(\text{CN})_6$ corresponds to transitions to the 4p orbitals of the Fe ions. The narrow width and the strong intensity of this band are due to the degeneracy of these 4p orbitals.

The main absorption band is shifted to higher energy for $\text{K}_3\text{Fe}(\text{CN})_6$ compared to $\text{Na}_4\text{Fe}(\text{CN})_6$. This shift is due to the increase in the real charge of the metallic cation when the oxidation state increases from +II to +III, accompanied by (1) a stabilization of the occupied levels (especially 1s orbitals), and (2) a destabilization of the antibonding levels because of the decreased metal to ligand distance. The energy shift is small between the two reference compounds, about 1 eV for both the edge and the pre-edge features.

Figure A1.7 shows the XANES spectra at Co K-edge of a $\text{Co}[\text{Fe}(\text{CN})_6]_{0.67} \cdot 4.6\text{H}_2\text{O}$ compound (Co^{2+} , high spin, red line), a $\text{K}_3\text{Co}(\text{CN})_6$ (Co^{3+} , Low spin, blue line) standard and a $\text{Rb}_{0.46}\text{Co}[\text{Fe}(\text{CN})_6]_{0.79} \cdot z\text{H}_2\text{O}$ compound (composed of a majority of Co^{3+} , black line). Again spectra were shifted vertically for comparisons.

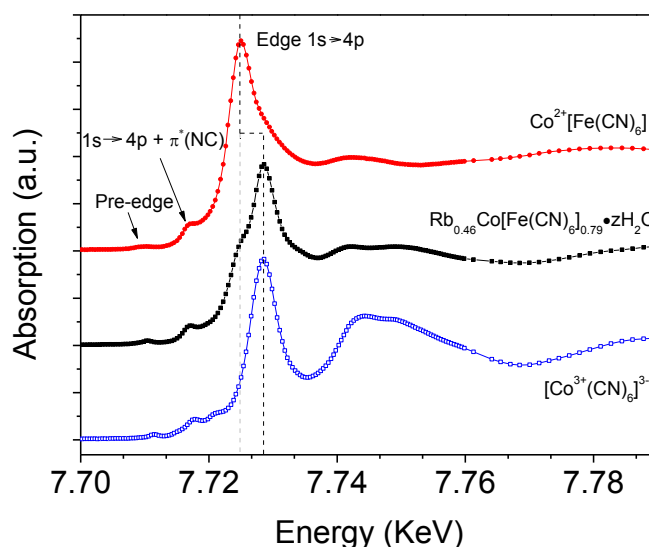


Figure A1.7. XANES spectra at the Co K-edge of $\text{Co}[\text{Fe}(\text{CN})_6]_{0.67} \cdot 4.6\text{H}_2\text{O}$ (red line), $\text{K}_3\text{Co}(\text{CN})_6$ (blue line) and $\text{Rb}_{0.46}\text{Co}[\text{Fe}(\text{CN})_6]_{0.79} \cdot z\text{H}_2\text{O}$ (black line).

For the $\text{Co}[\text{Fe}(\text{CN})_6]_{0.67} \cdot 4.6\text{H}_2\text{O}$ reference, we observe a transition from $1s (a_{1g})$ to $4p \pi^*(\text{CN}) (t_{1u})$ at 7.717 keV. The maximum absorption of the pre-edge structure is at 7.710 keV (forbidden transition from $1s (a_{1g})$ to $3d (e_g)$), while the maximum absorption of the edge is at 7.725 keV for the dipole allowed transition from $1s (a_{1g})$ to $4p (t_{1u})$.

For the $\text{K}_3\text{Co}^{3+}(\text{CN})_6$ standard, there is also a transition from $1s (a_{1g})$ to $4p \pi^*(\text{CN}) (t_{1u})$ at 7.718 keV. The pre-edge and main edge features are at 7.711 and 7.729 keV, respectively.

The maximum absorption of pre-edge is at 7.710 keV for the $\text{Rb}_{0.46}\text{Co}[\text{Fe}(\text{CN})_6]_{0.79} \cdot z\text{H}_2\text{O}$ compound. The spectrum is very close to that of $\text{K}_3\text{Co}(\text{CN})_6$ standard, with the edge maximum absorption at 7.729 keV. We notice that there is small shoulder at around 7.717 keV, which is corresponding to the Co^{2+} contribution. This spectrum strongly indicates that there is a majority of Co^{3+} ions and a minority of Co^{2+} ions in this compound.

The larger energy shift from Co^{2+} to Co^{3+} (3 eV) compared with that observed at the Fe K-edge for the metallocyanide references (1 eV) is due to the increase of the charge of the cation, which is accompanied by a spin state change of the Cobalt. This lead to a depopulation of the d orbitals of the metal (e_g^* antibonding states) with a strong decrease in the metal-to-ligand distance.

A.1.5.2 Sample preparation and measurement geometry

Powder samples were measured in transmission mode. 3 to 5 mg of sample were grinded with 30 mg of BN (*Alfa Aesar*, 99.5%) and then pressed into pellets (ca. 0.5 GPa of applied pressure). For thin films, XAS spectra were collected in partial fluorescence mode using a 30-element Ge solid state detector (Canberra). The angle between the incident beam and the axis of the detector is 90°, the films were oriented at 75° with respect to the incident beam.

Reference XAFS spectra of powder samples in which the Co absorber is present in octahedral environment but in different valence state were also recorded. The following standards were measured in transmission mode: $\text{Co}[\text{Fe}(\text{CN})_6]_{0.67} \cdot 4.6\text{H}_2\text{O}$ representative of a pure Co^{2+} contribution (synthesized following the procedure described in reference 9), and $\text{K}_3\text{Co}(\text{CN})_6$ ($\geq 90\%$, Alfa Aesar). We used $\text{K}_3\text{Fe}(\text{CN})_6$ ($\geq 99\%$, Sigma-Aldrich) and $\text{Na}_4\text{Fe}(\text{CN})_6$ ($\geq 99\%$, Sigma-Aldrich) as standards for Fe^{3+} and Fe^{2+} species surrounded by six cyanide ligands in regular arrangement.

Spectra were typically recorded using a 5 eV step (2 sec counting time) in the pre-edge range, a 0.4 eV step in the energy region corresponding to the main edge (with 3 sec counting per step) and a 0.05 Å⁻¹ *k*-step for the EXAFS region. In this energy region, we used a variable counting time, from 3 to 6 sec, because of the global decrease of the absorption.

A.1.5.3 Data extraction, normalization and fitting

The experimental XANES spectra were corrected for pre-edge and post-edge absorption and subsequently normalized. For the powder samples, the background was determined by a linear fit below the edge (from -150 to -30 eV below the edge). The standard procedure to correct for the post-edge absorption is to use a cubic spline. However, we found that using the procedure implemented in the ATHENA 0.9 software package¹⁰ is very sensitive to the clamping points chosen for the normalization range. As we observed that the absorption exhibit oscillations around a weakly decreasing function after pre-edge correction, we chose to normalize all XANES spectra by dividing by a constant factor determined as the average absorption over the 7.78 – 8.24 keV range for Co K-edge and 7.18 – 7.62 keV range for Fe K-edge. We checked that the choice of the energy range used for normalization has a very small influence on the amplitude of the white line (typically 2×10^{-3} per eV) that will be used for the evaluation of the $\text{Co}^{2+}/\text{Co}^{3+}$ ratio.

For the thin films, the spectra relative to each element of the Canberra detector were first inspected before summation. Spectra corresponding to deteriorated elements or presenting a large signal corresponding to diffraction by the Si(111) substrate were eliminated. We systematically observed a decreasing fluorescence signal before the Co and Fe absorption

edges. This is explained by an overlap between the fluorescence signal of the absorber and the scattered signal which has the same energy than the incident beam. If we consider the Co K-edge, the K α _{1,2} fluorescence signals are at 6930 and 6915 eV, respectively. By scanning the incident energy from 7.5 to 8.25 keV, there is a decreasing overlap between the scattered and fluorescence signals responsible for the decrease of the measured intensity in the pre-edge region. Because of this, we could not use the same normalization procedure than that used for the powder samples. Instead, the background was arbitrarily removed by subtracting a linear function chosen so that the absorption after the edge oscillates around a quasi constant value. The XANES spectra were then normalized by dividing by a constant factor determined as the average absorption over the same energy range as that used for the powder samples.

Co K-edge XANES spectra were subsequently fitted to the sum of two Lorentzian functions (representative of the discrete $1s \rightarrow 4p$ transitions for the Co²⁺ and Co³⁺ species) and of an arctangent function modeling transitions to the continuum states. Note that the sum of two arctangent functions is an arctangent function. The fit was then restricted to the [7.721-7.732 keV] energy range as shown in **Figure A1.8**. The list of fitted parameters is as follows: amplitude of the Lorentzian function representative of Co²⁺ species; amplitude and position of the Lorentzian function characteristics of Co³⁺; all parameters related to the arctangent function.

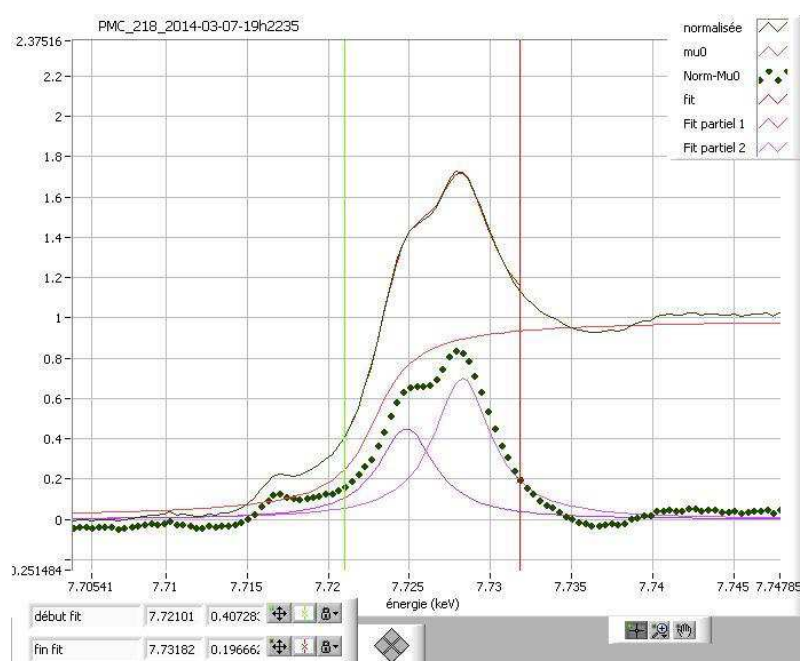


Figure A1.8. Room temperature normalized XANES spectra (experimental and calculated) of the RbCoFe film described in Chapter 4.

To reduce the number of refined parameters, the position and width of the first Lorentzian function were fixed (average values derived from the spectra of the powder sample recorded during photo-excitation). In contrast, the position of the second Lorentzian function was let free to vary, as it may overlap with absorption bands characteristics of the Co^{2+} species and related to multielectronic excitations. The Co^{2+} fraction was finally obtained by dividing the integral of the peak related to the Co^{2+} contribution by that found for the $\text{Co}[\text{Fe}(\text{CN})_6]_{0.67} \cdot 4.6\text{H}_2\text{O}$ reference sample which is representative of 100% Co^{2+} .

A.1.6 References

1. I. Horcas; R. Fernández; J. M. Gómez-Rodríguez; J. Colchero; J. Gómez-Herrero; A. M. Baro, WSXM: A software for scanning probe microscopy and a tool for nanotechnology. *Review of Scientific Instruments* **2007**, 78, 013705-1-013705-8.
2. L. G. Parratt, Surface studies of solids by total reflection of X-rays. *Phys. Rev.* **1954**, 359-369.
3. C. Braun Parratt32 V.1.5.2, HMI, Berlin Neutron Scattering Center, available upon request from the webpage: <http://www.hmi.de/bensc/instrumentation/instrumente/v6/refl/parratt.en.htm>.
4. *International Tables of Crystallography*. The Kynoch Press: Birmingham, 1968; Vol. III.
5. J. R.-Carvajal, Recent advances in magnetic structure determination by neutron powder diffraction. *J. Physica B* **1993**, 192, 55-69.
6. K. G. Malmqvist, Accelerator-based ion beam analysis - an overview and future prospects. *Radiation Physics and Chemistry* **2004**, 71, 817-827.
7. Mayer, M., Rutherford Backscattering Spectrometry (RBS). 2003.
8. O. Proux; V. Nassif; A. Prat; O. Ulrich; E. Lahera; X. Biquard; J.-J. Menthonnexa; J.-L. Hazemann, Feedback system of a liquid-nitrogen-cooled double-crystal monochromator: design and performances. *J. Synchrotron Rad* **2005**, 13, 59-68.
9. Escax-Bastet, V. Photomagnétisme dans des analogues cobalt-fer du bleu de Prusse : de l'excitation moléculaire à l'aimantation macroscopique. Université Paris VI, 2002.
10. B. Ravela; M. Newville, ATHENA, ARTEMIS, HEPHAESTUS: data analysis for X-ray absorption spectroscopy using IFEFFIT. *J. Synchrotron Rad* **2005**, 12, 537-541.

Appendix 2

Supplementary information on Chapter 2

A.2.1 Solution preparation

Preparation of 0.1 M MES buffer solution: 0.1 M MES solution at pH 5 was prepared by dissolving 21 g of MES in 1 L of water. The mixture was heated to 70°C for 15 min to speed up the dissolution and let cooled down to room temperature. The pH of the solution was adjusted to pH 5 by adding volumes of 1 M NaOH solution.

Preparation of 0.1 M NHS solution: 3 g of N-hydroxysuccinimide (NHS) was dissolved in 250 mL of 0.1M MES solution. The solution was heated to 70 °C under stirring for 15 to 20 min in order to help the dissolution and get homogeneous solution. The solution was let to cooled down to room temperature and stored at 4°C for further uses.

Preparation of 0.1M NHS/EDC (activation) solution: 0.959 g of EDC was dissolved in 50 mL of 0.1 M NHS buffer solution cooled at 4°C (water/ice bath). The solution was deoxygenated by Ar bubbling and kept at 4°C until the introduction of the Si-COOH surface. The EDC/NHS solution was prepared just prior its use for the activation of Si-COOH surfaces.

A.2.2 Complementary ATR-FTIR spectra

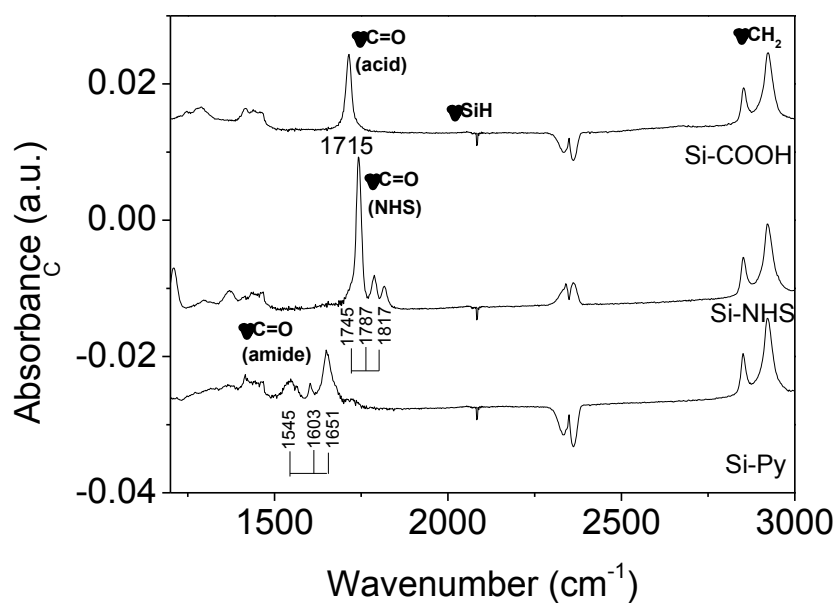


Figure A2.1. ATR-FTIR spectra (s polarization) of COOH, NHS and Pyridine terminated layers onto Si (111) surface. The spectrum of a hydrogenated H-Si (111) surface was used as reference.

Appendix 3

Supplementary Information for Chapter 3

A.3.1 Synthesis and characterization of the RbNiCr reference particles

To obtain particles of uniform size, we have adapted the multi-step protocol described by Prado and coworkers,⁴ which consists of a rapid mixing of the precursors to separate the nucleation and growth stages, followed by a regrowth step using drop wise addition. In the first step, 250 mL of an aqueous solution of NiCl₂ (2 mM) and RbCl (4 mM) was rapidly poured into an aqueous solution of K₃Cr(CN)₆ (250 mL, 2 mM) under vigorous stirring (800 rpm). 400 mL of the as-obtained solution was centrifuged (60,000 g, 30 min) and washed three times with distilled water. The mean size of the particles was subsequently increased by a second growth stage. 10 mL of the solution obtained at the end of the first step were diluted in 190 mL of ultrapure water to minimize particles aggregation during regrowth.¹⁹ Two solutions were drop wise added to this dilute solution: 80 mL of an aqueous solution containing RbCl (1.4 mM) and NiCl₂ (0.7 mM) and 80 mL of an aqueous solution of K₃Cr(CN)₆ (0.7 mM). Addition was carried out using a peristaltic pump at a rate of 1.5 mL.min⁻¹. The temperature of the reaction bath, adjusted to 20°C for the two steps, was kept constant using a thermostatic bath. The solution remained colorless after addition. This second step was repeated twice. A light green precipitate was recovered after three washings with deionized water (centrifugation at 26,400 g for 30 min), and was dried in ambient air. Only 8 mg of powder were obtained. A representative SEM images of the RbNiCr-A and RbNiCr-B particles are displayed in **Figure A3.1**. The sample shows strongly faceted cubic-like particles, with a low size polydispersity, 28 ± 3 nm.

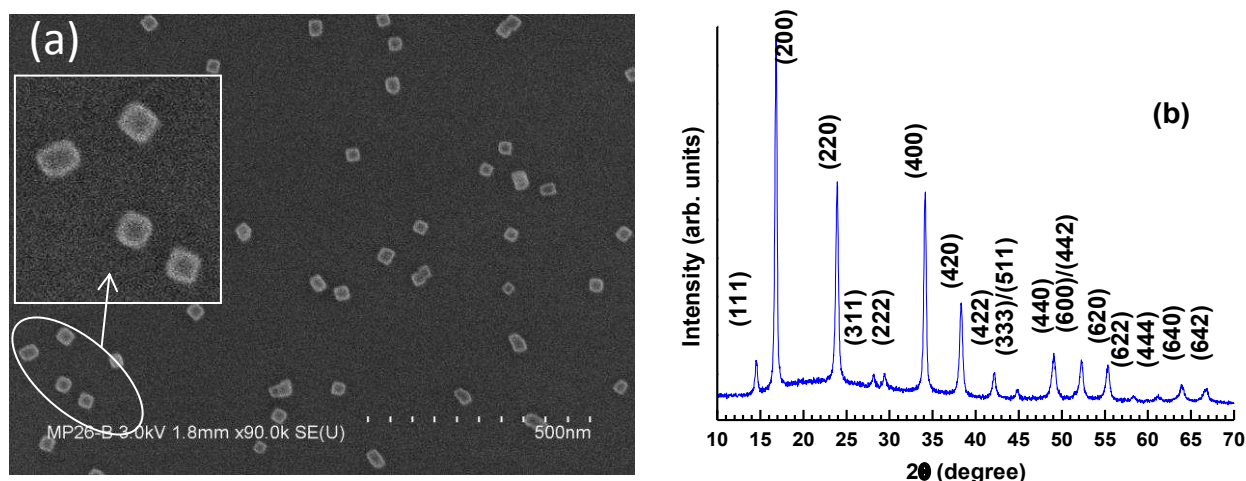


Figure A3.1. (a) SEM micrograph and (b) X-ray diffraction profile of the RbNiCr particles. ($K_{\alpha}(\text{Cu})$, $\lambda = 1.5418 \text{ \AA}$).

The diffraction pattern of the sample is shown in **Figure A3.1(b)**. All peaks can be indexed in the same face-centered cubic system. Refinement of the line positions by profile matching (LeBail analysis) yields a lattice parameter value of $10.479 \pm 0.005 \text{ \AA}$.

As the amount of powder recovered after synthesis was not sufficient for elemental analysis, its chemical composition was derived from EDS measurements carried out on the RbNiCr-B powder. We found Cr/Ni and Rb/Ni atomic ratio of 0.71 ± 0.01 and 0.125 ± 0.006 , respectively in very good agreement with the proposed formula.

A.3.2 Scanning Electron Microscopy (SEM) imaging

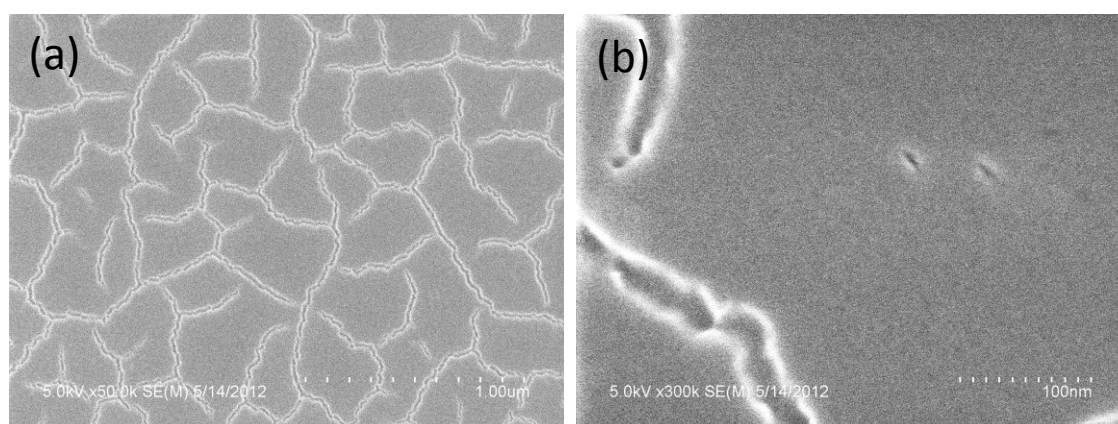


Figure A3.2. Plane view SEM images of the RbNiCr film with a thickness of 32.2 nm (from XRR) at different scales. Scale bars are indicated in each figure.

A.3.3 RBS spectra for RbNiCr films with different deposition time.

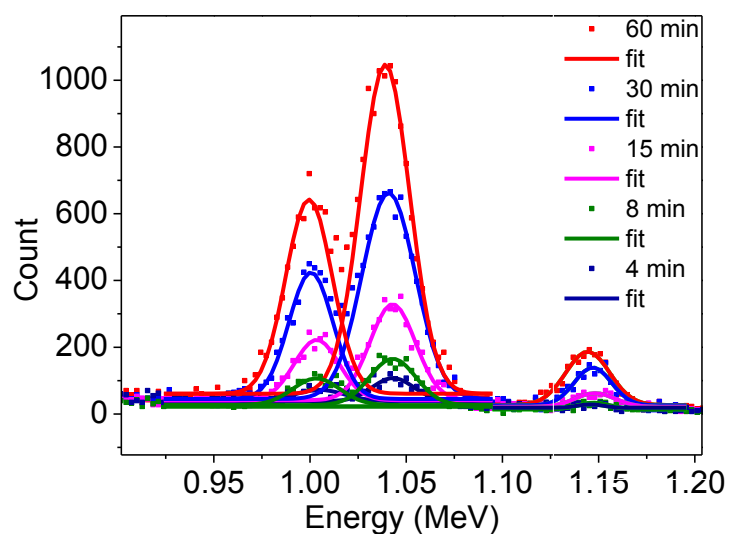


Figure A3.3. Partial RBS spectra of RbNiCr films with different deposition time. Scatters correspond to experimental data and lines are fits to Gaussian functions.

Note that film preparation is quite reproducible. A whole comparable series of RbNiCr films was prepared with similar deposition times, and the characterization of these films show a good agreement with the previous series. The areal density of the Ni, Cr and Rb of this second set of films are shown in **Table A3.1** for information.

Table A3.1. Areal density values of the Ni, Cr and Rb derived from RBS for a second series of RbNiCr films.

Sample	Deposition time [min]	Areal density [10^{14} atom / cm^2]			Rb/Ni	Cr/Ni
		Ni	Cr	Rb		
1	2	5.14	2.82	0.26	0.05	0.55
2	4	9.00	6.15	0.71	0.08	0.68
3	8	16.05	11.02	1.15	0.07	0.69
4	22	36.32	24.96	3.18	0.09	0.69
5	60	85.21	67.70	8.44	0.10	0.79

A.3.4 Characterizations of RbNiCr films prepared with different rotation rates

The layers prepared by varying the rotation speed of the substrates were also studied in detail. Their morphology, thickness, structure and chemical composition were investigated by AFM, XRR, XRD and RBS respectively.

A.3.4.1 AFM

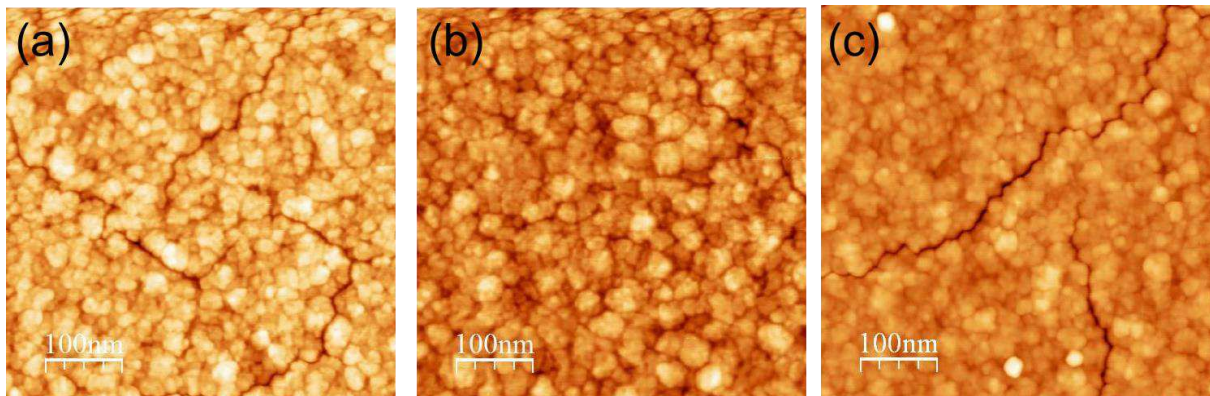


Figure A3.4. AFM images ($500 \times 500 \text{ nm}^2$) of the films corresponding to different rotation speeds: (a) 0 rpm, (b) 350 rpm and (c) 1400 rpm.

Figure A3.4 shows the AFM images of these films prepared with different rotation rate, these images indicate that all films have a similar granular morphology. Cracks are observed on all the layers, presumably because of shrinkage when films are dried.

A.3.4.2 XRR

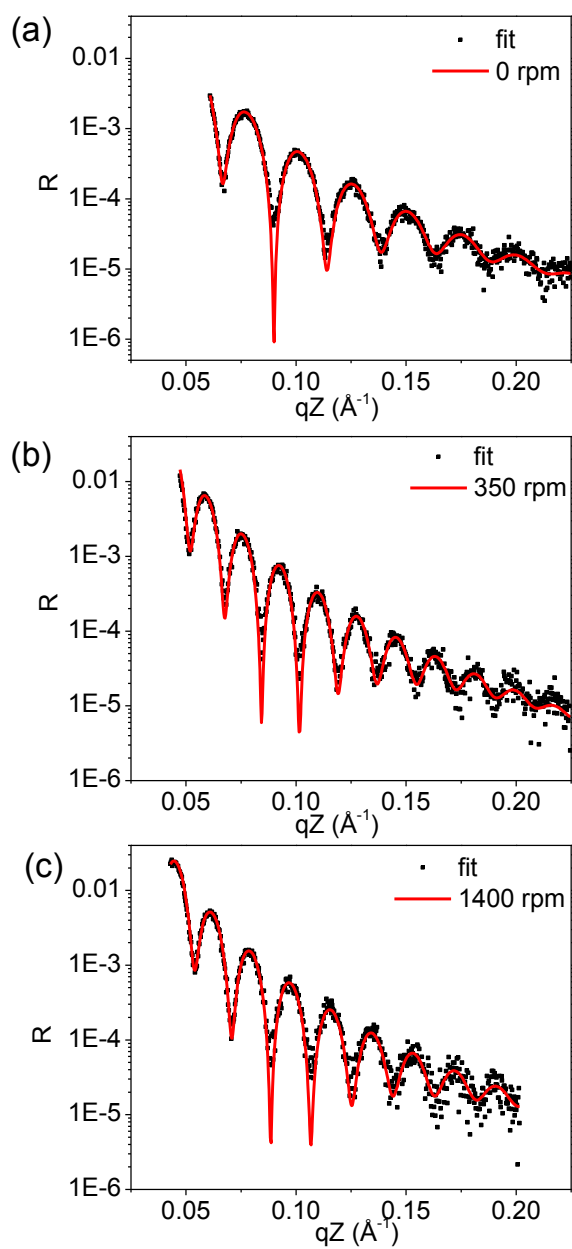


Figure A3.5. X-ray reflectivity profiles for films with rotation speed of (a) 0 rpm, (b) 350 rpm and (c) 1400 rpm. The black scatters show the experimental data, and the red line is the best fit.

Table A3.2. Fitted parameters for RbNiCr films grown with different rotation speeds derived from X-ray reflectivity data (deposition time of 1 h for all films).

Rotation rate (rpm)	RbNiCr layer			Pyridyl layer		
	t_{Layer} [nm]	ρ_{Layer} [$10^{23}\text{el. cm}^{-3}$]	σ_{Layer} [nm]	t_{ML} [nm]	ρ_{ML} [$10^{23}\text{el. cm}^{-3}$]	σ_{ML} [nm]
0	23.7	5.39	1.1	1.5	4.05	0.3
350	33.3	5.46	1.2	1.7	4.15	0.1
1400	32.2	5.43	1.1	1.7	4.08	0.2

A.3.4.3 XRD

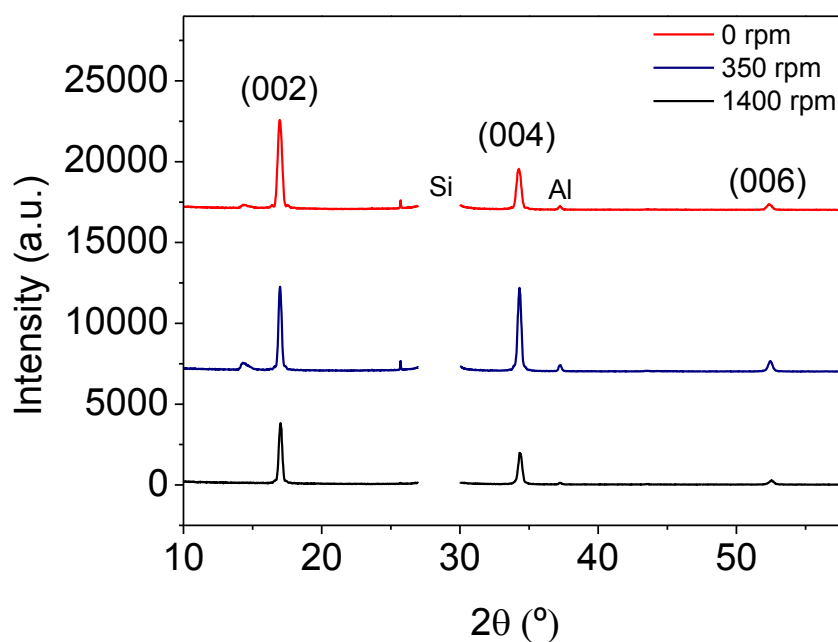


Figure A3.6. X-ray diffraction (XRD) patterns of RbNiCr films corresponding to different rotation rates, 0, 350 and 1400 rpm.

The crystallinity, as well as the (00 l) textured structure, is independent on the rotation speed of the substrate, as shown in **Figure A3.6**. The coherent length determined for the film with 0, 350 and 1400 rpm are 24.4, 34.5 and 32nm respectively, and the corresponding lattice parameter values are 10.45, 10.44 and 10.43Å.

A.3.4.4 RBS

Table A3.3. Areal density values of the Ni, Cr and Rb derived from RBS for samples with different rotation speeds.

Rotation rate (rpm)	Areal density 10^{14} atom / cm^2			Rb/Ni	Cr/Ni
	Ni	Cr	Rb		
0	68.61	55.58	6.57	0.10	0.81
350	99.65	76.77	9.04	0.09	0.77
1400	98.37	71.20	8.04	0.08	0.72

A.3.5 Full $M - H$ curves

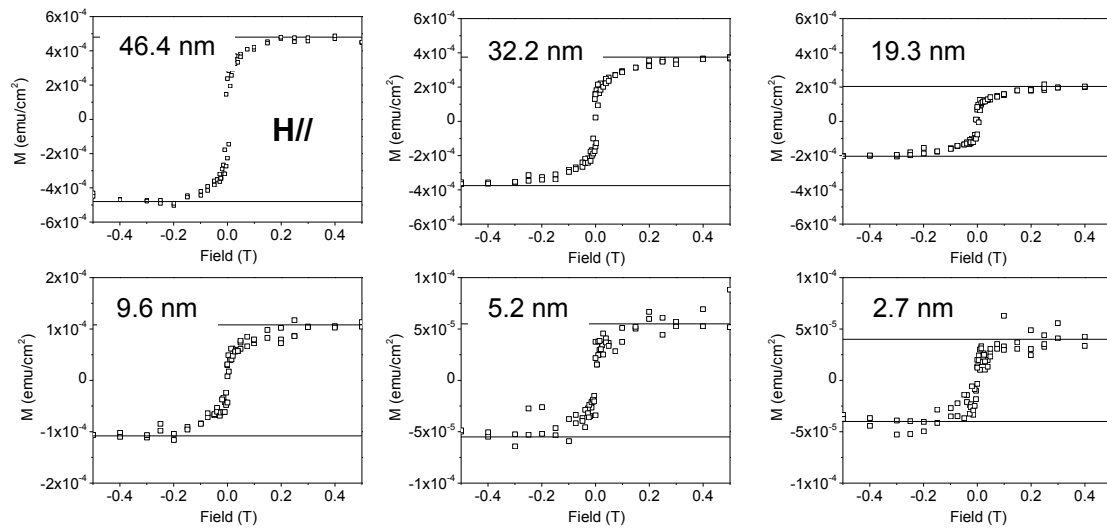


Figure A3.7. Hysteresis loops of RbNiCr film with different deposition time in the range of -5T to 5T. The external field is applied parallel to the surface.

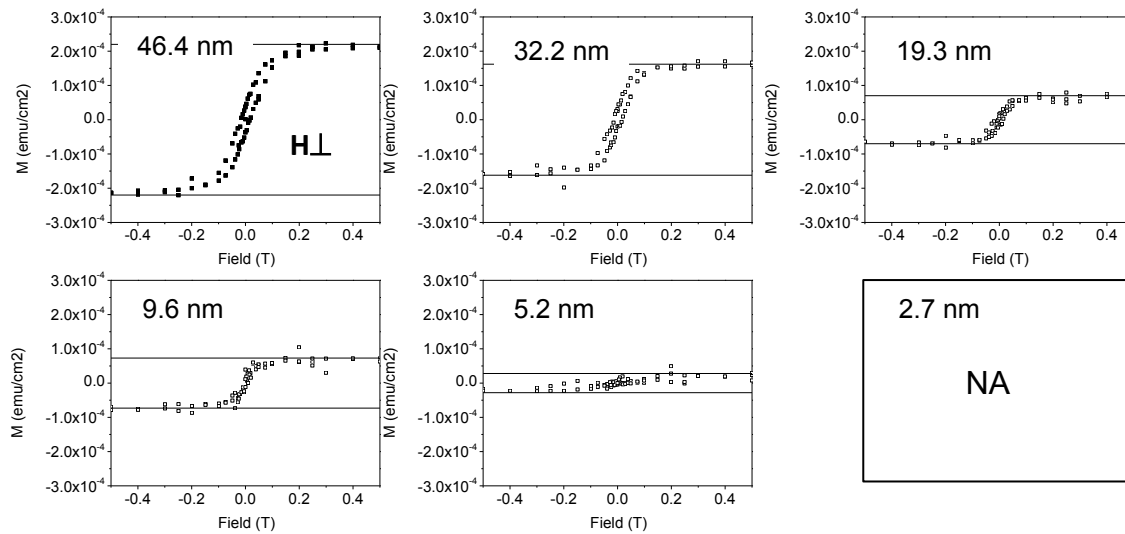


Figure A3.8. Hysteresis loops of RbNiCr film with different deposition time in the range of -5T to 5T. The external field is applied perpendicular to the surface.

A.3.6 Analysis of T_c and β values from Field cooled magnetization curve

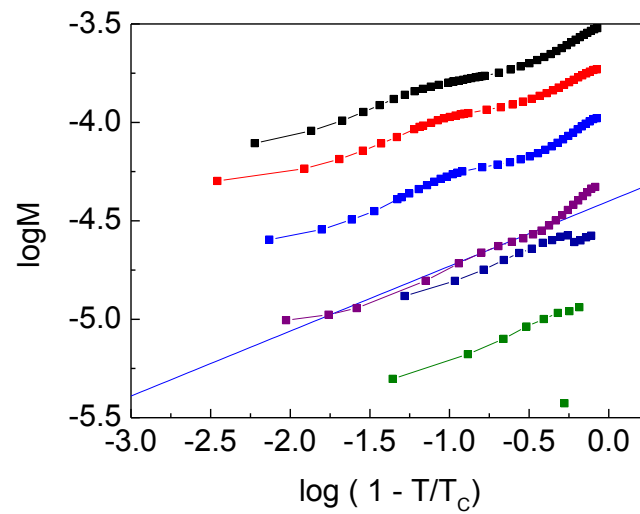


Figure A3.9. Plot of $\log M$ as a function of $\log(1 - T/T_c)$.

Table A3.4. T_c values and β values derived from Eq. 3.6 for RbNiCr films with different thicknesses.

t_{XRR} [nm]	T_c [K]	β
2.7	29	0.31
5.2	45.1	0.33
9.6	56.5	0.33
19.3	62.5	0.31
32.2	63.5	0.33

Appendix 4

Supplementary information for Chapter 4

A.4.1 Effect of solution deoxygenation

For this study, we selected a solution composition of 0.43 mM of RbNO_3 , 0.17 mM of $\text{Co(NO}_3)_6 \cdot 6\text{H}_2\text{O}$ and 0.17 mM of $\text{K}_3\text{Fe(CN)}_6$. The deposition time was fixed to one hour and we investigated the influence of the rotation of the substrate and of a deoxygenation of all solutions.

CoFe-1 and CoFe-3 were films grown using a rotation speed of 1400 rpm, while CoFe-2 and CoFe-4 films were deposited without rotation of the sample holder. The Co, Fe and Rb areal density values were obtained from Rutherford Backscattering Spectroscopy measurements by comparing the area of the corresponding peaks in the RBS spectrum to that of a reference standard measured in the same conditions. Only the Co areal density and the Rb/Co and Fe/Co atomic ratios are listed in **Table A4.1**.

Table A4.1. Co areal density and film composition as a function of the preparation conditions for 60 min deposition.

	Rotation speed (rpm)	Deoxygenated	Co areal density (atom/cm ²)	Composition
CoFe-1	1400	No	1.30×10^{16}	$\text{Rb}_{0.30 \pm 0.02} \text{CoFe}_{0.78 \pm 0.04} \cdot z\text{H}_2\text{O}$
CoFe-2	0	No	8.0×10^{15}	$\text{Rb}_{0.49 \pm 0.04} \text{CoFe}_{0.72 \pm 0.07} \cdot z\text{H}_2\text{O}$
CoFe-3	1400	Yes	1.04×10^{16}	$\text{Rb}_{0.37 \pm 0.02} \text{CoFe}_{0.72 \pm 0.04} \cdot z\text{H}_2\text{O}$
CoFe-4	0	Yes	5.0×10^{15}	$\text{Rb}_{0.62 \pm 0.06} \text{CoFe}_{0.80 \pm 0.04} \cdot z\text{H}_2\text{O}$

We can notice that the removal of oxygen in the solution of reactants has no drastic influence on the final composition of the films if we take into account the error bars on the Rb/Co and Fe/Co ratios. In addition, this parameter has no large impact on the growth rate of the film which is directly related to the quantity of deposited cobalt.

A.4.2 Scan Electronic Microscopy (SEM)

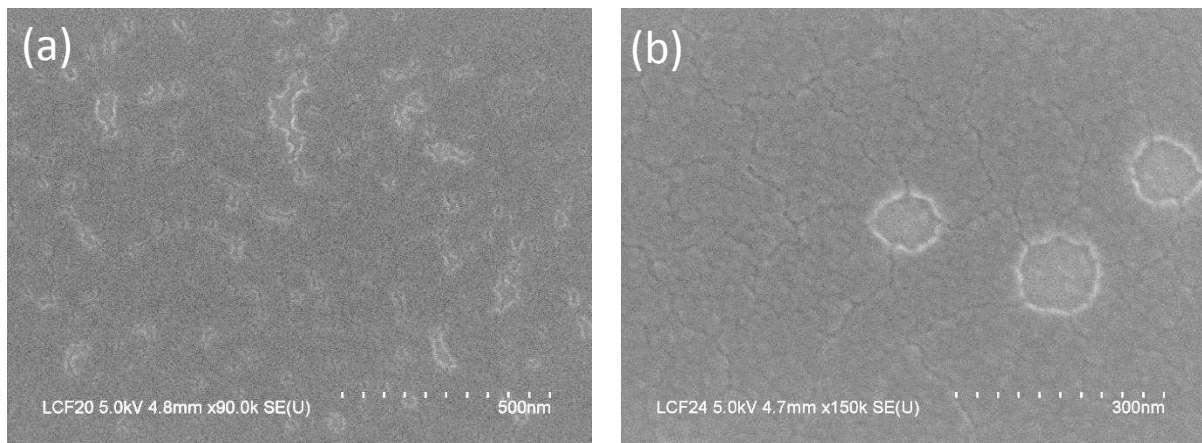


Figure A4.1. SEM images of the RbCoFe film obtained after (a) 15 min ($t_{\text{XRR}} = 14.5$ nm) and (b) 1 h ($t_{\text{XRR}} = 19.9$ nm). The full scale bar is 500 nm.

Appendix 5

Supplementary information for Chapter 5

A.5.1 Growth of Si (111)/RbNiCr layers monitored by FTIR measurements

The growth of a RbNiCr film was first monitored by IR spectroscopy measurements recorded between 400 and 4000 cm^{-1} wavenumber. The scheme of the experimental set-up is shown in **Figure 5.2** (chapter 5). Note that the solution of the Rb, Ni and $[\text{Cr}(\text{CN})_6]$ precursors was continuously flowing through the cell. Time zero of the experiment corresponds to the exposure of the Si surface to the solution. Each FTIR spectrum corresponds to an average of 100 scans recorded over 3 min. Both p and s polarizations were recorded for comparison, so the time interval between two spectra of the same polarization is 6 min. All spectra correspond to differential spectra, by reference to the spectrum of the Si surface exposed to water.

The full range IR spectra upon increasing deposition time are displayed in **Figure A5.1**. Besides changes in the 2120-2180 cm^{-1} region (stretching mode of the CN bridges), the vibration bands associated with water are also showing an evolution during deposition. In the differential spectra, we observe both a positive peak and a negative one in 1550-1800 cm^{-1} range and in the 3000-3500 cm^{-1} range, their specific assignment is indicated in reference¹. The negative peaks which amplitude continuously decreases with time are representative of liquid water. It is due to the fact that the evanescent IR wave is absorbed by the growing film which reduces the absorption by liquid water. In contrast, the positive peaks which amplitude continuously increases with time is attributed to zeolitic water molecules in the RbNiCr lattice, associated with the increased film thickness.

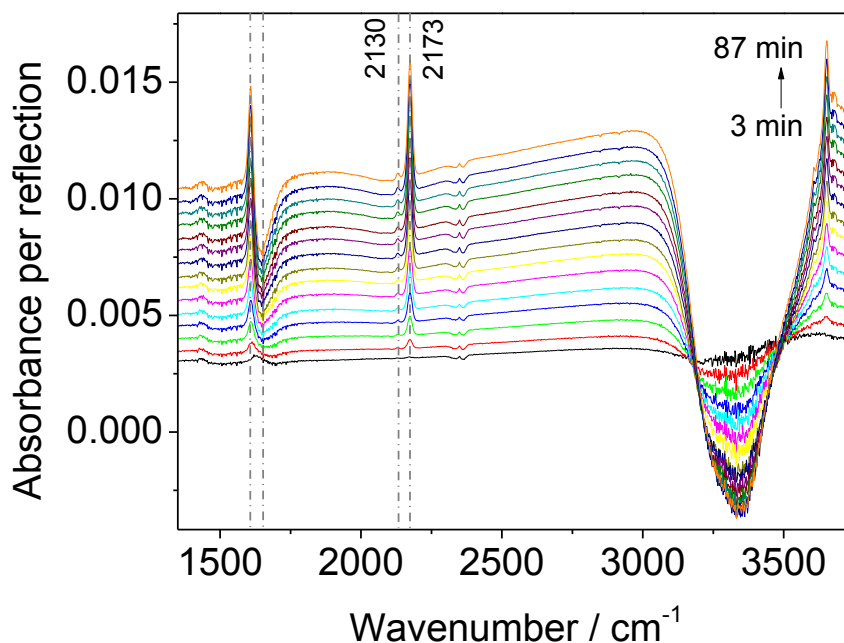


Figure A5.1. FTIR-spectra (p polarization) of a RbNiCr layer upon increasing deposition time. For each spectrum the reference is the as-prepared pyridyl terminated Si (111) surface prior to any film growth.

Figure A5.2(a) shows the same spectra in the 2000-2300 cm^{-1} range. Two peaks related to cyanide vibration modes are detected. Note that the stretching mode of free $[\text{Cr}(\text{CN})_6]$ species in water is at 2128 cm^{-1} .² We cannot observe the contribution of unreacted $[\text{Cr}(\text{CN})_6]^{3-}$ ions, because their concentration is not high enough and the cross section of the corresponding vibrator is rather low. Literature shows that the most intense IR band located at 2173 cm^{-1} is assigned to the stretching mode of $\text{Ni}^{2+}\text{-NC-Cr}^{3+}$ bridges³ and is thus indicative of the formation of the RbNiCr coordination network. The IR band located at 2130 cm^{-1} is attributed to non-bridging $\text{Cr}^{3+}\text{-CN}$ at the film surface.^{3,4} In her PhD work, M. Presle compared the IR spectra of $\text{Rb}_{0.1}\text{Ni}[\text{Cr}(\text{CN})_6]_{0.7}\cdot z\text{H}_2\text{O}$ nanoparticles of different size, and found that the ratio of the band intensities at 2135 cm^{-1} and at 2175 cm^{-1} increases when the particle size decreases, confirming that the peak at 2135 cm^{-1} should be assigned to surface species.⁵

During deposition, the intensity of the IR bands at 2173 cm^{-1} increases linearly with time as shown in **Figure A5.2(b)** and **4(c)**, which confirms that the growth rate of the RbNiCr film is constant (see **section 3.3.1** in chapter 3). Note that the evolution of the peak at 2130 cm^{-1} is also nearly linear, suggesting some increase of the surface roughness during deposition.

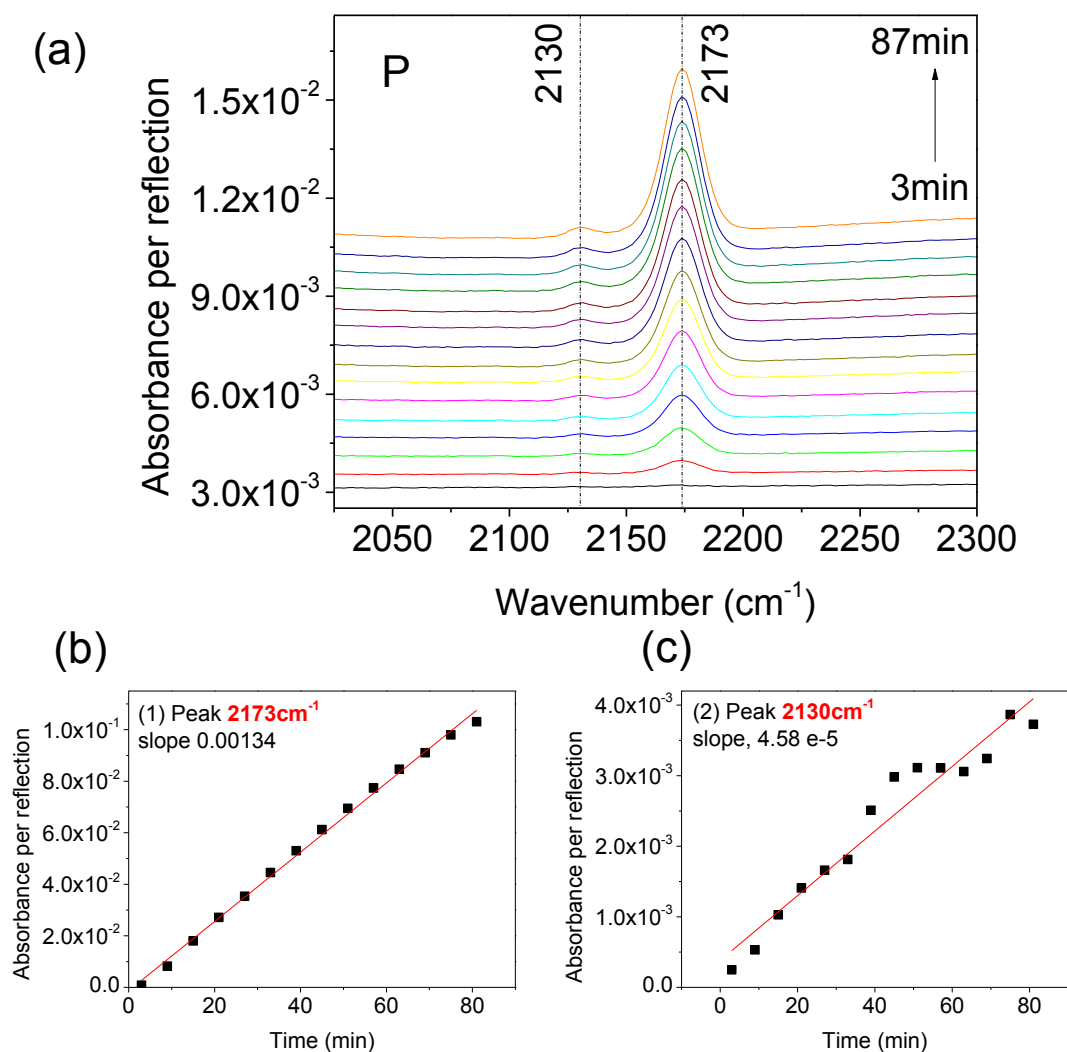


Figure A5.2. (a) IR spectra in p polarization measured during the growth of the RbNiCr film. (b) and (c) are the time dependences of the integral of the peaks at 2173 cm^{-1} and 2130 cm^{-1} , respectively. The red lines correspond to linear fits to the experimental data (black squares).

We also monitored the evolution of the IR bands during the rinsing stage. After removal of the solution of precursors, water was rapidly transferred into the cell and then removed. This operation was repeated several times. After one hour rinsing, we only observed a decreased by 1.8% of the main band at 2173 cm^{-1} , indicating some dissolution of the layer.

The X-ray diffraction pattern of the as-obtained film is similar to those of the layers studied in Chapter 3 using a different growth set-up (see **Figure A5.3**). The film displays exclusively the (002), (004) and (006) peaks. The chemical composition of the film derived from RBS also agrees with the $\text{Rb}_{0.08}\text{Ni}[\text{Cr}(\text{CN})_6]_{0.73} \cdot z\text{H}_2\text{O}$ formula, confirming that the preparation of the RbNiCr layers is quite robust and reproducible.

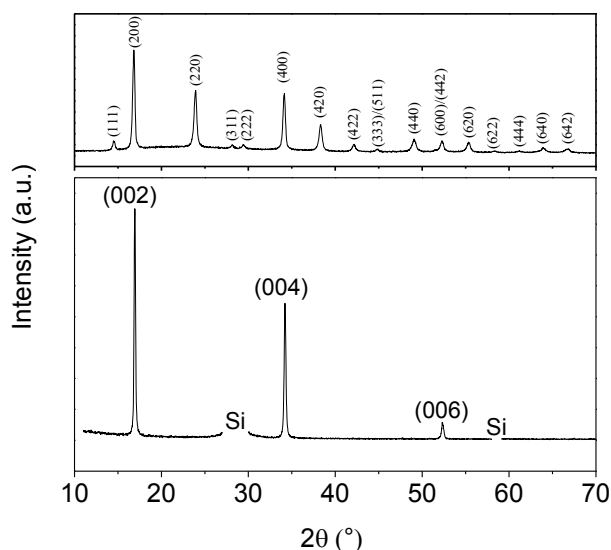


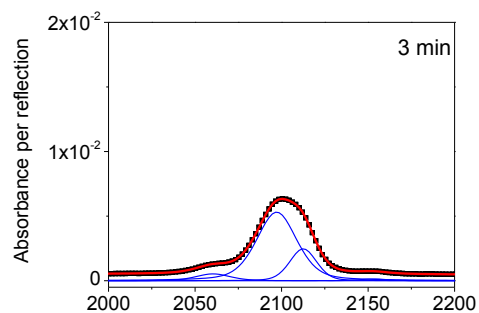
Figure A5.3. X-ray diffraction (XRD) patterns of the RbNiCr film grown in the FTIR cell for 15 min. On the top panel is the XRD pattern of RbNiCr nanoparticles for comparison.

A.5.2 Growth of Si (111)/RbCoFe layers monitored by FTIR measurements

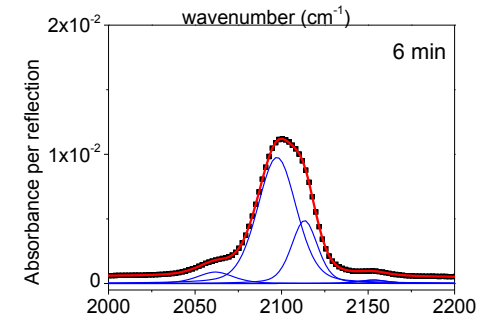
In a second set of experiments, the growth of a RbCoFe film was monitored by in situ IR measurements similar to the experiment performed on the RbNiCr film. Given the first stage of RbCoFe growth is quite fast, we only record FTIR spectra in p polarization. All spectra correspond to differential spectra, by reference to the spectrum of the Si (111)-pyridyl substrate exposed to water.

Figure A5.4 shows the differential FTIR spectra recorded for 3 to 15 min deposition time, in the 2000-2200 cm^{-1} range. Generally we observe an asymmetric broad peak that is evolving with deposition time. Four peaks are found by fitting this broad peak with Pseudo-Voigt functions, the width of each peak was fixed during the fitting, and the parameters are listed in **Figure A5.4**. The stretching mode of free $[\text{Fe}(\text{CN})_6]^{3-}$ species in water is at 2115 cm^{-1} and at 2037 cm^{-1} for $[\text{Fe}(\text{CN})_6]^{4-}$ species in water. We did not observe the former contribution probably because the concentration of unreacted $[\text{Fe}(\text{CN})_6]^{3-}$ is not high enough. The fitted peaks are related to different cyanide stretches based on different energy. Literature shows that the most intense peaks located at 2096 cm^{-1} and 2112 cm^{-1} are assigned to the stretching mode of $\text{Co}^{2+}\text{-NC-Fe}^{2+}$ and $\text{Co}^{3+}\text{-NC-Fe}^{2+}$ bridges. The peak located at 2152 cm^{-1} was reported to be the stretching mode of $\text{Co}^{2+}\text{-NC-Fe}^{3+}$ bridges and the peak located at 2064 cm^{-1} was proved to correspond to non-bridging $\text{Fe}^{3+}\text{-CN}$ at the film surface.^{3,6,7} Thus, the evolution of these four peaks with deposition time is indicative of the formation of a coordination network.

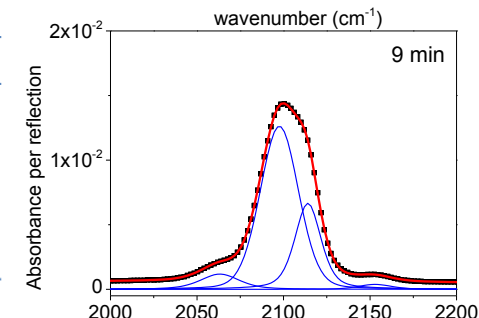
Position	Intensity	Width	Integral	Form
2061.5	0.0046	26.9	0.1607	44% Lor
2096.9	0.0484	26.0	1.6209	44% Lor
2112.4	0.0243	17.5	0.4839	14% Lor
2151.8	0.0011	25.3	0.0449	100% Lor



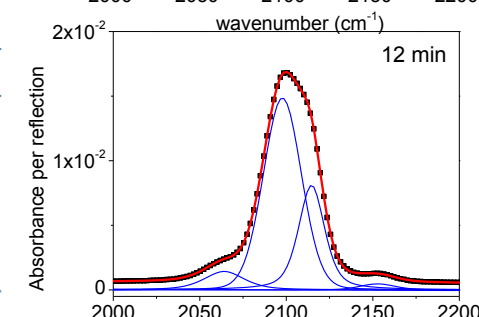
Position	Intensity	Width	Integral	Form
2062.7	0.0082	26.9	0.2829	43% Lor
2097.3	0.0884	26.0	2.7366	25% Lor
2113.4	0.0452	17.5	0.9632	30% Lor
2151.3	0.0021	25.3	0.0572	0% Lor



Position	Intensity	Width	Integral	Form
2063.5	0.0106	26.9	0.3730	47% Lor
2097.6	0.1144	26.0	3.3995	16% Lor
2114.1	0.0600	17.5	1.3306	40% Lor
2151.9	0.0031	25.3	0.0846	0% Lor



Position	Intensity	Width	Integral	Form
2063.9	0.0127	26.9	0.4563	54% Lor
2097.8	0.1346	26.0	3.9023	10% Lor
2114.7	0.0720	17.5	1.6315	46% Lor
2152.2	0.0040	25.3	0.1070	0% Lor



Position	Intensity	Width	Integral	Form
2064.4	0.0148	26.9	0.6237	100% Lor
2098.0	0.1514	26.0	4.3381	8% Lor
2115.0	0.0821	17.5	1.8848	49% Lor
2152.6	0.0050	25.3	0.1595	37% Lor

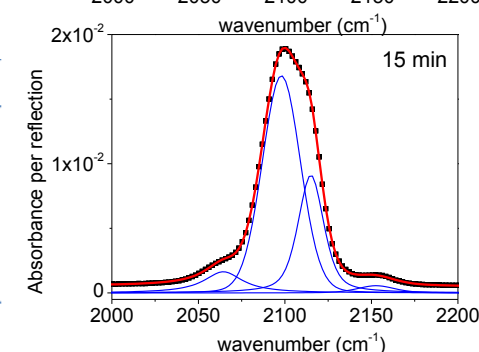


Figure A5.4. In situ IR spectra restricted to the wavenumber range characteristic of cyanide stretching modes for the RbCoFe film at increasing deposition time. The black scatters refer to experimental data, the red lines are the fitting curves, and the blue lines are the individual contributions.

Note that the intensity and the integral presented in the tables of **Figure A5.4** are experimental data not divided by the number of reflections (9 in the present case). The integral per reflection of the four peaks was found to increase with deposition time as shown in **Figure A5.5**. The increasing of the band at 2061 cm^{-1} , which has been assigned to non-bridging Fe^{3+} -CN species, might be associated with the increase of the grain size before the coalescence of the grain (see chapter 4). Another possibility is an increase in the surface roughness, which need to be further confirmed.

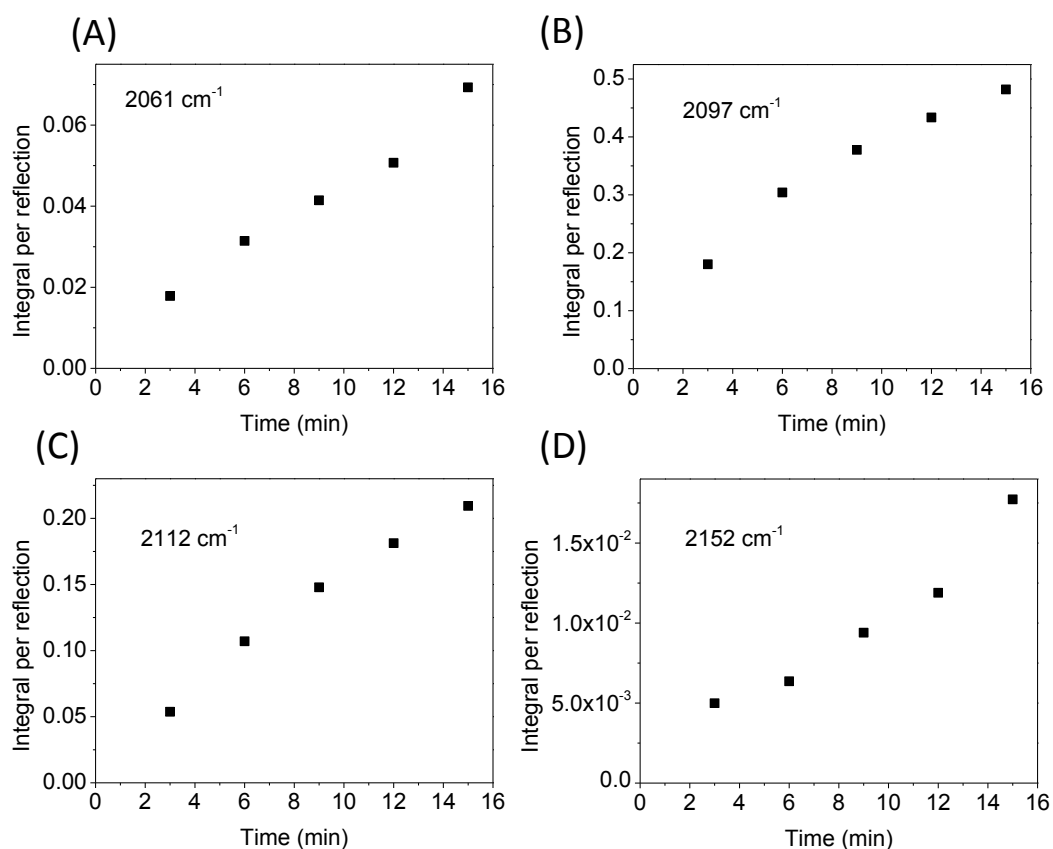


Figure A5.5. Time dependence of the integral per reflection of the peaks at (a) 2061 cm^{-1} ; (b) 2097 cm^{-1} ; (c) 2112 cm^{-1} and (d) 2152 cm^{-1} , the red lines are linear fits to the data.

Note that the as-obtained film corresponds to the one studied in **section 4.4** of Chapter 4. It exhibits the same morphology and structural features than the RbCoFe films grown in the standard cell.

A.5.3 References

1. V. Gadet. PhD thesis. Université Paris VI, Paris, 1992.
2. Nakamoto, K., *Infrared and raman spectra of inorganic and coordination compounds. Parts B: applications in coordination, organometallic and bioinorganic chemistry*. John Wiley & Sons, Inc.; Hoboken, New Jersey, 2009.
3. M. F. Dumont; E. S. Knowles; A. Guiet; D. M. Pajerowski; A. Gomez; S. W. Kycia; M. W. Meisel; D. R. Talham, Photoinduced magnetism in core/shell Prussian blue analogue heterostructures of $K_jNi_k[Cr(CN)_6]_l \cdot nH_2O$ with $Rb_aCo_b[Fe(CN)_6]_c \cdot mH_2O$. *Inorg. Chem.* **2011**, *50*, 4295-4300.
4. P. Bhatt; S. M. Yusuf; R. Bhatt; G. Schutz, Magnetic properties of nanoparticles of Prussian blue-based molecular magnets $M_3[Cr(CN)_6]_2 \cdot zH_2O$ (M=Fe, Co, and Ni). *Appl. Phys. A* **2012**, *109* (2), 459-469.
5. M. Presle. Synthèse et propriétés d'hétérostructure moléculaires de type multiferroïque à base d'analogues du bleu de Prusse. PhD dissertation. Ecole Polytechnique, France, 2011.
6. D. M. Pajerowski; T. Yamamoto; Y. Einaga, Photomagnetic $K_{0.25}Ni_{1-x}Co_x[Fe(CN)_6] \cdot nH_2O$ and $K_{0.25}Co[Fe(CN)_6]_{0.75y}[Cr(CN)_6]_{0.75(1-y)} \cdot nH_2O$ Prussian blue analogue solid solutions. *Inorg. Chem.* **2012**, *51*, 3648-3655.
7. D. M. Pajerowski; J. E. Gardner; D. R. Talham; M. W. Meisel, Anisotropic magnetism in Prussian blue analogue films. *New J. Chem.* **2011**, *35*, 1320-1326.